Development of a high-precision low-latency position feedback system for single-pass beamlines using stripline and cavity beam position monitors

Neven Blaskovic Kraljevic
Linacre College, Oxford

Thesis submitted in fulfilment of the requirements for the degree of Doctor of Philosophy at the University of Oxford

Trinity Term, 2015

Abstract

The FONT beam-based, intra-train feedback system has been designed to provide beam stability at single-pass accelerators, such as at the interaction point (IP) of the International Linear Collider. Two FONT feedback systems have been commissioned at the Accelerator Test Facility (ATF) at KEK, Japan, and the operation, optimisation and performance of these systems is the subject of this thesis. For each system, the accelerator is operated with two-bunch trains with a bunch separation of around 200 ns, allowing the first bunch to be measured and the second bunch to be subsequently corrected.

The first system consists of a coupled-loop system in which two stripline beam position monitors (BPMs) are used to characterise the incoming beam position and angle, and two kickers are used to stabilise the beam. A BPM resolution of about 300 nm has been measured. On operating the feedback system, a factor ~ 3 reduction in position jitter has been demonstrated at the feedback BPMs and the successful propagation of this correction to a witness BPM located 30 m downstream has been confirmed.

The second system makes use of a beam position measurement at the ATF IP that is used to drive a kicker to provide a local correction. The measurement is performed using a high-resolution cavity BPM with a fast decay time of around 20 ns designed to allow multiple bunches to be resolved. The linearity of the cavity BPM system and the noise floor of the electronics are discussed in detail. The performance of the BPM system under standard ATF operation and with the beam waist at the BPM is described. A BPM resolution of about 50 nm has been measured. This IP feedback system has been used to stabilise the beam position to the 75 nm level.

Acknowledgements

Foremost, I would like to thank my supervisor Phil Burrows for giving me the opportunity of performing cutting-edge research in the FONT group and for his continual guidance during the course of my DPhil degree. I have been fortunate to be part of a supportive research group; the effort and advice of all of its members has been central in obtaining the results contained in this thesis. To this end, I would like to thank Glenn Christian for many helpful and detailed discussions that have shaped the research presented herein, Colin Perry for his attention to detail and many insightful suggestions, and Young-Im Kim for bringing us up to speed in the operation and understanding of cavity BPM systems. I am grateful to my fellow DPhil students Douglas Bett, for teaching me the intricacies of the operation of the FONT system, Michael Davis, whose work laid the foundation for this thesis, and Talitha Bromwich, for continuing to advance the research performed so far. I would also like to thank TMD Technologies for sponsoring this work.

I have had the great opportunity to work at ATF in Japan, and would like to thank the ATF and KEK staff for their hospitality. I am grateful to Nobuhiro Terunuma, for his endless dedication, and the entire ATF collaboration, without whom operating the facility would have been impossible. I would especially like to thank Toshiaki Tauchi for leading the IP BPM effort at ATF and his continued involvement, both on and off shift. I am grateful to my fellow PhD students Oscar Blanco from LAL and Siwon Jang from KNU for their contribution towards the IP BPM project and their persevering support on shift.

It has been a pleasure to share many experiences with truly outstanding colleagues and friends, to whom I am very grateful. I have enjoyed an excellent company in the Particle Physics sub-department, from fellow students to post-docs, academics and secretaries. I would like to thank in particular Nazim Hussain, Krish Majumdar, Amy Cottle and Mireia Crispín. I have been lucky to share the ATF experience with fellow collaborators and I would like to thank Marcin Patecki and Juergen Pfingstner for expanding my horizons beyond the confines of the KEK site. I am also thankful to friends at Linacre College who have provided a fresh perspective, company and support when required.

Above all, it is my pleasure to thank my parents, Blanca Kraljevic and Nebojsa Blaskovic, for always believing in me and supporting me with endless enthusiasm at every stage of this endeavour.

Contents

List of Figures

List of Tables

Chapter 1

Introduction

1.1 Standard Model

Particle physics studies the fundamental building blocks of the universe. The research in this field deals with the nature of matter and energy, and the forces between them. Modern particle physics is explained in terms of a mathematical framework known as the Standard Model [1]. It specifies that the universe is composed of half-integer spin fermions and integer spin bosons, where the fermions constitute the basic units of matter and the bosons mediate the interactions.

The fundamental fermions, given in Table 1.1, consist of leptons and quarks. The three charged leptons have a charge of -1 (in units of elementary electric charge) and each one has an associated neutrino of no charge. The up-type and down-type quarks have a charge of $+\frac{2}{3}$ and $-\frac{1}{3}$ respectively. Quarks are bound together into pairs (mesons) and triplets (baryons) by the strong force producing composite particles collectively known as hadrons. The protons and neutrons that make up the nuclei of atoms are examples of baryons consisting of up and down quarks.

In the Standard Model, the interactions between the particles are governed by three fundamental forces: the strong, the weak and the electromagnetic forces. Quarks interact via all three forces, leptons do not experience the strong force and neutrinos are subject to the weak force only. The energy exchanged in the interactions is mediated by the appropriate bosons: the strong force is mediated by the gluon (g), the weak by the $W^{\pm}$ and Z^0 bosons and the electromagnetic by the photon (γ).

Table 1.1: Fundamental fermions of the Standard Model.

	Leptons		Quarks	
Generation	Charged leptons	Neutrinos	Up-type	Down-type
1	Electron (e)	Electron neutrino (ν_e)	Up (u)	Down (d)
2	Muon (μ)	Muon neutrino (ν_μ)	Charmed (c)	Strange (s)
3	Tau (τ)	Tau neutrino (ν_τ)	Top (t)	Bottom (b)

The Higgs boson completes the list of particles predicted by the Standard Model. Its existence was postulated by P. Higgs and others in 1964 to explain the masses of the particles in the model [2]. Since the discovery of the tau neutrino in 2000 [3], the Higgs boson remained the only Standard Model particle experimentally undetected. It was finally observed in 2012 at the Large Hadron Collider (LHC) at CERN in Geneva, Switzerland [4, 5]. Having measured its mass as 125.7±0.4 GeV [6], there is a strong case to develop a precision machine to study its properties in detail. The design and technology required for such a machine is the subject of the sections below.

1.2 Accelerators

Particle accelerators are the main tools used to study the fundamental particles of the Standard Model. Since the initial designs in the early 1930s [7], particle accelerators have continuously been improved to provide higher beam energies and intensities. The current energy record is held by the LHC that has begun delivering 13 TeV proton-proton collisions in 2015 [8].

1.2.1 Linear and circular accelerators

Modern accelerators consist of a series of accelerating cavities, each of which increments the energy of the particles that pass through it. Due to the nature of the fields in the cavities (Sec. 2.1.2), particles are accelerated in bunches and trains of many bunches can be produced. The beamline containing the cavities can follow either a linear or a circular trajectory. In the case of a linear accelerator, the particles are injected at one end and are extracted at their final energy at the other end. Conversely, particles in circular accelerators travel around the machine multiple times and only gain a fraction of their final energy in each circuit around the ring. Particles are kept in a circular path by bending magnets distributed around the beamline.

The two machine designs have advantages and disadvantages. A linear accelerator is a single-pass machine so the accelerated particles can only be used once. This is not the case in circular machines, but these present other challenges. First, the strength of the bending magnets has to be increased in parallel to the increasing particle energy in order to preserve a constant bending radius and keep the particles within the same circular path. Such circular accelerators, where the magnetic field strength is synchronised to the beam energy, are described as synchrotrons [9]. Secondly, charged particles travelling in curved trajectories emit synchrotron radiation in a direction tangential to the beam path [10]. The power radiated in a ring of radius ρ by particles of energy E and rest mass m_0 is [11]:

$$P_\gamma \propto \frac{1}{\rho^2} \left(\frac{E}{m_0} \right)^4 . \tag{1.1}$$

In order to achieve a net increase in the energy of the particles, the power supplied to the beam by the accelerating cavities must exceed P_γ every turn, which is increasingly difficult for larger $\frac{E}{m_0}$ ratios.

1.3 Colliders

Once particles have been accelerated, particle physics experiments can be performed by making them collide and observing what is produced using a particle detector. The energies of the colliding particles determine the interactions that can proceed, as sufficient energy has to exist to provide the mass of the final particles and any kinetic energy required to conserve momentum. The set-up that maximises the energy available to create new particles is one which involves the head-on collision of two accelerated beams of equal energy [12]. The location where the particles collide is described as the interaction point (IP).

The rate R at which a given particle interaction X will occur at the IP is given by:

$$R(X) = L\sigma(X), \tag{1.2}$$

where $\sigma(X)$ is the cross-section of the interaction and L is the luminosity. The cross-section has the units of area, typically in femtobarns (1 fb $\equiv 10^{-43}$ m^2), and a rare interaction will have a small cross-section. The luminosity is a property of the colliding beams, typically expressed in units of cm^{-2} s^{-1} [13], and is given by [11]:

$$L = H\frac{fN^2}{4\pi\hat{x}^*\hat{y}^*}, \tag{1.3}$$

where f is the bunch crossing frequency at the IP, N is the number of particles in each bunch, $\hat{x}^*$ and $\hat{y}^*$ are the horizontal and vertical beam sizes at the IP respectively, and H is a factor that accounts for electromagnetic forces between the two beams at the collision.

1.3.1 Hadron and lepton colliders

Particle colliders can accelerate and collide either hadrons or leptons. Due to their relatively larger mass, hadrons emit less synchrotron radiation power in circular accelerators of a given radius (Eq. 1.1) and can thus attain higher energies. The energy, however, is distributed among the constituent quarks and gluons so the energy of the fundamental particles involved in a collision will be smaller and their specific energy will be unknown. In addition to the unknown incoming kinematics of the constituent particles, the composite nature of the hadrons leads to the production of large backgrounds making particle identification inherently complicated [14].

Lepton colliders involve the collision of fundamental point-like particles, so the incoming beam kinematics of the colliding particles is known and the background is reduced. The energy of the incoming particles can be tuned to the resonant energy of a chosen interaction, thus increasing the cross-section and enhancing the rate of production [15]. The lower

Table 1.2: Design parameters for the ILC [19] and CLIC [20].

Parameter			ILC	CLIC
Energy		(GeV)	500	3000
Number of bunches		(bunches/train)	1312	312
Intensity		(10^{10} electrons/bunch)	2.0	0.372
Bunch separation		(ns)	554	0.5
Repetition rate		(Hz)	5	50
Main linac average gradient		(MV/m)	31.5	100
Horizontal IP beam size	$\hat{x}^*$	(nm)	474	40
Vertical IP beam size	$\hat{y}^*$	(nm)	5.9	1
Luminosity	L	(10^{34} cm^{-2} s^{-1})	1.8	5.9
Site length		(km)	31	48.4

background levels allow the particle detector to be designed for precision [14]. The design of a future machine to study the properties of the Higgs boson in detail would thus be a lepton collider.

1.3.2 Future colliders

The technology required for a future lepton collider is conditioned by the type of lepton chosen. Muon and tau leptons present a difficulty due to their short lifetimes of 2 μs and 300 fs respectively [6]. Although research towards a circular muon collider is ongoing, the short lifetime and the large particle backgrounds generated by the decaying muons make the design of such a machine extremely challenging [16]. Therefore, the next lepton collider will almost surely collide electrons and positrons.

The design of an electron-positron collider must take into account the energy dissipated by the particles through the emission of synchrotron radiation. This is critical for electrons, which being approximately 2000 times lighter than the proton [6], would emit $\sim 10^{13}$ times more power than protons travelling around the same circular path (Eq. 1.1). In fact, the 209 GeV collision energy achieved at the Large Electron-Positron Collider (LEP) at CERN [17] is considered to be close to the practical limit for a circular machine [18]. Therefore, in order to achieve lepton collisions at or close to the TeV scale, one must resort to linear electron-positron colliders.

At present there are two international collaborations working towards the next generation linear e^+e^- colliders: the International Linear Collider (ILC) and the Compact Linear Collider (CLIC). Some key parameters of both accelerators are given in Table 1.2 and the designs are described below.

International Linear Collider

The ILC [19] design consists of two superconducting linear accelerators, one for electrons and the other for positrons, pointing towards each other (Fig. 1.1). With an initial collision energy tunable from 200 to 500 GeV, the ILC is primarily designed

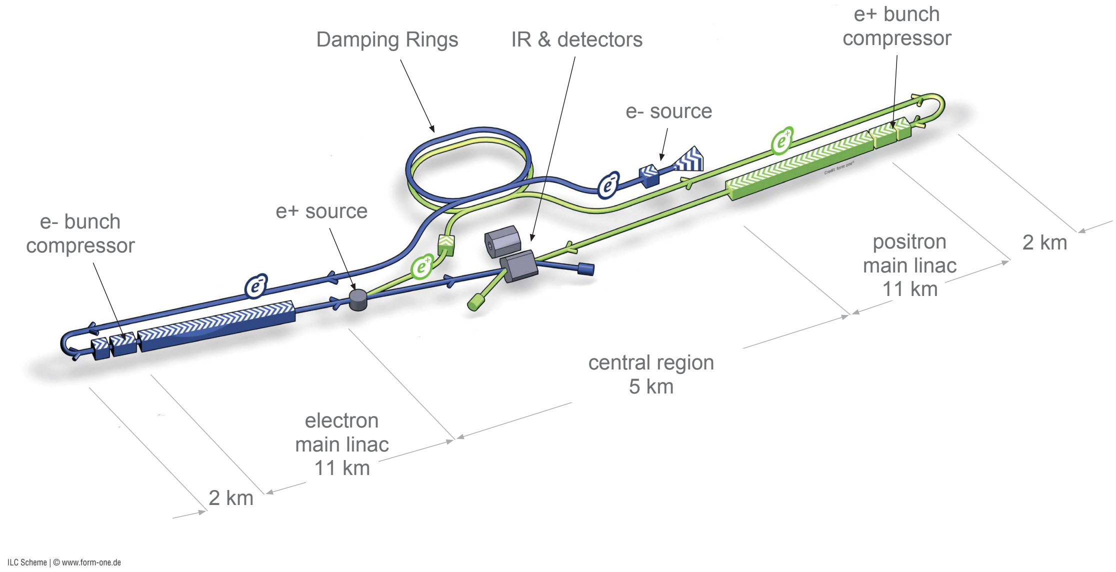

Figure 1.1: Schematic layout of the ILC [19].

as a Higgs factory with Higgs bosons predominantly produced via Higgs-strahlung (ee $\rightarrow$ ZH) and WW fusion (ee $\rightarrow \nu\nu$H) as shown in Fig. 1.2. The ILC expects to attain an integrated luminosity of 250 fb^{-1} after three years of operation at a collision energy of 250 GeV [21], producing about 80 000 Higgs bosons [22]. The ILC is designed with the option of extending the collision energy to 1 TeV in the future.

Compact Linear Collider

The CLIC [20] design is for a machine with an even larger collision energy. It makes use of a novel two-beam accelerating technique. A high current drive beam is accelerated using room temperature cavities to an energy of 2.38 GeV and then decelerated; the energy extracted from the deceleration is used to drive a lower current beam to 1.5 TeV (Fig. 1.3). In this way, electron-positron collisions at an energy of 3 TeV would be possible. The technology for CLIC is less developed than that for the ILC, and a prototype of the system is located at the CLIC Test Facility (CTF3) at CERN [23].

1.3.3 Feedback systems for linear colliders

Table 1.2 shows how both ILC and CLIC designs make use of a flat beam at the IP with $\hat{x}^* \gg \hat{y}^*$. This choice is influenced by the beam-beam effects present at the collision as the particles will be deflected in the electromagnetic field of the oncoming beam. As a result of the transverse acceleration, the particles emit beamstrahlung radiation [25] and acquire an unwanted energy spread δ_{BS}:

$$\delta_{\mathrm{BS}} \propto \frac{1}{(\hat{x}^* + \hat{y}^*)^2}. \tag{1.4}$$

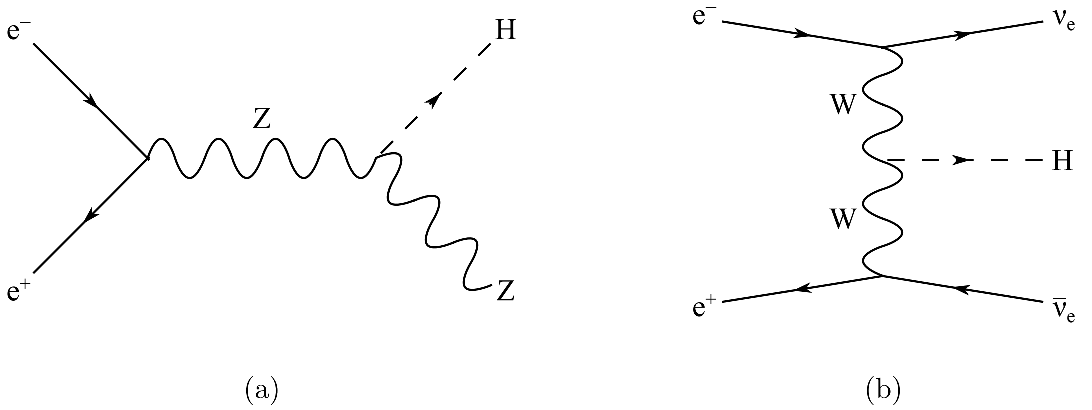

Figure 1.2: Feynman diagrams for production of Higgs bosons via (a) Higgs-strahlung and (b) WW fusion [24].

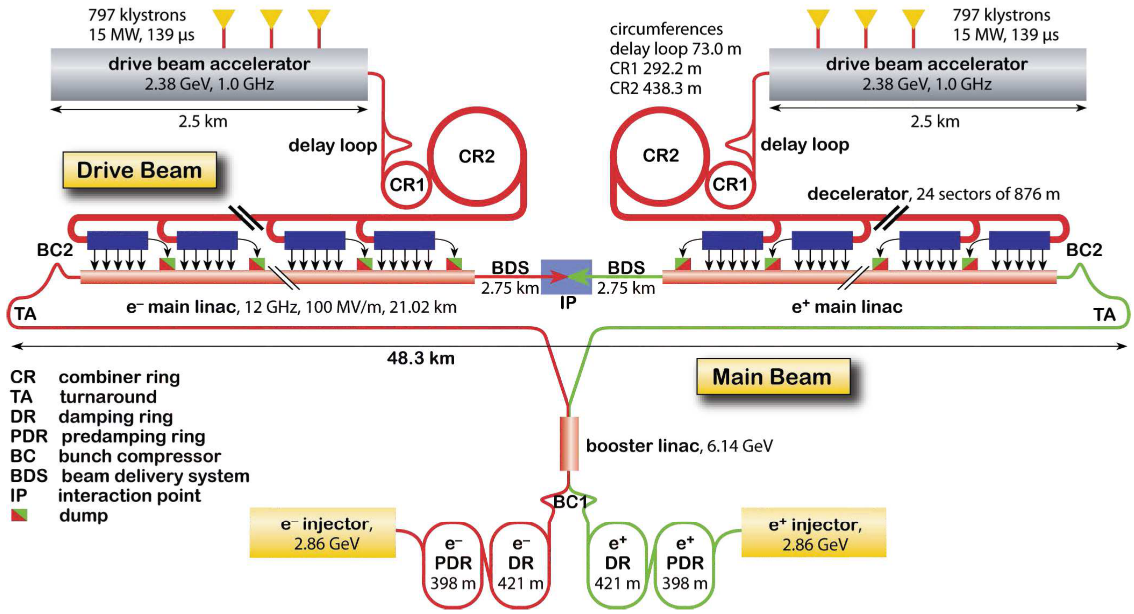

Figure 1.3: Schematic layout of CLIC [20].

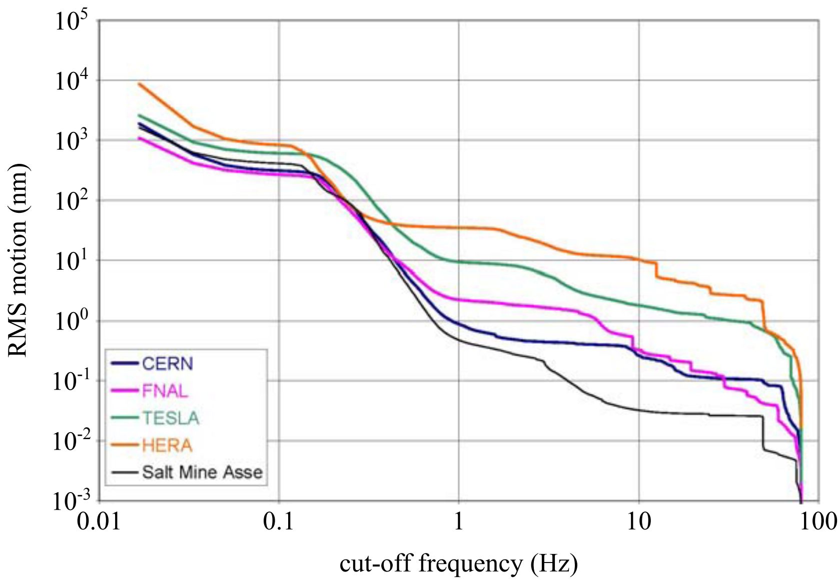

Figure 1.4: Vertical RMS ground motion, integrated above a cut-off frequency w, versus w for a range of locations [26].

Therefore, a flat beam minimises δ_{BS} whilst maximising the luminosity L (Eq. 1.3).

The accelerator designs call for vertical beam sizes of a few nanometres, giving paramount importance to the beam stability at the IP in order to achieve successful electron-positron collisions. Fig. 1.4 shows the ground motion measured at various sites as a function of frequency. Motion of up to the order of tens of nanometres is expected at the train repetition frequency of 5 Hz at the ILC. Therefore, an intra-train position feedback system is essential in order to achieve and maintain the luminosity at the collider.

Fig. 1.5 shows the design of such a feedback system in the region where the electron and positron beams cross. If a pair of bunches are transversely misaligned they will deflect each other; the deflection can then be measured using a beam position monitor (BPM) downstream of the interaction. The position measurement is processed and a feedback correction signal is generated and amplified. The correction is applied to the next bunch in the train using the kicker on the other incoming beam.

The feedback system is thus able to correct all bunches in the train after the first bunch. The delay loop (Fig. 1.5) stores the correction signal in order to ensure that the required kick is applied to all subsequent bunches. In this way, the initial correction is maintained whilst being continuously refined with the measurements performed on the later bunches.

1.4 Thesis outline

The work in this thesis is a contribution towards beam stabilisation at single-pass accelerators such as linear colliders. The experiments have been performed in the context of the FONT

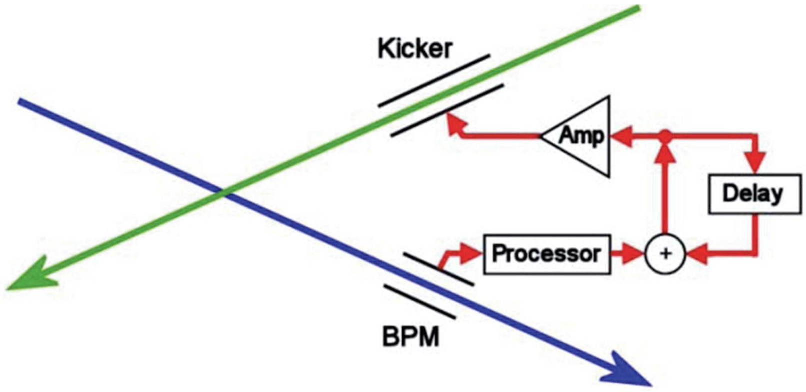

Figure 1.5: Schematic of an IP intra-train feedback system for an interaction region with a crossing angle [27].

intra-train feedback system, which is described in Chapter 2. The use of high-resolution cavity BPMs as an input to the feedback system has been studied. The operating principles of such BPMs are introduced in Chapter 3 and their performance using beam-based experiments at the Accelerator Test Facility are analysed in Chapter 4. The set-up, operation and results of an IP feedback system employing these BPMs is presented in Chapter 5. The thesis closes with conclusions and suggestions for further work in Chapter 6.

Chapter 2

Intra-train feedback at ATF

2.1 Concepts in beam dynamics

This section presents some basic concepts in beam dynamics that will be used throughout this thesis. A Cartesian coordinate system is used where z constitutes the longitudinal axis in the direction of beam propagation, and x and y are the transverse horizontal and vertical axes, respectively.

2.1.1 Transverse dynamics

The transverse motion of a particle in an accelerator is described by a modified sinusoidal oscillation known as a betatron oscillation [28]:

$$y = \sqrt{\beta(z)\epsilon}\cos(\mu(z) + \mu_0) \tag{2.1}$$

where β is the beta function, ϵ is the emittance, μ is the phase advance and μ_0 is a constant for any given particle. Each of these concepts is explained in the following paragraphs.

The phase advance $\mu(z)$ determines the phase of the sinusoidal oscillation at z relative to that at $z = 0$, and is set by the distribution of magnetic elements along the beamline. A phase advance of 2π between two points indicates that one period of the oscillation is completed over that distance. The phase parameter μ_0 describes the initial phase of any given particle at $z = 0$.

The term $\sqrt{\beta(z)\epsilon}$ specifies the amplitude of the sinusoidal oscillation. The emittance ϵ is a conserved quantity under Liouville's theorem [29]. Liouville's theorem does not apply when particles emit some of their own energy [29], such as electrons travelling through bending magnets, which allows the emittance to be reduced as described in Sec. 2.2. The beta function $\beta(z)$ modulates the amplitude of the beam's betatron oscillations along the beamline.

A simple magnet structure, known as a FODO lattice, consists of focusing and defocusing quadrupoles interspersed by drifts. Fig. 2.1 shows that the beta function is minimised at the defocusing quadrupole and maximised at the focusing quadrupoles. The figure illustrates that the beta function constitutes an envelope of the individual particle trajectories, and can be used to identify the location of the beam waist at the defocusing quadrupole.

The transverse position y and its divergence $y' = \frac{\mathrm{d}y}{\mathrm{d}z}$ can be plotted in phase space diagrams, as shown at each quadrupole in Fig. 2.1. The phase space ellipses encircle a nominal fraction of the particles, typically one standard deviation of a Gaussian beam [29]. At the quadrupoles, where $\frac{\mathrm{d}\beta}{\mathrm{d}z} = 0$, the ellipses' semi-axes coincide with y, y' coordinate axes. In these cases, the y and y' semi-axes give the beam size $\hat{y}$ and the divergence spread $\hat{y}'$, respectively. As shown in Fig. 2.1:

$$\hat{y} = \sqrt{\epsilon\beta(z)}; \tag{2.2}$$

$$\hat{y}' = \sqrt{\frac{\epsilon}{\beta(z)}}. \tag{2.3}$$

Thus, the area of the ellipse $\pi\hat{y}\hat{y}'$ is equal to the conserved quantity $\pi\epsilon$.

In the general case, where $\frac{\mathrm{d}\beta}{\mathrm{d}z} \neq 0$, the ellipse is rotated relative to the y, y' coordinate system. In order to describe the resulting ellipse, it is convenient to define the functions α and γ [11]:

$$\alpha(z) = -\frac{1}{2}\frac{\mathrm{d}\beta(z)}{\mathrm{d}z}; \tag{2.4}$$

$$\gamma(z) = \frac{1 + (\alpha(z))^2}{\beta(z)}. \tag{2.5}$$

The variables α, β and γ are collectively known as the Twiss parameters. Their relationship to a general phase space ellipse is shown in Fig. 2.2.

A beam is generally well modelled as a bivariate normal distribution in phase space [30]. Therefore, at the beam waist, where $\frac{\mathrm{d}\beta}{\mathrm{d}z} = 0$, no correlation is expected between the y and y' variables. This statement is demonstrated by the beam simulation presented in Sec. 2.8.

Finally, it is important to note that the beam transport of the state vector

$$\mathbf{y} = \begin{pmatrix} y \\ y' \end{pmatrix} \tag{2.6}$$

through a beamline element such as a drift, bending magnet or quadrupole can be expressed using the transfer matrix formalism [11]. The final state vector $\mathbf{y}_2$ can be expressed in terms of the initial vector $\mathbf{y}_1$ and the 2×2 transfer matrix $\mathbf{M}$:

$$\mathbf{y}_2 = \mathbf{M}\mathbf{y}_1. \tag{2.7}$$

Matrices from consecutive beamline elements can be multiplied together to obtain the transfer matrix between two points in the accelerator lattice, as discussed in Sec. 2.8.

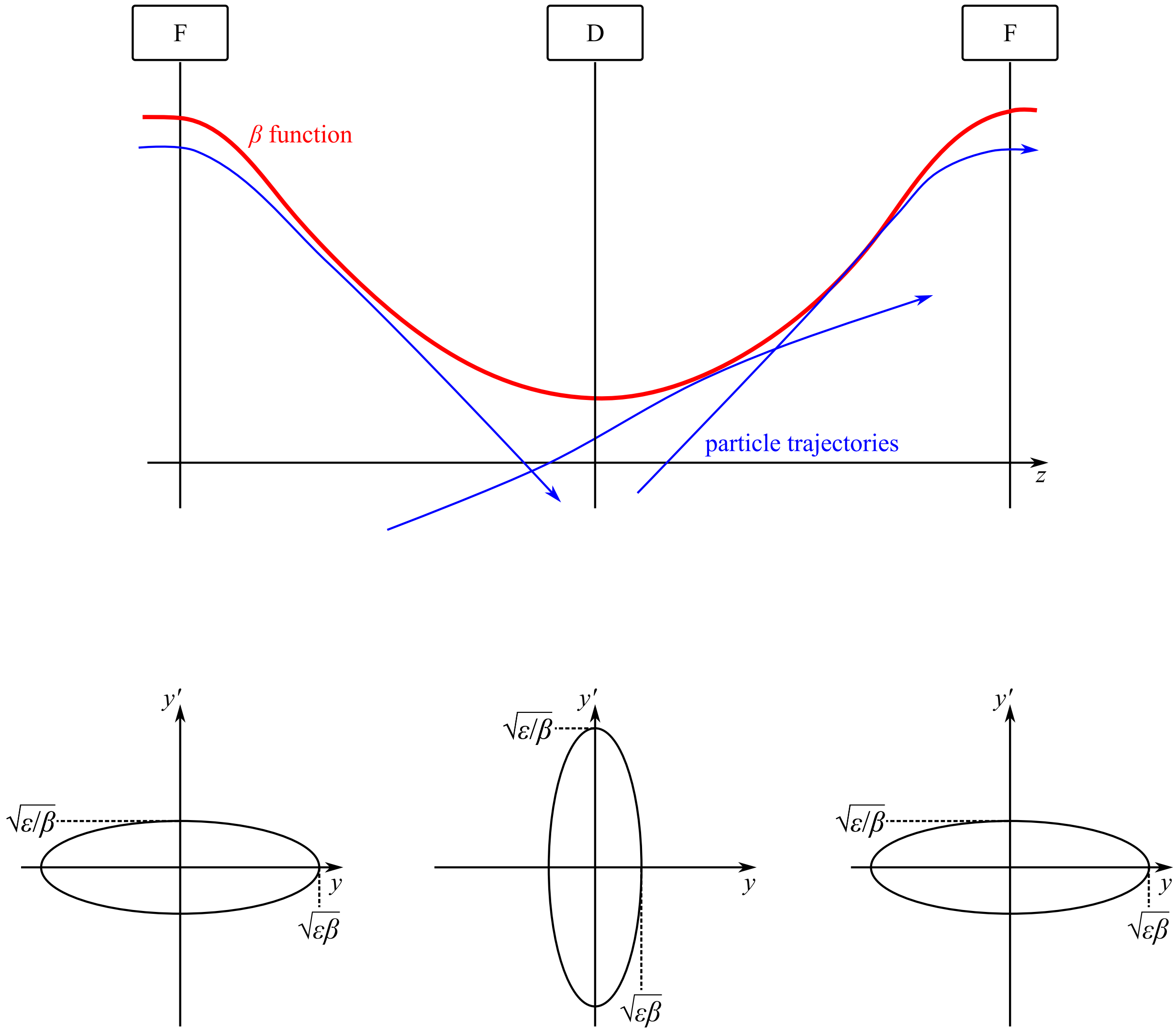

Figure 2.1: Top: $\beta(z)$ (red) and particle trajectories (blue) versus longitudinal distance z in a FODO lattice consisting of focusing (F) and defocusing (D) quadrupoles. Bottom: y' versus y phase space ellipses at each quadrupole. Adapted from [11].

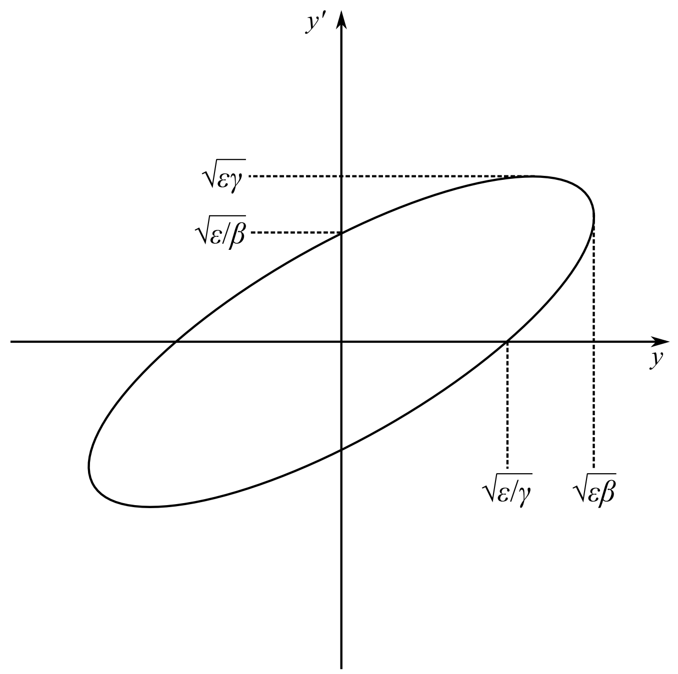

Figure 2.2: General ellipse in y' versus y phase space, and its relationship to the Twiss parameters α, β and γ [30].

2.1.2 Longitudinal dynamics

Consider a damping ring which consists of bending magnets and one or more accelerating cavities to restore the energy lost by synchrotron radiation. As the accelerating cavity is operated with a sinusoidal voltage, particles are grouped in bunches in order to receive approximately the same accelerating potential. The timing of the cavity accelerating voltage relative to the bunches is shown in Fig. 2.3 [11].

A synchronous bunch will receive an energy from the accelerating cavity that matches exactly the energy radiated away in the ring and will remain phase-locked to the accelerating voltage. Bunches arriving early at the cavity will receive more energy, thus taking a longer path around the ring and arriving back at the cavity later than in the previous turn. As this continues, the early bunches will eventually arrive at the cavity after the synchronous bunch and the reverse process will then follow.

These longitudinal oscillations of the bunches are described as synchrotron oscillations [11] and will affect the time of arrival of bunches extracted from the damping ring. The time interval Δt between a given bunch and the synchronous bunch can be expressed as a bunch phase Φ, which in radians is:

$$\Phi = 2\pi f \Delta t \tag{2.8}$$

where f is a frequency. Given the technique used to measure the bunch phase, described in

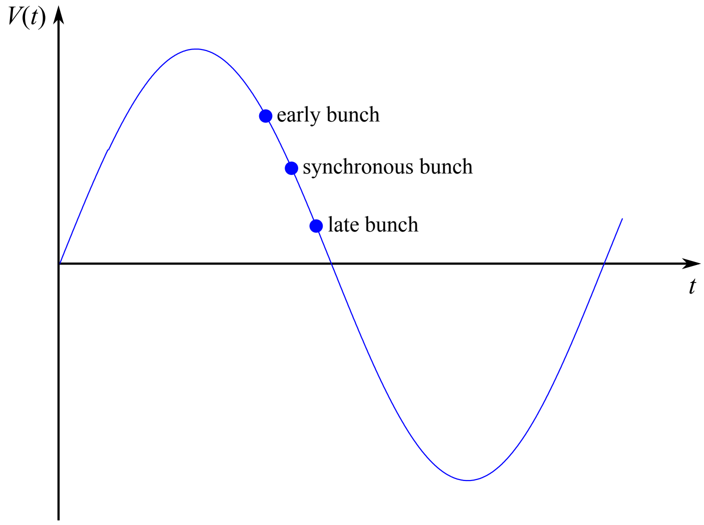

Figure 2.3: Accelerating voltage $V(t)$ versus time t, and the relative timing of early, late and synchronous electron bunches.

Sec. 2.4, $f = 714$ MHz is used in this thesis.

2.2 Accelerator Test Facility

The Accelerator Test Facility (ATF) is an accelerator at the High Energy Accelerator Research Organisation (KEK) [31] in Tsukuba, Japan. The ATF is designed as a test bed for the future generation of ILC-like linear electron accelerators. With beam operation starting in 1997, the original goal of the facility was to achieve the super low emittance beam required for future electron colliders [32]. The design parameters were achieved in 2001 [33].

In 2008, as part of the ATF2 project [34], the accelerator was upgraded. The original linear accelerator (linac) and damping ring (DR) were used, and the existing extraction line was replaced with one leading to an energy-scaled version of the compact focusing optics designed for the ILC [35]. The ATF2 design parameters are given in Table 2.1 and the layout of the facility is shown in Fig. 2.4.

The electrons at ATF are generated with a laser driven photo-cathode RF gun. For the results presented in this thesis, the accelerator was operated with a bunch repetition frequency of 3.12 Hz. The electron bunches are subsequently accelerated, over 90 metres, to an energy of 1.3 GeV by a room temperature linac [39]. The bunches are transported through the transfer line before being injected into the DR.

The beam is stored in the DR for over 100 ms [39], where the beam emittance is reduced through the process of radiative damping. In this process, the transverse betatron oscillations are damped as the electrons lose their momentum by emitting synchrotron radiation in the bends. Accelerating cavities in the ring restore the longitudinal momentum, thus preserving

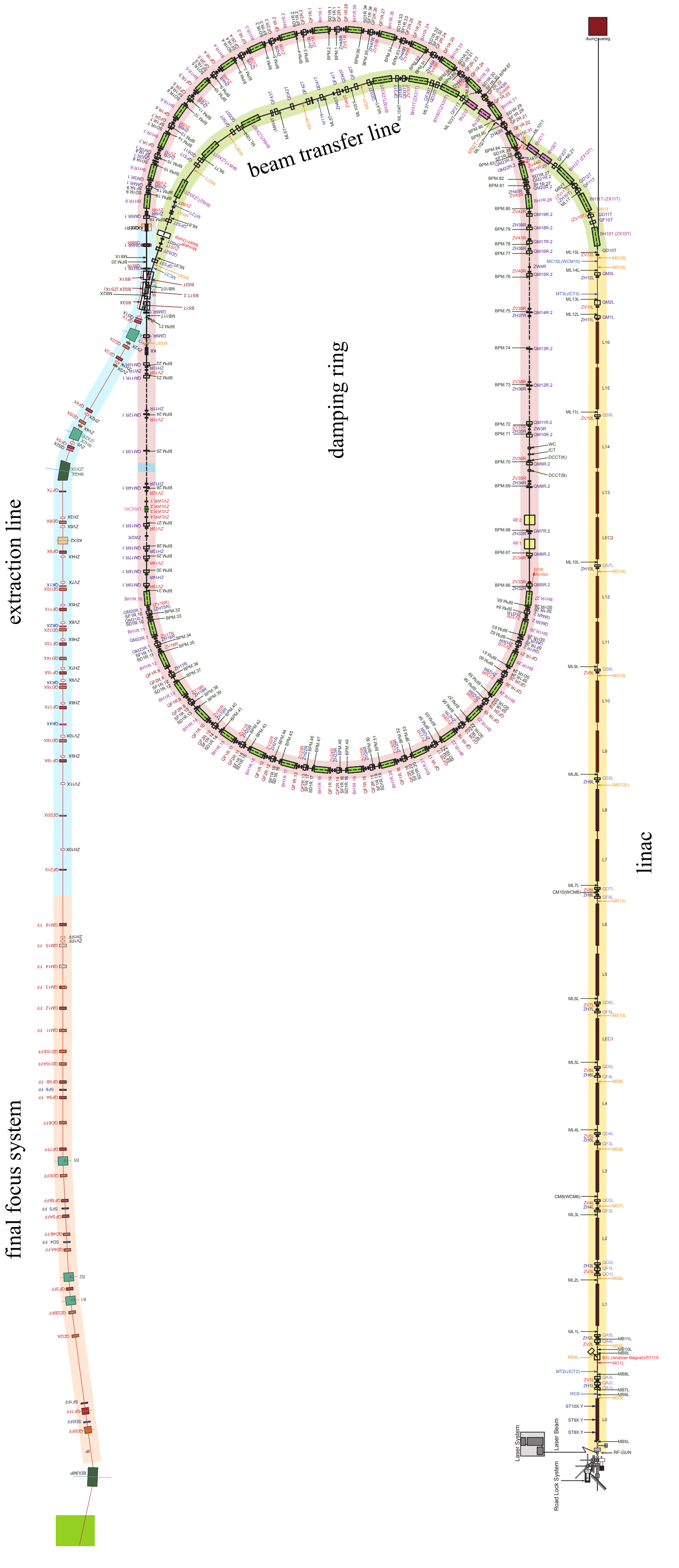

Figure 2.4: Layout of the ATF accelerator complex [38], indicating the five beamline sections.

Table 2.1: Design parameters for the ATF2 [36, 37].

Parameter			Design value
Energy		(GeV)	1.3
Intensity		(electrons/bunch)	1×10^{10}
Repetition rate		(Hz)	3.12
Horizontal emittance	ϵ_x	(m rad)	2×10^{-9}
Vertical emittance	ϵ_y	(m rad)	1.2×10^{-11}
Horizontal IP beam size	$\hat{x}^*$	(m)	2.8×10^{-6}
Vertical IP beam size	$\hat{y}^*$	(m)	3.7×10^{-8}
Horizontal IP beta function	β_x^*	(m)	4×10^{-3}
Vertical IP beta function	β_y^*	(m)	1×10^{-4}
RMS energy spread		(%)	0.08

the beam energy [40].

Once an electron bunch has been damped it can be extracted from the DR using a pulsed magnetic kicker [41], producing a single bunch in the extraction line. The ATF is also capable of extracting trains of two or three bunches with an ILC-like bunch separation of a few hundred nanoseconds. In this case, the linac injects bunches into the DR at the usual repetition rate but two (or three) bunches are stored before being extracted. Once the bunches have been damped, a single extraction kicker pulse extracts all the bunches.

When operating in multi-bunch mode, the separation of the bunches in the ring, and hence of the extracted train, can be adjusted by controlling the bunch injection timing. The maximum train length is set by the 300 ns flat top of the extraction kicker pulse [42]. The timing of the extraction kicker is adjusted in order to ensure a good extraction of all bunches.

The bunches travel through the extraction line which contains beam diagnostic devices, such as Optical Transition Radiation (OTR) systems for transverse beam size measurements and emittance reconstruction [43]. The beam then enters the final focus system (FFS) which culminates at the IP where the beam size is minimised, with a target vertical size of 37 nm [34].

The ATF2 presently has the following two goals [34]:

Goal 1: Demonstration of 37 nm beam size

Significant progress has been made towards this goal, achieving a measured beam size of 44 nm [44].

Goal 2: Demonstration of nanometre level beam stabilisation

This involves the use of intra-train feedback systems and the work contained in this thesis is an effort towards this goal.

2.3 Feedback on Nanosecond Timescales

The Feedback on Nanosecond Timescales (FONT) project was conceived in 1999 to achieve intra-train beam stabilisation, and hence successful collisions, at future linear colliders such as the ILC and CLIC. The first three iterations FONT1 [45], FONT2 [46] and FONT3 [47] comprised fully analogue systems designed for minimum latency; the shortest closed-loop latency achieved was 23 ns.

The subsequent versions, FONT4 and FONT5, were designed around a digital feedback board for added flexibility. Although this increases the signal processing time, the feedback latencies of 148 ns [48] for the FONT4 system and 159 ns [49] for the FONT5 set-up are sufficiently short to allow bunch-by-bunch feedback at the design ILC bunch spacing. Operated from 2005 to 2009, a FONT4 digital board could perform single-loop feedback, with an input from one BPM and an output to one kicker [50]. The FONT5 digital board is more sophisticated, allowing coupled-loop feedback with inputs from two BPMs and outputs to two kickers [51]. Two such FONT5 boards have been instrumented in the study presented in this thesis.

Since ATF only contains an electron beam, the FONT feedback system deployed at ATF makes use of the same beam for measurement and correction. The first bunch in a train is measured using one or more BPMs, and this information is processed in time to apply a correction to the next bunch. The feedback results presented in this thesis make use of trains of two bunches; the extension to three bunches has been tested successfully in the past [51].

Due to the large beam-beam deflection of misaligned beams at the IP, a sub-micron BPM resolution is sufficient to achieve the ILC requirement of detecting beam offsets of a fraction of a nanometre at the collision point [52]. This BPM resolution, as well as the required system latency for an intra-train feedback system at the ILC, have successfully been demonstrated with the FONT system [48], and the present work concentrates on extending the feedback system further in the context of the ATF2 goals presented in Sec. 2.2.

To this end, the FONT system is distributed along the extraction and final focus lines of the ATF. The locations of the relevant beamline elements are labelled in Fig. 2.5. The system consists of an upstream region in the extraction line, consisting of stripline BPMs P1, P2 and P3 and kickers K1 and K2. The stripline BPM MFB1FF, located at the beginning of the final focus line, can be used to monitor the propagation of the feedback correction performed in the upstream region. Finally, the IP region contains three cavity BPMs IPA, IPB and IPC (collectively known as IP BPMs) and a kicker IPK. The location of the nominal IP has been labelled.

Also shown in Fig. 2.5 are the ATF quadrupoles which in the extraction line are incrementally labelled QF[n]X if horizontally focusing or QD[n]X if horizontally defocusing. A similar pattern is followed in the final focus, with the 'X' suffix replaced by 'FF' and the indices placed in descending order. In this way, the quadrupoles QF1FF and QD0FF constitute the final doublet before the IP.

The FONT beamline elements are instrumented as shown in Fig. 2.6. Each of the BPMs

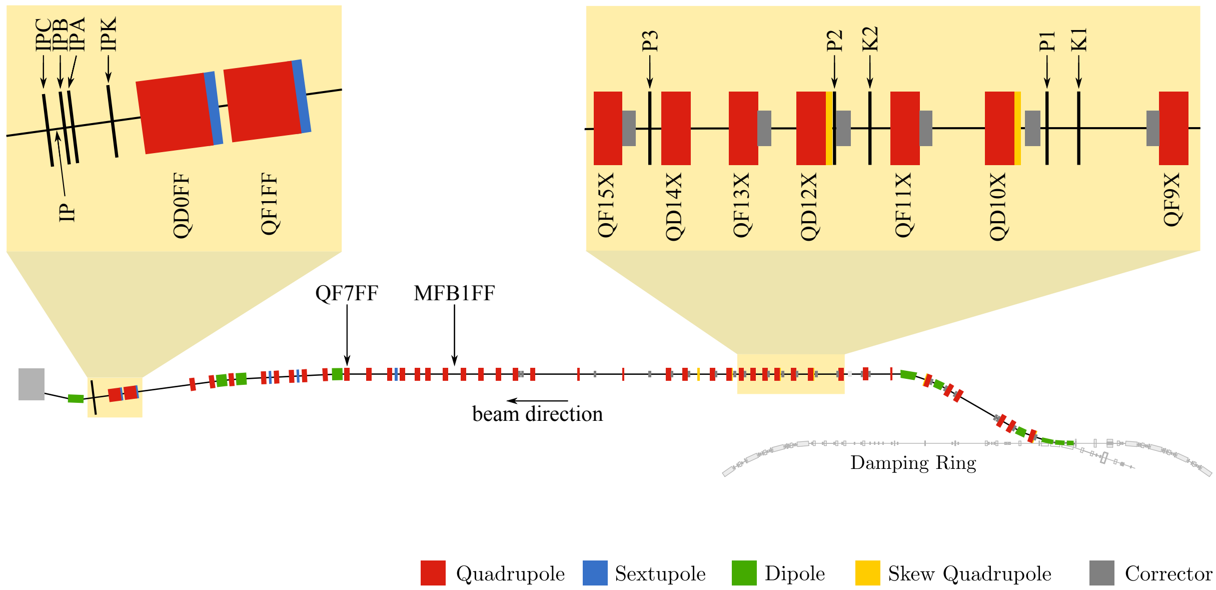

Figure 2.5: Layout of the ATF extraction and final focus lines [36], indicating the location of the stripline BPMs (P1, P2, P3 and MFB1FF), cavity BPMs (IPA, IPB and IPC) and kickers (K1, K2 and IPK) used by the FONT system. The locations of relevant quadrupoles ('Q') and of the nominal IP are shown.

is connected to its analogue processing electronics. Different electronics are used for the stripline and cavity BPMs; these are described in Sec. 2.4 and Chapter 3, respectively. The signals from the electronics are input into the corresponding FONT5 digital board, with two boards distributed as shown. The outputs of the FONT5 boards are used to drive the local kickers, as described in Sec. 2.6.

The set-up outlined in Fig. 2.6 can be used to operate two different feedback modes:

Upstream feedback

This mode of feedback makes use of BPMs P2 and P3 as inputs in order to drive kickers K1 and K2, and is described in Sec. 2.7.

IP feedback

This mode of feedback employs an IP BPM (for example, IPB) to operate the kicker IPK, and the results are presented in Chapter 5.

2.4 Stripline BPMs and analogue processor electronics

The processing electronics used for the stripline BPMs P1, P2, P3 and MFB1FF has been designed and developed by the FONT group with the goal of achieving a high position resolution with a low processing latency. The stripline BPM outputs are used to drive the upstream feedback system (Sec. 2.7) and as inputs to the beam propagation simulation

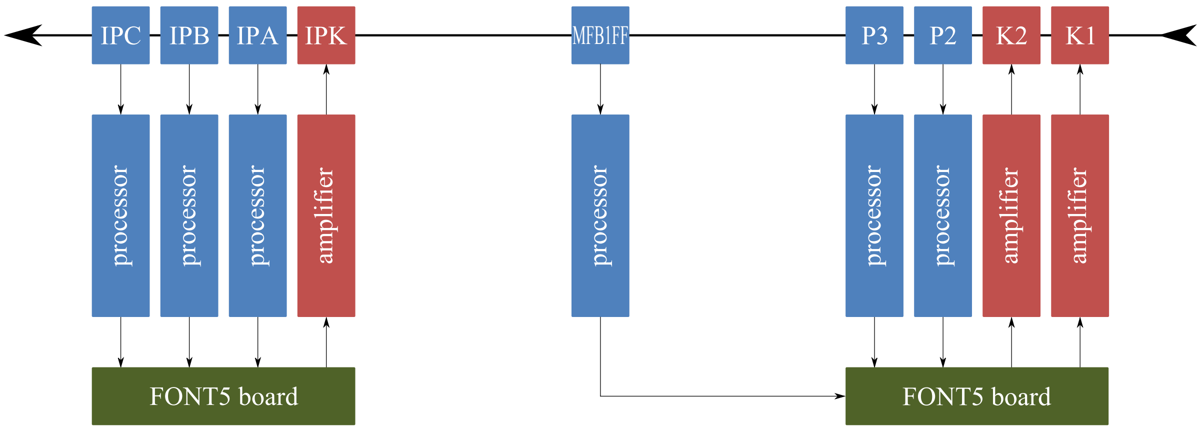

Figure 2.6: Block diagram of the operation of the FONT system including the BPMs with their processing electronics (blue), the FONT5 boards (green) and the kickers with their amplifiers (red).

(Sec. 2.8). In addition, they are used to provide measurements of the bunch phase and charge for the studies presented in later chapters.

A comprehensive report on the design, operation and results of the stripline BPM system can be found in [53] and in references contained therein. An outline of the system, with the aspects relevant to this thesis, is the subject of this section.

2.4.1 Stripline BPMs

The stripline BPMs at ATF consist of four strips of conducting material placed along the inner surface of the beam pipe. The strips are aligned with their lengths along the z direction, and are symmetrically distributed in x and y as shown in the BPM cross-section in Fig. 2.7. BPMs P1, P2 and P3 are each mounted on an x, y mover system developed by the University of Valencia IFIC group [54], with a range of motion of ± 1.5 mm in both axes and a minimum step size of 1 µm [53]. A photograph of P3 and its mover is given in Fig. 2.8.

When a bunch passes through the BPM, a voltage pulse is induced in the strips which is a function of the beam charge q, the BPM inner radius R, the impedance ρ of the measurement electronics and the x, y beam position within the BPM. The top and bottom strips, labelled 'T' and 'B' respectively, are used to determine the y position of a passing bunch. For the operating condition $y \ll R$, the voltages induced on the strips are [55]:

$$V_{\mathrm{T}}(t) \propto \big(1 + \frac{2y}{R}\big)\rho\frac{\mathrm{d}q}{\mathrm{d}t}, \tag{2.9}$$

$$V_{\mathrm{B}}(t) \propto \big(1 - \frac{2y}{R}\big)\rho\frac{\mathrm{d}q}{\mathrm{d}t}. \tag{2.10}$$

A similar set of equations can be obtained for x by using the other pair of strips, but the

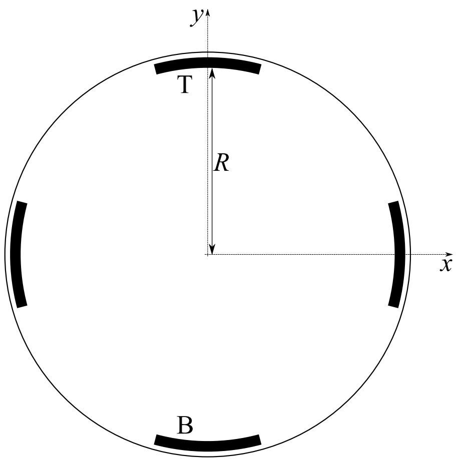

Figure 2.7: Cross-section of a stripline BPM, with the top (T) and bottom (B) strips labelled.

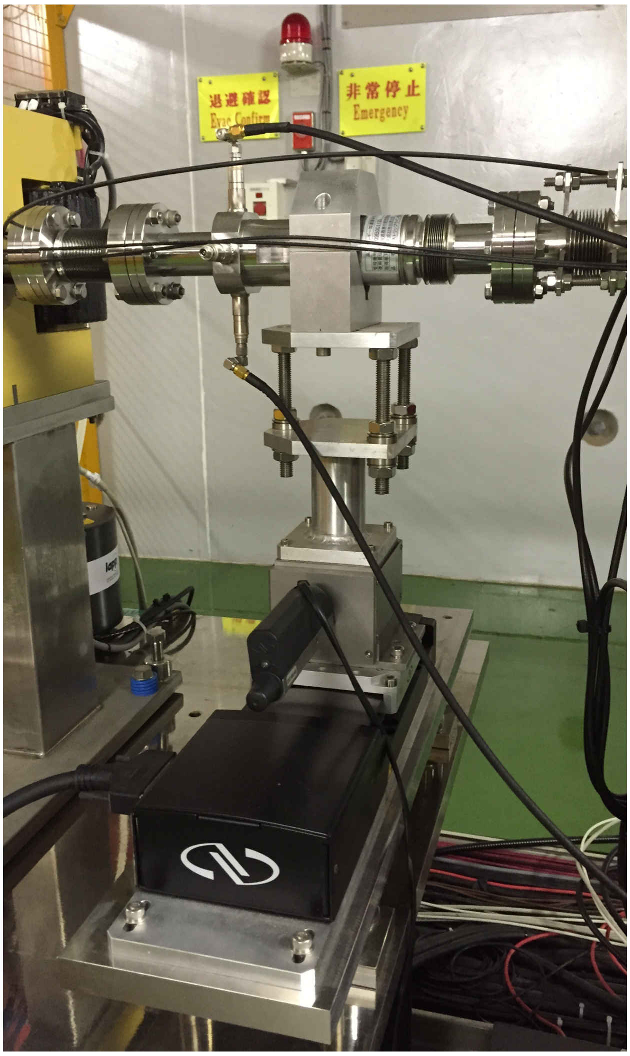

Figure 2.8: Photograph of the stripline BPM P3 and its mover in the ATF beamline.

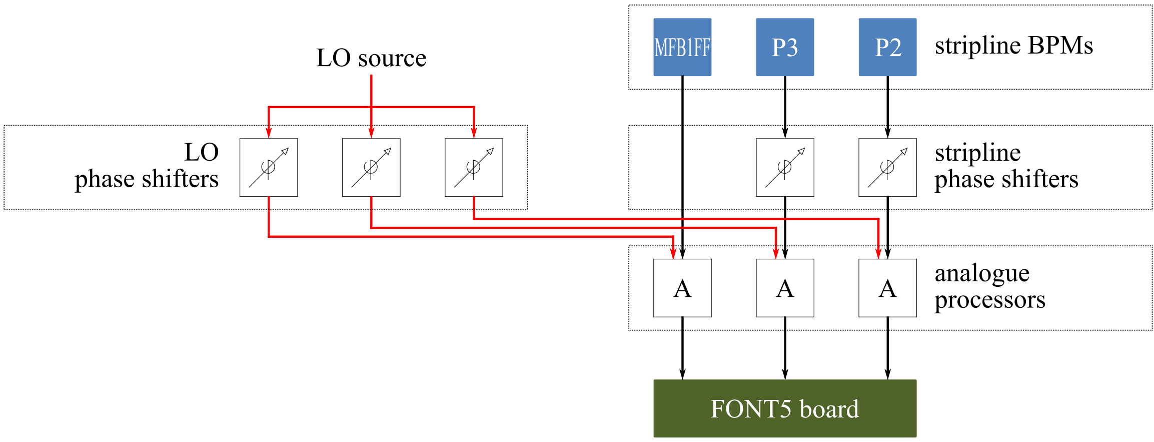

Figure 2.9: Block diagram of the system of stripline BPMs and their processing electronics (adapted from [53]). The LO signals are shown in red.

discussion below will proceed using y. The difference over sum processing scheme used by the FONT processors involves finding the sum V_Σ and the difference V_Δ of the stripline signals:

$$V_\Sigma(t) = g_\Sigma(V_\mathrm{T}(t) + V_\mathrm{B}(t)) \propto 2g_\Sigma\rho\frac{\mathrm{d}q}{\mathrm{d}t}, \tag{2.11}$$

$$V_\Delta(t) = g_\Delta(V_\mathrm{T}(t) - V_\mathrm{B}(t)) \propto 4g_\Delta\frac{y}{R}\rho\frac{\mathrm{d}q}{\mathrm{d}t}, \tag{2.12}$$

where g_Σ, g_Δ are gains set by the processing electronics. The ratio of V_Δ to V_Σ can be used to obtain a signal proportional to the beam position only:

$$\frac{V_\Delta}{V_\Sigma} = \frac{2}{R}\frac{g_\Delta}{g_\Sigma}y = k_s y \tag{2.13}$$

where k_s is the calibration constant of the BPM and processor system.

2.4.2 Analogue processor design

The stripline BPM signals are processed using the system shown in Fig. 2.9. Each of the BPMs is instrumented with its own analogue processor, whose functioning will be described below. A local oscillator (LO) signal, generated by the accelerator DR 714 MHz oscillator, is supplied to each processor and the processor outputs are digitised by the FONT5 board. As discussed in Sec. 2.5, the FONT5 board can record the data corresponding to three stripline BPMs. The BPMs selected here are P2, P3 and MFB1FF; dedicated resolution studies using P1, P2 and P3 have been documented in the past [56].

Also shown in Fig. 2.9 are the two sets of phase shifters used in the set-up:

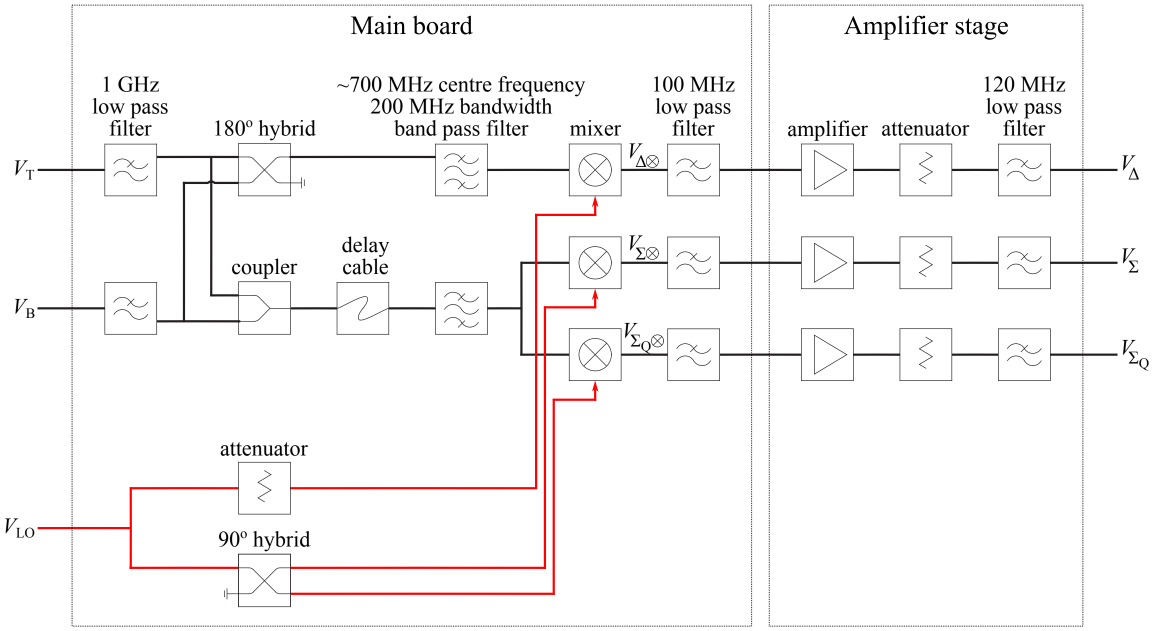

Figure 2.10: Block diagram of the stripline BPM analogue processor (adapted from [53]). The LO signals are shown in red.

LO phase shifters

These phase shifters vary the LO signal phase at the input to each processor.

Stripline phase shifters

For each of P2 and P3, a phase shifter is placed on one of the two stripline signals. Thus, the relative path length from the two strips to the BPM processor can be varied.

The components of the analogue processor are shown in Fig. 2.10. The inputs V_T and V_B are each passed through a low pass filter and are then split. A 180° hybrid is used to obtain $V_\mathrm{hybrid} = V_\mathrm{T} - V_\mathrm{B}$ and a resistive coupler produces $V_\mathrm{coupler} = V_\mathrm{T} + V_\mathrm{B}$. A band pass filter (BPF) on each of the V_hybrid and V_coupler signal paths selects a narrow range of frequencies around ~ 700 MHz, which matches the peak frequency component of the incoming signals [49].

The filtered V_hybrid signal constitutes an input to the Δ-channel mixer while the filtered V_coupler signal is split and used as input to both the Σ-channel and Σ_Q-channel mixers. These inputs arrive at their corresponding mixers at the same phase; this is adjusted by the delay cable on the V_coupler signal path. The LO signal distribution in the analogue processor ensures that the LO signals provided to the Δ-channel and Σ-channel mixers have the same phase, whereas the LO signal for the Σ_Q-channel mixer has a phase which is offset by 90°.

The mixer outputs are passed through low-pass filters to remove the up-mixed terms. The amplifier stage is designed to amplify the baseband signals to match the dynamic range of the FONT5 board inputs [49]. In this way, the V_Δ, V_Σ and V_{Σ_Q} signals are generated. A mathematical treatment of the analogue processor operation is provided in Sec. 2.4.3, explaining the role of the stripline and LO phase shifters.

2.4.3 Mathematical treatment of analogue processor operation

The signals V_{T} and V_{B} can be expressed as a Fourier series. The expressions for a given frequency ω are:

$$V_{\mathrm{T}}(\omega,t) = A_{\mathrm{T}}\sin(\omega t), \tag{2.14}$$
$$V_{\mathrm{B}}(\omega,t) = A_{\mathrm{B}}\sin(\omega t+\theta) = A_{\mathrm{B}}[\cos\theta\sin(\omega t)+\sin\theta\cos(\omega t)], \tag{2.15}$$

where $A_{\mathrm{T}}, A_{\mathrm{B}}$ are the amplitudes at the frequency ω and θ is the phase difference of $V_{\mathrm{B}}(\omega,t)$ relative to $V_{\mathrm{T}}(\omega,t)$. It is this phase difference that can be adjusted using the stripline phase shifters.

The coupler and 180° hybrid form the sum and difference of the stripline signals, respectively:

$$V_{\mathrm{coupler}}(\omega,t) = V_{\mathrm{T}}(\omega,t)+V_{\mathrm{B}}(\omega,t) = [A_{\mathrm{T}}+A_{\mathrm{B}}\cos\theta]\sin(\omega t)+A_{\mathrm{B}}\sin\theta\cos(\omega t), \tag{2.16}$$
$$V_{\mathrm{hybrid}}(\omega,t) = V_{\mathrm{T}}(\omega,t)-V_{\mathrm{B}}(\omega,t) = [A_{\mathrm{T}}-A_{\mathrm{B}}\cos\theta]\sin(\omega t)-A_{\mathrm{B}}\sin\theta\cos(\omega t). \tag{2.17}$$

As θ has been designed to be small [56], and can be minimised further using the stripline phase shifters, $\theta \ll 1$ can be used to simplify the expressions for V_{coupler} and V_{hybrid}. By applying $\sin\theta \sim \theta$ and $\cos\theta \sim 1$:

$$V_{\mathrm{coupler}}(\omega,t) \sim [A_{\mathrm{T}}+A_{\mathrm{B}}]\sin(\omega t), \tag{2.18}$$
$$V_{\mathrm{hybrid}}(\omega,t) \sim [A_{\mathrm{T}}-A_{\mathrm{B}}]\sin(\omega t)-A_{\mathrm{B}}\theta\cos(\omega t), \tag{2.19}$$

where $A_{\mathrm{B}}\theta \ll [A_{\mathrm{T}}+A_{\mathrm{B}}]$ has been used in Eq. 2.18. A corresponding simplification is not possible in Eq. 2.19 as $A_{\mathrm{T}} \sim A_{\mathrm{B}}$ with the beam approximately centred.

The LO signal supplied to the Δ-channel and Σ-channel mixers can be described by:

$$V_{\mathrm{LO}}(\omega_{\mathrm{LO}},t) = A_{\mathrm{LO}}\sin(\omega_{\mathrm{LO}}t+\phi_{\mathrm{LO}}) \tag{2.20}$$

where A_{LO} is its amplitude, ω_{LO} is its frequency and ϕ_{LO} is its phase difference relative to $V_{\mathrm{T}}(\omega,t)$ at the mixer input. This phase difference can be varied using the LO phase shifters. By noting that the LO signal has a 90° phase offset for the Σ_Q-channel mixer, the mixer outputs can be expressed as:

$$V_{\Delta\otimes}(\omega,t) = V_{\mathrm{hybrid}}(\omega,t)\times A_{\mathrm{LO}}\sin(\omega_{\mathrm{LO}}t+\phi_{\mathrm{LO}}), \tag{2.21}$$
$$V_{\Sigma\otimes}(\omega,t) = V_{\mathrm{coupler}}(\omega,t)\times A_{\mathrm{LO}}\sin(\omega_{\mathrm{LO}}t+\phi_{\mathrm{LO}}), \tag{2.22}$$
$$V_{\Sigma_Q\otimes}(\omega,t) = V_{\mathrm{coupler}}(\omega,t)\times A_{\mathrm{LO}}\cos(\omega_{\mathrm{LO}}t+\phi_{\mathrm{LO}}). \tag{2.23}$$

Given the narrow bandwidth of the V_{hybrid} and V_{coupler} signals at the inputs to the mixers, with a frequency approximately matching the LO frequency, the mixer operation can be calculated taking $\omega \sim \omega_{\text{LO}}$. The mixer outputs will thus contain two frequency components: one at baseband and one at a frequency of $2\omega_{\text{LO}}$. The low-pass filters following the mixers will remove the high frequency component, leaving the following signals at baseband:

$$V_\Delta = \tfrac{1}{2}A_{\text{LO}}[(A_{\text{T}} - A_{\text{B}})\cos\phi_{\text{LO}} - A_{\text{B}}\theta\sin\phi_{\text{LO}}], \tag{2.24}$$

$$V_\Sigma = \tfrac{1}{2}A_{\text{LO}}(A_{\text{T}} + A_{\text{B}})\cos\phi_{\text{LO}}, \tag{2.25}$$

$$V_{\Sigma_Q} = \tfrac{1}{2}A_{\text{LO}}(A_{\text{T}} + A_{\text{B}})\sin\phi_{\text{LO}}. \tag{2.26}$$

The signal filtering in the analogue processor sets the bandwidth of the output signals at $\sim$ 100 MHz. As the bunch length is in the range of 20 to 35 ps [57], the longitudinal charge profile within any individual bunch cannot be resolved [58]. This implies that the instantaneous beam current $\frac{\mathrm{d}q}{\mathrm{d}t}$ in Eqs. 2.11 and 2.12 can be treated as being proportional to the individual bunch charge q. In particular, applying this to V_Σ in Eq. 2.11 leads to the result:

$$V_\Sigma \propto q, \tag{2.27}$$

allowing the bunch charge to be deduced from the V_Σ processor output signal.

Combining Eqs. 2.25 and 2.26 gives:

$$\frac{V_{\Sigma_Q}}{V_\Sigma} = \tan\phi_{\text{LO}} \tag{2.28}$$

which, setting $\phi_{\text{LO}} \sim 0$ using the LO phase shifter, simplifies to:

$$\frac{V_{\Sigma_Q}}{V_\Sigma} \sim \phi_{\text{LO}}. \tag{2.29}$$

As the LO signal is derived from the DR 714 MHz oscillator, it is phase-locked to the accelerating cavity in the DR. However, bunch phase oscillations relative to the synchronous bunch, as described in Sec. 2.1.2, will lead to a variation in the bunch arrival time at the BPMs relative to the LO signal. The phase difference ϕ_{LO} between the stripline signals and the LO signal thus constitutes a measurement of the bunch phase. The measured train-to-train bunch phase variation is $\sim 0.5°$ RMS [56], with the phase being expressed as degrees of 714 MHz.

Eqs. 2.24 and 2.25 can be used to obtain:

$$\frac{V_\Delta}{V_\Sigma} = \frac{A_{\text{T}} - A_{\text{B}}}{A_{\text{T}} + A_{\text{B}}} - \frac{A_{\text{B}}}{A_{\text{T}} + A_{\text{B}}}\theta\tan\phi_{\text{LO}}. \tag{2.30}$$

The first term is proportional to the beam position (Eq. 2.13), whilst the second term couples the bunch phase measurement ϕ_{LO} into the expression for $\frac{V_\Delta}{V_\Sigma}$. The term y_{raw} can be defined as the measured $\frac{V_\Delta}{V_\Sigma}$, to be distinguished from the true beam position y. Using Eqs. 2.13, 2.30 and $\tan\phi_{\mathrm{LO}} \sim \phi_{\mathrm{LO}}$ gives:

$$y_{\mathrm{raw}} = k_s y - k_\phi \phi_{\mathrm{LO}}, \tag{2.31}$$

where k_s is the calibration constant defined in Eq. 2.13 and k_ϕ encapsulates the sensitivity of y_{raw} on ϕ_{LO}.

The undesired dependence of y_{raw} on ϕ_{LO} can be removed in two ways:

Using the stripline phase shifters

This method, used at P2 and P3, consists in setting the stripline phase shifters to minimise the path length difference from the two strips to the analogue processor. As θ tends to zero so does the phase sensitivity k_ϕ. By removing the sensitivity in hardware, the $y_{\mathrm{raw}} = \frac{V_\Delta}{V_\Sigma}$ calculation performed by the feedback algorithm on the FONT5 board is an accurate representation of the true beam position.

Using offline analysis

This method is used at MFB1FF and involves using data to fit k_ϕ in Eq. 2.31. The LO phase shifter (Fig. 2.9) is varied through a range of $\pm 10°$ in order to be able to measure the dependence of y_{raw} on ϕ_{LO}. The true beam position y can then be explicitly expressed in terms of y_{raw} and ϕ_{LO}:

$$y = \frac{1}{k_s}(y_{\mathrm{raw}} + k_\phi \phi_{\mathrm{LO}}). \tag{2.32}$$

Fig. 2.11 shows that there is no dependence of the true beam position y on the phase ϕ_{LO} following the procedures set up above.

2.4.4 Performance

The performance of the FONT stripline BPM system has been studied using the triplet of BPMs P1, P2 and P3 [53]. The results relating to the goals of low processing latency and high position resolution are reported here.

Processor latency

Bench test measurements show that the latency of an individual analogue processor module, from the V_{T} input to the V_Δ output of the amplifier stage, is 15.6 ± 0.1 ns.

Linear dynamic range

By displacing the BPM mover vertically, a linear processor response is observed over a dynamic range of ± 500 μm.

Position resolution

With the beam centred through the three BPMs, a position resolution of 291 ± 10 nm has been achieved for a bunch charge of ~ 1 nC.

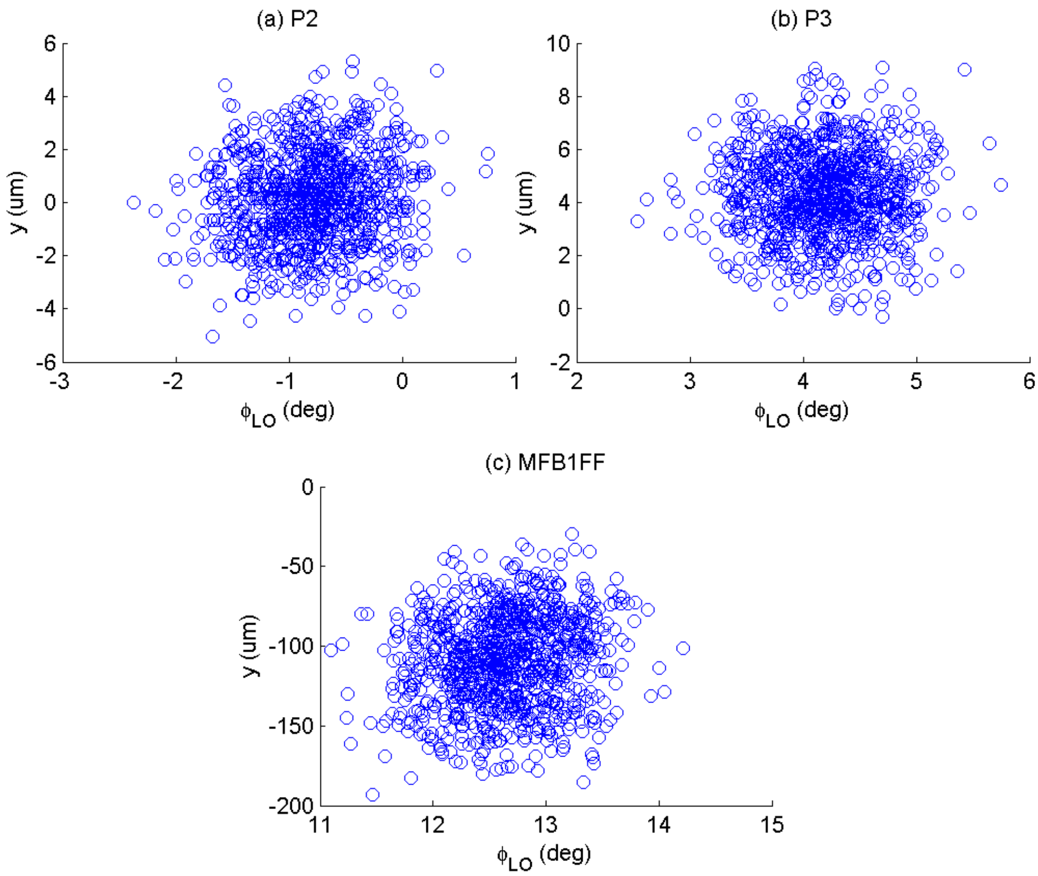

Figure 2.11: True beam position y versus phase ϕ_{LO} at (a) P2, (b) P3 and (c) MFB1FF.

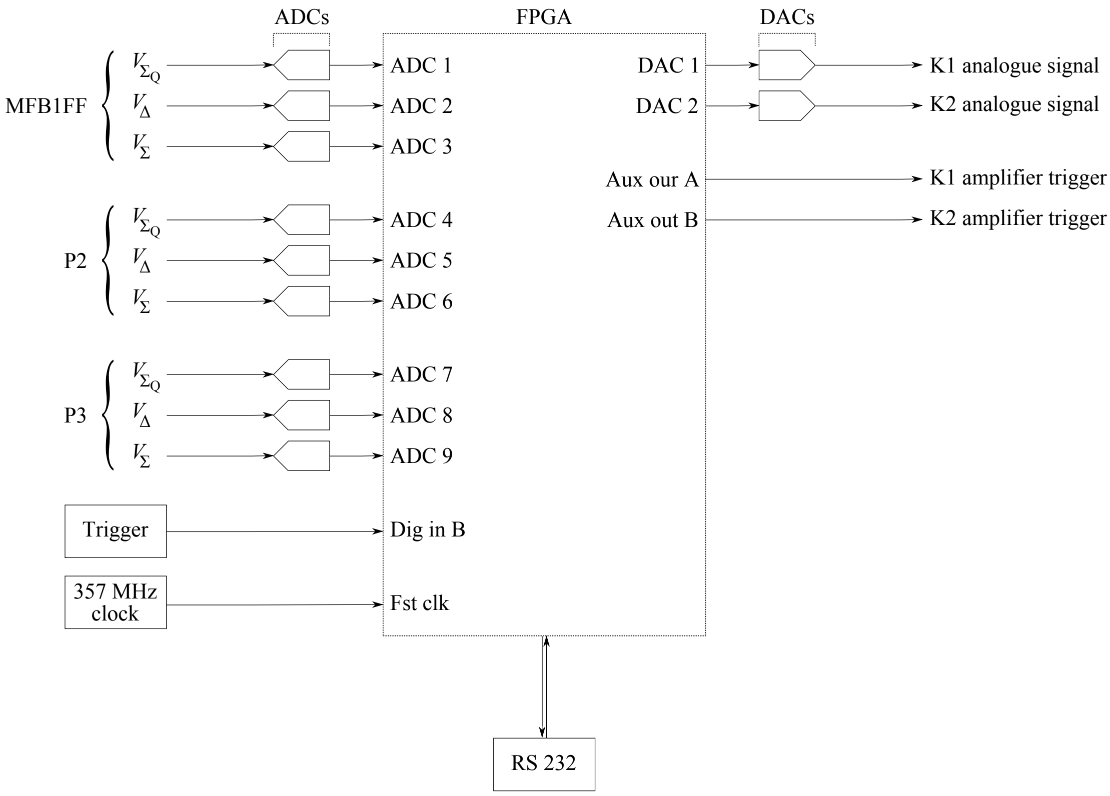

Figure 2.12: Block diagram of the FONT5 digital board. The inputs from BPMs P2, P3 and MFB1FF and the outputs to kickers K1 and K2 correspond to the FONT5 board instrumented in the upstream region.

2.5 FONT5 digital board

The two FONT5 boards used in this thesis constitute the basis for the digitisation of the processed BPM signals and for the operation of intra-train feedback. The boards were designed and produced in Oxford, and their structure is shown in Fig. 2.12. Each board is built around a Xilinx Virtex-5 field programmable gate array (FPGA) [59], which consists of an array of logic blocks that can be interconnected [60] by the user using a hardware description language (firmware).

The FONT5 board contains nine 14-bit analogue-to-digital converters (ADCs) used to digitise the processed BPM signals. Given the expected noise in the processed stripline BPM signals, only the most significant 13 bits are input to the FPGA for signal processing and data saving [53]. As the ADC input voltage range is ± 0.5 V, it follows that each ADC count in the 13-bit digitised signals corresponds to ~ 0.12 mV.

It is important to ensure that the intrinsic voltage offset of each ADC channel has been removed. This is achieved through the use of digital-to-analogue converters (DACs); the ones used for this purpose are referred to as trim DACs. Prior to each ADC, a trim DAC output is combined with the analogue signal (for example V_Δ, V_Σ or V_{Σ_Q}) to be digitised

[49]. By varying the trim DAC input (set through the FPGA), the digitised ADC signal can be nulled as required.

The ADCs are grouped in banks of three channels, with each bank sharing a common clock. A 357 MHz clock is used which is derived from the 714 MHz DR oscillator signal in order to ensure that the clock is stable relative to the synchronous bunches extracted from the DR. The ADC channel assignment shown in Fig. 2.12 corresponds to that used to instrument BPMs P2, P3 and MFB1FF in the upstream region.

The FONT5 board contains four 14-bit DACs with an output range of ± 0.5 V to drive the kickers used for intra-train feedback. Given the present requirements, only two of the four DACs are used at any given time. In addition to the analogue signals from the DACs, the board also generates the kicker amplifier triggers. The channel assignment used to drive kickers K1 and K2 with the FONT5 board in the upstream region is shown in Fig. 2.12. Both the kickers and kicker amplifiers are discussed further in Sec. 2.6.

A trigger signal that precedes the firing of the DR extraction kicker is provided to the FONT5 board. An internal delay on the board is then used to set the start of the sampling window relative to the external trigger signal. At present, the sampling window is 164 samples in length with a sampling frequency of 357 MHz set by the external clock. Finally, the board has a RS 232 serial interface for communication with a PC running the FONT data acquisition system (DAQ) software [49].

The firmware used on the FONT5 boards was designed to operate the coupled-loop upstream feedback presented in Sec. 2.7, where the positions at P2 and P3 are used to drive kickers K1 and K2. Using the ADC and DAC channel assignment shown in Fig. 2.12, the firmware generates the analogue outputs V_{K1} and V_{K2} to drive the kickers K1 and K2 according to:

$$V_{\mathrm{K1}} = G_{12}\left(\frac{V_\Delta}{V_\Sigma}\right)_{\mathrm{P2}} + G_{13}\left(\frac{V_\Delta}{V_\Sigma}\right)_{\mathrm{P3}}, \tag{2.33}$$

$$V_{\mathrm{K2}} = G_{22}\left(\frac{V_\Delta}{V_\Sigma}\right)_{\mathrm{P2}} + G_{23}\left(\frac{V_\Delta}{V_\Sigma}\right)_{\mathrm{P3}}, \tag{2.34}$$

where G_{kp} are pre-loaded gains for each pair of kicker k and BPM p. For a two-bunch train, the V_Δ and V_Σ signals are sampled on the data corresponding to the first bunch in order to drive the kickers in time to correct the second bunch. For a given bunch, the P2 signals are typically digitised 14 ns earlier than those from P3 as a result of the bunch time of flight from P2 to P3 and the different signal path lengths from the BPMs to the FONT5 board; the firmware was designed with this scenario in mind. Full details of the development of this version of firmware, and of the operation of the FONT5 board, are presented in [51].

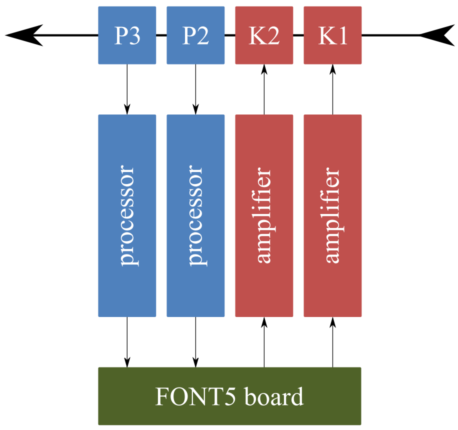

Figure 2.13: Block diagram of the upstream feedback system.

2.6 Kickers and kicker amplifiers

The FONT set-up contains three stripline kickers (Fig. 2.5) with K1 and K2 upstream and IPK in the IP region. Each of the kickers consists of two parallel conducting strips placed along the top and bottom of the beampipe. Driven with input signals from one end, each kicker can deflect the beam in the y direction [61]. The two upstream kickers were provided by the SLAC laboratory [62], whilst IPK is a modified stripline BPM designed in Oxford [63] with the fabrication arranged by KEK.

The analogue outputs from the FONT5 board DAC channels are ultimately applied to the stripline kickers but each signal is first amplified in two stages. The first stage of amplification is achieved using a Mini-Circuits ZPUL-21 [64] amplifier providing 21 dB gain. The second stage calls for an amplifier that can deliver a high current with a rise-time of a few tens of nanoseconds. The required amplifier was developed and manufactured for this purpose by TMD technologies [65] and can provide ±30 A of drive current with a rise-time of 35 ns from the time of the input signal to reach 90 % of peak output. The output pulse length is specified to be up to 10 μs. The TMD amplifier needs to be triggered in advance of the bunch arrival; these triggers are generated by the FONT5 board through the 'Aux out' digital output channels. The configuration of DAC and digital outputs is shown in Fig. 2.12 for the upstream set-up and in Fig. 5.2 for the IP feedback set-up.

2.7 Upstream feedback

The upstream feedback system has been designed to stabilise both the beam position y and angle y' at the entrance to the ATF FFS. This system is operated using the BPMs P2 and P3 and the kickers K1 and K2. The experimental set-up is shown in Fig. 2.13.

The feedback system is built around two main feedback loops: P2 to K1 and P3 to K2. In each loop, the design phase advance from the kicker to the BPM is $\sim 90°$, as this maximises the BPM response to the kicker. Furthermore, to achieve both beam position and angle stabilisation, the desired phase advance between the two kickers is also $\sim 90°$. In practice, it is difficult to exactly achieve the desired phase advances and so the upstream feedback is operated as a coupled system where the kicks at K1 and K2 are both given by linear combinations of the beam positions measured at P2 and P3.

Previous beam tests using the upstream feedback system have achieved beam stabilisation at the level of 400 nm at one of the two feedback BPMs [66] and a measurement of the reduction in beam position jitter at witness BPMs located within a metre from the feedback BPMs [49]. The propagation of the beam stabilisation was studied at the IP, where a 10 % reduction has been measured when operating the upstream feedback system [56]. The work presented below shows the effect of the upstream feedback as measured by the stripline BPM MFB1FF, located 26 m downstream from P3 (Fig. 2.5), to assess the functioning of both the feedback system and the beam transport into the FFS.

2.7.1 Mathematical treatment of feedback operation

The feedback results presented throughout this thesis were obtained in interleaved mode. In this mode, alternate trains are operated with feedback off and on. The data where the feedback is off are used to characterise the undisturbed beam and to identify drifts in the incoming beam conditions.

For a given two-bunch train, let y_1 and y_2 be the positions of the first and second bunch, respectively, in a given BPM with no feedback correction applied. The corrected position of the second bunch, Y_2, can then be expressed as:

$$Y_2 = y_2 - gy_1 - \delta_2, \tag{2.35}$$

where g is the feedback gain and δ_2 is a constant offset that can be applied to the second bunch. Throughout this thesis, $g = 1$ as the two bunches have similar position jitters and the positions of the two bunches are highly correlated. The use of δ_2 is shown for IP feedback in Sec. 5.4.

Eq. 2.35 assumes a perfect feedback calculation and a linear kicker response. In this model, a non-zero Y_2 results from an imperfect bunch-to-bunch position correlation or due to BPM measurement errors. Taking the standard deviation of Eq. 2.35 over a feedback run gives [67]:

$$\sigma_{Y_2}^2 = \sigma_{y_1}^2 + \sigma_{y_2}^2 - 2\sigma_{y_1}\sigma_{y_2}\rho_{12}, \tag{2.36}$$

where σ_{Y_2}, σ_{y_1} and σ_{y_2} are the standard deviations (or position jitters) of the Y_2, y_1 and y_2 position distributions and ρ_{12} is the correlation of y_1 to y_2. The data obtained in an interleaved feedback run can be used to obtain σ_{y_1}, σ_{y_2} and ρ_{12} from the set where the feedback is off. The σ_{Y_2} jitter prediction thus obtained using Eq. 2.36 can be compared to the measured value when the feedback is on to assess if the feedback system is operating as expected.

In the feedback analysis performed in this thesis, triggers in which one or both of the bunches is missing are removed. Missing bunches are identified by applying a cut on the bunch charge. For the stripline BPMs, the cut is made on the V_Σ signal and the threshold is typically set to 500 ADC counts, corresponding to a bunch charge of 0.1×10^{10} electrons (Fig. 3.20).

In addition, a flier rejection technique is adopted to remove triggers containing beams with extraneous orbits. The flier rejection technique consists in removing triggers in which the bunch position is more than 3 standard deviations away from the mean position in each set of feedback on and feedback off data. The cut is performed twice: any extraneous triggers are removed following the first cut, the mean and standard deviation are recalculated and the cut is repeated. The double-cut approach ensures that the second cut is performed well in case the original mean and standard deviation are greatly affected by a large discrepancy introduced by one trigger. The flier rejection procedure typically removes fewer than 2 % of the triggers.

2.7.2 Kicker scan and gain calculation

The effect of the kick imparted by the kickers K1 and K2, as measured at the BPMs P2 and P3, is determined by operating the kickers in constant DAC mode. In this mode, the firmware timing remains unchanged but the DAC output is set by the chosen constant DAC setting [51]. Kicker scans are performed for the two kickers in turn, with the kicks applied to the second bunch in each two-bunch train.

Fig. 2.14 shows the results of the K1 and K2 kicker scans. For the purpose of the feedback gain calculation that follows, the positions at P2 and P3 are expressed in their uncalibrated form $\frac{V_\Delta}{V_\Sigma}$ and the kicker voltages are given in DAC counts. The offsets $\delta(\frac{V_\Delta}{V_\Sigma})$ provided to the second bunch, as measured at the two BPMs, can be expressed in terms of the kicker voltages V_{K1} and V_{K2}:

$$\begin{pmatrix} \delta\left(\frac{V_\Delta}{V_\Sigma}\right)_{\mathrm{P2}} \\ \delta\left(\frac{V_\Delta}{V_\Sigma}\right)_{\mathrm{P3}} \end{pmatrix} = \begin{pmatrix} H_{12} & H_{22} \\ H_{13} & H_{23} \end{pmatrix} \begin{pmatrix} V_{\mathrm{K1}} \\ V_{\mathrm{K2}} \end{pmatrix} \tag{2.37}$$

where the response matrix elements H_{kp} are the gradients, in units of (ADC/ADC)/DAC, of the linear fits to the data in Fig. 2.14 for each of the kicker k and BPM p pairs. The values of the gradients are given in Table 2.2.

Eq. 2.37 can be rewritten to express the kicker voltages required to operate the feedback given the measured $\frac{V_\Delta}{V_\Sigma}$ of the first bunch at each BPM. Noting that the kick is applied in the opposite direction to the offset of the first bunch:

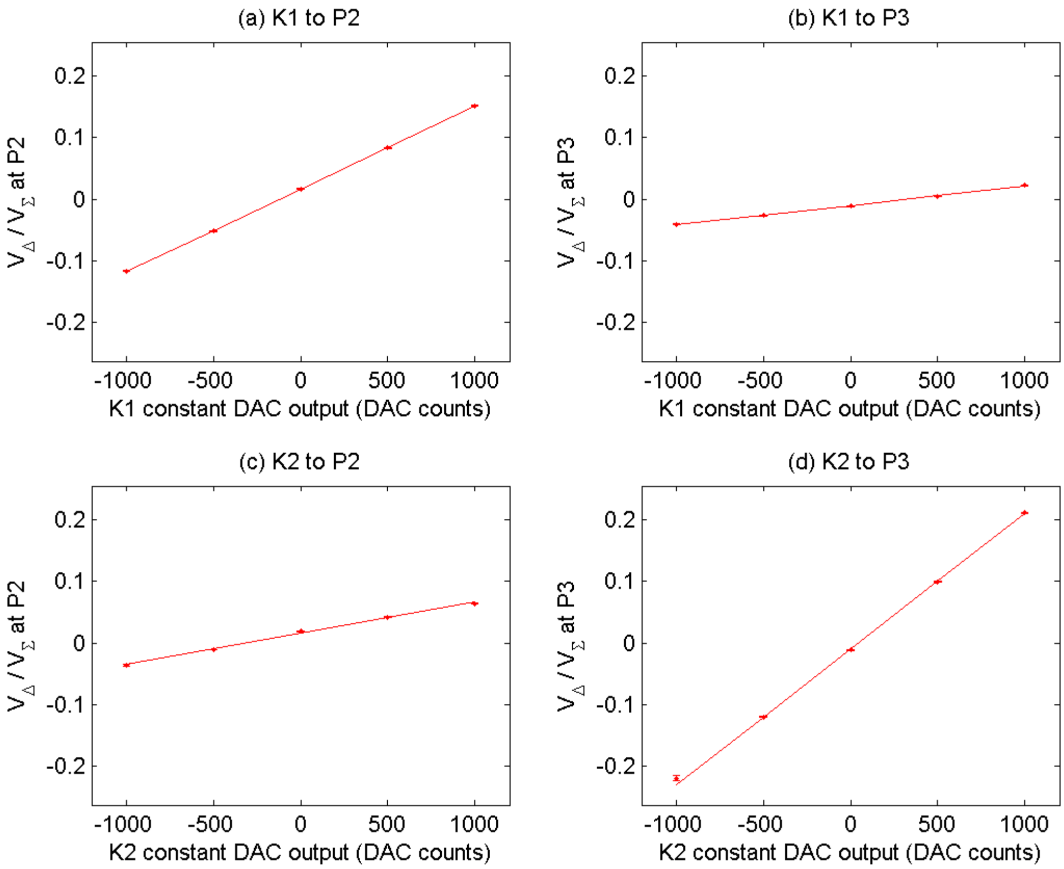

Figure 2.14: Mean $\frac{V_\Delta}{V_\Sigma}$ measured at BPMs P2 and P3 versus constant DAC settings applied to kickers K1 and K2 for each of the combinations: (a) K1 to P2, (b) K1 to P3, (c) K2 to P2 and (d) K2 to P3. Standard errors are given. The lines show linear χ^2 fits to the data.

Table 2.2: Linear χ^2 fit gradients H for mean $\frac{V_\Delta}{V_\Sigma}$ measured at BPMs P2 and P3 versus constant DAC settings applied to kickers K1 and K2. The errors on the gradient are derived from the standard errors on the mean $\frac{V_\Delta}{V_\Sigma}$ measured at each DAC setting.

Kicker-to-BPM pair	H $(10^{-7}\times(\mathrm{ADC/ADC})/\mathrm{DAC})$
K1 to P2	1347 ± 5
K1 to P3	317 ± 5
K2 to P2	509 ± 6
K2 to P3	2204 ± 7

$$\begin{pmatrix} V_{\mathrm{K1}} \\ V_{\mathrm{K2}} \end{pmatrix} = -\mathrm{inv} \begin{pmatrix} H_{12} & H_{22} \\ H_{13} & H_{23} \end{pmatrix} \begin{pmatrix} \left(\frac{V_\Delta}{V_\Sigma}\right)_{\mathrm{P2}} \\ \left(\frac{V_\Delta}{V_\Sigma}\right)_{\mathrm{P3}} \end{pmatrix}. \tag{2.38}$$

A comparison of Eq. 2.38 with Eqs. 2.33 and 2.34 shows that the feedback gains are thus given by:

$$\begin{pmatrix} G_{12} & G_{13} \\ G_{22} & G_{23} \end{pmatrix} = -\mathrm{inv} \begin{pmatrix} H_{12} & H_{22} \\ H_{13} & H_{23} \end{pmatrix}. \tag{2.39}$$

2.7.3 Upstream feedback results

For the results presented here, ATF was operated in two-bunch mode with a bunch spacing of 187.6 ns. The beam was centred in P2 and P3 using the BPM movers, and was steered approximately through the centre of MFB1FF using the vertical dipole corrector magnet ZV1FF located 6 m upstream of MFB1FF. The stripline phase shifters described in Sec 2.4 were set up on P2 and P3, reducing the residual phase sensitivity to under 0.26 µm/° (with the phase expressed as degrees of 714 MHz). Given the bunch phase jitter of 0.48° measured for this data set, one expects the effect of the residual phase sensitivity to contribute less than 125 nm to the position resolution at the feedback BPMs [53]. Offline analysis (Eq. 2.32) was used to remove the phase sensitivity at MFB1FF for the results presented below. Once the set-up was complete, both K1 and K2 kicker scans were performed in order to calculate the feedback gain coefficients, as presented in Sec. 2.7.2.

The position distributions in Fig. 2.15 show the performance of the upstream feedback. As expected, the first bunch is not affected by the feedback as this bunch is only measured. For the second bunch, the reduction in position jitter is evident not only at the feedback BPMs P2 and P3 but also, to the same extent, at MFB1FF. The feedback's action to centre the beam can be noted at P3 where both the first and second bunches have an incoming offset of 4 µm, which is subsequently corrected by the feedback. In the case of P2, a static position offset of 7 µm exists between the first bunch and second bunch, which could in principle be removed by using the δ_2 offset in Eq. 2.35. As the first bunch is centred in P2, the feedback does not correct the mean position of the second bunch at this BPM, as observed. The mean position of the beam for the two bunches at P2, P3 and MFB1FF is given in Table 2.3 for both data with feedback off and on.

The time-sequence of the data for the feedback run is shown in Fig. 2.16. A random variable component, and a correlated slower drift, are seen in the incoming beam positions; the feedback acts to remove both components. A slower position feedback system, operating at the train repetition frequency, could in principle remove the correlated drift. To this end, the slower ATF train-to-train feedback system [68] may be upgraded for operation on two-bunch trains in the future.

Table 2.4 shows the effect of the feedback on the position jitter, defined as the standard deviation of the measured positions. The feedback reduces the jitter by a factor of four at

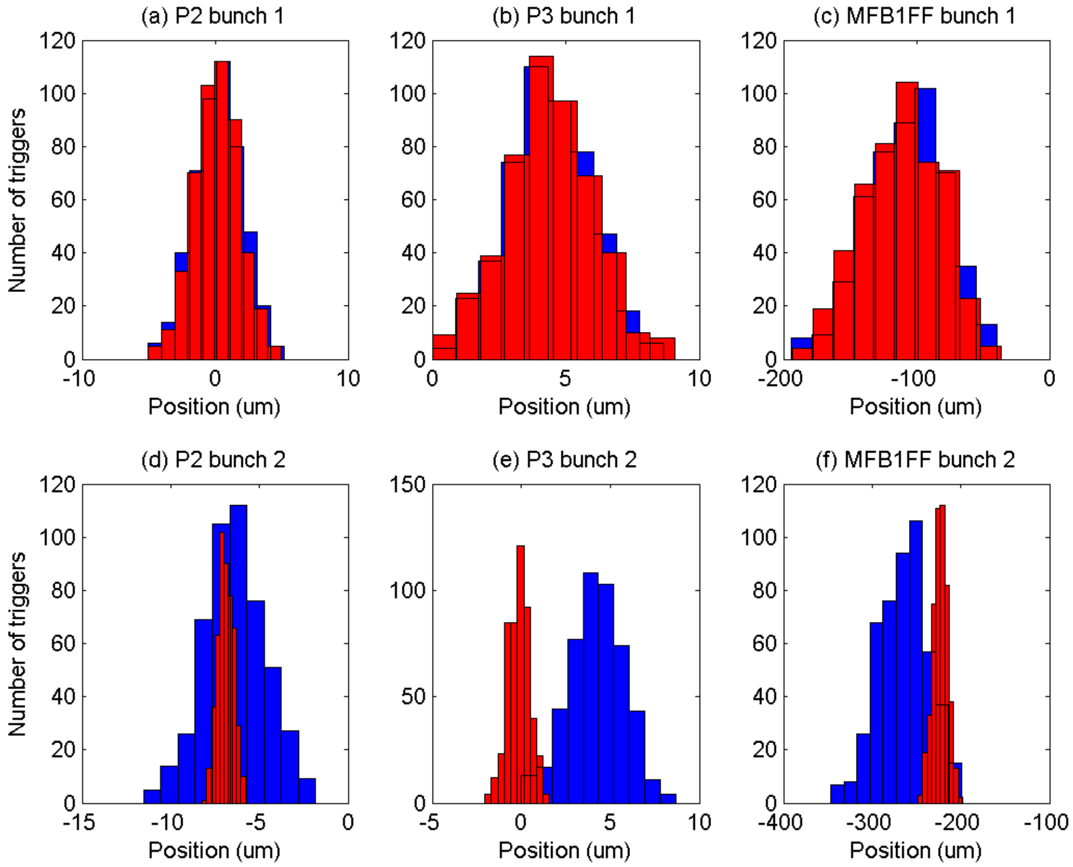

Figure 2.15: Distributions of positions with feedback off (blue) and feedback on (red) measured for the first bunch at (a) P2, (b) P3 and (c) MFB1FF and for the second bunch at (d) P2, (e) P3 and (f) MFB1FF.

Table 2.3: Mean position with feedback off and on for bunches 1 and 2 at P2, P3 and MFB1FF. Standard errors are given.

	Mean position (μm)			
	Bunch 1		Bunch 2	
BPM	Feedback off	Feedback on	Feedback off	Feedback on
P2	$+0.20 \pm 0.08$	$+0.09 \pm 0.08$	-6.40 ± 0.08	-6.92 ± 0.02
P3	$+4.35 \pm 0.07$	$+4.37 \pm 0.08$	$+4.21 \pm 0.07$	-0.14 ± 0.03
MFB1FF	-108.1 ± 1.3	-111.0 ± 1.3	-264.6 ± 1.2	-223.1 ± 0.4

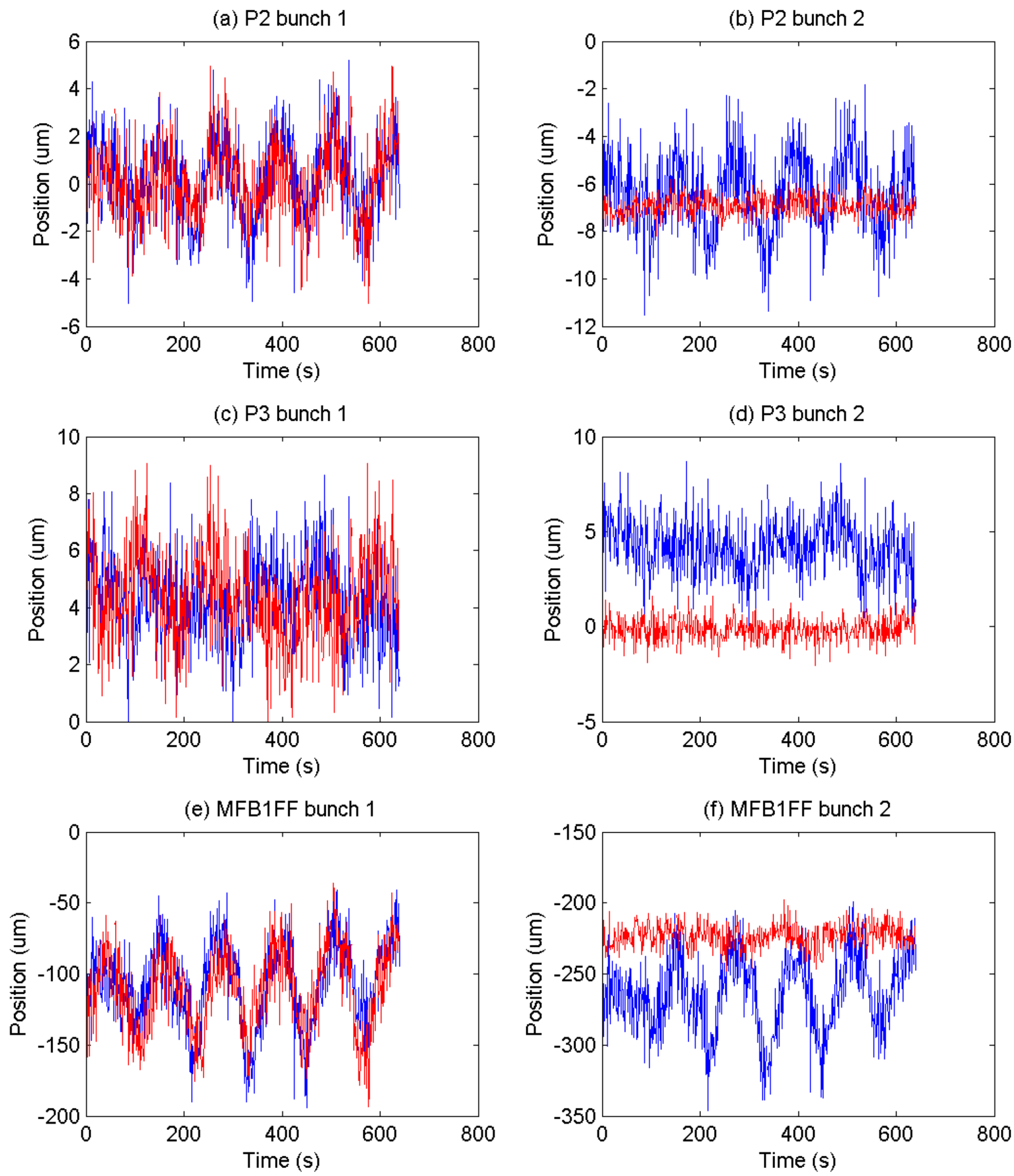

Figure 2.16: Position versus train extraction time measured for the first bunch at (a) P2, (c) P3 and (e) MFB1FF and for the second bunch at (b) P2, (d) P3 and (f) MFB1FF, with feedback off (blue) and feedback on (red).

Table 2.4: Position jitter with feedback off and on for bunches 1 and 2 at P2, P3 and MFB1FF. Standard errors are given.

	Position jitter (µm)			
	Bunch 1		Bunch 2	
BPM	Feedback off	Feedback on	Feedback off	Feedback on
P2	1.80 ± 0.06	1.70 ± 0.05	1.74 ± 0.06	0.44 ± 0.01
P3	1.56 ± 0.05	1.66 ± 0.05	1.55 ± 0.05	0.61 ± 0.02
MFB1FF	29.9 ± 1.0	29.4 ± 0.9	27.5 ± 0.9	8.3 ± 0.3

Table 2.5: Position correlation ρ_{12} of bunch 1 to bunch 2 measured at P2, P3 and MFB1FF with feedback off and on. The errors on ρ_{12} correspond to 68.3 % confidence intervals.

	ρ_{12} (%)	
BPM	Feedback off	Feedback on
P2	$+96.9 \pm 0.3$	-25 ± 4
P3	$+93.3 \pm 0.6$	$+15 \pm 4$
MFB1FF	$+98.3 \pm 0.2$	-14 ± 4

P2 and by a factor of 2.5 at P3. The jitter is stabilised well below the micron-level, with a measured jitter of 440 ± 10 nm at P2 and 610 ± 20 nm at P3. The feedback correction also propagates successfully into the FFS, with a reduction of jitter by a factor of 3.3 at MFB1FF.

A high bunch-to-bunch correlation is necessary to achieve these reductions in position jitter. Fig. 2.17 shows the bunch 2 position versus bunch 1 position measured at P2, P3 and MFB1FF. A large incoming bunch-to-bunch position correlation in excess of 93 % is measured at the three BPMs (Table 2.5). The feedback then acts to remove the position components that are correlated between the two bunches, reducing the correlation to around 0 %.

Following Sec. 2.7.1, the expected position jitter that could be achieved by a perfect feedback system and a linear kicker response can be calculated. Applying Eq. 2.36 to this feedback run gives an expected jitter for bunch 2 with the feedback on, σ_{Y_2}, of 0.45 µm at P2 and 0.57 µm at P3. The larger result obtained at P3, linked to its lower bunch-to-bunch position correlation, suggests that it is performing with a worse position resolution than P2 in this data set. The expected jitters agree closely with the measured jitters (Table 2.4) indicating that the feedback system is functioning well.

2.8 ATF simulation

The propagation of the beam can be studied from the upstream feedback system, through the FFS and to the IP by using the transfer matrix formalism described in Sec. 2.1.1. The

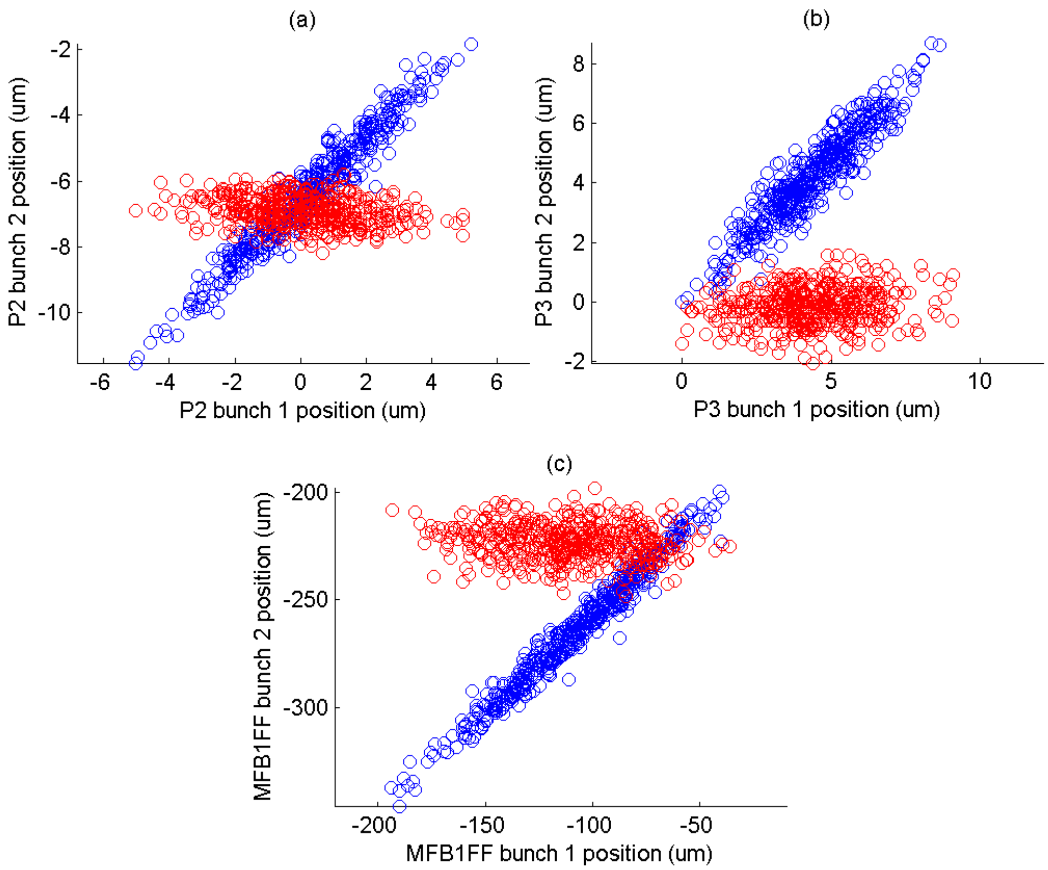

Figure 2.17: Bunch 2 position versus bunch 1 position measured at (a) P2, (b) P3 and (c) MFB1FF, with feedback off (blue) and feedback on (red).

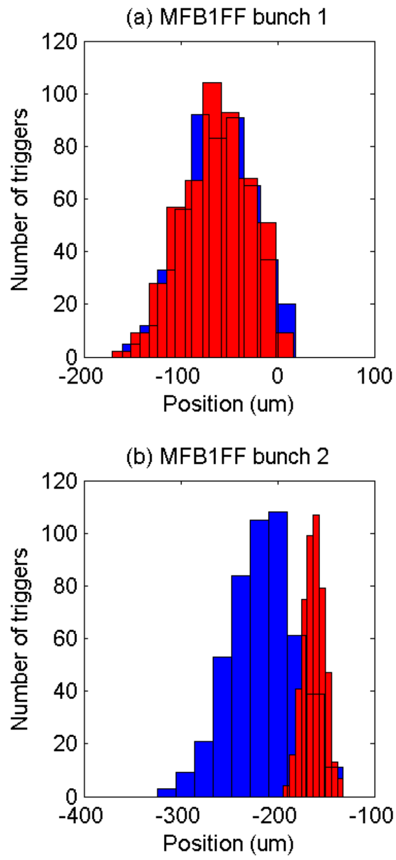

Figure 2.18: Distributions of positions at MFB1FF obtained by propagating the measured positions at P2 and P3, for (a) the first bunch and (b) the second bunch, with feedback off (blue) and feedback on (red).

transfer matrices used to transport the vertical beam position y and angle y' between any two elements of the ATF lattice are calculated using the ATF MAD model [69] maintained by the ATF collaboration. On each occasion, the configuration of the magnet settings used on the given shift are loaded from the ATF file repository. For the results presented below, the measured P2 and P3 vertical positions of the individual triggers are used to calculate the position y (and angle y') at any other downstream location, such as MFB1FF or the IP.

2.8.1 Propagation to MFB1FF

As P2 and P3 are located downstream of both kickers K1 and K2, the measured positions at the two BPMs can be propagated downstream using the same transfer matrices regardless of whether the feedback is on or off. The position distributions thus propagated to MFB1FF are shown in Fig. 2.18 for the feedback run presented in Sec. 2.7.3. The position jitters deduced from these distributions, referred to as propagated jitters, are given in Table 2.6.

The propagated positions at MFB1FF follow similar distributions as the measured positions in Fig. 2.15. The mean position of the propagated distributions is arbitrary as the

Table 2.6: Position jitter propagated to MFB1FF with upstream feedback off and on for bunches 1 and 2. Standard errors are given.

	Position jitter (μm)	
Bunch	Feedback off	Feedback on
1	35.2 ± 1.1	34.4 ± 1.1
2	34.2 ± 1.1	10.9 ± 0.3

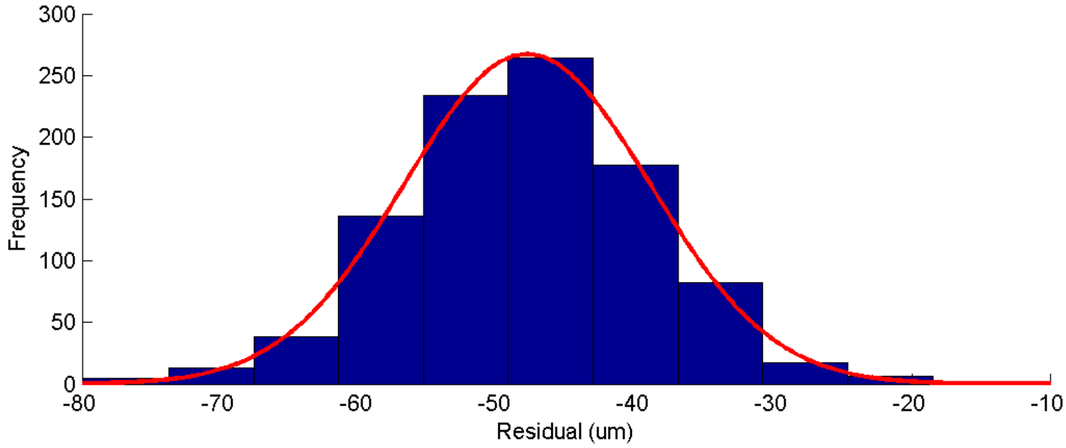

Figure 2.19: Distribution of the position residuals at MFB1FF. The red line shows a Gaussian fit to the data.

BPM mover positions are not modelled. A comparison of the measured jitters in Table 2.4 and the propagated jitters in Table 2.6 shows that the propagated jitter is ~ 20 % too large. This results from the finite position resolution of P2 and P3 introducing an error in the propagated beam position estimate; the value of the BPM resolution is estimated below.

As is discussed in detail in the context of the IP BPMs in Sec. 4.7, a triplet of BPMs can be used to obtain an estimate of the BPM position resolution. A linear combination of the positions at two BPMs (in this case, P2 and P3) is used to estimate the position at a third (MFB1FF), and the residuals between the measured and predicted positions at the third BPM are computed on a trigger-by-trigger basis. The distribution of these residuals, calculated across the first bunches of all the triggers of the feedback run, is shown in Fig. 2.19.

The Gaussian fit to the distribution of residuals in Fig. 2.19 has a width of 8.87 ± 0.15 μm which, when divided by the geometric factor (Eq. 4.28), gives a BPM resolution estimate of 315 ± 5 nm. This resolution estimate is said to be obtained using the geometric method, in that the beam transport model between the BPMs has been used. The BPM resolution is close to the value of 291 ± 10 nm measured using the system of P1, P2 and P3 [53] and hence indicates that the resolution of MFB1FF is consistent with that of the other three stripline BPMs and that the beam transport between P2, P3 and MFB1FF is understood to the level given by the BPM resolution.

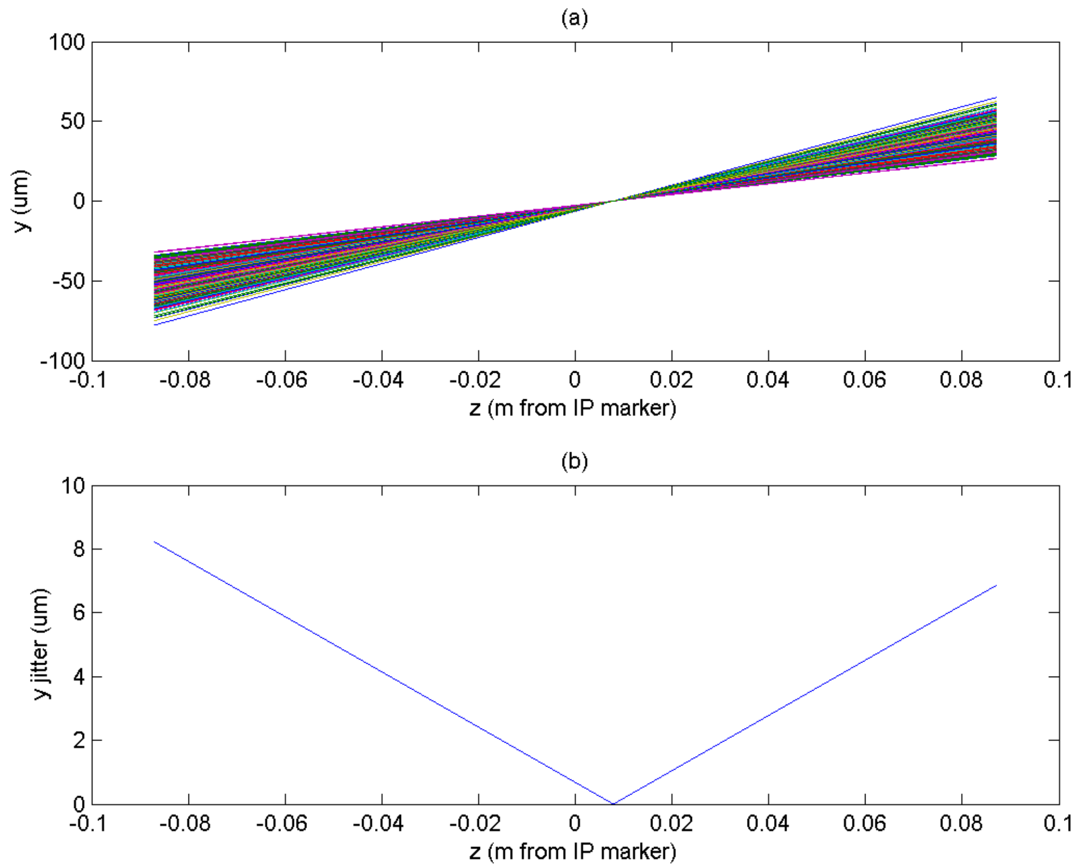

Figure 2.20: (a) Vertical bunch position y, for each trigger, versus longitudinal distance z from the IP marker; the beam paths are obtained by propagating the measured beam positions at P2 and P3. (b) The resulting vertical position jitter versus longitudinal distance z from the IP marker.

2.8.2 Propagation to the IP

The measured beam positions at P2 and P3 can be propagated further along the FFS to the IP. By calculating the propagated beam position y and angle y' at the IP, the beam paths through the IP region can be reconstructed. Given the absence of magnetic elements in the beamline within a metre of the IP (Fig. 2.5), a ballistic beam transport model can be used in this region [70], that is, straight-line trajectories can be assumed for the individual bunches. The beam path reconstruction thus obtained over many triggers, with the upstream feedback off, is shown in Fig. 2.20(a).

The paths can be used to calculate the propagated position jitter, as a function of the longitudinal distance z from the IP marker, which is shown in Fig. 2.20(b). The focusing of the beam can be seen clearly, with an estimated minimum jitter of 9.4 ± 0.3 nm. It is important to note that the propagated jitter obtained at the IP is an underestimate as the propagation model excludes any x-to-y position coupling, energy dependence or non-linear effects. However, it does outline some features of the beam transport in the IP region that will be used in this thesis.

Table 2.7: Longitudinal distance Δz of the beam waist from the IP marker in the ATF model, for bunches 1 and 2 with feedback off and on. In each case, the beam waist is downstream of the IP marker.

	Δz (mm)	
Bunch	Feedback off	Feedback on
1	7.98	7.96
2	7.97	7.91

Table 2.8: Beam position and angle jitter propagated to the beam waist in the IP region with upstream feedback off and on for bunches 1 and 2. Standard errors are given.

	Position y jitter (nm)		Angle y' jitter (urad)	
Bunch	Feedback off	Feedback on	Feedback off	Feedback on
1	9.5 ± 0.3	10.1 ± 0.3	89 ± 3	87 ± 3
2	9.4 ± 0.3	3.6 ± 0.1	87 ± 3	28 ± 1

The location of the waist is displaced from the IP marker defined in the ATF model. The analysis is repeated for data from the same feedback run with the upstream feedback off and on, and for both bunches in the two-bunch trains. The results in Table 2.7 show that the location of the beam waist for this data set is consistently located about 8 mm downstream of the IP marker. In the absence of further BPM measurements, one cannot comment whether the beam waist was not correctly placed at the physical location of the IP or whether the model does not predict the longitudinal location of the beam waist accurately. In either case, the figure of merit is the level of jitter at the waist and the results that follow give the propagated beam positions and angles at the point 7.97 mm downstream of the IP marker.

The effect of the upstream feedback on the beam position y at the waist is shown in Fig. 2.21, and the effect on the beam angle y' is presented in Fig. 2.22. It can be seen that in the linear model used to propagate the positions to the IP, both the position and angle have been stabilised, as expected. The values of the propagated position and angle jitters, with the upstream feedback off and on, are given in Table 2.8. The model predicts a factor ~ 3 reduction in both the position and angle jitter, matching the level of correction measured at the feedback BPMs. In particular, assuming no sources of beam jitter between the upstream feedback system and the IP, the linear transport model predicts a reduction in position jitter from 10 nm to 4 nm at the waist in the IP region on operating the upstream feedback system.

A comparison of Figs. 2.21 and 2.22 shows an interesting observation regarding the slow correlated orbit drift identified in the upstream BPMs in Sec. 2.7.3: the drift predominantly appears in the y' degree of freedom at the beam waist. This suggests that the driving source of this drift affects only one dimension of the y, y' phase space plots discussed in Sec. 2.1.1, and this dimension lies along the y' axis at the phase advance of the beam waist.

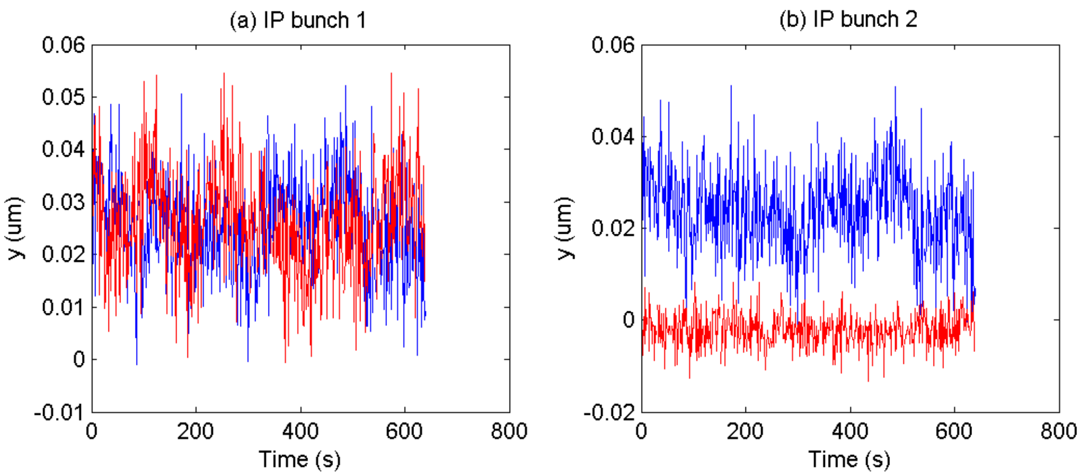

Figure 2.21: Position y propagated to the beam waist in the IP region versus train extraction time, for (a) the first bunch and (b) the second bunch, with upstream feedback off (blue) and on (red).

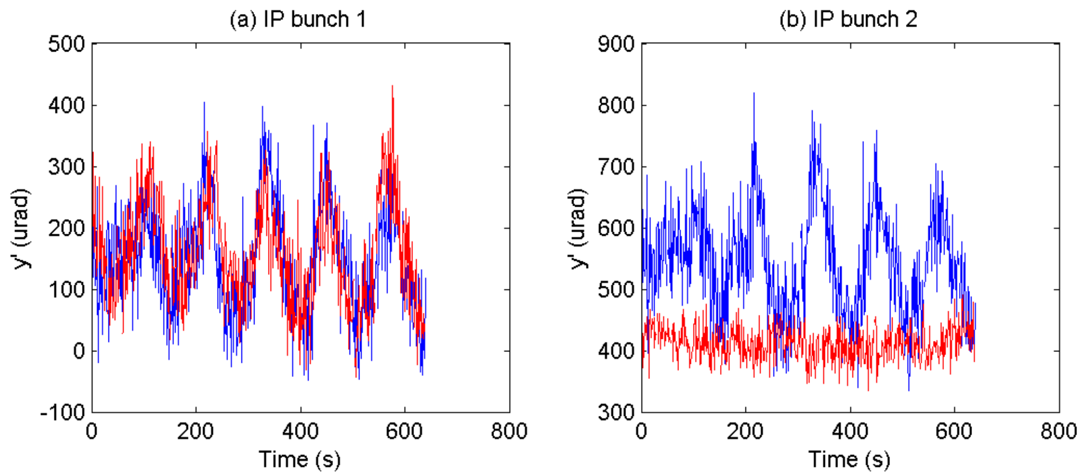

Figure 2.22: Beam angle y' propagated to the beam waist in the IP region versus train extraction time, for (a) the first bunch and (b) the second bunch, with upstream feedback off (blue) and on (red).

2.8.3 Position-angle correlation in the IP region

The beam position y and angle y' propagated to the beam waist can be used to plot a y, y' phase space diagram, as shown in Fig. 2.23(a). As expected, following from Sec. 2.1.1, no y to y' correlation is seen at the waist. Fig. 2.23(b) shows the corresponding y, y' scatter plot obtained when the beam is propagated to a location 1 mm downstream of the waist. As a result of the large beam angle jitter $\sigma_{y'}$ in the IP region and the small beam position jitter σ_y at the waist, the position y of any given trigger when measured off the waist is strongly determined by its angle y'. This is illustrated by the large position-angle correlation in Fig. 2.23(b), which in this case is over 99 %.

As any trigger's beam position off-waist is basically determined by its angle, and given that the beam angle is conserved in the absence of magnetic elements in the beamline, it follows that the vertical beam positions between off-waist locations will be highly correlated. This can be illustrated by propagating the beam to the BPM IPC located downstream of the IP (Fig. 2.5) which can be used as a witness off-waist BPM.

Fig. 2.24 shows the interrelationship between the positions at IPC and those on-waist and off-waist. As expected, no correlation is observed with the beam position on-waist but a high correlation is noted with the beam off-waist. The correlation of the position at IPC with that at different longitudinal distances z_r from the beam waist is shown in Fig. 2.25. A sharp transition is observed between there being no correlation when $z_r = 0$ to there being a high correlation otherwise.

These results illustrate the principle used in Sec. 4.4 where beam measurements from two BPMs in the IP region are used to determine whether one BPM is off-waist and the other is on-waist (and thus have a low correlation) or whether both BPMs are off-waist (and hence have a high correlation). From Fig. 2.25, one can see that in this configuration, the hypothesis of whether the beam waist is at one of the BPMs can be tested with a longitudinal precision of a fraction of a millimetre.

2.9 Summary

This chapter has presented an outline of concepts in transverse and longitudinal dynamics used in this thesis, and an overview of the ATF and the goals of the FONT project at this facility. The functioning of the FONT stripline BPMs and their associated analogue processing electronics has been described, explaining how the beam position, bunch phase and extracted charge can be measured. The FONT5 digital board, the stripline kickers and the kicker amplifiers were described in the context of the operation of intra-train feedback.

The configuration of the stripline BPMs P2 and P3 and kickers K1 and K2 used in the upstream feedback system was described in terms of its ability to stabilise both the beam position and angle. The performance of the feedback system was analysed both at the feedback BPMs and its propagation to the stripline BPM MFB1FF located 30 metres downstream. A factor ~ 3 reduction in position jitter was measured at P2 and P3, in line

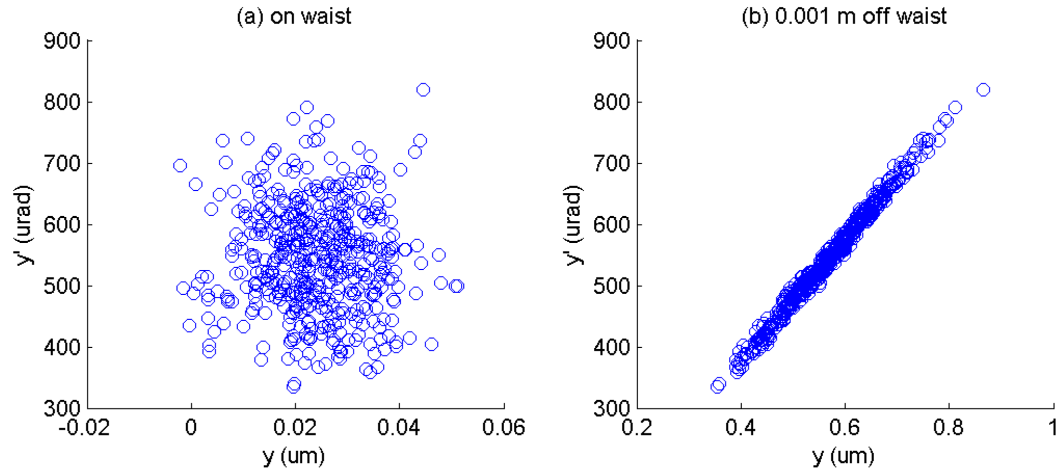

Figure 2.23: Beam angle y' versus position y propagated to (a) the waist and (b) 1 mm downstream of the waist.

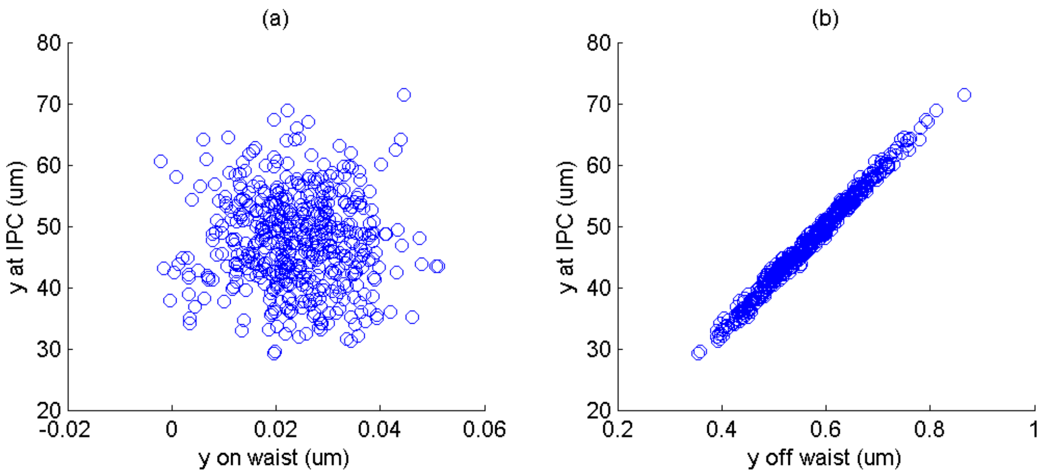

Figure 2.24: Beam position y propagated to IPC versus beam position y propagated to (a) the waist and (b) 1 mm downstream of the waist.

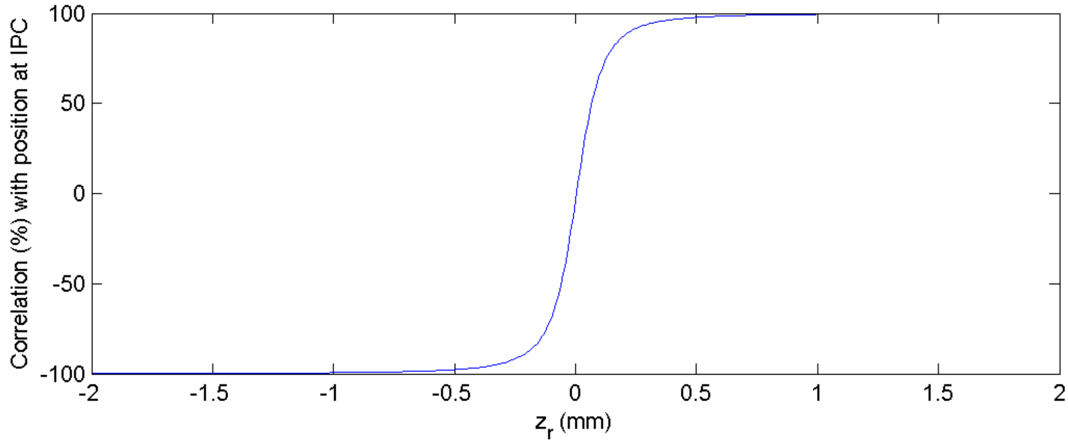

Figure 2.25: Correlation of $y(z_r)$ to y_{IPC}, versus longitudinal distance z_r from the waist, where $y(z_r)$ and y_{IPC} are the vertical beam positions propagated to z_r and to IPC, respectively.

with the expectation given the measured incoming beam jitter and bunch-to-bunch position correlation. The propagation of this level of correction to MFB1FF was demonstrated.

A MAD model of the ATF was used to study the propagation of the beam from the upstream feedback system to MFB1FF. Linear transfer matrices were used to predict the position of each bunch at MFB1FF by using the measured bunch positions at P2 and P3. A comparison of the measured and predicted positions at MFB1FF gave a BPM resolution estimate of 315 ± 5 nm for the P2, P3 and MFB1FF system of BPMs. The beam was propagated further to the IP region, and the propagated jitter at the beam waist was reported. It was noted that the linear transfer model almost certainly underestimates the level of jitter at the beam focus, and the chapters that follow will concentrate on the operation of a local IP feedback system to stabilise the beam position jitter at the IP.

Chapter 3

IP BPM operating principles

3.1 Cavity BPM theory

A charged beam travelling through a cavity-like structure in a beamline will set up an electromagnetic oscillation. Cavity BPMs exploit the fact that the amplitude of a suitable electromagnetic mode will scale with the offset of the beam from the electrical centre of the cavity.

3.1.1 Cavity modes

The IP BPMs at ATF have a rectangular cross-section, allowing the use of an x, y, z Cartesian coordinate system where z lies along the centre of the beampipe. The induced voltage V_{ind} in a cavity is proportional to the electric field $\mathbf{E}$ of the beam in the direction of its path $\mathbf{r}$ [71]:

$$V_{\mathrm{ind}} \propto \int_{\mathbf{r}_1}^{\mathbf{r}_2} \mathbf{E}.\mathrm{d}\mathbf{r}. \tag{3.1}$$

Transverse magnetic (TM) modes have the property of an electric field with a component along z and, hence, will be excited by the beam travelling in the same direction. TM modes are classified according to the integer number m, n, l of half-period variations of the field in the x, y, z directions, respectively.

TM modes used in cavity BPMs have fields that are z-independent, that is, $l = 0$. For these modes, the components of $\mathbf{E}$ are [72]:

$$E_x = 0, \tag{3.2}$$

$$E_y = 0, \tag{3.3}$$

$$E_z = E_{mn} \sin\left(\frac{m\pi(x + \frac{a}{2})}{a}\right) \sin\left(\frac{n\pi(y + \frac{b}{2})}{b}\right) e^{i2\pi f_{mn} t}, \tag{3.4}$$

where the boundaries of the cavity are $-\frac{a}{2} \leq x \leq \frac{a}{2}$ and $-\frac{b}{2} \leq y \leq \frac{b}{2}$, f_{mn} is the resonant frequency of mode mn in the cavity and t is time. The E_{mn} amplitude is specific to each mode, but in each case scales with the charge of the bunch. The resonant frequency is given by [73]:

$$f_{mn} = \frac{c_0}{2}\sqrt{\left(\frac{m}{a}\right)^2 + \left(\frac{n}{b}\right)^2} \tag{3.5}$$

where c_0 is the electromagnetic wave velocity.

In a cavity BPM system, two types of cavity are required: reference and dipole cavities.

A reference cavity is designed for strong excitation of the monopole mode TM_{110}. Fig. 3.1(a) shows the E_z field in the transverse plane x, y at an instant of time for an example rectangular cavity. The electrical centre of the cavity, at $(x, y) = (0, 0)$, constitutes a stationary point of E_z when differentiated with respect to x or y. Being a stationary point, E_z is independent of small excursions in x and y around the cavity electrical centre as demonstrated by taking a first-order Taylor expansion of Eq. 3.4 around $x = 0$ and $y = 0$:

$$\mathrm{TM}_{110} : E_z = E_{11}\sin\left(\frac{\pi x}{a} + \frac{\pi}{2}\right)\sin\left(\frac{\pi y}{b} + \frac{\pi}{2}\right)e^{i2\pi f_{11}t} \approx E_{11}e^{i2\pi f_{11}t}. \tag{3.6}$$

Thus, for the usual operating conditions where the beam is close to the cavity electrical centre, the reference cavity signal can be treated as being independent of beam position.

A dipole cavity provides the dipole modes TM_{120} and TM_{210}. Fig. 3.1(b) and (c) show the transverse profile of E_z for the two modes at an arbitrary point in time. The dependence of their amplitude on beam offset is obtained by performing a Taylor expansion of Eq. 3.4 around $x = 0$ and $y = 0$:

$$\mathrm{TM}_{120} : E_z = E_{12}\sin\left(\frac{\pi x}{a} + \frac{\pi}{2}\right)\sin\left(\frac{2\pi y}{b} + \pi\right)e^{i2\pi f_{12}t} \approx -E_{12}\frac{2\pi y}{b}e^{i2\pi f_{12}t}; \tag{3.7}$$

$$\mathrm{TM}_{210} : E_z = E_{21}\sin\left(\frac{2\pi x}{a} + \pi\right)\sin\left(\frac{\pi y}{b} + \frac{\pi}{2}\right)e^{i2\pi f_{21}t} \approx -E_{21}\frac{2\pi x}{a}e^{i2\pi f_{21}t}. \tag{3.8}$$

When the beam passes through the cavity centre, both modes have $E_z = 0$. However, when the beam passes off-centre, the TM_{120} mode is excited with an amplitude proportional to the vertical offset y, whilst the TM_{210} mode's amplitude scales with the horizontal offset x. A strong dependence on beam offset is achieved as $\frac{\partial E_z}{\partial y}$ and $\frac{\partial E_z}{\partial x}$ are maximal for the TM_{120} and TM_{210} modes, respectively, at the cavity centre. The choice of an asymmetric rectangular cavity, where $a \neq b$, allows the two dipole modes to be decoupled through their different resonant frequencies, as given by Eq. 3.5.

As shown in Eqs. 3.6–3.8, both the reference and dipole cavity signals are oscillating in time at a frequency f_{mn}. The time-dependence in the dipole cavity signal can thus be removed by mixing it with the reference cavity signal, as described in Sec. 3.3.

Each cavity has an associated quality factor Q, defined as [74]:

$$(Q)_{mn} = 2\pi f_{mn}\frac{\text{average energy stored}}{\text{energy loss/second}}. \tag{3.9}$$

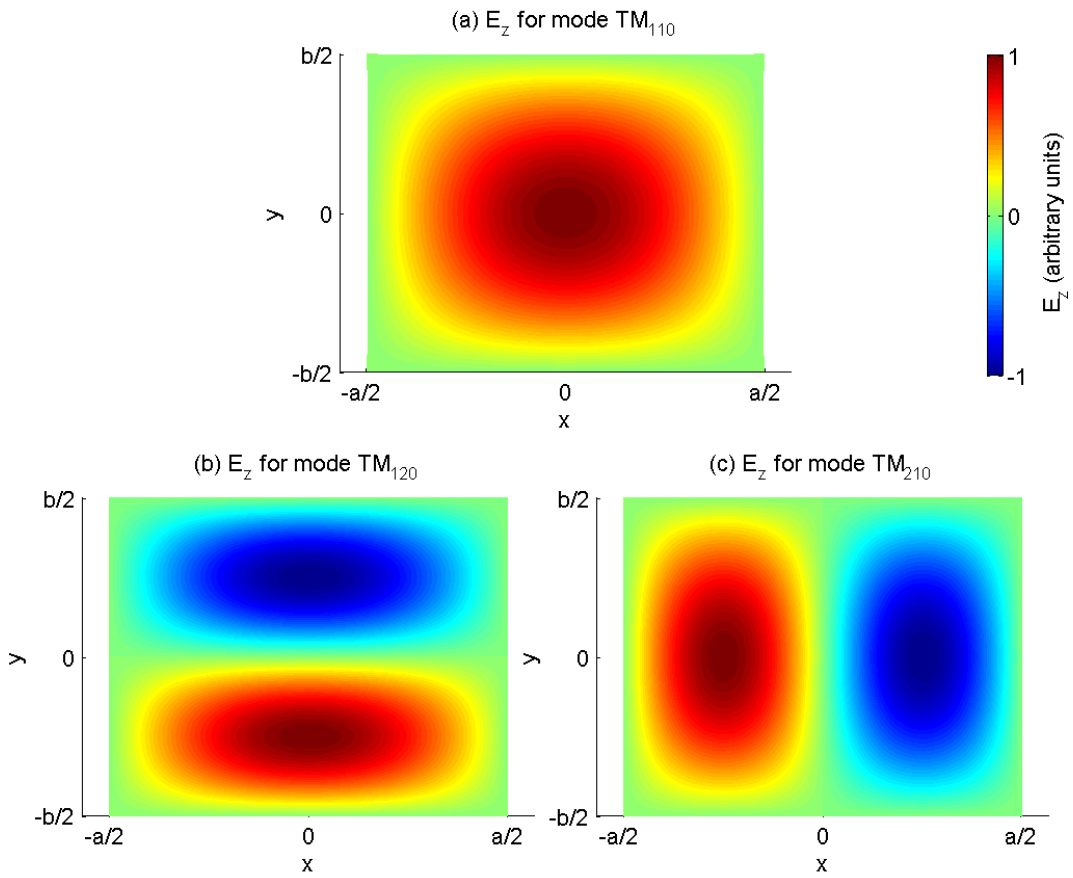

Figure 3.1: E_z versus x and y of a rectangular cavity for (a) the monopole mode TM_{110}, (b) the dipole mode TM_{120} and (c) the dipole mode TM_{210}. The E_z values are normalised to a maximum amplitude of 1 arbitrary unit for each mode.

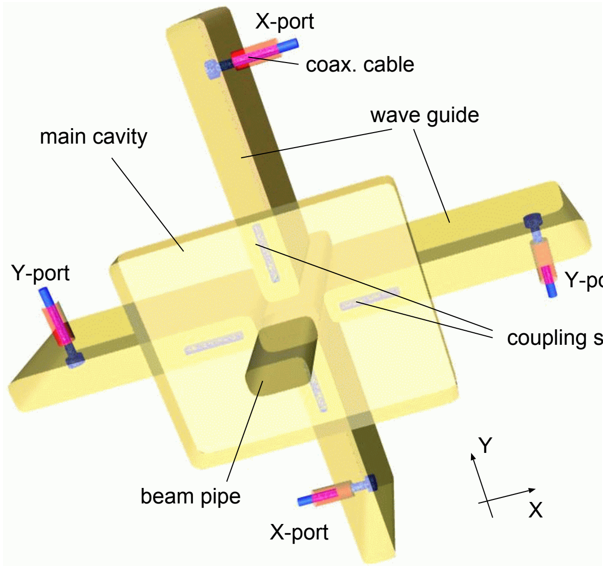

Figure 3.2: Structure of a rectangular cavity with waveguides [76].

Thus, a cavity which loses its energy quickly will have a lower Q. The Q of the cavity itself, ignoring losses due to any external circuit, is called the internal quality factor, Q_0.

3.1.2 Cavity signal extraction

The signals from the reference and dipole cavities are coupled out using electrical antennae. In the case of the reference cavity, the antenna can be placed directly into the cavity as the monopole mode couples most strongly.

For the dipole cavities, a spatial filtering technique is used to suppress the monopole mode from being extracted [75]. The technique is essential as the monopole mode can have a wide frequency spectrum with an amplitude that is orders of magnitude greater than that of the dipole modes. The spatial filtering is achieved by placing thin coupling slots in the transverse faces of the cavity which lead into waveguides, as shown in Fig. 3.2. The waveguides are sufficiently small that only modes whose frequency is greater than or equal to the dipole mode are supported; the monopole mode, of a lower frequency, is not coupled.

The use of thin coupling slots arranged with their long sides parallel to the magnetic field of either the TM_{120} or TM_{210} mode ensures that the two dipole modes are coupled into orthogonal waveguides: the TM_{210} couples into the two vertical waveguides whilst the TM_{120} propagates into the two horizontal waveguides. The slot arrangement further suppresses the extraction of the monopole mode, as its magnetic field is locally perpendicular to each slot.

The distribution of the fields for the TM_{210} mode is shown in Fig. 3.3; the one for the TM_{120} mode would be identical but with the x and y coordinates interchanged. The antennae used to read out the voltage are located towards the ends of the waveguides as shown in Fig. 3.2. The two x ports will read out the same signal but with a relative π-phase difference, and similarly for the y ports. When using two-port read-out, the pair of signals

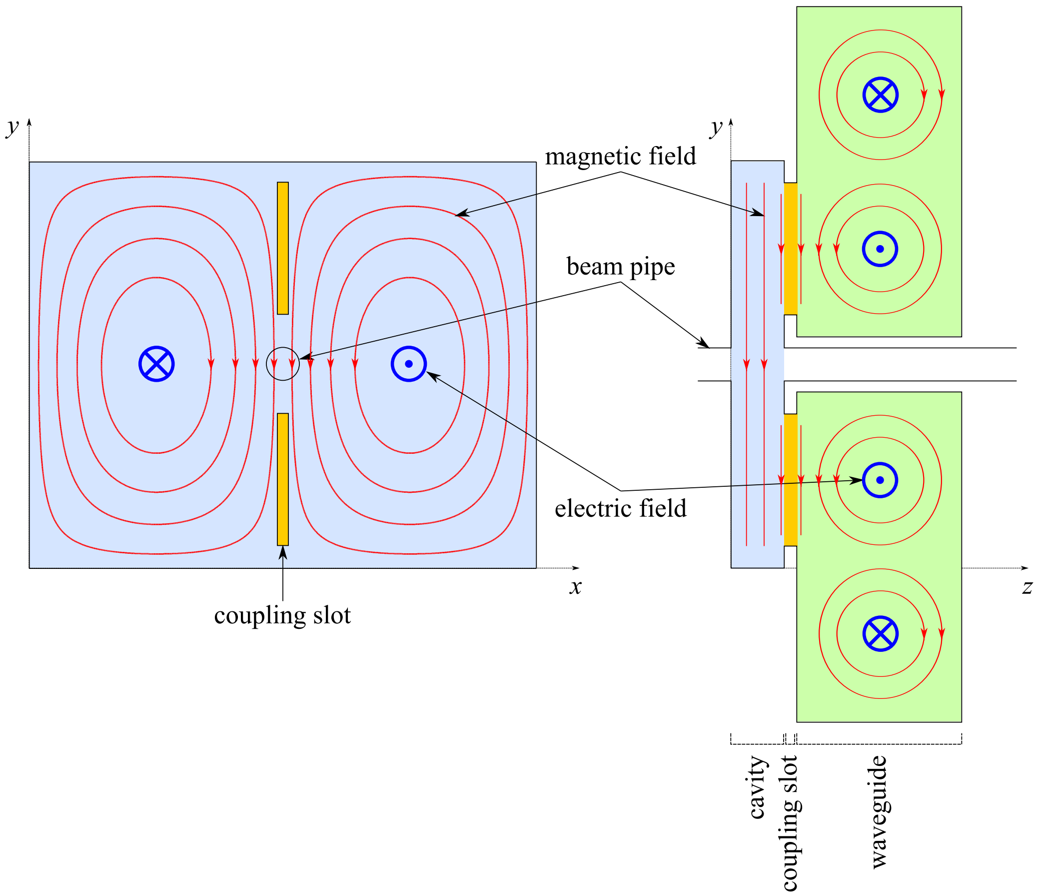

Figure 3.3: Electric fields (blue) and magnetic fields (red) for the TM_{210} mode versus (left) x and y, and (right) y and z, of a rectangular cavity. Only the two waveguides that couple to this mode are shown.

can be combined using a 180° hybrid, doubling the signal power and cancelling unwanted monopole components.

3.1.3 Cavity signal output

The signals obtained from the cavities are both sinusoidally oscillating (Eqs. 3.6–3.8) and exponentially decaying. The sinusoidal component is characterised by the mode frequency f_{mn} (Eq. 3.5); the exponential decay follows the decay constant τ_{mn} specific to the rate of dissipation of energy from the cavity. The signal voltage scales with the bunch charge q.

The choice of τ_{mn} plays an important role in cavity design. When operating with multiple closely-spaced bunches, a fast signal decay is desirable as it limits signal contamination between bunches. However, increasing the cavity decay time allows for longer waveforms to be digitised and analysed. In this respect, multi-sample averaging successfully improves the BPM resolution, as shown in Section 4.2.5.

The amplitude of the dipole cavity signal is proportional to the bunch offset as described in Section 3.1.1. However, there are other mechanisms that also excite the dipole mode.

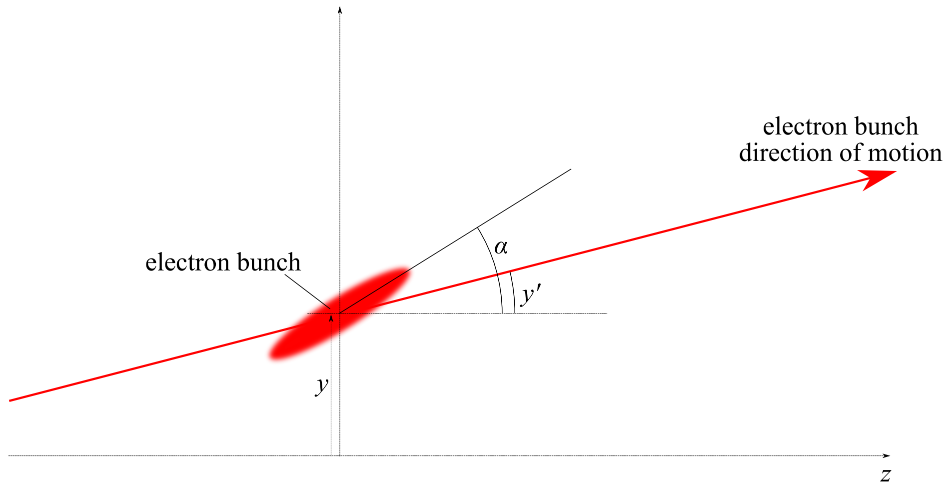

Figure 3.4: Illustration showing the vertical offset y, pitch y' and angle of attack α of a bunch travelling in an accelerator.

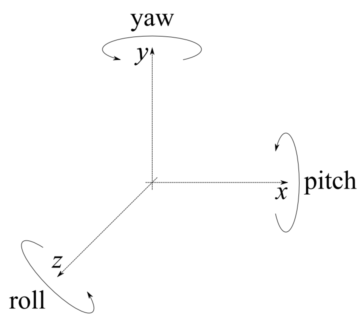

Figure 3.5: Definition of pitch $y' = \frac{\mathrm{d}y}{\mathrm{d}z}$, yaw $x' = \frac{\mathrm{d}y}{\mathrm{d}z}$ and roll in an accelerator coordinate system where the z axis points in the direction of beam propagation.

Fig. 3.4 shows a bunch with a vertical offset y, pitch y' and angle of attack α. The pitch $y' = \frac{\mathrm{d}y}{\mathrm{d}z}$, yaw $x' = \frac{\mathrm{d}y}{\mathrm{d}z}$ and roll are defined in Fig. 3.5. Non-zero y' [76] and α [77] also generate the dipole mode, but with a phase difference of $\pi/2$ relative to that due to the vertical bunch offset y. This phase difference is essential to allow the position dependence to be isolated from the angular dependence.

Consider a dipole mode with a frequency f_{dip} and a decay constant τ_{dip}. In the limits of $\alpha \ll 1$ and $y' \ll 1$, the dipole cavity mode contributions can be expressed [78]:

$$V_y \propto qye^{-\frac{t}{2\tau_{\mathrm{dip}}}} \sin(2\pi f_{\mathrm{dip}} t), \tag{3.10}$$

$$V_\alpha \propto -q\alpha e^{-\frac{t}{2\tau_{\mathrm{dip}}}} \cos(2\pi f_{\mathrm{dip}} t), \tag{3.11}$$

$$V_{y'} \propto qy'e^{-\frac{t}{2\tau_{\mathrm{dip}}}} \cos(2\pi f_{\mathrm{dip}} t). \tag{3.12}$$

The combined dipole mode voltage is given by the sum of the components:

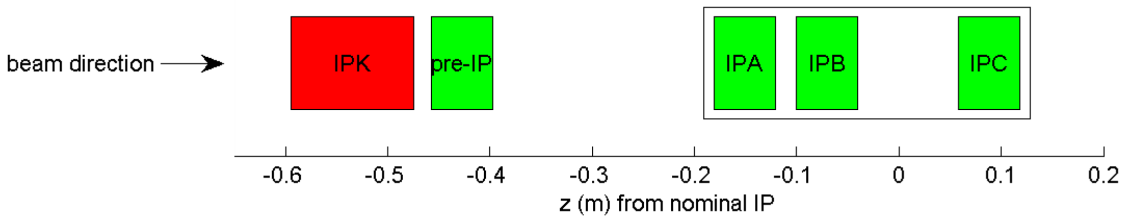

Figure 3.6: Relative longitudinal positions (z) of the kicker IPK and the BPMs pre-IP, IPA, IPB and IPC in the ATF beamline. The centre positions of the elements, as well as the length of IPK, are extracted from the ATF lattice model, version 5.2 [80]. The length of the BPMs is chosen for display purposes.

$$V_{\mathrm{dip}} = V_y + V_\alpha + V_{y'}. \tag{3.13}$$

The reference cavity signal is independent of beam position and angle. Its waveform can be stated as follows:

$$V_{\mathrm{ref}} \propto q e^{-\frac{t}{2\tau_{\mathrm{ref}}}} \sin(2\pi f_{\mathrm{ref}} t), \tag{3.14}$$

where f_{ref} is the frequency of the monopole mode in the reference cavity and τ_{ref} is its decay constant.

3.2 IP BPMs at ATF

The IP area at ATF contains devices to measure both the beam size and beam position of the electron bunches. This is achieved using a beam size monitor (BSM) at the IP and a triplet of BPMs distributed around the IP. A schematic of the beamline elements is shown in Fig. 3.6. The IP and the three BPMs are enclosed within a vacuum chamber. The stripline kicker IPK is located upstream of the IP vacuum chamber, and the two reference cavities for the IP BPMs are situated downstream of the chamber. There are two further cavity BPMs, pre-IP and PIP, respectively located upstream and downstream of the IP BPMs, whose beam position measurements are processed and published directly to the ATF control system [79].

The BSM located at the IP is known as the Shintake Monitor [81]. It makes use of a laser interference fringe pattern in the plane perpendicular to the beampipe. The interaction of the electron beam with the laser fringes produces Compton-scattered photons that are measured using a downstream photon detector. By scanning the fringe pattern vertically, a modulation in the number of Compton photons is observed. The modulation is deeper when the vertical electron bunch size is smaller; this dependence allows the electron bunch spot size to be determined. The Shintake Monitor is designed to measure spot sizes as small as 20 nm [82] and has been central to the small beam size measurements at ATF [36].

Table 3.1: Longitudinal distances between the centres of the IP BPMs [85, 86].

	Longitudinal distance (mm)
IPA to IPB	80.8 ± 0.1
IPB to IPC	174.2 ± 0.5

Table 3.2: Design parameters for the IP BPM dipole [88] and reference [89] cavities.

			Dipole cavities		Reference cavities	
Parameter			x port	y port	x cavity	y cavity
Resonant frequency	f_{mn}	(GHz)	5.712	6.426	5.711	6.415
Internal quality factor	$(Q_0)_{mn}$		4959	4670	1201	1229
Decay time	τ_{mn}	(ns)	18.72	17.23	33.16	30.03

The vacuum chamber described here, along with the IP BPM triplet and its mover system, was installed at ATF in July 2013, replacing the previous IP BPM doublet. The IP BPMs were designed and delivered by the KNU group [83] with the BPM mover system and vacuum chamber fabricated and commissioned by the LAL group [84]. The distances between the centres of the IP BPMs is given in Table 3.1.

The two upstream BPMs IPA and IPB constitute a single block whilst IPC is independent, as shown in the technical drawing of the system given in Fig. 3.7(b). The IP BPMs have an external cross-section of 11 cm $\times$ 11 cm, and are made from aluminium for low mass, with approximately 1 kg per BPM [87]. The drawing of a single IP BPM is given in Fig. 3.8(b). The BPM design replicates the dipole mode resonant frequency of the previous IP BPMs, making the electronics for the signal processing compatible for either set of BPMs. The new BPMs have the novelty of a lower quality factor Q_0 giving faster signal decay times and minimising signal contamination between different bunches. The design parameters for the IP BPM resonant frequency, quality factor and decay time are listed in Table 3.2. The measured resonant frequencies of the cavities used until October 2014 are shown in Table 3.3. These cavities were subsequently replaced by copies manufactured with the same design but with stricter machining tolerances for a better relative alignment between the BPMs (particularly between IPA and IPB) as described in Sec. 4.7.

Table 3.3: Measured resonant frequencies for the IP BPM dipole [88, 90] and reference [91] cavities. The errors on the y dipole cavity frequencies are deduced from the spread of repeated measurements; the same errors are assumed for the x frequencies.

	Resonant frequency (GHz)	
Cavity	x	y
IPA	5.697 ± 0.001	6.409 ± 0.001
IPB	5.698 ± 0.001	6.409 ± 0.001
IPC	5.699 ± 0.001	6.408 ± 0.001
Reference	5.698 ± 0.003	6.410 ± 0.003

Table 3.4: Parameters for the IP BPM mover system [85].

IP BPM block	Full range (µm)	Calibration (µm/V)
IPA-IPB	248	31.015 ± 0.012
IPC	300	30.002 ± 0.007

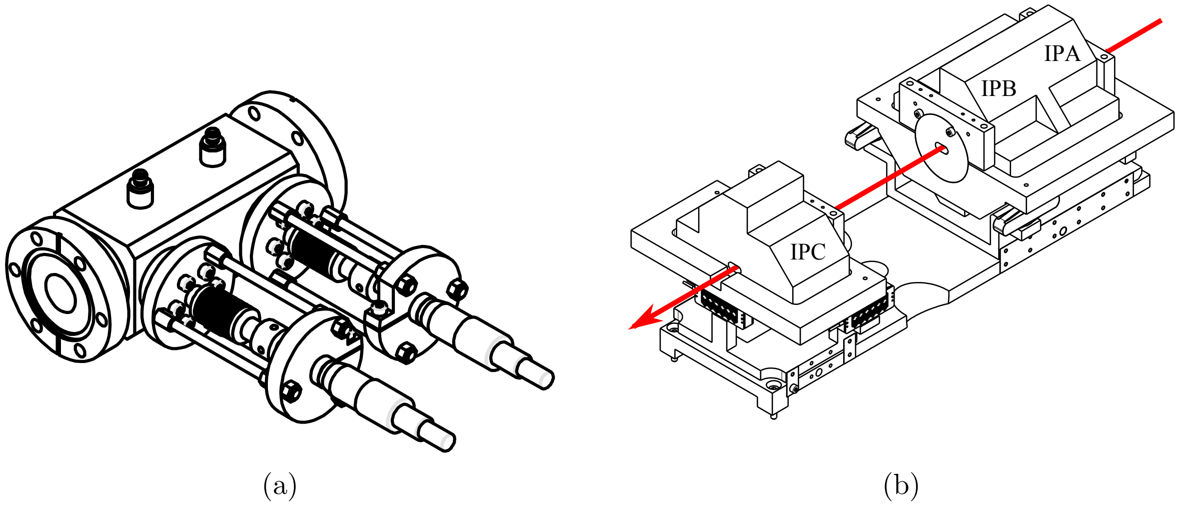

Figure 3.7: Technical drawings of the IP BPM (a) reference cavity block containing x and y reference cavities [92] and (b) dipole cavity block housing BPMs IPA, IPB and IPC [93].

The two BPM blocks (Fig. 3.7(b)) are each mounted on an x, y mover system. Each mover system consists of three vertical sub-movers and one horizontal mover, which allows the block to be moved in x and y and also to be rotated around the x and z axes. Both mover systems are equipped with a feedback system that ensures a block stability of better than 2 nm once the position is set [85]. The IPA-IPB and IPC mover systems are manufactured by the companies Cedrat and PI, respectively, and have slightly different specifications as given in Table 3.4. The mover system reads out its position in volts; the corresponding position can be obtained by using the appropriate calibration constant.

The x and y reference cavities for the IP BPM system are placed downstream of the IP vacuum chamber. The reference cavities have a circular cross-section, with a diameter of 42.95 mm for the x cavity and 38.65 mm for the y cavity, compared to the beampipe diameter of 16 mm [87] as shown in Fig. 3.8(a). The cavities are made from stainless steel and are equipped with a vertical tuning pin that can be used to adjust the monopole mode frequency within a range of ±35 MHz [91]. The assembly of the two reference cavities is shown in Fig. 3.7(a). The design parameters are provided in Table 3.2.

3.3 Electronics

The dipole cavity output described in Eq. 3.13 has a characteristic frequency of several GHz. In order to extract the amplitude of the signal at different phases, the waveform is mixed

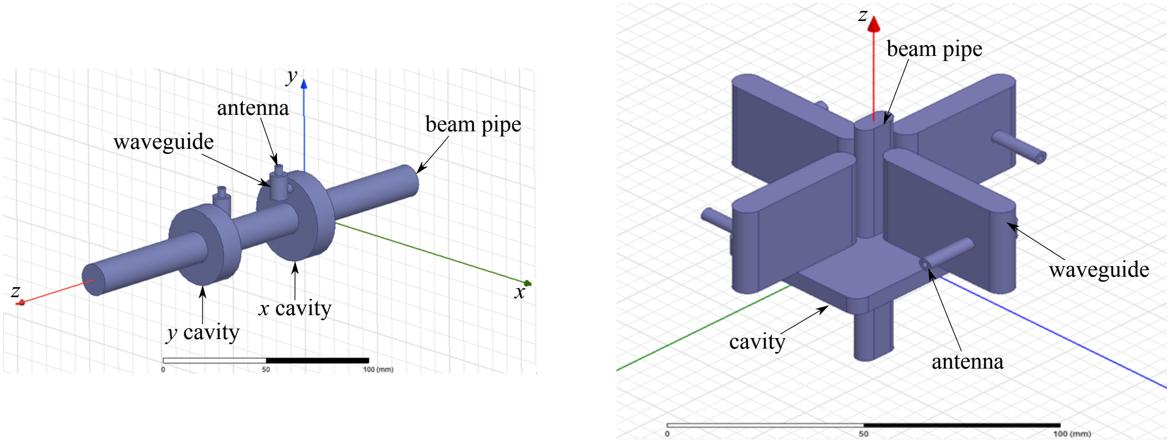

(a) (b)

Figure 3.8: Drawings of the IP BPM (a) reference and (b) dipole cavities [87].

with a similarly high-frequency signal in order to produce an intermediate frequency (IF) output that can be digitised. The process is described as heterodyne if the mixer output has non-zero frequency; otherwise, if the output signal is at baseband, the system is described as homodyne.

Heterodyne systems require further down conversion in order to extract the position-dependent signal from the mixer output. The additional stage of down conversion can be performed digitally and details of such a processing technique used at ATF can be found in [79]. However, the longer latency associated with the digital down conversion makes this approach unsuitable for fast feedback applications.

The two systems described in this thesis each use an analogue processing scheme to produce a pair of signals I, Q at baseband that can be combined linearly to produce a signal I' that is proportional to beam position. The baseband signal can be achieved after one or two analogue mixing stages. The two systems are presented below.

3.3.1 Single-stage signal processing

Single-stage electronics are simpler from the point of view of the number of components. Fig. 3.9 shows a simplified schematic of such a system, where the RF amplifiers typically placed before and after the mixers have been omitted for clarity. The principle behind the design is that the position-dependent dipole signal is mixed directly with the position-independent reference signal to produce position-dependent signals I, Q at baseband.

The x or y pair of dipole cavity outputs is combined using a 180° hybrid as described in Section 3.1.2. Subsequently, both the dipole and reference cavity signals are passed through BPFs centred around their respective resonant frequencies, f_{dip} and f_{ref}, in order to remove any remaining unwanted modes.

A limiting amplifier can be used on the reference path to produce a fixed-amplitude

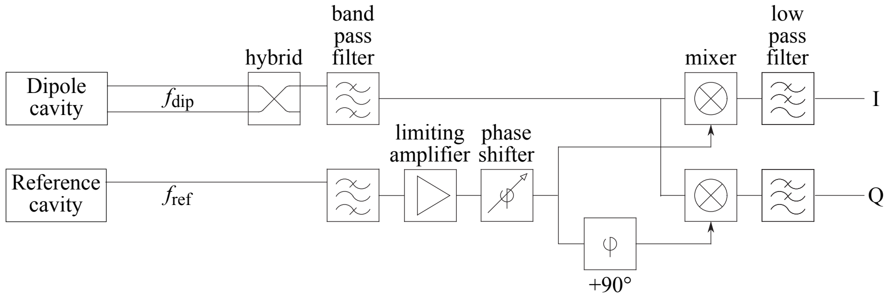

Figure 3.9: Simplified block diagram of a single-stage downmixer.

sinusoidally-varying reference signal. The amplitude of the output is constant regardless of bunch charge and remains limited for a duration longer than the cavity decay time. In this arrangement, the reference signal becomes a perfect LO signal for the mixer as it contains no bunch information other than the critical feature of being phase-locked to the bunch arrival. The limiting amplifier component is however optional; the KNU electronics presented in Section 3.4.1 replaces the role of the limiting amplifier by using a reference signal whose power lies in a range where the mixer output is independent of the reference amplitude [90].

The phase shifter on the reference path allows its phase relative to the dipole signal to be varied before feeding both the dipole and reference signals into a mixer. A second mixer, where the reference signal phase has been shifted by 90°, allows the quadrature component to be extracted. The final low-pass filters remove the upmixed components, as shown in detail below, in order to produce the two baseband signals I, Q.

A mathematical treatment of the I-mixer and the subsequent low-pass filter is presented here. For the analysis, the dipole signal (Eq. 3.13) can be split into the position (V_y) and angle-dependent ($V_\alpha + V_{y'}$) terms; the position-dependent term will be considered first. Using Eqs. 3.10 and 3.14, the mixer inputs can be expressed as:

$$V_{\text{dip}}(y) = A_y \sin(2\pi f_{\text{dip}} t) y q e^{-\frac{t}{2\tau_{\text{dip}}}}, \tag{3.15}$$

$$V_{\text{ref}} = A_{\text{ref}} \sin(2\pi f_{\text{ref}} t + \Delta\phi), \tag{3.16}$$

where $\Delta\phi$ is the phase difference between the two mixer inputs and $A_{\text{dip}}, A_{\text{ref}}$ are constants. The mixer multiplies the two inputs,

$$\begin{aligned} V_I(y) &= V_{\text{dip}}(y) \times V_{\text{ref}} \\ &= A_y A_{\text{ref}} \sin(2\pi f_{\text{dip}} t) \sin(2\pi f_{\text{ref}} t + \Delta\phi) y q e^{-\frac{t}{2\tau_{\text{dip}}}} \\ &= A_y A_{\text{ref}} \tfrac{1}{2} \left(\cos(2\pi(f_{\text{dip}} - f_{\text{ref}})t - \Delta\phi) - \cos(2\pi(f_{\text{dip}} + f_{\text{ref}})t + \Delta\phi)\right) y q e^{-\frac{t}{2\tau_{\text{dip}}}}, \end{aligned} \tag{3.17}$$

and the low-pass filter removes the high frequency component giving:

$$V_I(y) = A_y A_{\mathrm{ref}} \tfrac{1}{2} \cos(2\pi(f_{\mathrm{dip}} - f_{\mathrm{ref}})t - \Delta\phi) y q e^{-\frac{t}{2\tau_{\mathrm{dip}}}}. \tag{3.18}$$

The frequency and phase differences between the dipole and reference cavity signals can be encapsulated in the quantity θ_{IQ}, defined as follows:

$$\theta_{IQ} = 2\pi(f_{\mathrm{dip}} - f_{\mathrm{ref}})t - \Delta\phi. \tag{3.19}$$

For a perfect homodyne system, where $f_{\mathrm{dip}} = f_{\mathrm{ref}}$, θ_{IQ} is independent of time and its value is determined by the phase difference $\Delta\phi$. Eq. 3.18 can be rewritten in terms of θ_{IQ} to give:

$$V_I(y) = A_y A_{\mathrm{ref}} \tfrac{1}{2} \cos(\theta_{IQ}) y q e^{-\frac{t}{2\tau_{\mathrm{dip}}}}. \tag{3.20}$$

For the angle-dependent terms in the dipole signals, Eqs. 3.15 and 3.20 become:

$$V_{\mathrm{dip}}(\alpha, y') = (A_{y'} y' - A_\alpha \alpha) \cos(2\pi f_{\mathrm{dip}} t) q e^{-\frac{t}{2\tau_{\mathrm{dip}}}}, \tag{3.21}$$

$$V_I(\alpha, y') = -(A_{y'} y' - A_\alpha \alpha) A_{\mathrm{ref}} \tfrac{1}{2} \sin(\theta_{IQ}) q e^{-\frac{t}{2\tau_{\mathrm{dip}}}} \tag{3.22}$$

where $A_{y'}, A_\alpha$ are constants.

The position and angle contributions to V_I in Eqs. 3.20 and 3.22, respectively, can be combined to give:

$$V_I(y, \alpha, y') = A_{\mathrm{ref}} \tfrac{1}{2} (A_y y \cos\theta_{IQ} - (A_{y'} y' - A_\alpha \alpha) \sin\theta_{IQ}) q e^{-\frac{t}{2\tau_{\mathrm{dip}}}}. \tag{3.23}$$

A similar expression can be obtained for V_Q by noting that the reference signal used for the Q-mixer undergoes a 90° phase shift: $\Delta\phi \to \Delta\phi + \pi/2$. The transformation to $\Delta\phi$ is equivalent to $\theta_{IQ} \to \theta_{IQ} - \pi/2$ and applying this change to Eq. 3.23 gives V_Q:

$$V_Q(y, \alpha, y') = A_{\mathrm{ref}} \tfrac{1}{2} (A_y y \sin\theta_{IQ} + (A_{y'} y' - A_\alpha \alpha) \cos\theta_{IQ}) q e^{-\frac{t}{2\tau_{\mathrm{dip}}}}. \tag{3.24}$$

From Eqs. 3.23 and 3.24, it is clear that if the phase shifter on the reference cavity path is adjusted such that $\theta_{IQ} = 0$, then V_I would be proportional to the position offset y and independent of y' and α whilst simultaneously V_Q would be proportional to a combination of the angular terms y' and α and independent of y.

In most cases it is impractical to set the phase shifter with sufficient precision, and a deconvolution of the position and angle terms can be performed in analysis. A pure position signal I' and a pure angular signal Q' can be obtained by performing linear combinations of I and Q using θ_{IQ}:

$$V_{I'} = \quad V_I \cos\theta_{IQ} + V_Q \sin\theta_{IQ} = A_{\mathrm{ref}} \tfrac{1}{2} q e^{-\frac{t}{2\tau_{\mathrm{dip}}}} A_y y, \tag{3.25}$$

$$V_{Q'} = -V_I \sin\theta_{IQ} + V_Q \cos\theta_{IQ} = A_{\mathrm{ref}} \tfrac{1}{2} q e^{-\frac{t}{2\tau_{\mathrm{dip}}}} (A_{y'} y' - A_\alpha \alpha), \tag{3.26}$$

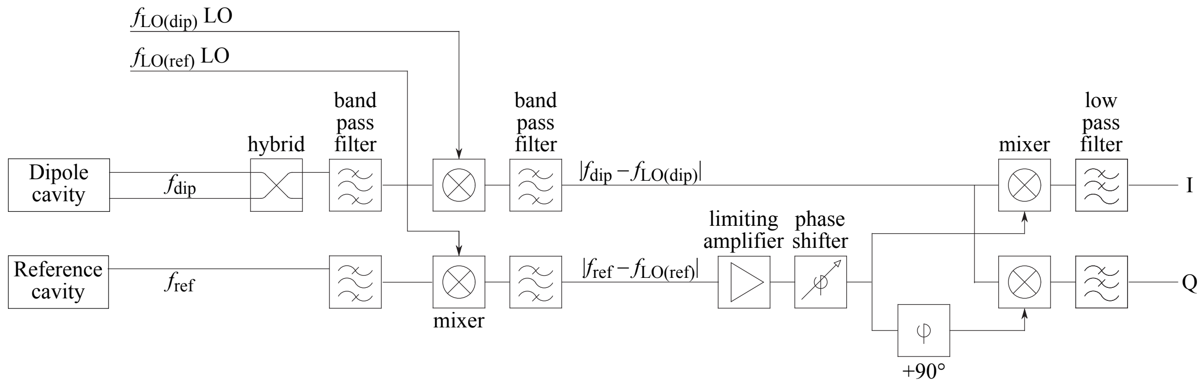

Figure 3.10: Simplified block diagram of a two-stage downmixer.

where Eqs. 3.23 and 3.24 were used to obtain the right hand side of Eqs. 3.25 and 3.26. The value of θ_{IQ} can be obtained experimentally from a BPM calibration as explained in Section 3.6.3.

3.3.2 Two-stage signal processing

Two-stage electronics first reduce the frequency of the dipole and reference cavity signals before mixing one against the other. Fig. 3.10 shows a simplified schematic of such a system, where the RF amplifiers typically placed before, in between and after the mixers have been omitted for clarity. The system resembles a single-stage processor with the addition of a first stage of RF mixing on both the dipole and reference signal paths, each followed by a BPF to remove the upmixed components. The first-stage mixers are driven by external, continuous LO signals (sinusoidally-varying signals of constant frequency and amplitude). For perfect mixers, the final base-band signals I, Q are independent of the LO source as long as the same LO signal is used for both first-stage mixers, as demonstrated in the mathematical treatment below.

The input signals can be specified as follows:

$$\text{Dipole cavity :} \quad V_{\text{dip}} = \left\{ \begin{array}{l} A_y y \sin(2\pi f_{\text{dip}} t) \\ \qquad +(A_{y'} y' - A_\alpha \alpha) \cos(2\pi f_{\text{dip}} t) \end{array} \right\} q e^{-\frac{t}{2\tau_{\text{dip}}}}; \tag{3.27}$$

$$\text{Reference cavity :} \quad V_{\text{ref}} = A_{\text{ref}} \sin(2\pi f_{\text{ref}} t + \Delta\phi); \tag{3.28}$$

$$\text{LO for dipole :} \quad V_{\text{LO(dip)}} = A_{\text{LO(dip)}} \sin(2\pi f_{\text{LO(dip)}} t + \Delta\phi_{\text{LO(dip)}}); \tag{3.29}$$

$$\text{LO for reference :} \quad V_{\text{LO(ref)}} = A_{\text{LO(ref)}} \sin(2\pi f_{\text{LO(ref)}} t + \Delta\phi_{\text{LO(ref)}}) \tag{3.30}$$

where $f_{\text{LO(dip)}}, f_{\text{LO(ref)}}$ are the frequencies of the two LO signals (Fig. 3.10), $\Delta\phi_{\text{LO(dip)}}$, $\Delta\phi_{\text{LO(ref)}}$ are the phases of the LO signals relative to the dipole cavity signal at the inputs to the first-stage mixers and all A terms are constants.

After the first-stage mixers, the dipole and reference signals are downmixed to:

$$V_{\mathrm{dip}\,\otimes\,\mathrm{LO(dip)}} = A_{\mathrm{LO(dip)}}\tfrac{1}{2}\left\{\begin{aligned} &A_y y\cos(2\pi(f_{\mathrm{dip}}-f_{\mathrm{LO(dip)}})t-\Delta\phi_{\mathrm{LO(dip)}}) \\ &\quad -(A_{y'}y'-A_\alpha\alpha)\sin(2\pi(f_{\mathrm{dip}}-f_{\mathrm{LO(dip)}})t-\Delta\phi_{\mathrm{LO(dip)}})\end{aligned}\right\} q e^{-\frac{t}{2\tau_{\mathrm{dip}}}}, \tag{3.31}$$

$$V_{\mathrm{ref}\,\otimes\,\mathrm{LO(ref)}} = A_{\mathrm{ref}}A_{\mathrm{LO(ref)}}\tfrac{1}{2}\cos(2\pi(f_{\mathrm{ref}}-f_{\mathrm{LO(ref)}})t+\Delta\phi-\Delta\phi_{\mathrm{LO(ref)}}). \tag{3.32}$$

The second-stage mixers which produce the baseband signals I, Q can be treated as the mixers in the single-stage system presented in Section 3.3.1. The signals $V_{\mathrm{dip}\,\otimes\,\mathrm{LO(dip)}}$ and $V_{\mathrm{ref}\,\otimes\,\mathrm{LO(ref)}}$ in Eqs. 3.31 and 3.32 take the role of the input signals V_{dip} and V_{ref}, respectively, of the single-stage system. Thus, the I, Q signals of the two-stage downmixer can be expressed as:

$$V_I(y,\alpha,y') = A_{\mathrm{ref}}A_{\mathrm{LO(dip)}}A_{\mathrm{LO(ref)}}\tfrac{1}{8}(A_y y\cos\theta_{IQ} - (A_{y'}y' - A_\alpha\alpha)\sin\theta_{IQ})qe^{-\frac{t}{2\tau_{\mathrm{dip}}}}, \tag{3.33}$$

$$V_Q(y,\alpha,y') = A_{\mathrm{ref}}A_{\mathrm{LO(dip)}}A_{\mathrm{LO(ref)}}\tfrac{1}{8}(A_y y\sin\theta_{IQ} + (A_{y'}y' - A_\alpha\alpha)\cos\theta_{IQ})qe^{-\frac{t}{2\tau_{\mathrm{dip}}}}, \tag{3.34}$$

where

$$\theta_{IQ} = 2\pi(f_{\mathrm{dip}} - f_{\mathrm{LO(dip)}} - f_{\mathrm{ref}} + f_{\mathrm{LO(ref)}})t - \Delta\phi_{\mathrm{LO(dip)}} - \Delta\phi + \Delta\phi_{\mathrm{LO(ref)}}. \tag{3.35}$$

By using a common LO signal for the two first-stage mixers, $f_{\mathrm{LO(dip)}} = f_{\mathrm{LO(ref)}}$ and $\Delta\phi_{\mathrm{LO(dip)}} - \Delta\phi_{\mathrm{LO(ref)}} =$ constant, so the expression for θ_{IQ} reduces to that for the single-stage downmixers in Eq. 3.19. Thus, for perfect mixers, any dependence of I, Q of the two-stage system on the external LO frequency and phase is removed.

3.4 Electronics at ATF

Since the installation of the triplet of IP BPMs at ATF, two sets of signal processing electronics have been used. The first is the KNU electronics, a single-stage downmixer designed by the KNU group [83] in parallel to the development of the IP BPM triplet. The second is the Honda electronics, a two-stage downmixer developed by Y. Honda and colleagues at KEK in 2008 [76] for use on previous incarnations of the IP BPM system. The processing scheme in each set of electronics is described below.

3.4.1 Signal processing in the KNU electronics

The KNU electronics is a single-stage downmixer of the type described in Sec. 3.3.1. The KNU electronics block diagram in Fig. 3.11 contains the key components introduced for general single-stage downmixers in Fig. 3.9. An individual set of electronics exists for each

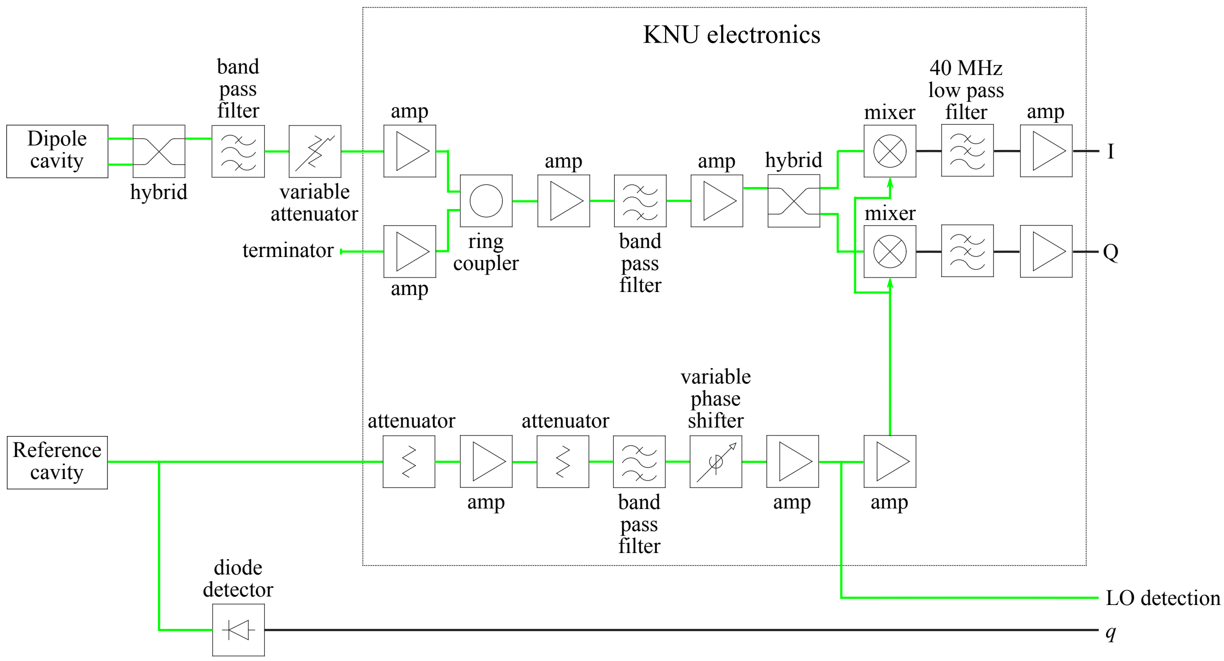

Figure 3.11: Block diagram of the KNU single-stage downmixer (adapted from [87]). Signals in green are at C-band; signals in black are at baseband.

of the x and y axes for each of the three IP BPMs. For each of x and y, the reference cavity signal, which acts as the LO, is split four ways before the electronics: three of the outputs are used for the IP BPM processors and the fourth output is passed through a diode detector for use as a bunch charge q indicator.

The KNU electronics has some specific features. The signals coming from the two ports of the dipole cavity are first amplified before being combined in the ring coupler (a particular type of 180° hybrid). Amplifying before combining the two signals introduces the risk that the unwanted in-phase components of the two signals may saturate the amplifiers before being removed by the coupler [94]. For this reason the use of an external 180° hybrid, to combine the signals from the two dipole cavity ports before the KNU electronics, was considered. In this set-up, the combined signal constitutes one of the KNU electronics port inputs whilst the other port input is terminated. This approach leaves the ring coupler unused, introducing an unwanted signal loss of 3 dB.

As discussed in Sec. 3.3.1, the mixers producing the I and Q signals have the feature that one of the inputs of the Q mixer has undergone a 90° phase change. This is achieved in the KNU electronics by using a hybrid coupler on the dipole signal path, which introduces a 90° phase change to one of its outputs and no phase change to the other output. The reference signal inputs to the mixers are obtained from a power divider and are, hence, in phase.

The KNU electronics has the feature of a remotely-controlled phase shifter on the reference cavity signal path which can be controlled from the ATF Control Room over the ATF network. This simplifies phasing of the signals such that the I signal is maximally proportional to position offset.

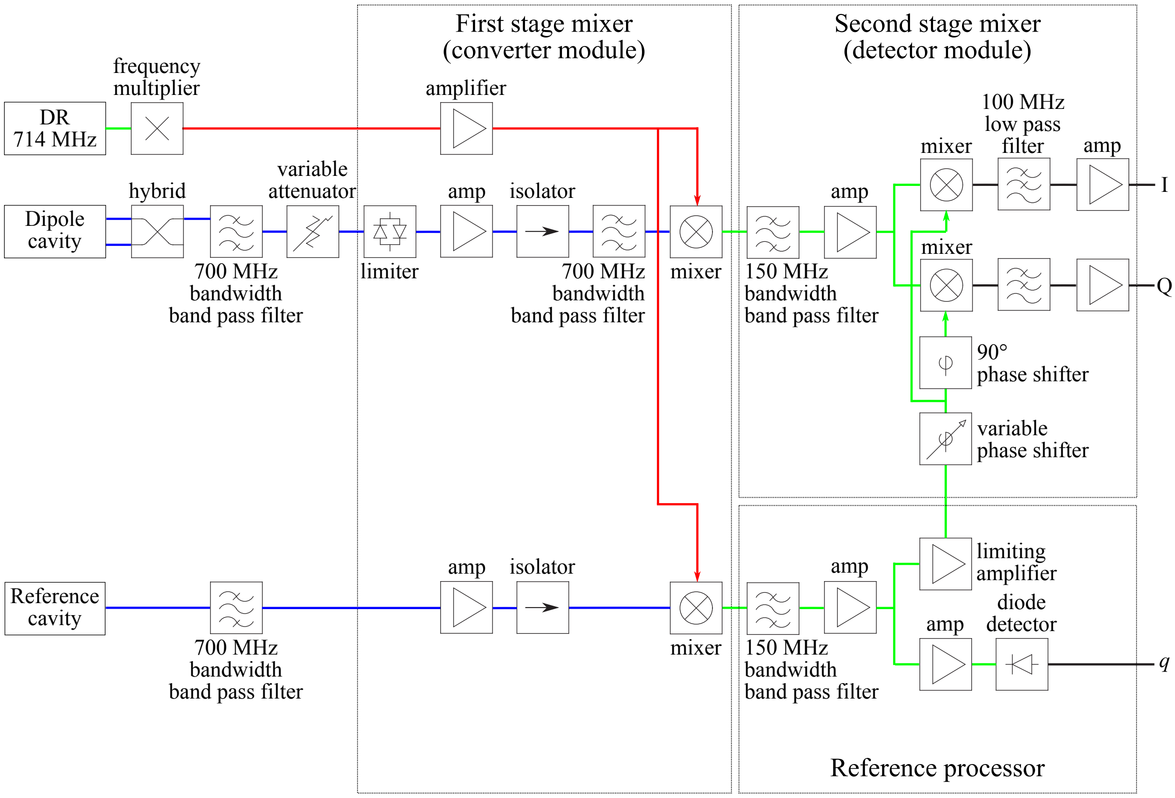

Figure 3.12: Block diagram of the Honda two-stage downmixer (adapted from [71]). The colour key to the frequencies of the signals is given in Table 3.5.

The KNU electronics remains in its commissioning stage, with further modifications being performed at KNU [95]. As a result, the KNU electronics has not been used for the results presented in this thesis.

3.4.2 Signal processing of the Honda electronics

The Honda electronics is a two-stage downmixer like that introduced in Sec. 3.3.2. Its block diagram in Fig. 3.12 contains the key parts given for general two-stage downmixers in Fig. 3.10. Photographs of the two stages of the Honda electronics are given in Fig. 3.13. The dipole cavity signal level entering the first-stage mixer can be adjusted by using the variable attenuator (Fig. 3.12), which can be set between 0 and 70 dB in steps of 10 dB and can be controlled from the ATF Control Room over the ATF network.

The two boxes labelled first and second stage mixers in Fig. 3.12 contain components enclosed within the individual NIM crate modules known as converter and detector modules, respectively. There is a single converter module for x which, when provided with a single LO input, can downmix up to three IP BPM dipole cavity signals plus one reference cavity signal. Similarly, there is a converter module for y that can also handle three IP BPM dipole cavity signals and a reference cavity signal. Regarding the second stage downmixers, there are six individual detector modules, which can each downmix a post-first-stage dipole signal

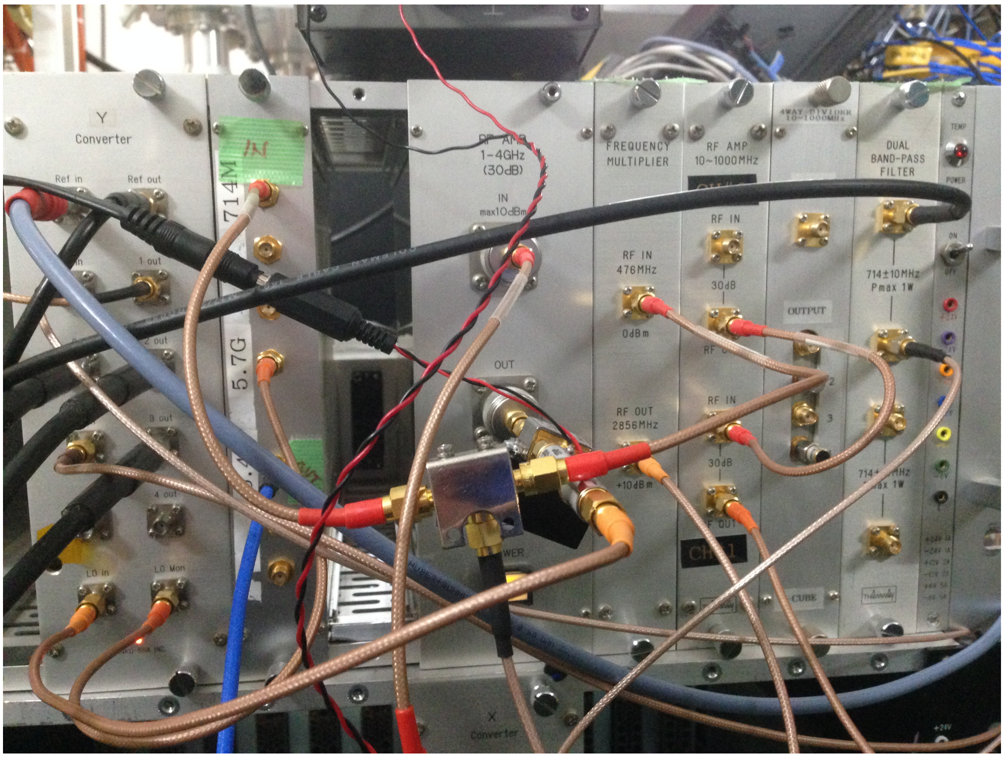

(a)

(b)

Figure 3.13: Photographs of (a) the first and (b) the second stages of the Honda electronics [96].

Table 3.5: Colour key for Fig. 3.12 with the design frequencies of the x and y signals in the different stages of the Honda electronics.

		Frequency (MHz)	
Colour	Description	x signals	y signals
Blue	Cavity signals before first mixer	5712	6426
Red	LO signal for first mixer	6426	5712
Green	DR 714 MHz, and cavity signals after first mixer	714	714
Black	I and Q after second mixer, and reference diode	0	0

using a post-first-stage reference signal.

The LO signal used for the first stage of the Honda electronics is derived from the accelerator DR 714 MHz oscillator. This signal is up-multiplied appropriately such that it produces an LO signal which is 714 MHz away from the design resonant frequency to be downmixed. One notes that the x cavity modes are designed to be 8 times 714 MHz, whereas the y cavity modes are 9 times 714 MHz. The Honda electronics up-multiplies the LO signal to 9 times 714 MHz when downmixing the x reference and dipole cavity signals, whilst using an LO signal of 8 times 714 MHz when downmixing the y reference and dipole cavity signals. By having a 714 MHz difference between the LO and cavity signals in either case, the output of the first-stage mixers is always 714 MHz. The frequencies of the different parts of the Honda electronics are shown in Table 3.5.

The LO signals for both the x and y first-stage downmixers are obtained from a single source of DR 714 MHz signal, as shown in Fig. 3.14. The frequency of the 714 MHz signal is first multiplied by a factor 8 to be used as the LO signal for the y first-stage mixer. The LO signal power input to both converter modules has to be in the working range of 0 to 3 dBm [97], for which a series of RF amplifiers is used. The LO signal monitor output from the y first-stage mixer is an amplified version of the LO signal input, and this 5712 MHz signal is mixed against a copy of the DR 714 MHz oscillator to produce the 6426 MHz LO signal for the x first-stage mixer.

The reference processing section in Fig. 3.12 splits the post-first-stage reference signal into two. One output is amplified and then passed through a diode detector to be used as a bunch charge q indicator. The other input is passed through a limiting amplifier to produce a suitable LO signal for the second-stage downmixer, as discussed in Sec. 3.3.2. Using the current hardware, up to four copies of the LO signal for the second-stage downmixers are available at any given time. The successful operation of the limiting amplifier has been demonstrated even at the lowest operating bunch charge of 0.05×10^{10} electrons, as presented in Sec. 3.5.1.

The fact that the reference cavity signal needs to travel through the reference processing electronics whilst the dipole cavity signal passes directly from the first to the second stage mixer introduces a complication. The problem can be overlooked with slower decaying cavity signals, as the dipole cavity signal has not decayed much by the time that the delayed reference cavity signal arrives to the second-stage mixer. However, the low-Q IP BPMs used

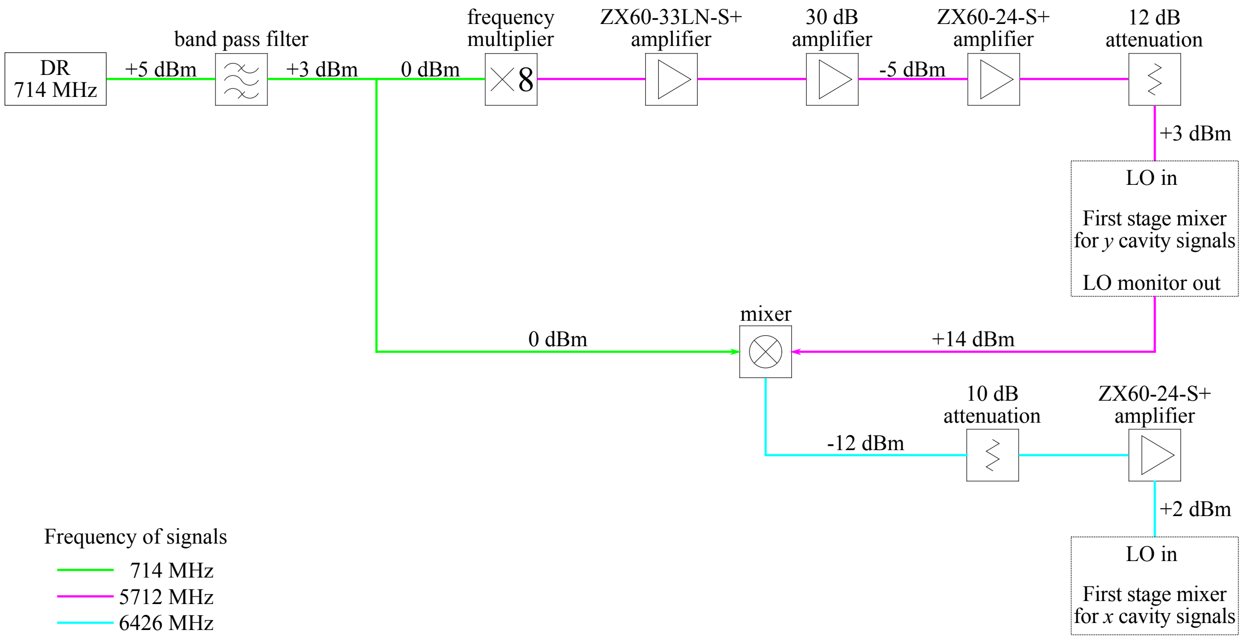

Figure 3.14: LO signal distribution for the x and y first stage downmixers of the Honda electronics. The signal power levels are measured using spectrum analyser HP 8593E. The colour key to the frequencies of the signals is given in the legend.

here require that the dipole cavity signals are delayed to match the delay introduced by the reference signal processing. This is detailed in Sec. 3.5.2.

3.5 Signals in the Honda electronics

3.5.1 Effect of the limiter in the second stage of the Honda electronics

As discussed in Sec. 3.4.2, the reference cavity signal must have an amplitude independent of bunch charge before being used to down-mix the dipole cavity signal in the second stage mixer of the Honda electronics. A limiting amplifier is used for this purpose, as shown in Fig. 3.12. The limiting amplifier module produces four copies of the limited reference signal, which can then be used as the LO signal for four detector modules.

The four limited reference signal outputs were measured using the beam to generate the reference cavity signals. Fig. 3.15 shows the four waveforms digitised on a Tektronix TDS7154B digital oscilloscope [98]. Fig. 3.15(a) was generated by a single bunch with a low charge of 0.05×10^{10} electrons; a higher bunch charge of 0.5×10^{10} electrons was used to obtain Fig. 3.15(b).

It can be seen that all four limited reference signals are limited to a common constant voltage. The duration during which the constant voltage is sustained is longer when the bunch charge is higher, as the signal power level into the limiter is larger. In any case, the constant voltage lasts at least 150 ns, even at the lowest charge setting. As shown in Fig. 3.17 in Sec. 3.5.2, the full duration of the dipole cavity signal is under 100 ns so, with the timing suitably adjusted, the full dipole cavity signal can be down-mixed using a constant limited reference cavity signal.

The large noise on the traces in Fig. 3.15 before the signal arrival was later tracked down, in December 2014, to a damaged cable carrying the signals from the reference cavity. Additionally, bench-test measurements [99] show that the input voltage to the limiting amplifier module should be minimised whilst ensuring that the output is suitably limited; in this regime, the phase shift introduced by the module becomes almost insensitive to the input signal level. Once the damaged cable was replaced, the output from the reference cavity was attenuated by 40 dB to bring the signal level down to the optimum regime deduced from the bench-tests.

3.5.2 Synchronisation of the inputs to the second stage of the Honda electronics

The timing of the dipole and reference cavity signals at the second stage mixer of the Honda electronics has to be carefully set so that the dipole cavity signal arrives when the limited reference cavity signal is already present. Fig. 3.16(a) shows that the reference cavity and IPB dipole cavity signals are synchronous at the output of the converter module of the Honda electronics. Fig. 3.16(b) presents the two signals at the input to the detector module.

Comparing Fig. 3.16(a) and Fig. 3.16(b) it can be seen that the limiting amplifier and associated components on the reference cavity signal path have the expected effect of limiting the reference cavity signal amplitude but also delay it by ~ 30 ns relative to the dipole cavity signal. To compensate the reference cavity signal delay, 8 metre RG 58 delay cables were prepared and placed on each dipole cavity signal path between the converter and detector modules. The outcome, with the delay cables in place, is shown in Fig. 3.17.

3.6 Digital signal processing

The I and Q signals obtained from the Honda electronics are digitised and then processed to extract the beam position. The signals are combined to produce I' which is proportional to bunch position (as given in Eq. 3.25) and Q' which depends on bunch angle (as given in Eq. 3.26). Both I' and Q' also scale with the bunch charge, requiring charge normalisation. This section addresses the signal digitisation, sources of charge normalisation and the position calibration of the IP BPMs.

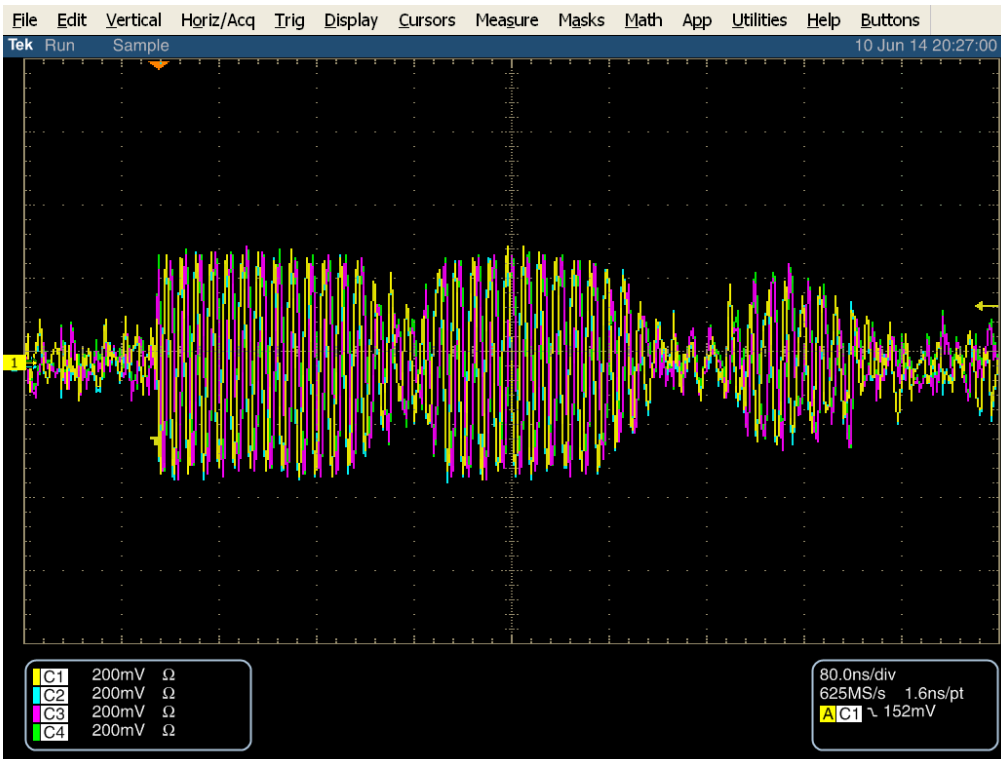

(a)

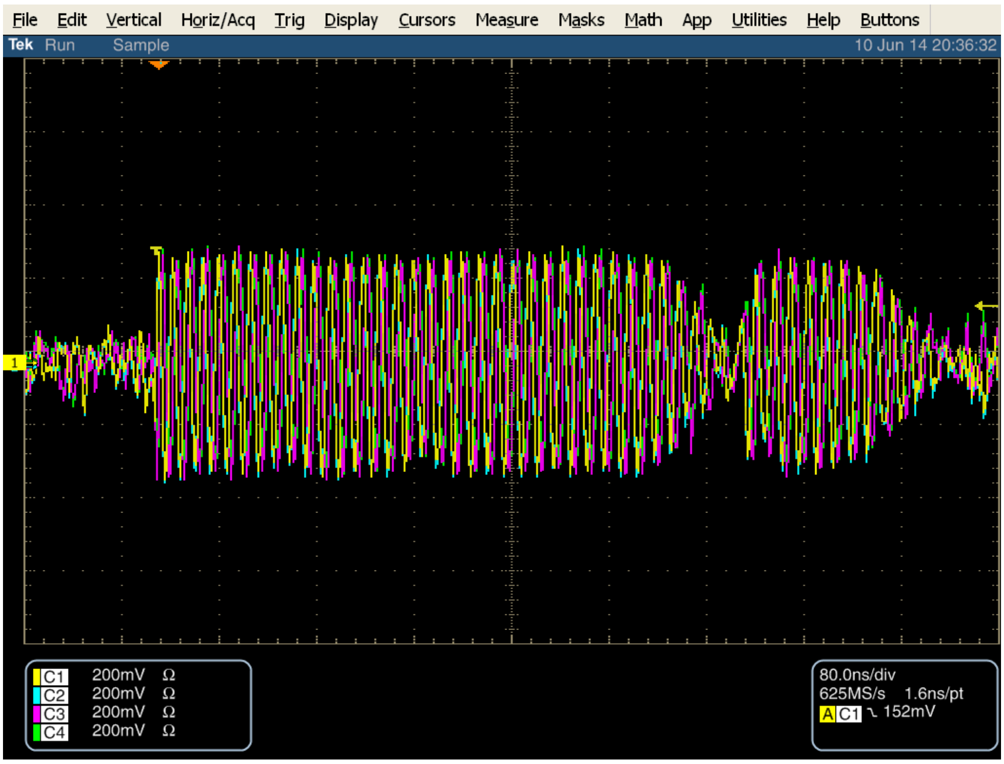

(b)

Figure 3.15: Oscilloscope traces for the reference cavity input to four detector modules of the Honda electronics. The waveforms are generated by a single bunch with (a) $(0.05 \pm 0.01) \times 10^{10}$ electrons and (b) $(0.50 \pm 0.01) \times 10^{10}$ electrons. The same axis settings are used in both cases.

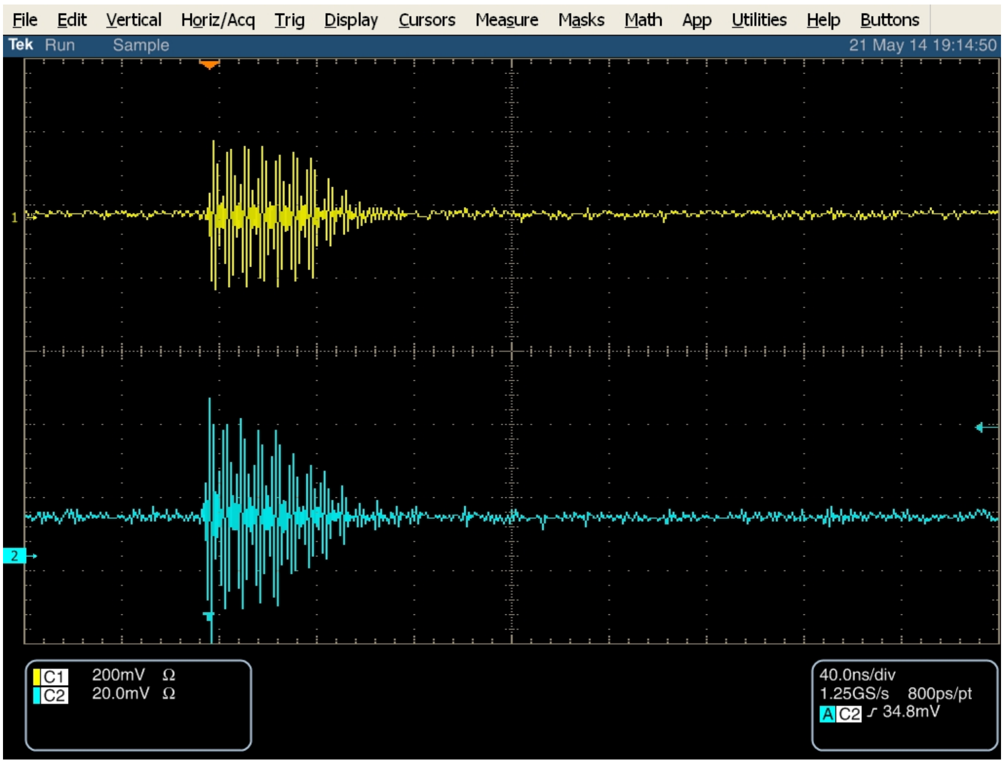

(a)

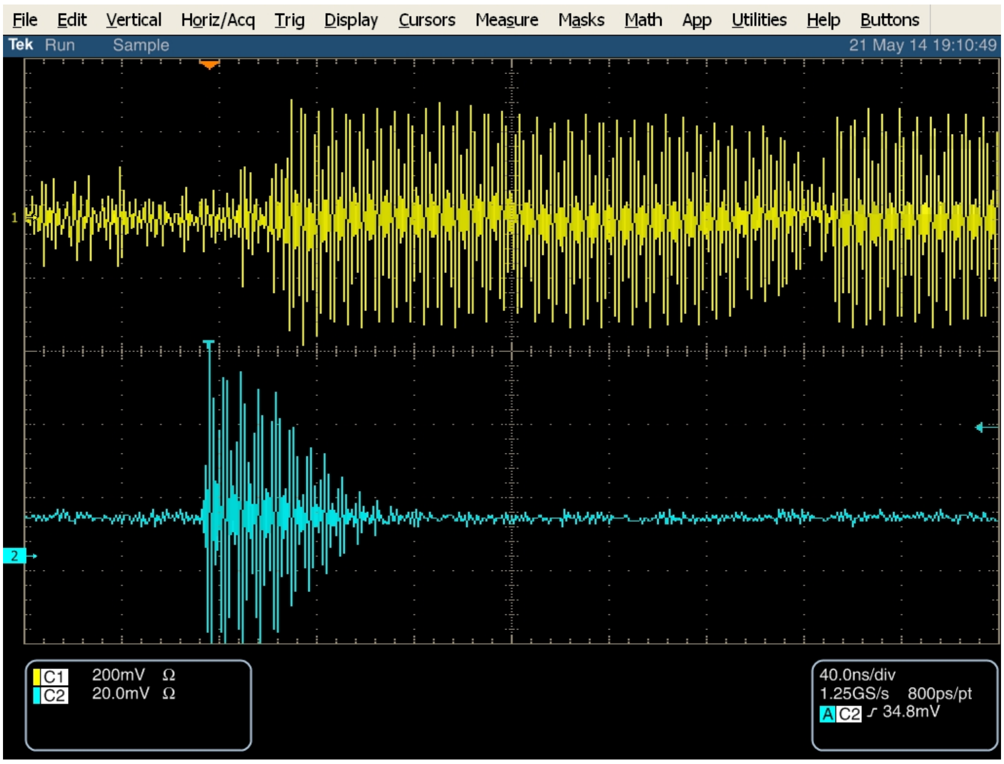

(b)

Figure 3.16: Oscilloscope traces for the reference cavity (yellow) and IPB dipole cavity (cyan) signals at (a) the output of the converter module and (b) the input to the detector module of the Honda electronics, in the absence of delay cables on the dipole cavity signal path. The same axis settings are used in both cases.

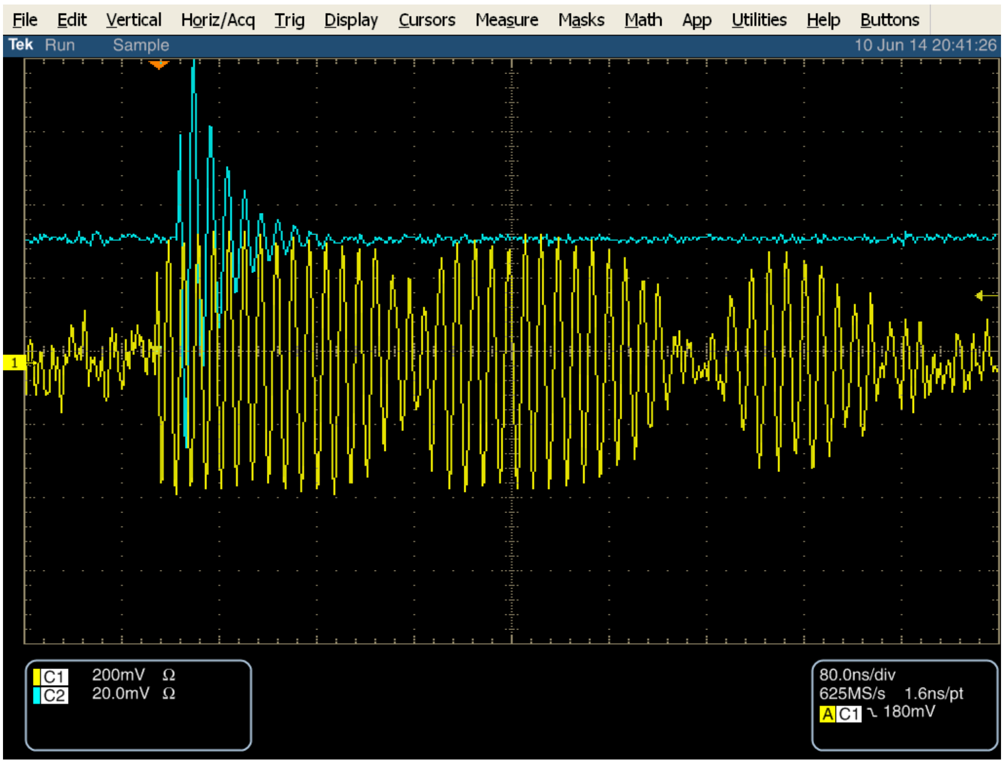

Figure 3.17: Oscilloscope traces for the reference cavity (yellow) and IPA dipole cavity (cyan) signals at the input to the detector module of the Honda electronics, in the presence of delay cables on the dipole cavity signal path.

3.6.1 Signal digitisation

The FONT5 board (Sec. 2.5) is used to digitise the I and Q waveforms, along with the reference diode signal described in Sec. 3.6.2. Example I and Q waveforms obtained using the Honda electronics whilst operating with two-bunch trains are shown in Fig. 3.18. An example reference diode signal also obtained in two-bunch mode is given in Fig. 3.19. The waveforms show that the cavity signals have a fast decay time compared to the $\sim$ 200 ns bunch separation, which is essential to prevent signal contamination between consecutive bunches.

The digitisation frequency of the FONT5 board is 357 MHz, giving a separation of consecutive samples of 2.8 ns. The simplest approach to process the data is to consider the digitised voltage at an optimum sample number for each bunch. A sample number shortly after the peak is generally chosen because early sample numbers, at and before the waveform peak, are exposed to transient effects whilst late sample numbers yield a poor signal-to-noise ratio [71]. The choice of sample number is further discussed in Sec. 4.2.4. The cable lengths of the I and Q signals are matched so the same sample number is used for both. Single-point sampling is the technique used in the feedback firmware algorithm. An alternative technique is to use multiple sample numbers and perform averaging. Multi-sample averaging is discussed in Sec. 4.2.5.

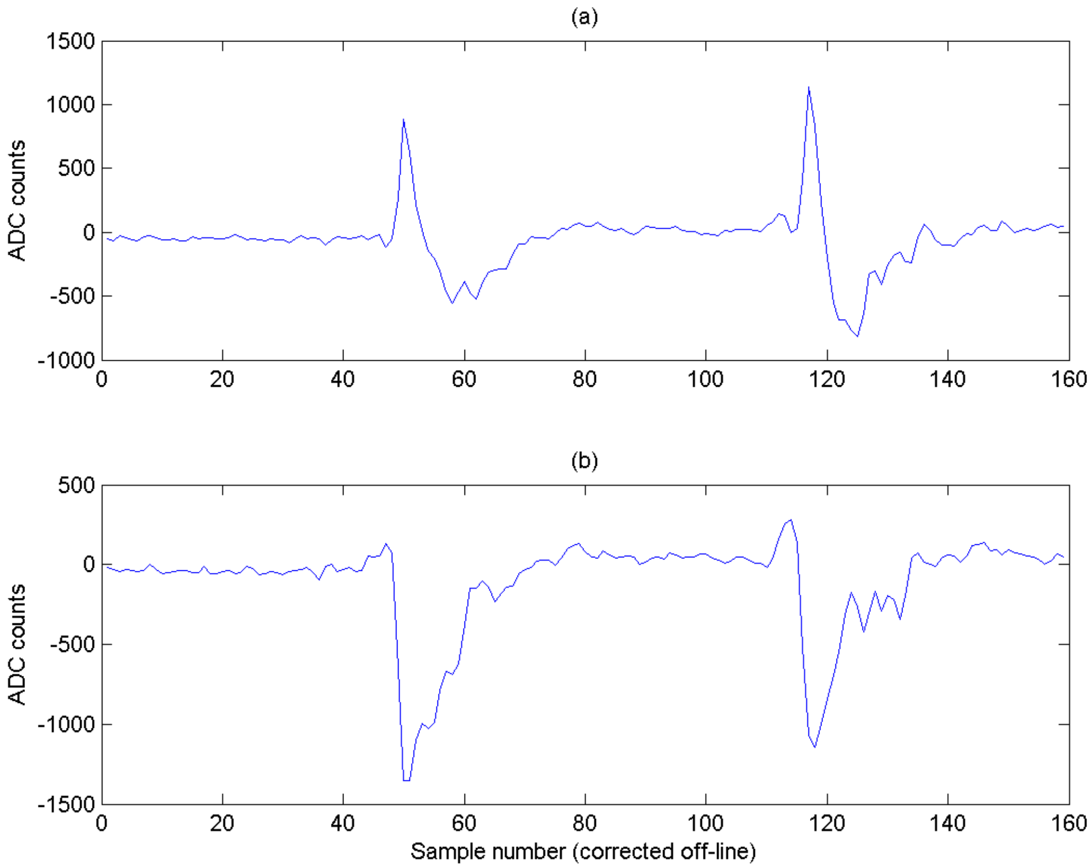

Figure 3.18: Digitised ADC counts versus sample number for (a) the I channel and (b) the Q channel using the Honda electronics. The waveforms correspond to a single trigger over a vertical calibration of IPB in 2-bunch mode. The data was taken with a variable attenuator setting of 20 dB and both bunches are approximately 18 µm off-centre vertically. The sample number of the Q signal has been corrected to remove the delay introduced by the Q signal delay cables described in Sec. 5.1.2.

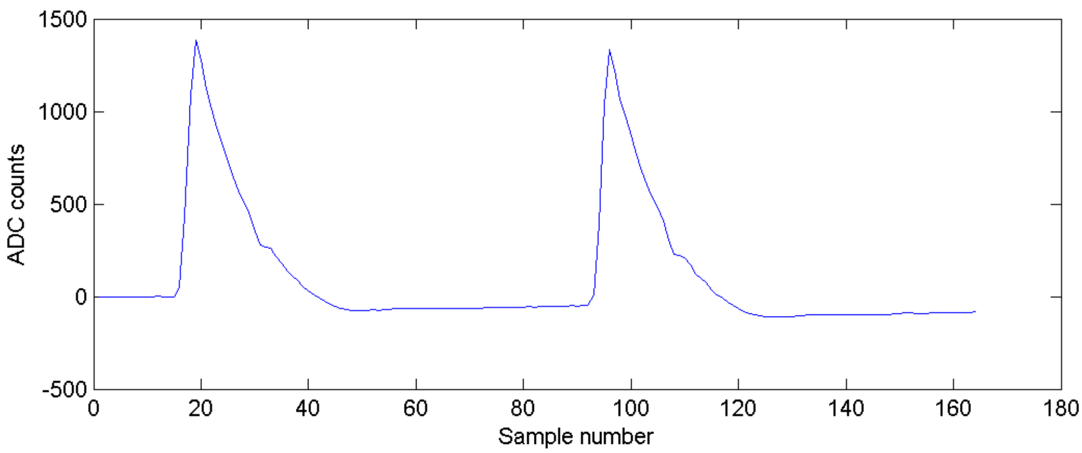

Figure 3.19: Digitised ADC counts versus sample number for the reference diode signal from the Honda electronics. The waveform corresponds to a single trigger in 2-bunch mode.

3.6.2 Charge normalisation

Three sources of charge information are available. The first option is to split the reference cavity signal (governed by Eq. 3.14) and pass it through a diode detector to produce an exponentially-decaying waveform that scales with charge; this signal is referred to as the reference diode signal. An example of a reference cavity diode signal is given in Fig. 3.19. Another option is to use the V_Σ signal from one of the FONT stripline BPMs, whose on-peak amplitude is proportional to charge (Sec. 2.4.3). The third alternative is to use one of the Integrating Current Transformers (ICTs) installed in the ATF beamline, such as EXT ICT in the extraction line. An ICT consists of a set of coils placed in the magnetic field of a passing electron bunch; the magnetic field then induces a current in the coils. The ICT integrates the induced current to give a value proportional to the bunch charge [100].

The ICT measurement has two limitations. First, it is published to the ATF database and hence would be unavailable as an input for intra-train feedback. Secondly, it is configured for single-bunch operation, producing unreliable results when operating with two-bunch trains. It is however a good tool to compare with the reference diode and stripline V_Σ charge measurements.

The correlations between the three charge measurements performed simultaneously over a bunch charge scan are presented in Fig. 3.20. The pedestal of the signals (that is, the charge reported when no charge is present) can be removed using the FONT5 board trim DACs (Sec. 2.5) when digitising the stripline and cavity BPM signals or using the ATF control system when collecting the ICT data. Any residual pedestals, deduced from an empty beam extraction, are removed in the analysis presented here.

The scatter plots in Fig. 3.20 show a strong correlation between the three measurements, with a correlation in excess of 99.8 % between any pair of measurements over the full scan. A straight-line fit is performed to the data with a bunch charge above 0.15×10^{10} electrons. The fit shows that the linearity is preserved in the low-charge limit for the stripline V_Σ and ICT measurements. However, a deviation from linearity is observed for the IP reference diode: an effect intrinsic to diode detectors where the diode output scales with the square of the input at low voltages, whilst scaling linearly at higher voltages [101].

The non-linear response of the diode detector at low voltages limits operation at low bunch charges, but also introduces a fixed offset to the measurement. The reference diode measurement r can be expressed in terms of the true bunch charge q as

$$r = tq + s \tag{3.36}$$

where t, s are constants. If I' is normalised using the reference diode signal r, then the expression for the position would be:

$$\frac{I'}{r} = \frac{I'}{tq + s} = \frac{I'}{tq(1 + \frac{s}{tq})} = \frac{I'}{tq} - \frac{I's}{t^2q^2} + \dots \tag{3.37}$$

using a Taylor expansion for $(1 + \frac{s}{tq})^{-1}$ where the offset s is small. The term proportional to

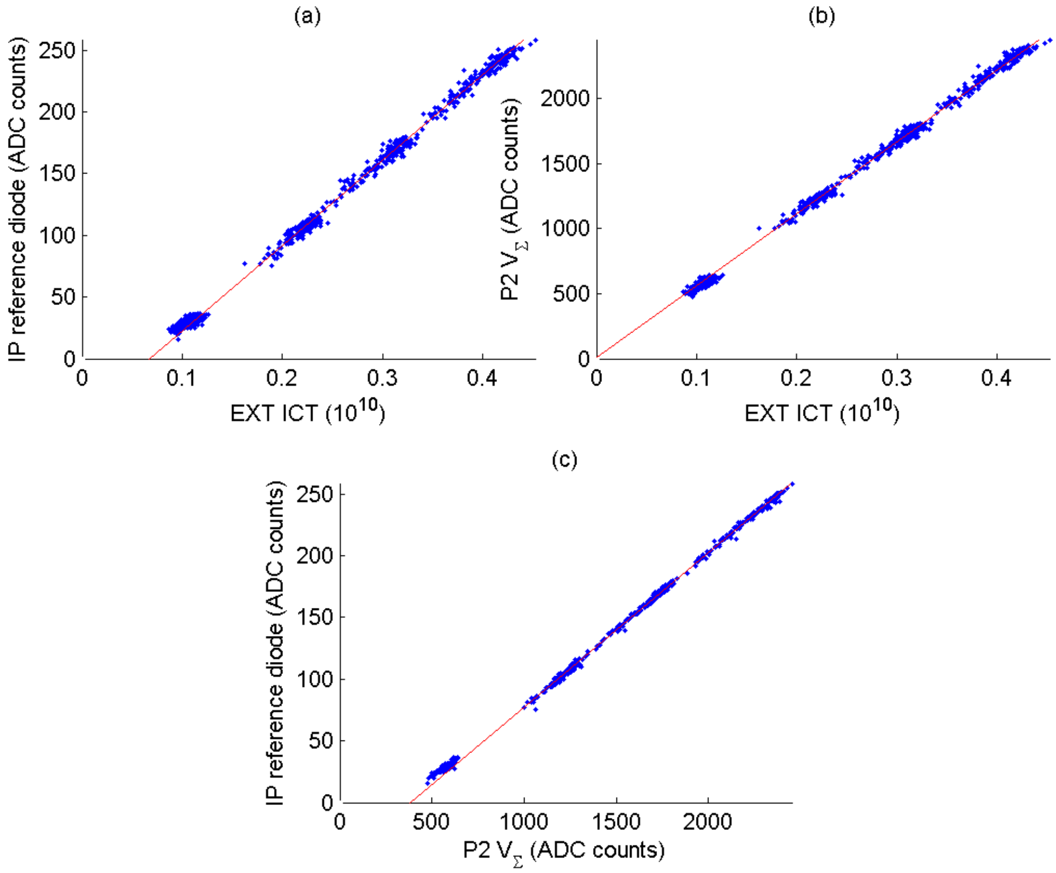

Figure 3.20: Correlations between three measurements of bunch charge for 800 triggers taken over a charge scan from 0.06×10^{10} to 0.5×10^{10} electrons per bunch: (a) reference diode versus extraction line ICT; (b) stripline P2 V_Σ versus extraction line ICT; and (c) reference diode versus stripline P2 V_Σ. Signal pedestals, which are deduced from an empty beam extraction to be 14.40 ± 0.09 ADC counts for the P2 V_Σ, -0.70 ± 0.20 ADC counts for the reference diode and -0.018×10^{10} electrons for the ICT, have been removed. The straight line fits are applied using the data with charge above 0.15×10^{10} electrons.

$\frac{I'}{q}$ is the required one, whilst the unwanted higher order terms will couple charge fluctuations into apparent position jitter.

In view of the limitations introduced by the reference diode, charge normalisation is performed in this thesis using the stripline V_Σ signal whenever possible. The reference diode is used, however, for IP feedback and its associated analysis (Chapter 5) due to the difficulty of delivering the upstream stripline V_Σ signal to the FONT5 board at the IP such that it arrives synchronously to the IP BPM I and Q signals.

3.6.3 IP BPM position calibration

A BPM position calibration is performed by exercising the appropriate BPM mover in steps of known displacement over the dynamic range of the BPM. A centred beam with minimum angle relative to the cavity BPM is desired prior to the calibration in order to reduce the amplitude of unwanted signals. Also, the beam waist is placed at the BPM to reduce the beam jitter. A small beam jitter of ~ 100 nm enables successful calibrations to be performed even over the smallest BPM dynamic range of a few microns when operating at a variable attenuator setting of 0 dB. The beam set-up procedure is detailed in Sec. 4.1.

The result from an example calibration, obtained at a variable attenuator setting of 0 dB, is shown in Fig. 3.21, where charge (q) normalisation is performed using the stripline P2 V_Σ. Having chosen an optimum sample number in the I and Q waveforms, Fig. 3.21(a) shows the variation of $\frac{I}{q}$ and $\frac{Q}{q}$ over 11 consecutive mover steps.

Fig. 3.21(b) displays a scatter plot of $\frac{Q}{q}$ against $\frac{I}{q}$. The points lie along a line that can be interpreted as the $\frac{I'}{q}$ axis. Eqs. 3.25 and 3.26, used to define I' and Q', can be re-expressed in matrix form as follows:

$$\begin{pmatrix} I' \\ Q' \end{pmatrix} = \begin{pmatrix} \cos\theta_{IQ} & \sin\theta_{IQ} \\ -\sin\theta_{IQ} & \cos\theta_{IQ} \end{pmatrix} \begin{pmatrix} I \\ Q \end{pmatrix}. \tag{3.38}$$

The matrix formalism shows that the $\frac{I'}{q}, \frac{Q'}{q}$ set of axes constitute a 2D transformation of the $\frac{I}{q}, \frac{Q}{q}$ set of axes through a counter-clockwise angle of θ_{IQ}. Hence, the angle that the straight-line fit makes with the positive $\frac{I}{q}$ axis constitutes θ_{IQ}, which in this case is 0.16 rad.

Using the calculated θ_{IQ}, $\frac{I'}{q}$ can be computed for each trigger using:

$$\frac{I'}{q} = \frac{I}{q}\cos\theta_{IQ} + \frac{Q}{q}\sin\theta_{IQ}. \tag{3.39}$$

$\frac{I'}{q}$ is plotted against mover setting in Fig. 3.21(c). As $\frac{I'}{q}$ is proportional to the position, the gradient of the straight-line fit can be used to determine the calibration constant k converting $\frac{I'}{q}$ units to position units. This requires the use of the appropriate µm/V mover calibration in Table 3.4, which gives $k = -0.168$ (ADC/ADC)/µm for the calibration in Fig. 3.21. The factor k allows the position to be reconstructed from the raw I, Q and q signals by applying:

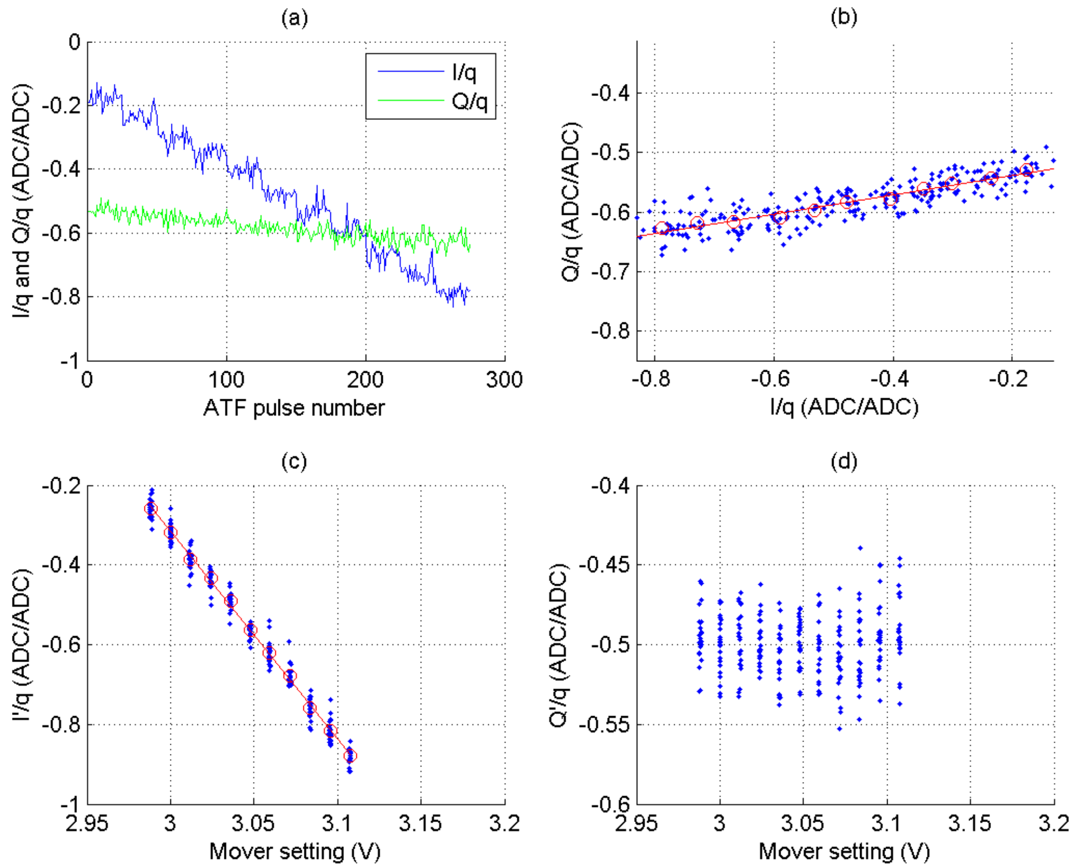

Figure 3.21: Plots for a vertical calibration of IPB: (a) $\frac{I}{q}$ and $\frac{Q}{q}$ at a chosen sample number as a function of ATF pulse number; (b) $\frac{I}{q}$ versus $\frac{Q}{q}$ scatter plot with straight line fit used to determine θ_{IQ}; (c) $\frac{I'}{q}$ versus mover setting with straight line fit of gradient k; and (d) $\frac{Q'}{q}$ versus mover setting. The charge q used for normalisation is the stripline BPM P2 V_{Σ} signal.

$$y = \frac{1}{k}\left(\frac{I}{q}\cos\theta_{IQ} + \frac{Q}{q}\sin\theta_{IQ}\right). \tag{3.40}$$

A similar analysis can be performed to obtain $\frac{Q'}{q}$ using:

$$\frac{Q'}{q} = -\frac{I}{q}\sin\theta_{IQ} + \frac{Q}{q}\cos\theta_{IQ}. \tag{3.41}$$

The plot of $\frac{Q'}{q}$ against mover setting shown in Fig. 3.21(d) confirms that the angle components of the beam remain unaltered during the BPM mover scan.

In order to estimate the errors on k and θ_{IQ}, the calibration procedure can be repeated. Performing eight consecutive calibrations, whilst operating at a variable attenuator setting of 0 dB, gave a spread of θ_{IQ} values with a standard deviation of 0.9° and a distribution of k values with a standard deviation of 1.7 % of the mean value of k. These spreads can be treated as the characteristic errors for a given calibration run.

3.7 Summary

This chapter has introduced the components required for the operation of a cavity BPM system, where the position-dependent dipole cavity signal is mixed with the position-independent reference cavity signal to produce a position-dependent signal that can be digitised. The system of three IP BPMs used in this thesis was introduced in the context of the beamline element configuration in the IP area at ATF. The general structure and operation of single-stage and two-stage signal processing electronics was explained, and the particular design of the KNU electronics and the Honda electronics at ATF was described. The importance of the relative timing of the dipole and reference cavity signals at the input to the second stage of the Honda electronics was illustrated, and the digital signal processing, charge normalisation and BPM position calibration procedure were explained.

Chapter 4

IP BPM performance

4.1 Beam set-up

Beam set-up is required to ensure a centred beam in the IP BPMs. Additionally, for BPM calibration (Sec. 3.6.3) and studies involving a single BPM (Sec. 4.4), the beam waist can be shifted longitudinally to the location of the BPM to reduce beam jitter and ease the operation of the BPM. The necessary beam set-up techniques are presented in this section.

4.1.1 Beam centering

A well steered beam through the IP BPMs is required to keep the signal levels small and prevent the electronics from saturating. The beam needs to be centred in each BPM in both x and y, and the beam trajectory has to be kept along the BPM longitudinal axis. The beam position and angle relative to the IP BPMs can be adjusted by steering the beam or moving the IP BPM movers, as detailed in Table 4.1.

As presented in Sec. 3.2, the IP BPM movers can move the IPA-IPB and IPC blocks independently in the x and y directions and rotate the blocks around the x and z axes. Therefore, the mover system can be used to adjust the x and y positions and y' pitch of IPC and either IPA or IPB. In order to centre all three BPMs with respect to the beam, the pitch of the IPA-IPB block can be set, even though this sacrifices the ability to set the pitch of the individual BPMs IPA and IPB. The x' yaw of the BPMs cannot be adjusted.

Table 4.1: Methods to adjust the x and y position and y' pitch of the beam relative to the IP BPMs using beam steering and BPM mover settings

	Method	
Target	Using beam	Using IP BPM movers
Adjust x position	Move QD0FF x mover	Move IP BPM x mover
Adjust y position	Move QD0FF y mover	Move IP BPM y mover
Adjust y' pitch	Move QF7FF y mover	Move IP BPM y submovers

In addition to the BPM mover system adjustment, the beam can be steered appropriately through the IP BPMs by changing the vertical and horizontal position of upstream quadrupoles. Displacing any quadrupole horizontally or vertically adds a dipole field horizontally or vertically, respectively, and the strength of the introduced dipole field is proportional to the quadrupole offset [102]. Hence, the x and y movers of the QD0FF magnet, the last quadrupole before the IP BPMs, are used to impart a small dipole kick to the beam which results in the beam being displaced horizontally and vertically at the IP BPMs. Also, the fact that the QF7FF magnet constitutes an image point of the IP in the vertical plane allows the magnet to be displaced vertically to apply a dipole kick to the beam which propagates to an almost pure y' pitch change at the IP [103].

4.1.2 Longitudinal shifting of beam waist

Minimising the jitter at the BPM studied is important as the smaller spread of positions allows cleaner calibrations to be performed and enables all the bunches to be kept within the linear dynamic range of the BPM. The jitter is minimised by shifting the beam waist along z onto the location of the BPM in question. The z-coordinate of the focal point can be different in the x and y planes. In order to reduce the effect of any residual x-to-y position correlation at the IP, both the x and y position jitters are minimised at the BPM.

Varying the currents of the final doublet quadrupoles QF1FF and QD0FF, which changes their focusing strengths, allows the waist to be moved longitudinally onto the BPMs. Simulations have been performed using the beam tracking code Lucretia [104] to calculate the effect of final doublet current changes on the beam size at a point in the IP region. Given that the beam jitter scales with beam size [79], the effect of the quadrupole currents on the x and y position jitters can be deduced.

Fig. 4.1 shows that the y beam size at the beam waist varies with both the QD0FF and QF1FF currents. Conversely, the x beam size is seen to depend only on the QF1FF current and is largely independent of the QD0FF current. Therefore, the procedure followed is to perform a QF1FF current scan first to place the x waist on the desired BPM. Then, a QD0FF current scan allows the y waist to be placed on the same BPM, whilst leaving the x waist approximately unchanged.

Fig. 4.2 shows the results of a QF1FF current scan to place the x waist on IPB. Varying the QF1FF current also changes the beam position, so the beam is re-centred in x at each point of the scan. As the jitters are large, an attenuation of 20 dB is set on both x and y signals from the cavity, giving a wide dynamic range but also limiting the resolution to ~ 200 nm. A minimum x jitter of 1.70 ± 0.12 µm is obtained at a QF1FF current setting of 125 A and this current is selected for the subsequent operation.

Fig. 4.3 shows the results of a subsequent QD0FF current scan to place the y waist also on IPB. In order to measure the small vertical beam position jitter, the y cavity signal attenuation is set to zero for this scan. Removing the attenuation introduces a tight dynamic range and the beam is repeatedly re-centred vertically to within a few microns of the cavity electrical centre. Given the large horizontal jitter, a 20 dB attenuation on the x cavity

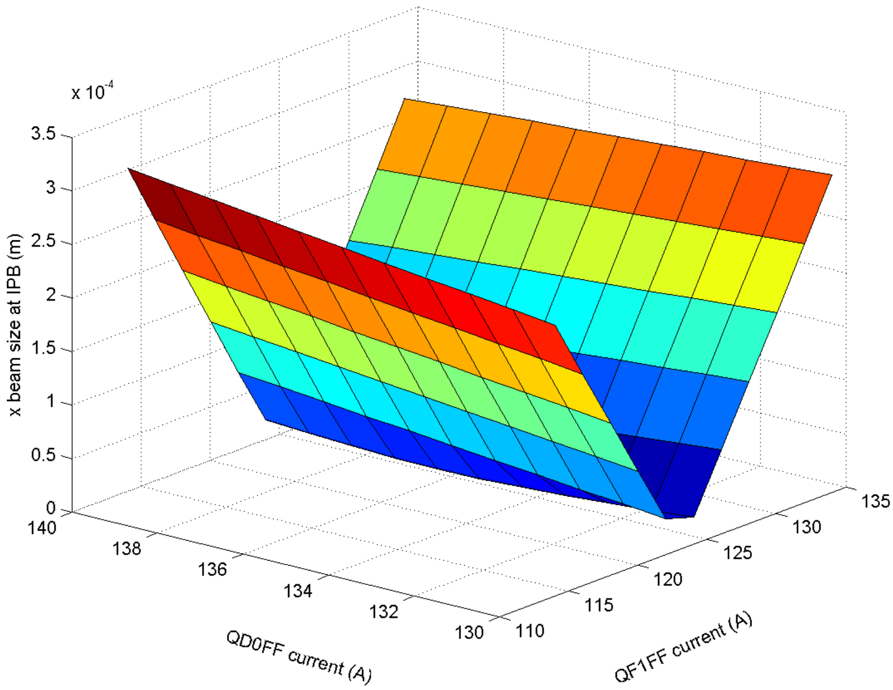

(a)

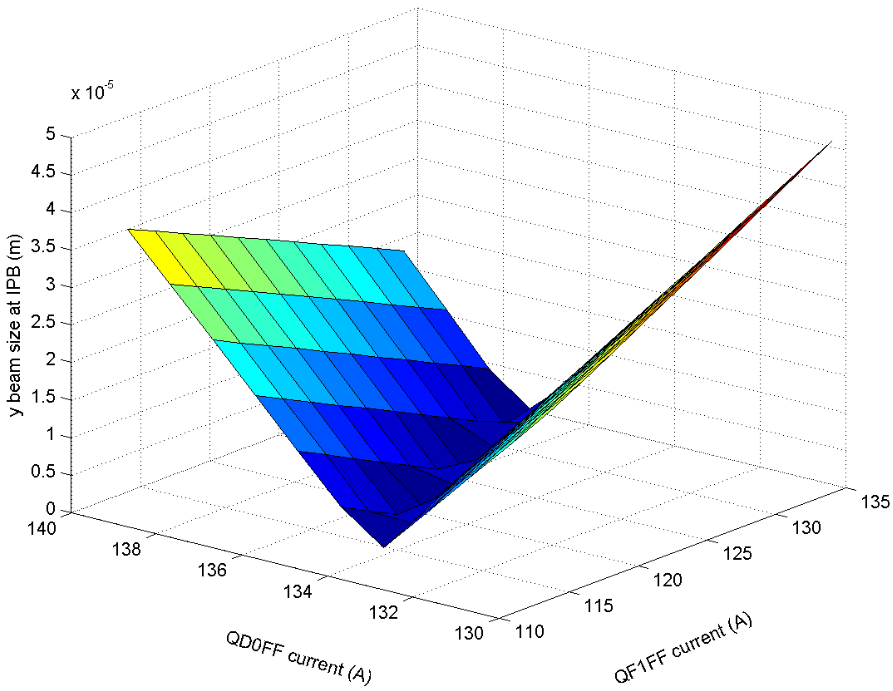

(b)

Figure 4.1: Simulated (a) x and (b) y beam size at IPB as a function of QD0FF and QF1FF currents.

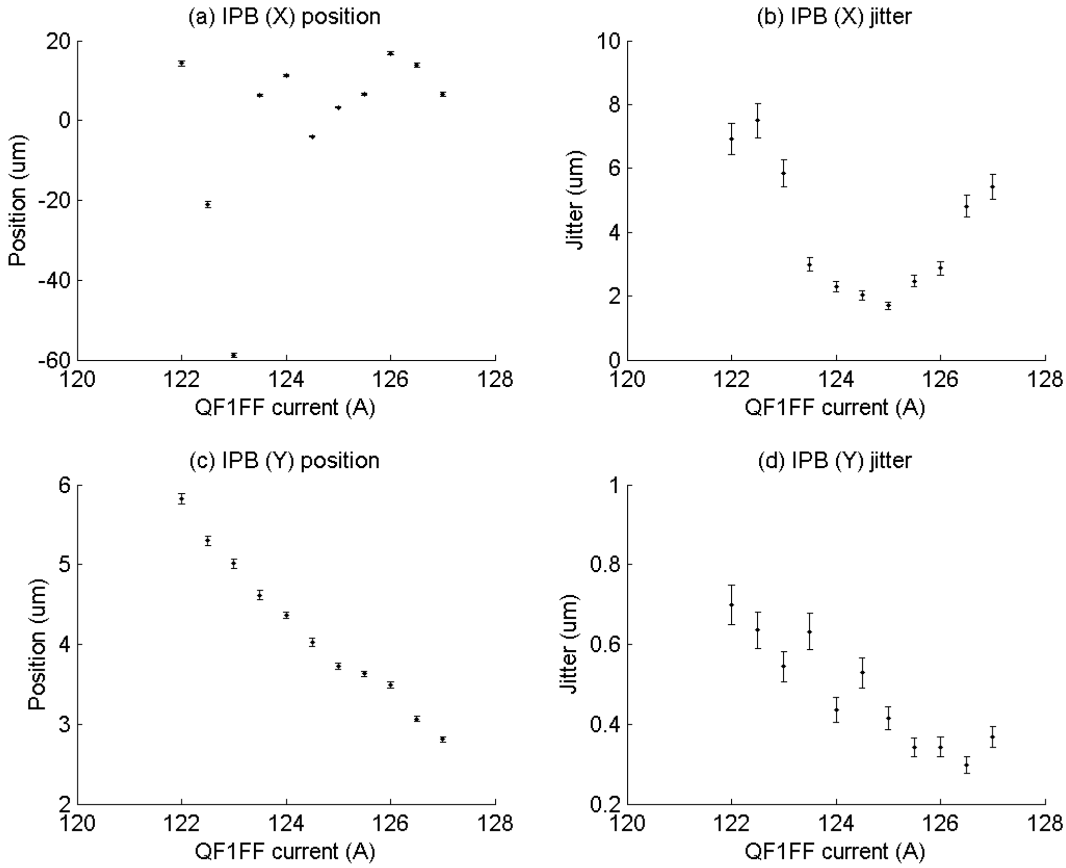

Figure 4.2: Position at IPB in (a) x and (c) y over a QF1FF current scan, and the corresponding position jitter in (b) x and (d) y. Standard errors on the mean and jitter are given. The QD0FF current is fixed at 137.4 A.

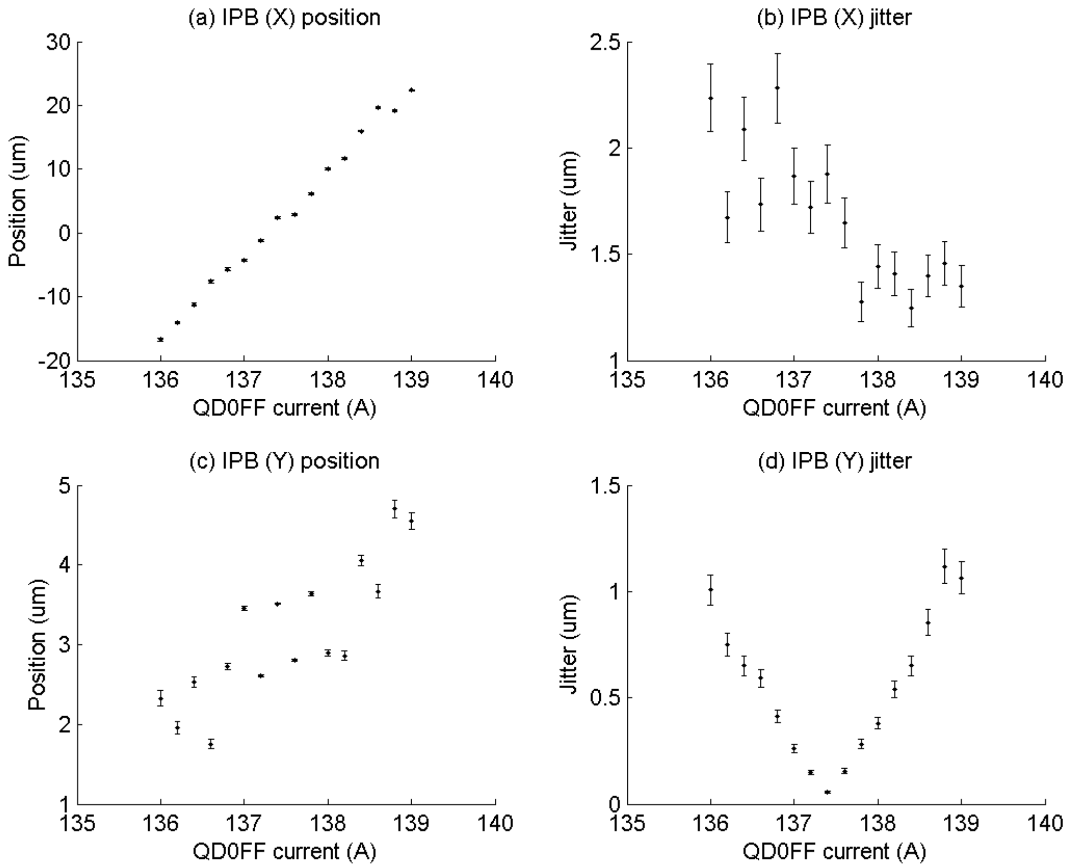

Figure 4.3: Position at IPB in (a) x and (c) y over a QD0FF current scan, and the corresponding position jitter in (b) x and (d) y. Standard errors on the mean and jitter are given. The QF1FF current is fixed at 125 A.

signals is suitable. A minimum y jitter of 58 ± 4 nm is achieved at a QD0FF current setting of 137.4 A.

4.2 Sample number dependence

The dependence of the I, Q waveforms on sample number is dominated by the exponentially decaying envelope of the signal. Additionally, a residual sinusoidal component and an erratic but static feature are observed in the waveforms. These features are presented in this section, along with a study of sample point selection optimisation and multi-sample averaging.

4.2.1 Mean-subtracted waveforms

An erratic component is present in the I, Q waveforms, which is largest when no input attenuation is used. Fig. 4.4 shows a typical example of the erratic waveform showing how it is displaced over a BPM mover scan. The static nature of this erratic component allows it

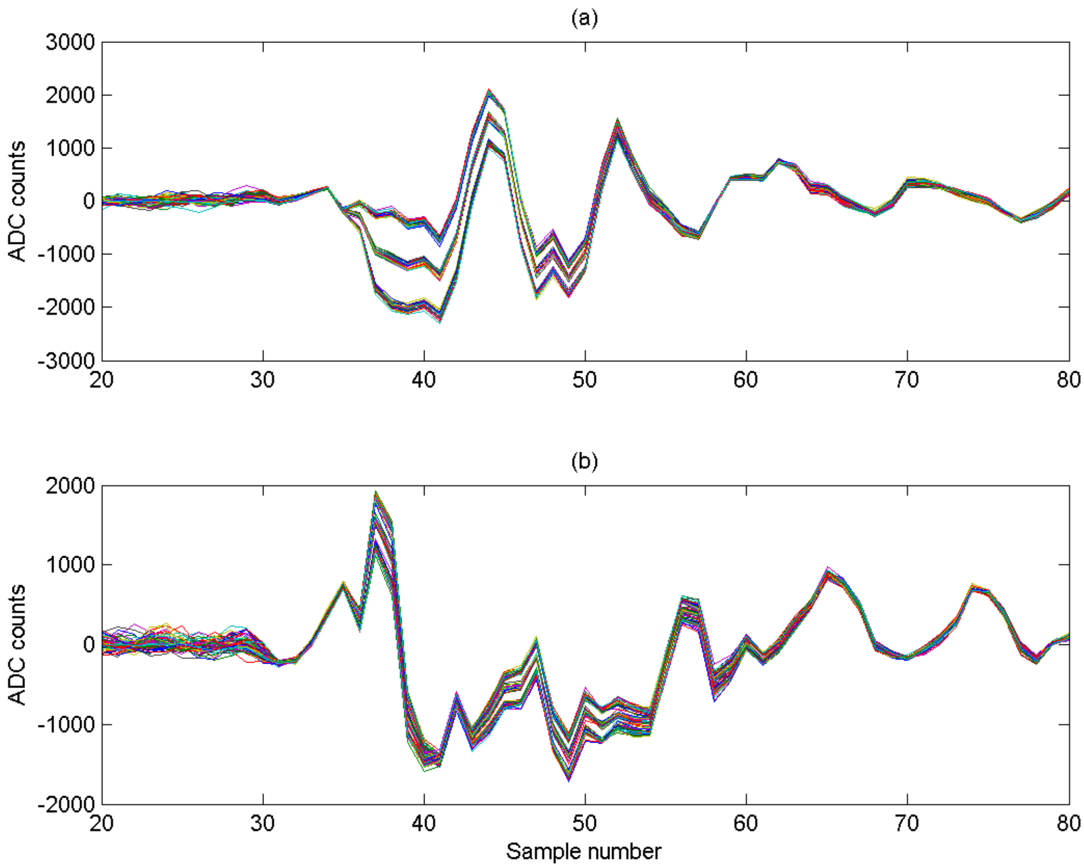

Figure 4.4: Digitised ADC counts versus sample number for (a) the I channel and (b) the Q channel using the Honda electronics with no input attenuation. The waveforms correspond to the set of triggers at BPM mover settings of 0 and ± 1.8 μm taken over a vertical calibration of IPB.

to be removed by subtracting the mean waveform from all waveforms, as shown in Fig. 4.5.

The amplitude of the erratic component of the waveform scales with the variable attenuator setting suggesting that it originates from an unwanted position-independent mode in the dipole cavity. The erratic waveform introduces an offset to the absolute position obtained from the IP BPM system, and the offset is sample number dependent. However, at any given sample number, this offset is static over a large ensemble of triggers, allowing successful calibrations even with no input attenuation and enabling small beam jitters to be measured (as detailed in Sec. 4.4). Any residual jitter of the apparently static, erratic component may constitute a limiting factor to the IP BPM resolution.

4.2.2 Dipole and reference cavity frequency mismatch

The mean-subtracted I, Q waveforms presented in Fig. 4.5 are not perfectly at baseband. The slow sinusoidal oscillation, most noticeable in Fig. 4.5(b), is a consequence of the frequency mismatch between the dipole and reference cavities. If $f_{\mathrm{dip}} \neq f_{\mathrm{ref}}$, then Eq. 3.19

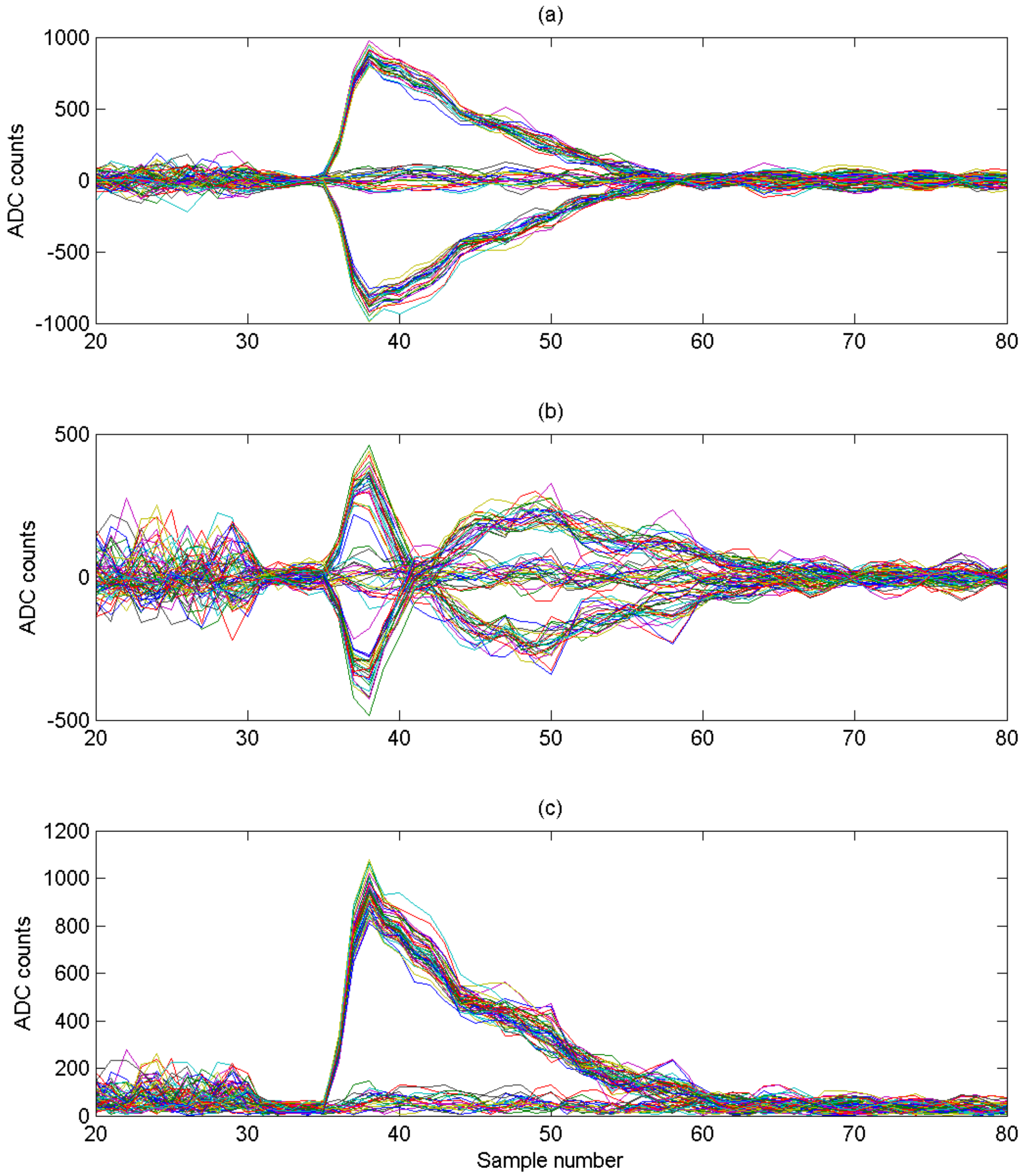

Figure 4.5: Mean-subtracted digitised ADC counts versus sample number for (a) the I channel and (b) the Q channel for the data presented in Fig. 4.4, and (c) the mean-subtracted I, Q signal quadrature sum $\sqrt{I^2 + Q^2}$.

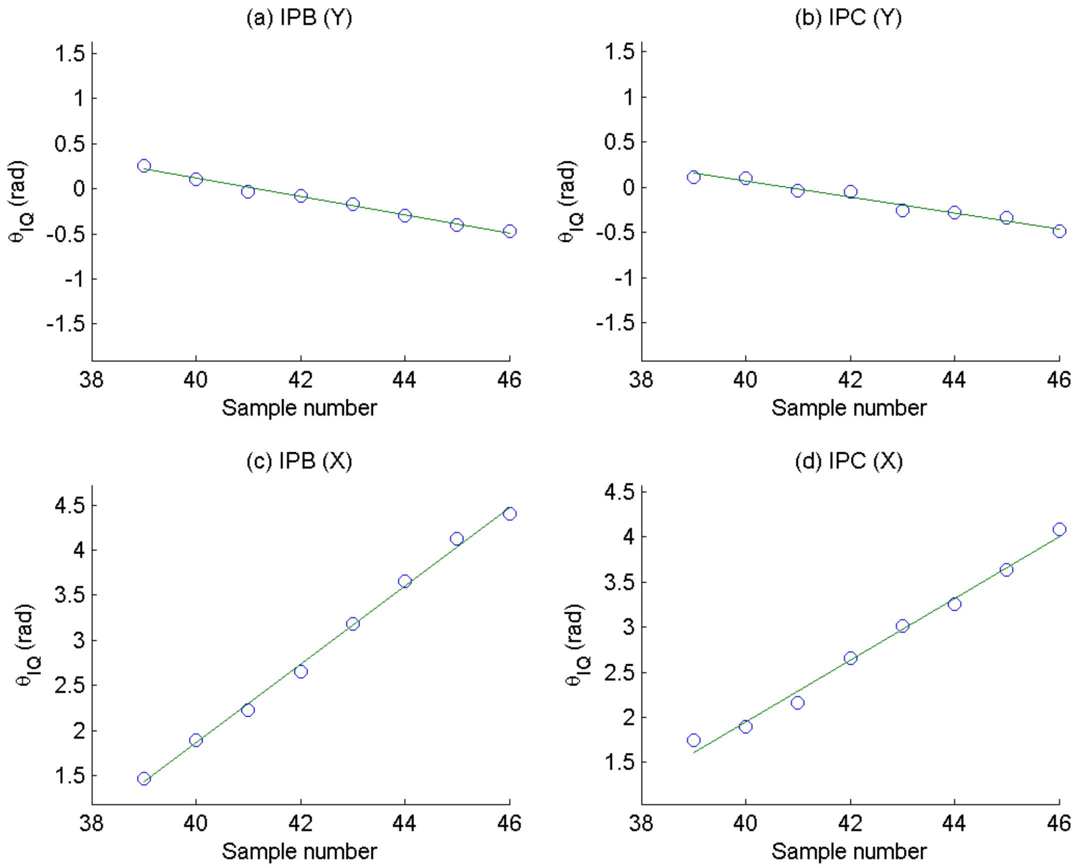

Figure 4.6: θ_{IQ} versus sample number for the vertical beam position signal from (a) IPB and (b) IPC, and for the horizontal signal from (c) IPB and (d) IPC. The lines show linear fits to the data.

indicates that θ_{IQ} varies linearly with time,

$$\theta_{IQ} = 2\pi(f_{\text{dip}} - f_{\text{ref}})t + \text{constant}, \tag{4.1}$$

and hence Eqs. 3.33–3.34 show that I and Q oscillate sinusoidally at a frequency $f_{\text{dip}} - f_{\text{ref}}$.

Fig. 4.6 illustrates the time-dependence of θ_{IQ} evaluated at each sample from the calibration runs for IPB and IPC. In each case, the rate of change of θ_{IQ} is approximately constant. The frequency mismatch $f_{\text{dip}} - f_{\text{ref}}$ is related to the gradient m of θ_{IQ} versus sample number (in units of rad/sample) by:

$$f_{\text{dip}} - f_{\text{ref}} = \frac{m f_s}{2\pi}, \tag{4.2}$$

where f_s is the digitiser sampling frequency, which for the FONT5 board is 357 MHz (Sec. 2.5).

The values of $f_{\text{dip}} - f_{\text{ref}}$ correspond to the frequency difference between the dipole and reference cavity signals at the input to the second stage of the Honda electronics. As both y

Table 4.2: Frequency mismatch between reference and dipole cavity signals at the input to the second stage of the Honda electronics, deduced from frequency measurements of the cavity modes (Table 3.3) and from the gradient of θ_{IQ} vs. sample number (Fig. 4.6).

Signals		Frequency mismatch (MHz)	
Dipole	Reference	From cavity measurements	From θ_{IQ} vs. sample number
IPB (y)	Ref (y)	-1 ± 3	-5.7 ± 0.3
IPC (y)	Ref (y)	-2 ± 3	-5.0 ± 0.4
IPB (x)	Ref (y)	$+30 \pm 3$	$+24.7 \pm 0.6$
IPC (x)	Ref (y)	$+29 \pm 3$	$+19.4 \pm 0.8$

dipole and y reference cavity signals are downmixed by the same frequency LO signal in the first stage of the Honda electronics, the values of $f_{\mathrm{dip}} - f_{\mathrm{ref}}$ also correspond to the frequency mismatch of these signals at the input to the first stage. Table 4.2 shows the frequency mismatches obtained from the rate of change of θ_{IQ}, compared to those deduced from the cavity signal frequency measurements in Table 3.3.

The frequency mismatches in Table 4.2 show an approximate agreement between the values obtained using the two methods. A systematic error may be present in the values deduced from the cavity frequency measurements if the reference cavity tuning pin setting (Sec. 3.2) was changed since the measurements were performed. In all cases, the frequency mismatch between the reference and dipole cavity signals, and thus the frequency of the I and Q signals, is 30 MHz or less, so the final 100 MHz low-pass filters in the Honda electronics (Fig. 3.12) are suitable.

4.2.3 Signal level dependence on sample number

When performing a BPM calibration, a θ_{IQ} and a calibration factor k are obtained for each sample following the calibration procedure described in Sec. 3.6.3. Fig. 4.7 presents k versus sample number. As the I' signal is normalised by the charge q, the k factor has units of (I' ADC counts / charge ADC counts) / µm. The sign of k can change between positive and negative by adding an arbitrary angle of π to θ_{IQ}, as can be seen from Eq. 3.40, so the absolute value of k is plotted.

The variation of k depicts the expected exponential decay of the cavity signal output. The point with maximum k, which is sample 38 for the data set presented here, is referred to as the 'peak sample' and constitutes the sample with the maximum cavity output. The peak sample also corresponds to the peak of the quadrature sum $\sqrt{I^2 + Q^2}$ presented in Fig. 4.5(c).

4.2.4 Jitter dependence on sample number

Due to the fast decay time of the IP BPM cavities, the signal-to-noise ratio varies rapidly over the course of the waveform. As the signal decays, a sample in the tail of the waveform

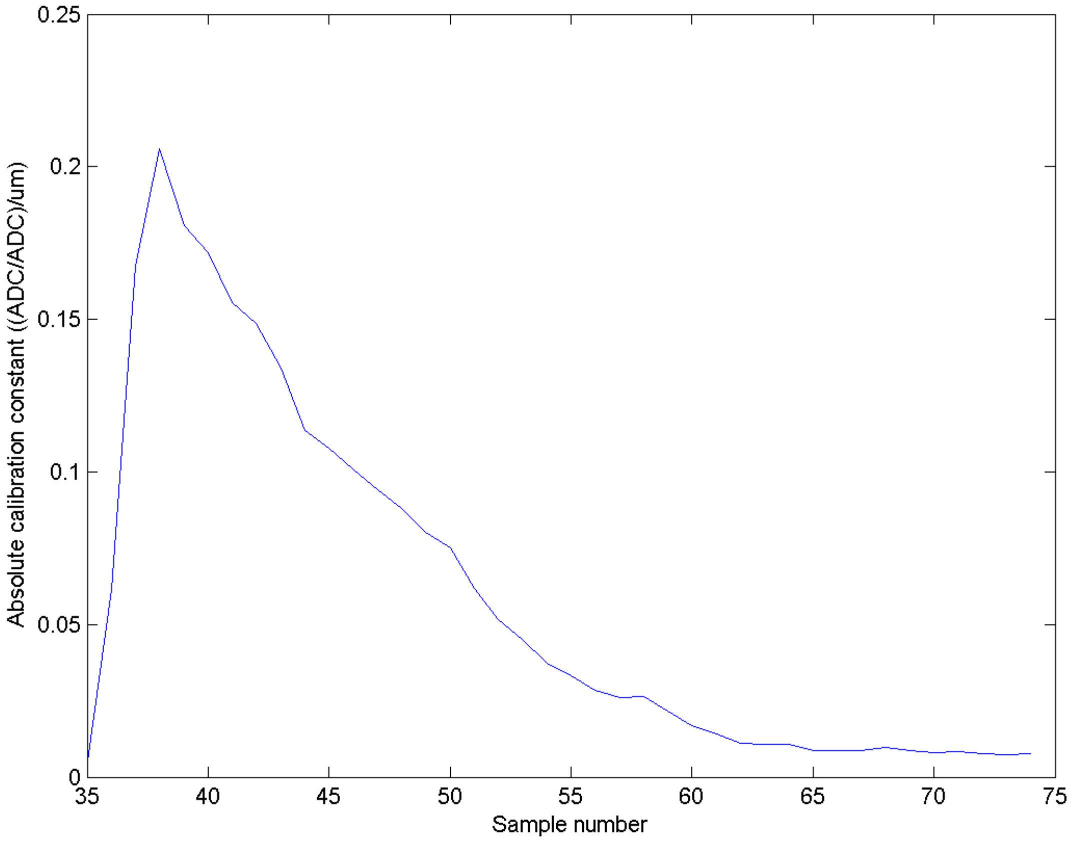

Figure 4.7: Absolute calibration constant k, in units of (I' ADC counts over stripline BPM P2 V_Σ ADC counts) per μm, versus sample number for the data in Fig. 4.4.

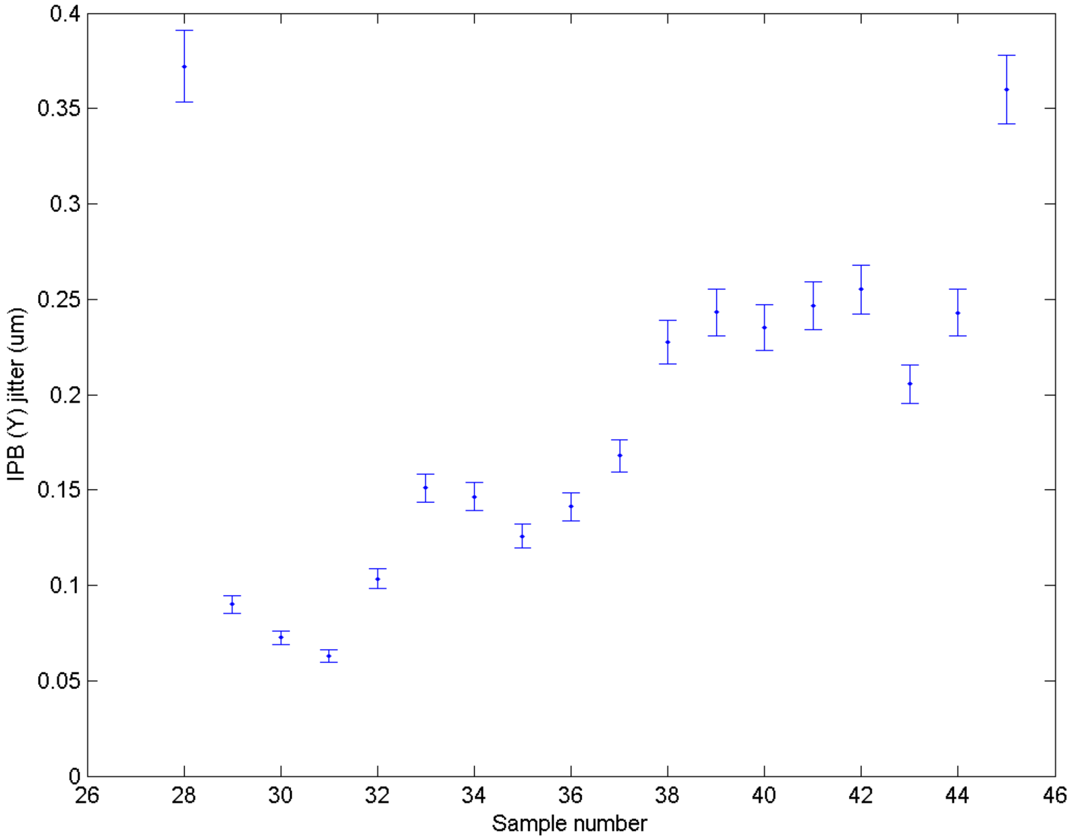

Figure 4.8: Measured single-sample vertical position jitter at IPB versus sample number. Standard errors on the jitter are given. The results are obtained using data set A from 30 May 2014, discussed in Sec. 4.4.2.

has a lower signal-to-noise ratio and, if used alone, has a worse resolution than a sample close to the peak of the waveform. As discussed in Sec. 4.4, the BPM system reports a resolution-limited jitter measurement when the true beam jitter is comparable to or smaller than the BPM resolution. Under resolution-limited conditions, the jitter measured acts as an indication of the system resolution.

Here we specifically look at the position jitter deduced at each individual sample number. A calibration is performed at each sample and the jitter deduced from each individual sample is presented. Fig. 4.8 shows such a plot of jitter versus sample number, which broadly resembles the variation of the cavity signal output over a waveform.

The point reporting lowest jitter is treated as the optimum sample number for single-point sampling in the subsequent analysis. The optimum sample number is identified at the start of each shift.

Even though the variation of the signal-to-noise ratio justifies the general shape of Fig. 4.8, it does not explain the presence of the bumps in Fig. 4.8. These features are found to be associated to the electronics signal processing and are discussed in Sec. 4.4.

4.2.5 Multi-sample averaging

The position information obtained from multiple sample points can be combined by averaging. The procedure followed is to first calibrate and measure the position y_i of the beam at each sample i. The average position $\bar{y}_{jk}$ is then obtained by averaging the positions obtained over the range of samples j to k:

$$\bar{y}_{jk} = \frac{\left(\sum_{i=j}^{k} y_i\right)}{\left(\sum_{i=j}^{k} i\right)}. \tag{4.3}$$

Calibrating at each sample allows the local θ_{IQ} to be determined at each point of the waveform, and the position (I') component to be extracted at each point. Other techniques to combine the information from multiple samples have been explored in the past [56].

For each sample window j to k, the position jitter $\bar{\sigma}_{jk}$ can be computed by taking the standard deviation (std) of $\bar{y}_{jk}$:

$$\bar{\sigma}_{jk} = \mathrm{std}(\bar{y}_{jk}). \tag{4.4}$$

Fig. 4.9 shows the plot of $\bar{\sigma}_{jk}$ versus k for a range of sample windows j to k, using the same data set presented in Fig. 4.8. The results show how averaging using samples around the peak lowers the jitter measurement from 63 ± 3 nm using single-point sampling in Fig. 4.8 to 47 ± 2 nm with multi-sample averaging in Fig. 4.9. This is indicative of the jitter measurement being resolution-limited, and the resolution improving with averaging, as discussed in Sec. 4.4.

4.3 System linearity

In a linear system, the electronics output signals I and Q would scale with the electronics input from the dipole cavity. If the dipole cavity signal is attenuated using the variable attenuator in Fig. 3.12, the electronics output signals I and Q, and consequently the calibration constant k, are expected to scale accordingly. Similarly, I and Q are expected to scale with the bunch charge; k should remain unaffected by the bunch charge. The dependence of k on attenuation and bunch charge is studied to assess the system's linearity.

4.3.1 System linearity versus attenuation

The variable attenuator on the dipole cavity signal path at the input to the Honda electronics was varied from 0 to 50 dB in steps of 10 dB, whilst the bunch charge remained stable at $\sim 0.5 \times 10^{10}$ electrons per bunch. A calibration was performed at each attenuation setting.

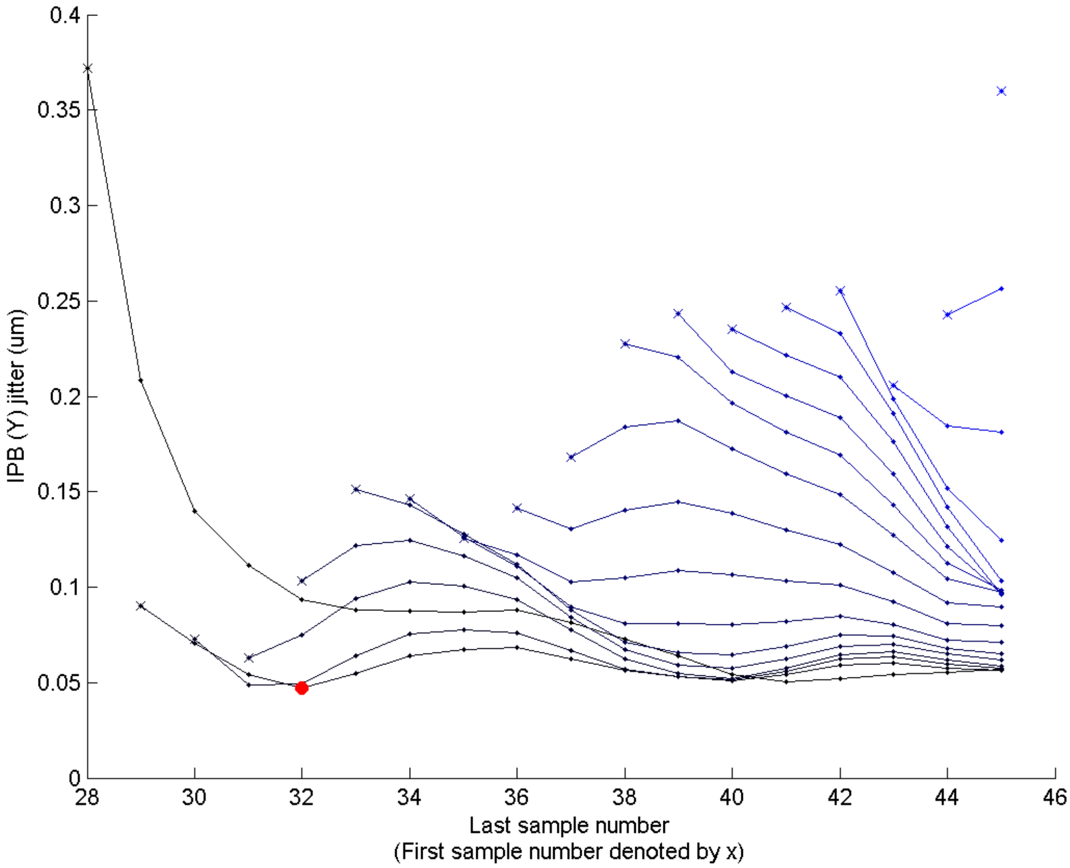

Figure 4.9: Measured vertical position jitter $\bar{\sigma}_{jk}$ using multi-sample averaging for a range of sample windows j to k versus k. Each line represents a different j, defined by the sample number of the cross ($\times$) at the start of the given line. The point labelled $\bullet$ gives the minimum measured jitter using averaging for this data set, which is 47 ± 2 nm by averaging samples 29 to 32. The results are obtained using data set A from 30 May 2014, discussed in Sec. 4.4.2.

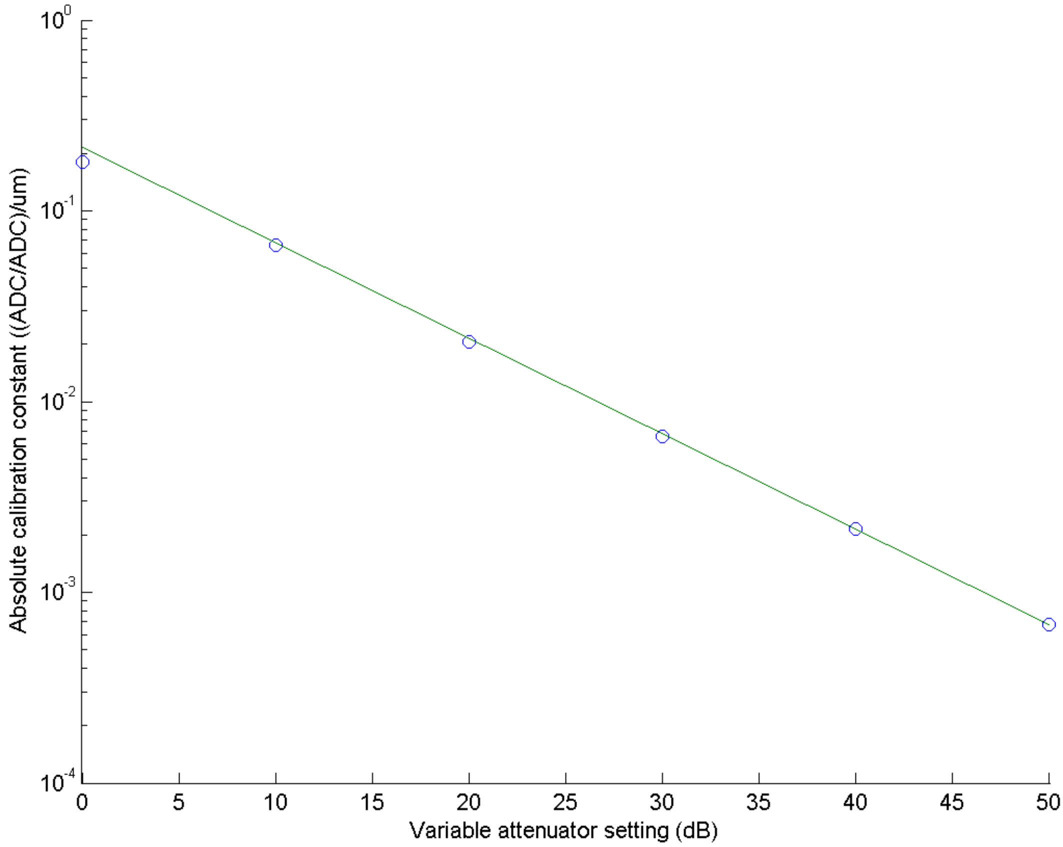

Figure 4.10: Absolute calibration constant k, in units of (I' ADC counts over stripline BPM P2 V_Σ ADC counts) per μm, versus attenuation. The line represents a linear scaling of the calibration constant at 50 dB to lower attenuation settings.

The mover range used for the calibrations was scaled with the attenuation, with narrower ranges for lower attenuations.

The absolute calibration constant k is plotted versus attenuation in Fig. 4.10. A logarithmic scale is used on the k axis to match the logarithmic nature of the decibel scale [74] used for the attenuation; a voltage ratio $\frac{V_1}{V_2}$ across the variable attenuator corresponds to an attenuation A_{dB} in dB of:

$$A_{\mathrm{dB}} = 20 \log_{10} \frac{V_1}{V_2}. \tag{4.5}$$

The calibration constant is seen to scale well with attenuation down to 10 dB confirming a linear response of the electronics. The deviation from the expected scaling at 0 dB may indicate that the electronics is beginning to saturate with the higher signal levels.

4.3.2 System linearity versus bunch charge

The bunch charge was varied from $\sim 0.1 \times 10^{10}$ up to $\sim 0.8 \times 10^{10}$ electrons, with the variable attenuator at the dipole cavity signal input to the electronics set to 0 dB. A calibration was performed for each of six bunch charges, where the charge-normalisation of the I and Q signals was performed using the stripline BPM MFB1FF V_Σ measurement. MFB1FF was fitted with attenuation to allow its processor to remain linear for the full range of charges being studied.

The study was performed measuring the vertical beam position with the specific set-up described in Sec. 4.5, where the IPB signal was split into two sets of electronics. As discussed in Sec. 4.5, splitting the signal attenuates it by ~ 7.1 dB, so the performance of the system reported here is comparable to one working at a charge a factor 2.3 smaller if no splitter is used.

The results obtained are shown in Fig. 4.11, where the absolute calibration constant k is plotted against the bunch charge. A pronounced dependence of k on charge is observed even though such a dependence should not exist. The value of k is seen to drop by 30 % from a charge of $\sim 0.1 \times 10^{10}$ to a charge $\sim 0.8 \times 10^{10}$. It is worth noting that the calibration plots appear linear for each individual calibration.

The dependence of k on charge indicates a system non-linearity: the I and Q signals do not scale purely with charge, so $\frac{I'}{q}$ is not charge independent. The non-linearity may originate from a dipole cavity signal that is not perfectly proportional to charge or electronics components that are saturating at high signal levels. It may also be a consequence of the reference cavity signal not being sufficiently well limited before being used as the LO signal to down-mix the dipole cavity signal in the second stage of the Honda electronics.

In spite of the unwanted dependence of k on charge, it is worth noting that the bunch charge has been scanned over a very wide range of charges. Typically the accelerator is operated at a single charge setting, and the charge variation has a standard deviation of the order of 0.01×10^{10} electrons per bunch.

In order to minimise the effect of charge on the IP BPM performance, care has been taken to calibrate the BPMs at the same charge as that at which they were subsequently operated. In the case where a charge scan was performed, such as in Sec. 4.5.2, the appropriate calibration constant to each charge is used to compute the beam positions.

4.4 Position jitter minimisation on waist

The beam set-up procedure described in Sec. 4.1 is followed to centre the beam and place the beam waist at IPB. By minimising the jitter at the BPM, the performance of the BPM is tested close to its resolution limit. Assuming that the system noise is uncorrelated with the beam position jitter, the two quantities can be treated as independent Gaussian distributions. The two contributions combined give the measured position jitter σ_{m}:

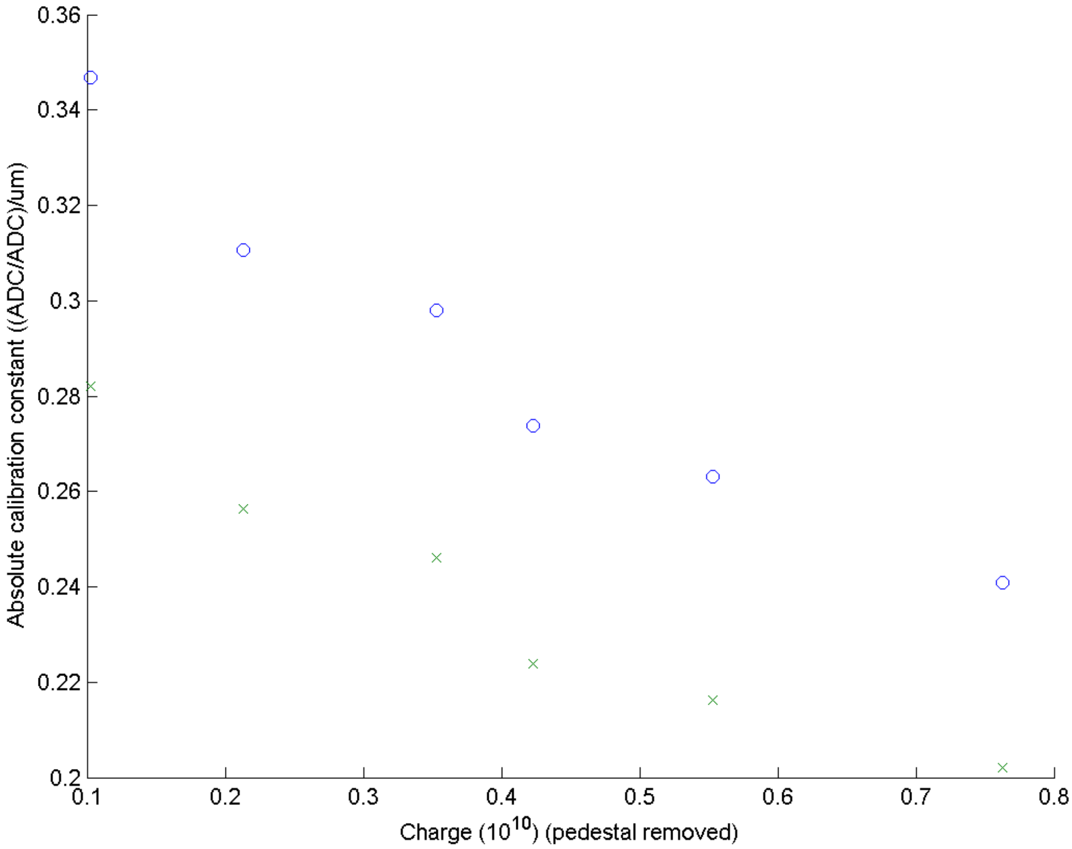

Figure 4.11: Absolute calibration constant k, in units of (I' ADC counts over stripline BPM MFB1FF V_{Σ} ADC counts) per μm, versus charge in units of 10^{10} electrons per bunch measured by the extraction line ICT. The data was taken with the vertical IPB signal split into the first (blue circles) and second (green crosses) set of electronics described in Sec. 4.5.

$$\sigma_{\mathrm{m}}^2 = \sigma_{\mathrm{t}}^2 + \sigma_{\mathrm{r}}^2 \tag{4.6}$$

where σ_{t} is the true beam position jitter and σ_{r} is the BPM resolution. Therefore, by minimising the true beam jitter, the measured jitter constitutes an upper limit to the BPM resolution.

After minimising the position jitter at IPB, any correlation between the measured position at the BPM and other beam parameters can be studied. The procedure followed, described in Sec. 4.4.1, consists in removing the dependence of the measured position on these correlated quantities and studying the resulting position jitter. In this way, the contributions to the measured position jitter can be identified and classified as true beam jitter measurements or resolution-limiting effects of the BPM system.

The method of subtracting the correlated quantities is applied to two data sets obtained on the same shift under the same accelerator configuration, but that report different vertical position jitters at IPB. The conditions under which the two data sets were taken are described in Sec. 4.4.2. The correlated quantities being subtracted are explained in Sec. 4.4.3, the results of the analysis are given in Sec. 4.4.4 and a discussion of the results is presented in Sec. 4.4.5. The scaling of the position jitter measurement with the attenuation between the cavity BPM and the electronics is studied in Sec. 4.4.6.

4.4.1 Correlated component subtraction

Assume that the vertical beam position measured at IPB, y_{B}, is correlated with a parameter v such as the bunch phase, charge or position measured at another BPM. For illustration, Fig. 4.12(a) shows the correlation observed between y_{B} and the vertical beam position measured at PIP. Assuming a linear dependence of y_{B} on v allows y_{B} to be expressed as:

$$y_{\mathrm{B}} = \alpha v + \beta \tag{4.7}$$

where α and β are constants. The values of these constants are obtained by performing a least-squares fit to the data, as shown in Fig. 4.12(a).

Having calculated α and β, the residuals δ_{B} between the measured y_{B} positions and the straight-line fit can be computed; the results are shown in Fig. 4.12(b). As expected, δ_{B} shows no dependence on v. Taking the standard deviation of δ_{B} thus gives a measurement of the beam position jitter at IPB with the dependence of y_{B} on v removed, and this will be computed for a range of parameters v below.

The analysis can be repeated with the dependence of y_{B} on multiple correlated components $v_1, v_2, ...$ In this case, y_{B} is expressed as:

$$y_{\mathrm{B}} = \sum_i \alpha_i v_i + \beta \tag{4.8}$$

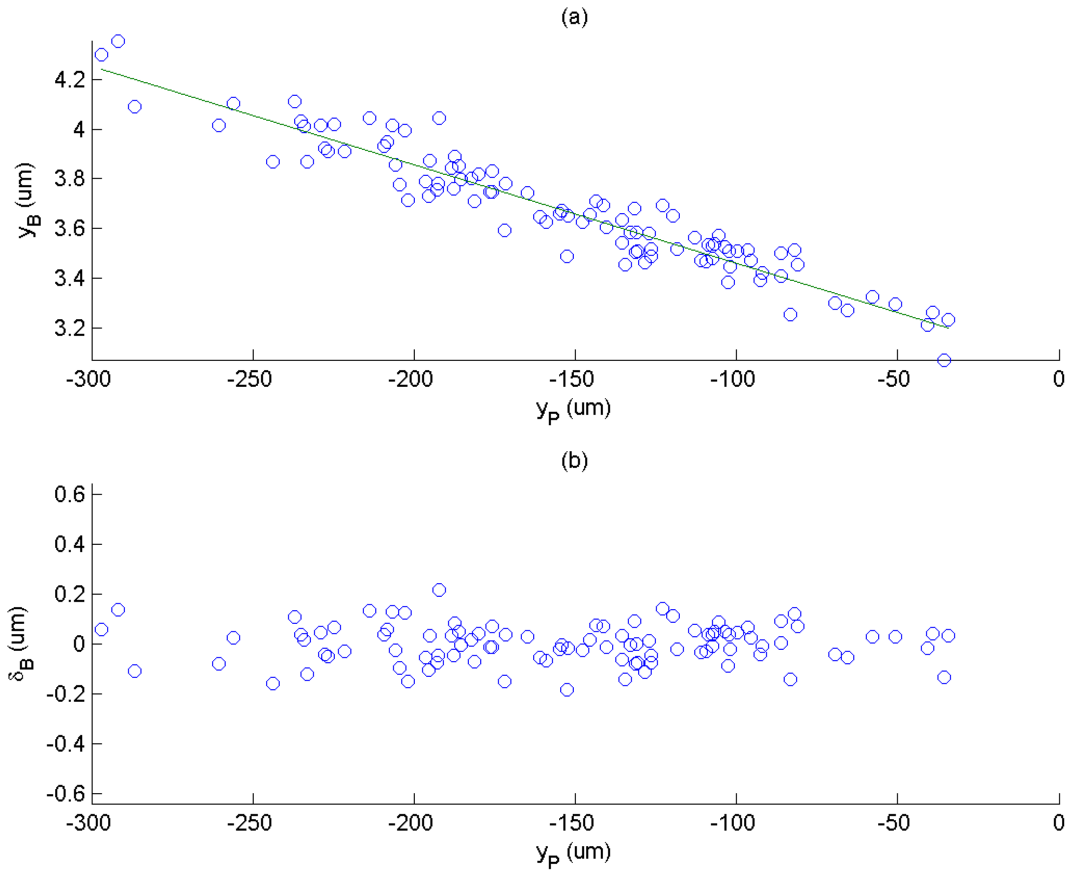

Figure 4.12: (a) Vertical beam position measured at IPB, y_{B}, versus that measured at PIP, y_{P}; the green line is a least-squares fit to the data. (b) Residuals δ_{B} between the measured y_{B} positions and the straight-line fit versus y_{P}.

where the constants $\alpha_1, \alpha_2, ...$ and β are found using a least-squares fit approach as described above.

4.4.2 Data sets

The two data sets were obtained on 30 May 2014 and were operated with 0 dB attenuation at the input to the electronics for best resolution. The shift followed ATF beam size tuning where an IP beam size of ~ 70 nm was achieved [105]. As the beam jitter is expected to be ~ 20 % of the beam size [106], a beam jitter of ~ 15 nm is predicted at the waist. At the start of the IP BPM shift, the set-up procedure in Sec. 4.1 was followed to centre the beam and place the waist on IPB.

Data set A was taken an hour after beam set-up. The mean charge for the data set is 0.46×10^{10} electrons per bunch with a standard deviation of 0.05×10^{10} electrons; this is a typical operating charge for IP BPM and FONT shifts that can be readily obtained at ATF. The jitter versus sample number plot in Fig. 4.8 shows that the smallest measured jitter for this data set is 63 ± 3 nm using single-point sampling and, from Fig. 4.9, multi-sample averaging brings the jitter measurement down to 47 ± 2 nm. These are amongst the smallest direct jitter measurements obtained at the IP (at the time of writing). The fact that the measured jitter improves on averaging suggests that the measurement is limited by the resolution of the BPM system.

Data set B was taken seven hours after beam set-up. The accelerator configuration, namely the QD0FF and QF1FF currents, were set to the same values as for the first data set. The charge is comparable, with a mean of 0.44×10^{10} and a standard deviation of 0.04×10^{10} electrons. However, the position jitter measurement is drastically higher: at 212 ± 15 nm and 208 ± 15 nm for single-point sampling and multi-sample averaging, respectively. The consistency of the measurements using the two methods (with and without averaging) suggests that the true jitter is considerably greater than the resolution.

4.4.3 Correlated quantities studied

The following variables are examined for correlations with the measured beam position at IPB:

(1) Vertical position at PIP
As discussed in Sec. 2.8.3, the correlation of the vertical position at IPB with the vertical position measured at a witness off-waist BPM in the IP region (such as PIP) can be used to determine whether or not the vertical beam waist is located at IPB. A correlation of the positions measured at IPB and PIP indicates that a component of the IPB position jitter results from the beam waist being off IPB. Consequently, removing this correlation acts to correct the waist drift off IPB.

(2) Horizontal position at IPB
The x, y position correlation in the IP region can be measured by finding the correlation between the horizontal and vertical beam position measurements at IPB. No x to y correlation is expected as, if it existed, it would imply that the much larger horizontal beam size and jitter would be coupling into the vertical plane.

(3) Horizontal position at PIP
With PIP located downstream of the beam waist at IPB, a measurement of the horizontal beam position at PIP can be used as a measurement of the beam yaw x' in the IP region. Thus, a correlation between the vertical beam position at IPB and the horizontal position at PIP would indicate a x', y position correlation in the IP region. Since horizontal-to-vertical position coupling is minimised at the IP, no x', y position correlation is expected.

(4) Bunch phase
Following from Sec. 3.3.2, the I, Q outputs from the electronics are expected to have no dependence on the relative phase between the bunch arrival and the LO phase. As discussed in Sec. 2.4.3, measurements at the upstream stripline BPMs have shown that the beam orbit is independent of the bunch phase. Therefore, the positions deduced from the Honda electronics are expected to have no correlation with the bunch phase. This statement is tested explicitly by measuring the correlation of the beam position measured at IPB with the bunch phase measured at P3.

(5) Bunch charge
The I and Q signals obtained from the IP BPM electronics are charge-normalised (Sec. 3.6.3) when obtaining the beam position (Eq. 3.40) and, thus, the resulting position measurement is expected to be independent of the bunch charge. This statement is studied by finding the correlation of the beam position measured at IPB with the P3 V_Σ signal, which is used as an independent measurement of the bunch charge.

In the context of this analysis, a non-zero correlation of y_B with parameters (1), (2) and (3) indicates that the position jitter measured at IPB is larger as a result of a real beam effect (being off-waist or having horizontal-to-vertical beam coupling), and the jitter could in principle be reduced by addressing the properties of the beam propagation. Conversely, a non-zero correlation of y_B with variables (4) and (5) reveals a limitation of the IP BPM system as the beam position readout is contaminated by bunch phase and charge signals.

4.4.4 Results

The correlation of y_B with the bunch phase, charge and vertical position at PIP is computed as a function of sample number, and the results are shown for data sets A and B in Figs. 4.13(a) and 4.14(a), respectively. The measured position jitter at each sample number, with and without correlated component subtraction, is shown in Figs. 4.13(b) and 4.14(b).

The minimum jitter achieved before and after removing each of the correlated quantities listed in Sec. 4.4.3 is shown in Table 4.3. For any given trigger, the position measurements

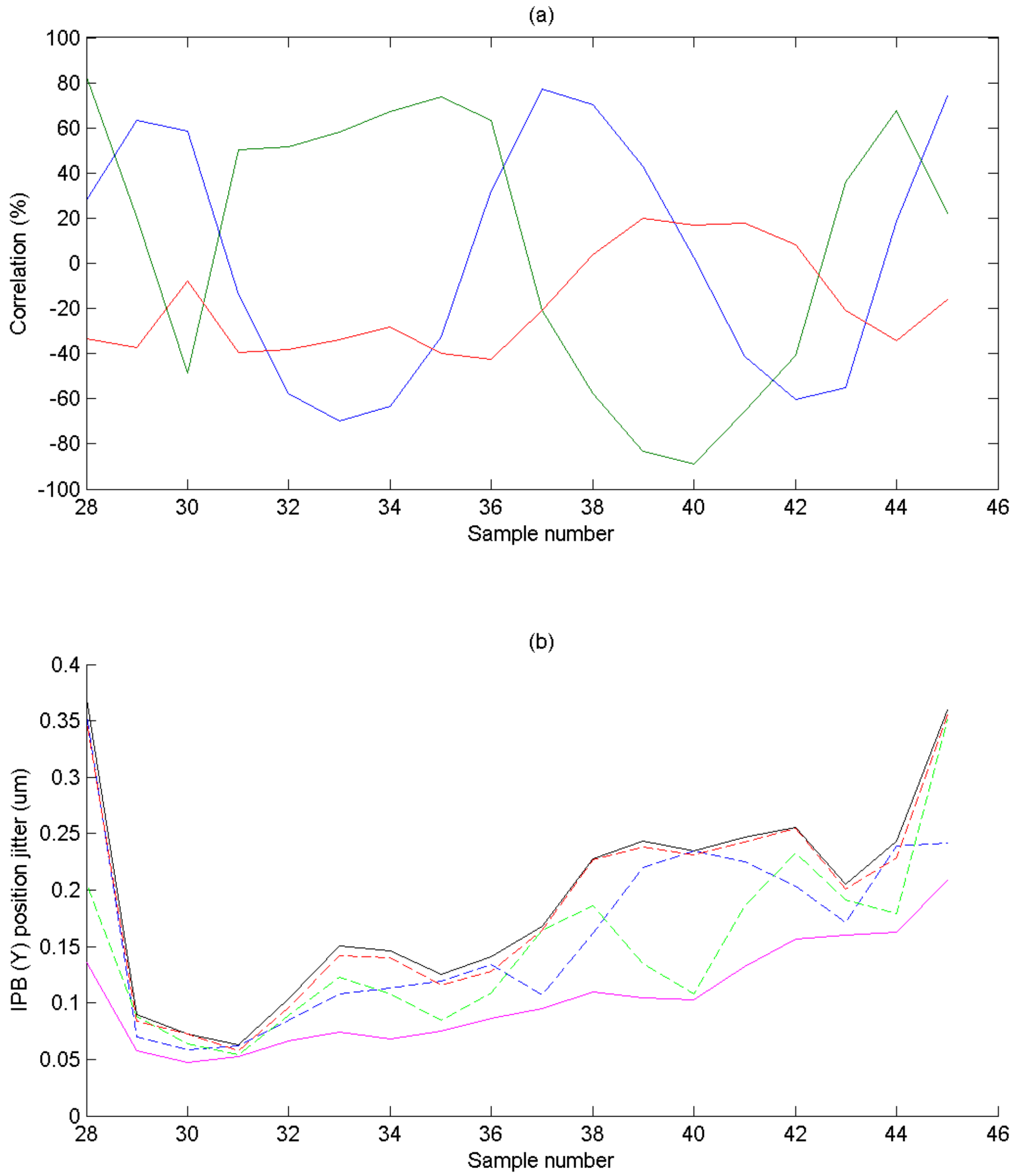

Figure 4.13: For data set A: (a) correlation of vertical position at IPB with bunch phase (blue), charge (green) and vertical position at PIP (red) versus sample number; (b) vertical position jitter at IPB versus sample number: without correlated components subtracted (black), with bunch phase (blue), charge (green) and vertical position at PIP (red) subtracted and with all three components subtracted (magenta).

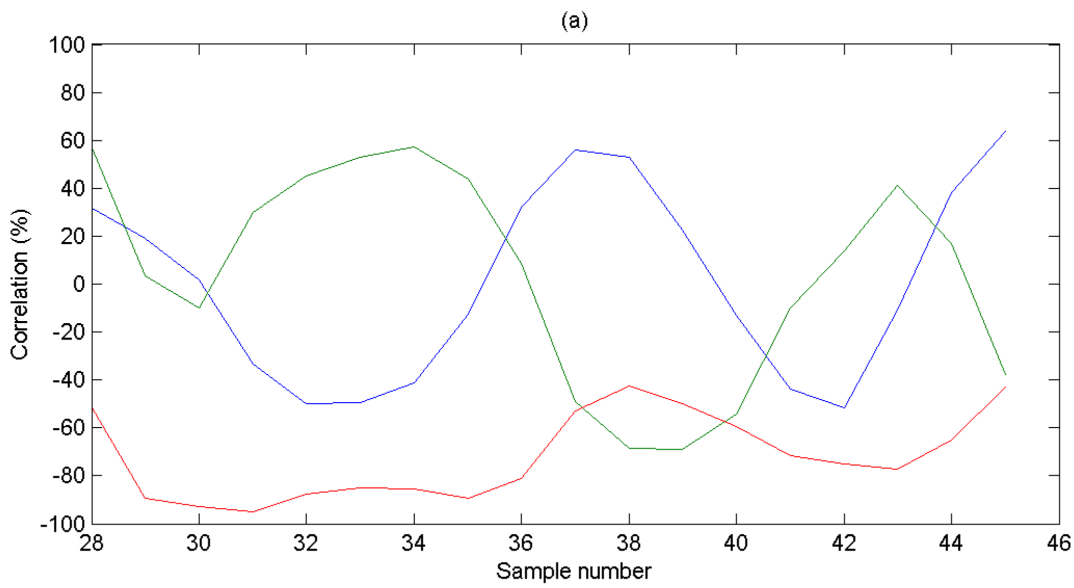

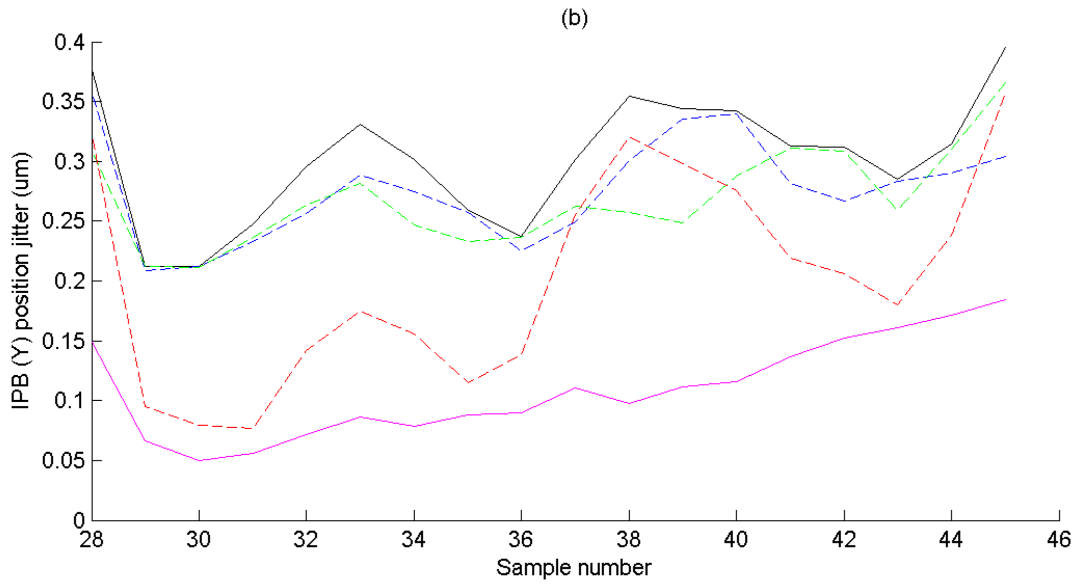

Figure 4.14: For data set B: (a) correlation of vertical position at IPB with bunch phase (blue), charge (green) and vertical position at PIP (red) versus sample number; (b) vertical position jitter at IPB versus sample number: without correlated components subtracted (black), with bunch phase (blue), charge (green) and vertical position at PIP (red) subtracted and with all three components subtracted (magenta).

Table 4.3: Vertical position jitter at IPB for data set A (waist on IPB) and data set B (waist close to IPB) before and after correlated component subtraction, using single-point sampling and multi-sample averaging. Standard errors on the jitter are given.

	Vertical position jitter at IPB (nm)			
	Data set A		Data set B	
Correlated quantity subtracted	Single-point	Averaging	Single-point	Averaging
None	63 ± 3	47 ± 2	212 ± 15	208 ± 15
(1) Vertical position at PIP	58 ± 3	40 ± 2	77 ± 5	44 ± 3
(2) Horizontal position at IPB	63 ± 3	47 ± 2	191 ± 14	191 ± 14
(3) Horizontal position at PIP	62 ± 3	46 ± 2	186 ± 13	186 ± 13
(4) Bunch phase at P3	59 ± 3	46 ± 2	209 ± 15	206 ± 15
(5) Bunch charge at P3	54 ± 3	45 ± 2	211 ± 15	208 ± 15
(1), (4) & (5)	47 ± 2	38 ± 2	50 ± 4	41 ± 3
(1), (2), (3), (4) & (5)	46 ± 2	38 ± 2	49 ± 3	40 ± 3

obtained at each sample after removing the dependence on one or more of the correlated quantities can be averaged over a range of samples using the multi-sample averaging technique introduced in Sec. 4.2.5. The lowest position jitters thus achieved are also shown in Table 4.3.

4.4.5 Discussion

Removing the dependence of y_B on the vertical beam position at PIP has the largest effect, reducing the measured vertical jitter at IPB in data set B from ~ 210 nm to 77 ± 5 nm using single-point sampling and to 44 ± 3 nm using multi-sample averaging. The reduction in jitter illustrates that the larger jitter measured at IPB in this data set is a result of the beam waist drifting away from IPB in the six-hour interval between the two data sets. On removing the effect of the waist drift, the measured jitters in the two data sets become comparable.

For data set A, removing the correlation with the vertical beam position at PIP has a greater effect on the IPB position jitter when employing multi-sample averaging than when using single-point sampling. This can be explained by the fact that the QD0FF current scan used to place the waist on IPB was analysed on-shift using single-point sampling. The precision with which the waist could be placed was limited by the single-point resolution used. On subsequently using multi-sample averaging, the improved resolution allows the fact of being slightly off-waist to be measured and corrected for.

The correlation of y_B with the horizontal beam position measured at IPB and PIP is consistently low and consequently removing the correlation with these parameters has little effect on the IPB position jitter quoted in Table 4.3. This suggests that any x to y or x' to y coupling in the IP region is below the limit that can be detected using the IP BPMs.

A dependence of reported position on bunch phase and charge is observed, revealing a non-ideal performance of the BPM system. A significant correlation, approaching 90 %, is observed in Figs. 4.13(a) and 4.14(a). The correlation is seen to vary approximately sinusoidally with sample number. The correlation with the two parameters appears to be out of step: the peak correlation with bunch phase at sample 37 corresponds to a correlation with charge that is crossing zero and conversely at sample 40.

As shown in Figs. 4.13(b) and 4.14(b), removing the correlation with bunch phase and charge lowers the measured jitter. The effect of the two parameters is complementary, as the reduction in jitter is dominated by applying one or the other parameter depending on the sample number. The effect of the two can be combined with the result shown. Removing the correlation with bunch phase and charge improves the plot of measured position jitter versus sample number. The bumps observed in the raw measurement are lifted, and the resultant dependence matches the smooth behaviour expected from the signal level variation deduced from Fig. 4.7.

Subtracting the correlation of y_{B} with the bunch phase, charge and vertical beam position at PIP gives a position jitter at IPB of ~ 50 nm using single-point sampling and ~ 40 nm with multi-sample averaging. These results are obtained consistently for both data sets. Averaging is seen to lower the measured position jitter at IPB as a result of the improvement in the resolution.

Using averaging also results in a better agreement of the position jitter measured with and without subtracting bunch phase and charge. For data set A, removing only the correlation with the vertical beam position at PIP to correct for being off-waist, produces a beam jitter of 40 ± 2 nm whilst further removing the dependence on bunch phase and charge produces a consistent result of 38 ± 2 nm. It suggests that averaging exploits the fact that the y_{B} position correlation with bunch phase and charge changes between positive and negative giving an average correlation that tends to zero. Hence, the unwanted dependence of reported IP BPM position on bunch phase and charge is mitigated by averaging.

4.4.6 Scaling of position jitter measurement with attenuation

Having minimised the position jitter at IPB, the variable attenuation at the dipole cavity output can be increased to study the performance of the system as the signal-to-noise ratio becomes smaller. The variable attenuator was varied from 0 to 40 dB in steps of 10 dB. The signals from the BPM were calibrated at each attenuation and the position jitter was measured. Fig. 4.15 shows the measured jitter as a function of the attenuation setting.

On applying an attenuation of 40 dB, the BPM resolution is much larger than the beam jitter of ~ 40 nm measured at 0 dB. Therefore, following Eq. 4.6, the measured jitter σ_{m} at 40 dB is effectively equal to the BPM resolution σ_{r} at that attenuation. The lines in Fig. 4.15 are obtained by taking the 40 dB jitter as the resolution and scaling this value for the lower attenuations.

It can be seen that in the regime between 20 and 40 dB, where the resolution is at least an order of magnitude larger than the true beam jitter, the measured jitter matches the scaled prediction. Removing the correlation with bunch phase and charge improves the

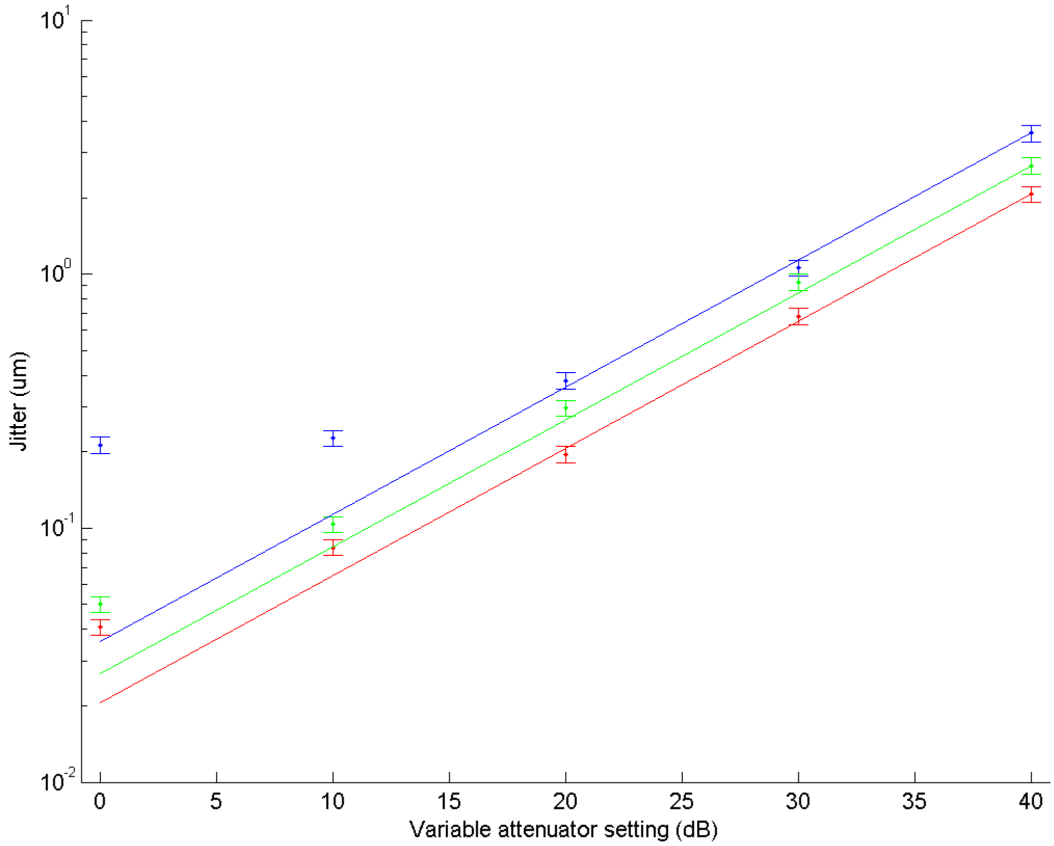

Figure 4.15: Measured vertical position jitter at IPB versus attenuation, using single-point sampling without (blue) and with (green) correlated component subtraction, and multi-sample averaging with correlated component subtraction (red). The correlated components subtracted are the bunch phase, charge and vertical beam position at PIP. Standard errors on the jitter are given. The lines represent a linear scaling of the jitter at 40 dB to lower attenuation values.

jitter measurement with single-point sampling, as discussed in Sec. 4.4.5, and multi-sample averaging lowers the measured jitter further.

At attenuations of 10 dB and 0 dB, the raw jitter measurements are dominated by true beam jitter resulting from the beam waist being displaced from IPB. Removing the correlation with the vertical position at PIP brings the jitter down to values closer to the extrapolated prediction.

Even after removing the correlation with the bunch phase, charge and vertical position at PIP, the extrapolated resolution remains below the jitter measurements for the 0 dB and 10 dB attenuation settings. There are two factors responsible for this observation. First, the true beam jitter σ_{t}, expected at the scale of a few tens of nanometres, is combining with the resolution σ_{r} to give the measured beam jitter σ_{m} as given by Eq. 4.6. Secondly, the resolution is likely to be worse than that extrapolated from 40 dB as the effect of non-linearities are more pronounced with larger signal levels.

The values of σ_{t} and σ_{r} at 0 dB cannot be both uniquely determined from the results presented. However, the BPM resolution at 0 dB with multi-sample averaging can be expected to lie between the minimum measured jitter of $\sim$ 40 nm and the extrapolated resolution of 22 nm. These results are quoted for an operating charge of $\sim 0.45 \times 10^{10}$ electrons per bunch.

4.5 Noise floor limit to the resolution

A specific set-up can be used to determine the resolution limit set by the electronics noise. The set-up takes the signal from one BPM and splits it to form inputs into two sets of electronics. By comparing the two outputs, the noise from the electronics can be estimated.

As shown in Fig. 4.16, the signals from the two y ports of, say, IPB are combined using a hybrid, filtered and passed through a variable attenuator as in the usual set-up for the Honda electronics (cf. Fig. 3.12). The signal is then split using a Mini-Circuits splitter, model ZX10R-14-S+, which introduces a loss of $\sim$ 7.1 dB at the operating frequency of 6.4 GHz [107]. The two outputs of the splitter are then processed by two nominally identical channels of the Honda electronics. A common reference cavity signal, obtained from the same limiter module, is used to down-mix both copies of the dipole signal. Delay cables are placed on the dipole cavity signal paths between the first and second stage mixer modules, as described in Sec. 3.5.2.

The signal from each set of electronics is calibrated using the procedure detailed in Sec. 3.6.3. Using the calibrations, position measurements y_1 and y_2 can be obtained for the two sets for each trigger. Each measurement can be expressed as a sum of the true bunch position y_{t}, which is common to both, and an offset ϵ_1, ϵ_2 respectively, which originates from the noise in the electronics and which is uncorrelated:

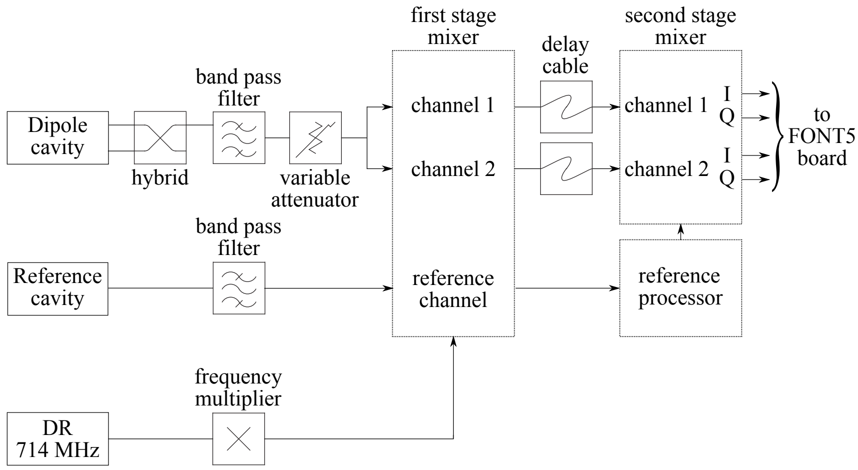

Figure 4.16: Block diagram schematic for 2-on-1 resolution study.

$$y_1 = y_{\mathrm{t}} + \epsilon_1, \tag{4.9}$$

$$y_2 = y_{\mathrm{t}} + \epsilon_2. \tag{4.10}$$

Given the common y_{t} term, the difference between y_1 and y_2 is given solely in terms of ϵ_1 and ϵ_2:

$$y_1 - y_2 = \epsilon_1 - \epsilon_2. \tag{4.11}$$

A set of $y_1 - y_2$ measurements was collected for a few hundred triggers. Given that ϵ_1 and ϵ_2 are uncorrelated, its standard deviation is [67]:

$$\big(\mathrm{std}(y_1 - y_2)\big)^2 = \big(\mathrm{std}(\epsilon_1)\big)^2 + \big(\mathrm{std}(\epsilon_2)\big)^2. \tag{4.12}$$

The terms $\mathrm{std}(\epsilon_1), \mathrm{std}(\epsilon_2)$ are the errors introduced by the electronics noise which constitutes the noise floor limit to the resolution, σ_{n}. Assuming $\mathrm{std}(\epsilon_1) = \mathrm{std}(\epsilon_2) = \sigma_{\mathrm{n}}$ gives:

$$\sigma_{\mathrm{n}} = \frac{\mathrm{std}(y_1 - y_2)}{\sqrt{2}}. \tag{4.13}$$

Applying the method above to a data set where the IPB signal was split, operating at a bunch charge of $(0.81 \pm 0.01) \times 10^{10}$, gives a noise floor limit to the resolution of 36.0 ± 1.1 nm using single-point sampling and 23.0 ± 0.7 nm with 7-sample averaging. Note that given the 7.1 dB splitter, the signal level input to the electronics has been attenuated by a factor of 2.3 so the quoted resolution limit is equivalent to that obtained at a charge of 0.36×10^{10} in the absence of the splitter. The noise floor limit to the resolution is therefore comparable to the 22 nm resolution extrapolation to 0 dB obtained with the beam waist at a single BPM with a charge of $\sim 0.45 \times 10^{10}$ electrons per bunch, as discussed in Sec. 4.4.6.

Table 4.4: Mean position and jitter measured by the two sets of electronics for the data set discussed in the text. Results using single-point sampling and multi-sample averaging are shown. Standard errors on the mean and jitter are given.

	Single sample		Averaging	
	Mean position (nm)	Position jitter (nm)	Mean position (nm)	Position jitter (nm)
y_1	-216 ± 6	129 ± 4	452 ± 6	128 ± 4
y_2	1084 ± 6	136 ± 4	585 ± 6	127 ± 4

The mean position and jitter for this resolution data set are quoted in Table 4.4. The position jitter measurements obtained from the two sets are in close agreement, particularly with multi-sample averaging. The position deduced from the two sets, however, shows a large discrepancy of over 1 μm with single-point sampling. The discrepancy arises from the static erratic feature present in the I and Q waveforms discussed in Sec. 4.2.1. The difference between the positions reported by the two sets of electronics confirms that the erratic feature is not the same for both. Averaging the results over 7 samples reduces the discrepancy to 130 nm.

An alternative method of calculating σ_n is to replace y_2 in Eq. 4.13 by a prediction of y_1. The prediction, y_1^{pred}, is obtained from a linear combination of y_2 and $\frac{Q'}{q}$ signals from both sets of electronics. Eq. 4.13 thus becomes:

$$\sigma_\mathrm{n} = \frac{\mathrm{std}(y_1^{\mathrm{meas}} - y_1^{\mathrm{pred}})}{\sqrt{2}} \tag{4.14}$$

where y_1^{meas} is the measured position using the first set of electronics.

To obtain y_1^{pred}, one first performs a least-squares fit to:

$$y_1 = \alpha_{y_2} y_2 + \alpha_{Q'_1}\frac{Q'_1}{q} + \alpha_{Q'_2}\frac{Q'_2}{q} + \alpha_1 \tag{4.15}$$

where y_1 and y_2 are the measured positions in the two sets of electronics, $\frac{Q'_1}{q}$ and $\frac{Q'_2}{q}$ are the measured charge-normalised Q' signals of the two sets of electronics and α_{y_2}, $\alpha_{Q'_1}$, $\alpha_{Q'_2}$ and α_1 are fit constants. The fit is performed over the few hundred triggers of the data set. Once the fit constants are obtained, the right hand side of Eq. 4.15 can be used to find a prediction, y_1^{pred}, for each trigger.

The motivation for each of the terms in Eq. 4.15 is as follows. The position y_1 should correlate strongly to y_2, and with correctly calibrated electronics, the scale factor α_{y_2} should be one. The terms $\frac{Q'_1}{q}$ and $\frac{Q'_2}{q}$ are included for completeness to account for errors in the measured θ_{IQ} which would couple some position signal into the Q' readout; as such, $\alpha_{Q'_1}$ and $\alpha_{Q'_2}$ are expected to be zero. The final fit parameter α_1 accounts for fixed offsets between the two sets of electronics; these offsets are depicted by the discrepancy between the mean position of y_1 and y_2 in Table 4.4.

Table 4.5: Noise floor limit to the resolution σ_n using the direct residual method (Eq. 4.13) and by fitting (Eq. 4.14). Results using single-point sampling and multi-sample averaging are shown. Standard errors are given.

	σ_n (nm)	
Method	Single sample	Averaging
Direct residual	36.0 ± 1.2	23.0 ± 0.7
Fitting α_{y_2} & α_1	34.1 ± 1.1	22.9 ± 0.7
Fitting α_{y_2}, $\alpha_{Q'_2}$ & α_1	34.0 ± 1.1	22.6 ± 0.7
Fitting α_{y_2}, $\alpha_{Q'_1}$, $\alpha_{Q'_2}$ & α_1	33.8 ± 1.1	22.3 ± 0.7

Table 4.5 shows the results for σ_n obtained after fitting the different parameters in Eq. 4.15. The results obtained using the direct residual method in Eq. 4.13 is added for comparison. The values for σ_n are consistent among the different methods. The difference between the direct residual method and fitting α_{y_2} and α_1 can be explained as the fit is at liberty to set α_{y_2} whilst the direct residual method effectively performs the same calculation but is constrained to $\alpha_{y_2} = 1$; however, the difference between the two methods is negligible. Adding $\frac{Q'_1}{q}$ and $\frac{Q'_2}{q}$ to the fit does not lower the resolution limit confirming that θ_{IQ} has been correctly determined.

4.5.1 Dependence on attenuation

The noise floor limit to the resolution can be determined as a function of the setting of the variable attenuator between the cavity and the splitter shown in Fig. 4.16. The two sets of electronics are calibrated for each attenuation setting from 0 to 50 dB in steps of 10 dB, operating at a charge set to $\sim 0.8 \times 10^{10}$ electrons per bunch. Fig. 4.17 shows the position jitter measured by the two sets of electronics and the noise floor limit to the resolution σ_n at each attenuation. A close agreement is observed at each attenuation setting between the jitter measured by the two sets of electronics, which is expected given that two nominally identical channels of the Honda electronics are being used.

At large attenuations, the measured position jitter is seen to agree with the noise floor limit to the resolution, confirming that the measured jitter is completely limited by the system noise. Thus, one obtains three resolution estimates at 50 dB: σ_n and one corresponding to the jitter measured in either set of electronics. The expected scaling of these resolutions to lower attenuation values is shown by the lines in Fig. 4.17.

In the regime between 30 and 50 dB, the measured position jitter matches the scaled prediction as the resolution remains much larger than the true position jitter. At lower attenuations, the measured jitter tends towards the true beam jitter which is hence estimated to be ~ 100 nm.

The evaluated σ_n tracks the extrapolated prediction closely. Reducing the attenuation increases the signal level for a given beam offset. If the electronics noise is considered alone and is assumed to be signal-independent, then an increase in signal results in a correspondingly

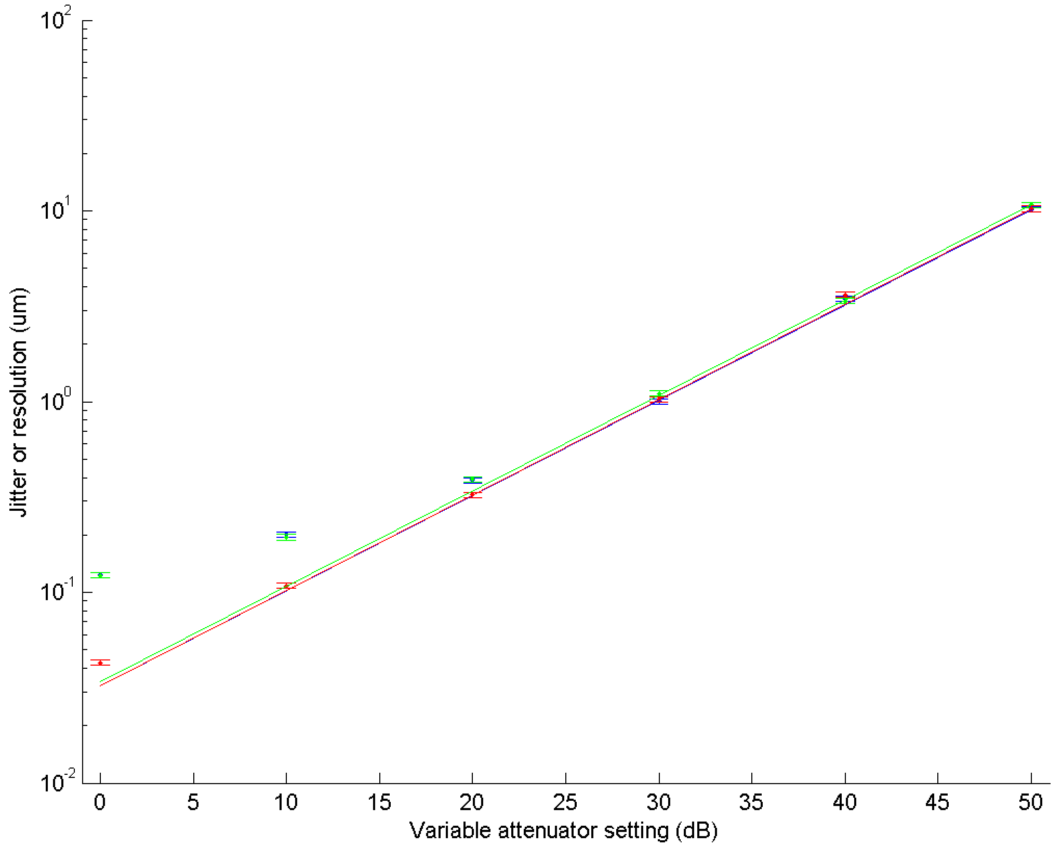

Figure 4.17: Measured vertical position jitter in the two sets of electronics, y_1 (blue) and y_2 (green), and noise floor limit to the resolution σ_{n} (red) versus attenuation. Multi-sample averaging is used. Standard errors are given. The lines represent a linear scaling of the values at 50 dB to lower attenuation settings.

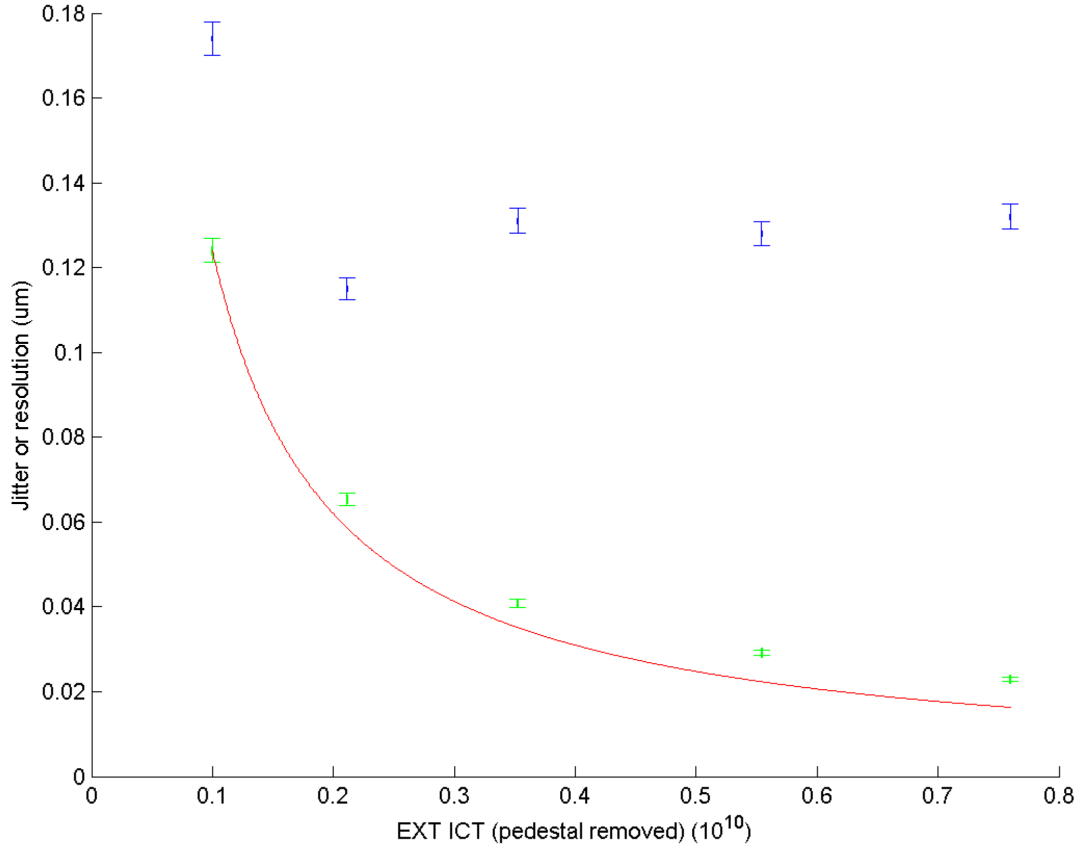

Figure 4.18: Measured vertical position jitter in the first set of electronics y_1 (blue) and noise floor limit to the resolution σ_n (green) versus bunch charge q. Multi-sample averaging is used. The charge is measured by the extraction line ICT and quoted in units of 10^{10} electrons per bunch. Standard errors are shown. The red line gives the dependence $\sigma_\mathrm{n} = 1/q$ by scaling σ_n at the lowest charge.

higher signal-to-noise ratio and an improved resolution.

In the limit of 0 dB attenuation, a deviation between the measured and predicted σ_n is observed. This suggests that the signal levels handled by the electronics are too high, causing a non-linear response in some of its components. The non-linearity degrades the system's resolution compared to the expectation from signal-to-noise considerations alone.

4.5.2 Dependence on charge

The noise floor limit to the resolution can be studied as a function of bunch charge. The two sets of electronics are calibrated at each charge as discussed in Sec. 4.3.2. Fig. 4.18 shows the jitter measured by one of the sets of electronics as a function of charge, with the variable attenuator set to 0 dB. The jitter is observed to tend towards $\sim$ 130 nm at high charges which constitutes an estimate of the true beam position jitter at the time of the study.

The noise floor limit to the resolution, σ_n, is evaluated at each charge setting, as shown in Fig. 4.18. Assuming that the resolution scales purely with the signal level, then the dependence of resolution on charge q is expected to take the form:

$$\sigma_{\mathrm{n}} \sim \frac{1}{q}. \tag{4.16}$$

The line in Fig. 4.18 shows the predicted dependence in Eq. 4.16, taking the lowest-charge point as a starting point. The measured σ_{n} points follow the expected behaviour closely but are always slightly above the line, suggesting that the resolution tends asymptotically towards a limiting value [79]. Given the particularity of splitting the IPB signal in this study, the resolution of the system reported in Fig. 4.18 is comparable to one operating at a charge a factor 2.3 smaller in the absence of the splitter.

4.6 Beam trajectory interpolation between IPB and IPC

The analysis in the preceding sections has concentrated on the functioning of a single BPM. The present section will address the performance of BPMs IPB and IPC whilst operating with nominal ATF optics. In this mode of operation, the beam waist is located at the nominal IP at the mid-point between IPB and IPC. The optics used was inherited from the preceding ATF shift dedicated to beam size minimisation.

The beam was centred in each BPM by performing the procedure outlined in Sec. 4.1.1. Following this procedure, the QF7FF y mover setting was changed by 300 µm to adjust the beam pitch y' in the IP region. The change in mover setting is an order of magnitude larger than the typical quadrupole mover adjustments used during beam tuning [108] and may have enhanced the effects of wakefields on the bunches. The cumulative effect of these wakefields can increase the beam size and beam position jitter at the IP [109] and may have resulted in an unwanted increment in the measured position jitter reported below [110].

Each trigger's beam position was measured at IPB and IPC, in both x and y directions. The procedure was repeated with variable attenuator settings in the range of 0 to 50 dB. Subsequently, each BPM was calibrated in x and y for each variable attenuator setting. The calibrations were performed as described in Sec. 3.6.3 with the beam waist on the BPM being calibrated. The results obtained with the variable attenuator set to zero are reported first; a comparison with the results obtained at higher attenuations is presented in Sec. 4.6.5. All results make use of multi-sample averaging.

4.6.1 Measured results

The mean position and jitter measured at IPB and IPC are presented in Table 4.6. The results show that the beam is well centred in the two BPMs. A vertical position jitter of 3.1 µm is measured at both BPMs, a measurement which is reproduced consistently for attenuation settings up to 40 dB (above which the measurement becomes resolution-limited).

Table 4.6: Mean position and jitter measured at BPMs IPB and IPC for the data set discussed in the text. Standard errors on the mean and jitter are given.

	Mean position (μm)		Position jitter (μm)	
BPM	x	y	x	y
IPB	-0.10 ± 0.06	-0.76 ± 0.10	1.86 ± 0.04	3.14 ± 0.07
IPC	-1.46 ± 0.10	-0.05 ± 0.10	3.05 ± 0.07	3.11 ± 0.07

Table 4.7: Minimum horizontal x and vertical y interpolated position jitters for the data set discussed in the text, and the longitudinal distances z from the IP at which they occur.

	Position jitter (μm)	z from IP (mm)
x	1.8	-74
y	0.082	$+0.3$

Given the absence of magnetic elements in the IP region, a linear transport model can be assumed. The beam paths thus interpolated in the vertical plane between IPB and IPC are shown in Fig. 4.19. The figure shows clearly how the beam is focused at the IP.

The paths can be used to calculate the position jitter as a function of the longitudinal distance z; the results for x and y are shown in Fig. 4.20. These position jitters are referred to as interpolated jitters. The minimum interpolated jitters, and the longitudinal distances at which they occur, obtained for this data set are given in Table 4.7. The minimum jitters identify the location of the beam waist in the x and y directions. The y beam waist is found to be almost at the IP, which follows from the vertical beam size minimisation performed at the IP in the preceding shift.

4.6.2 Simulation

The measured interpolated y position jitter σ_{i} is a combination of the true jitter at the waist and an error introduced by the BPM resolution. To understand the contribution of the two effects, the following simulation was performed.

The IP beam position and pitch were determined for each trigger by propagating the measured beam positions at the upstream stripline BPMs P2 and P3. The linear transfer matrix method was used as described in Sec. 2.8, giving a minimum propagated jitter of 9.0 nm at a longitudinal distance of 0.8 mm upstream of the IP marker in the ATF model. In order to achieve a symmetric solution about the IP, the beam waist was placed on the IP marker by displacing the z coordinate axis by 0.8 mm. As noted in Sec. 2.8.2, the 9.0 nm jitter estimate constitutes an underestimate as the propagation model excludes any x-to-y position coupling, energy dependence or non-linear effects.

For the purposes of this simulation, the propagated IP position jitter σ_{prop} was increased in order to better reflect the expected jitters. An increased beam jitter was simulated by including a random offset to the predicted IP positions y_{prop}, whilst the predicted beam pitch

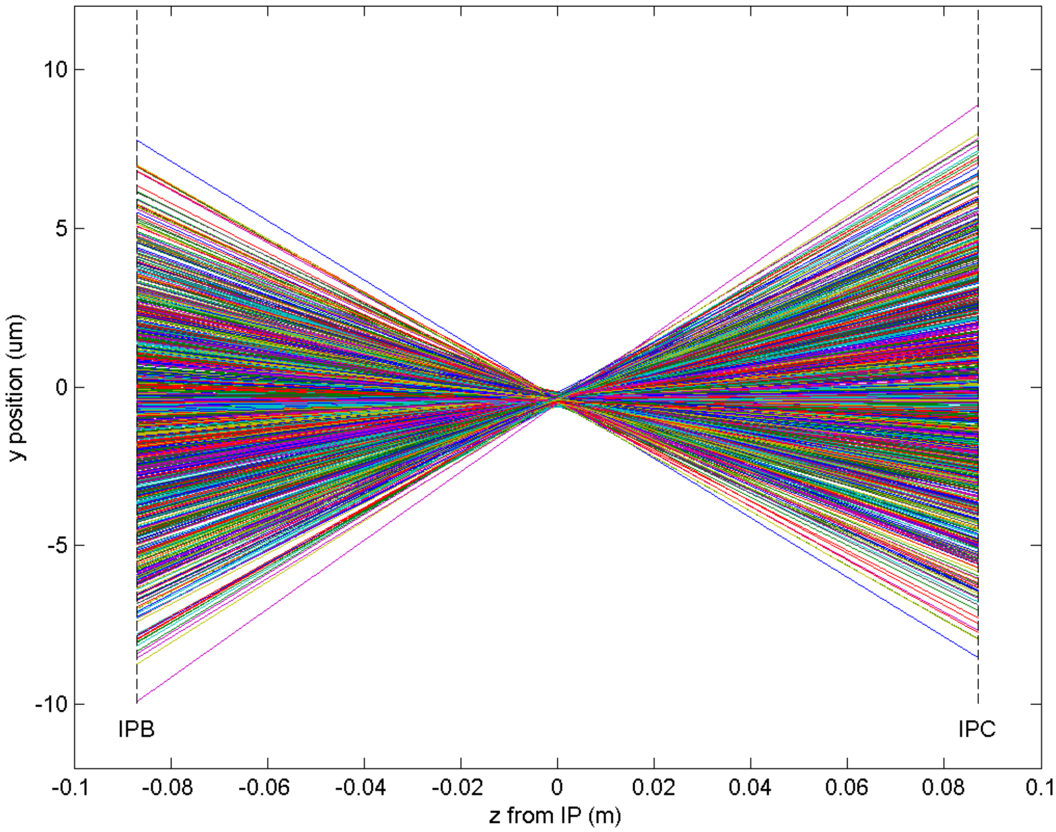

Figure 4.19: Vertical bunch position y, for each trigger, versus longitudinal distance z from the IP. The beam paths are obtained from a linear interpolation of the measured beam positions at IPB and IPC.

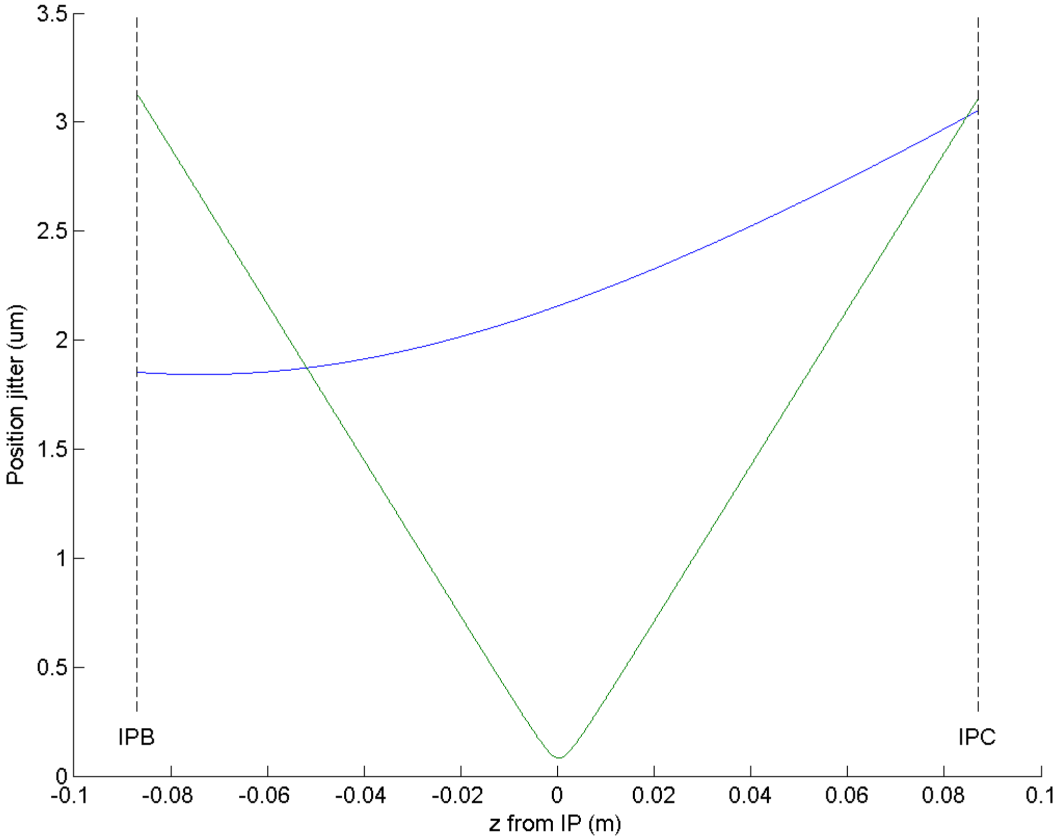

Figure 4.20: Horizontal (blue) and vertical (green) position jitter versus longitudinal distance z from the IP. The position jitter is obtained by interpolating the measured positions at IPB and IPC.

y'_{prop} was unchanged. The resulting position y_{t} can be expressed as:

$$y_{\text{t}} = y_{\text{prop}} + y_{\text{rand}}, \tag{4.17}$$

where the random offsets y_{rand} are drawn from a normal distribution with a standard deviation σ_{rand}. Consequently, the jitter of y_{t} is:

$$\sigma_{\text{t}}^2 = \sigma_{\text{prop}}^2 + \sigma_{\text{rand}}^2. \tag{4.18}$$

This combined jitter, σ_{t}, constitutes the true beam position jitter in this simulation in the sense that the effect of the IP BPM resolution on the measurement has not been included.

The measured interpolated jitter σ_{i}, which does include the IP BPM measurement errors, was simulated as follows. The IP beam position y_{t} and pitch y'_{prop} were used to obtain the beam positions at IPB and IPC. A random measurement error, with a standard deviation equal to the BPM resolution σ_{r}, was then applied to the individual IPB and IPC positions. These simulated measurements at the two BPMs were then interpolated to the IP to obtain σ_{i}.

Fig. 4.21 shows the simulation results for two cases. The first is the ideal case where the BPMs have perfect resolution, that is, $\sigma_{\text{r}} = 0$. Here, the measured positions IPB and IPC are sufficient to reconstruct the IP position perfectly and, hence, the interpolated jitter matches the true jitter for all jitters. For the second case, a realistic BPM resolution of 40 nm is assumed, as suggested by the study in Sec. 4.4. Under these circumstances, the ability to resolve small IP jitters by interpolating the positions at IPB and IPC is limited by the BPM measurement errors.

The simulation shows that a smaller jitter can be resolved when interpolating the positions from two BPMs than can be achieved with a single BPM. As discussed in Sec. 4.4, in the single BPM case, the true beam jitter σ_{t} and the resolution σ_{r} add in quadrature to give the measure jitter σ_{m}:

$$\sigma_{\text{m}}^2 = \sigma_{\text{t}}^2 + \sigma_{\text{r}}^2. \tag{4.19}$$

In the case where the positions at two BPMs are averaged, the effective resolution of the interpolated measurement becomes $\sigma_{\text{r}}/\sqrt{2}$, so the corresponding expression for the interpolated jitter σ_{i} becomes:

$$\sigma_{\text{i}}^2 = \sigma_{\text{t}}^2 + \tfrac{1}{2}\sigma_{\text{r}}^2. \tag{4.20}$$

This dependence is shown in Fig. 4.21, achieving a good agreement with the simulated results.

The improvement in the system resolution on using two BPMs can be explained in terms of the reduction in error. The interpolation effectively takes the mean of the beam positions

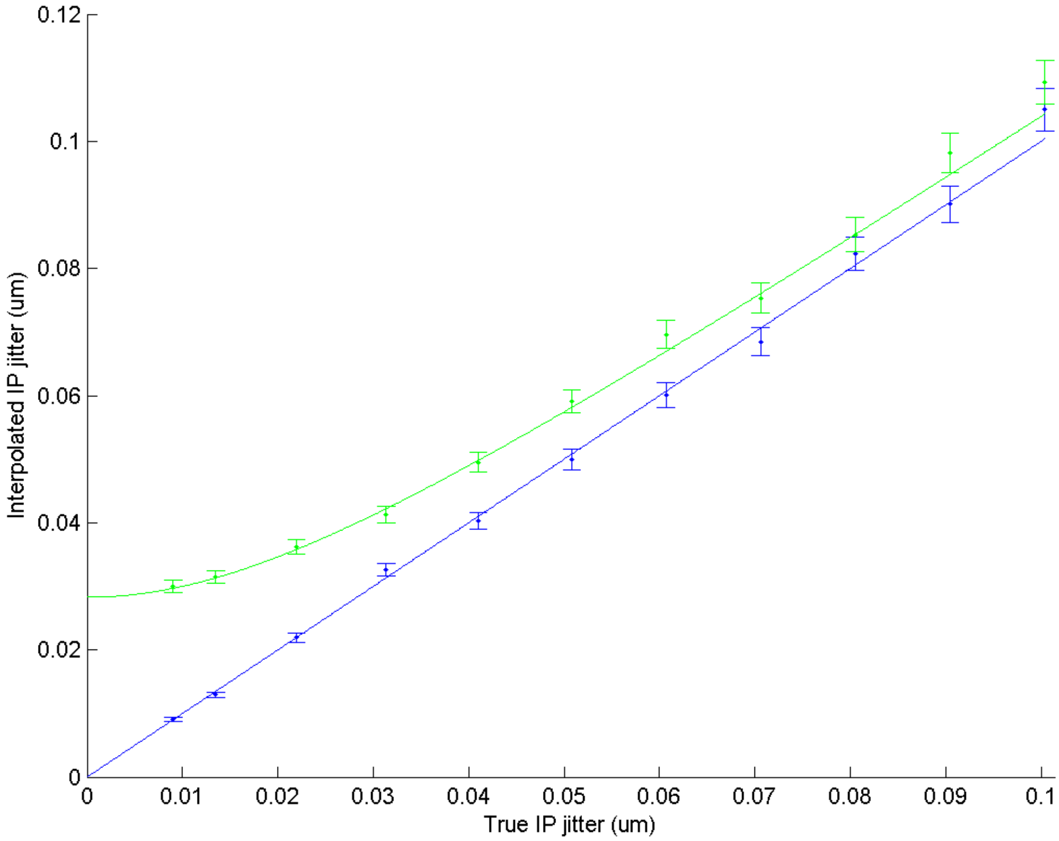

Figure 4.21: Simulation of interpolated position jitter at the IP versus true IP position jitter for BPMs with a resolution of 0 (blue) and 40 nm (green). The lines show the expected dependence (Eq. 4.20).

at IPB and IPC. The two measurements, for any trigger, have uncorrelated errors and so the standard error on the mean is a factor $\sqrt{2}$ smaller than the resolution of the individual measurements [67].

4.6.3 Comparison of measured and simulated results

The measured interpolated y position jitter of 82 nm given in Table 4.7 can be interpreted in terms of the simulation presented in Sec. 4.6.2. Assuming that the individual BPM resolutions are ~ 40 nm, the measured interpolated jitter suggests that the true beam jitter was ~ 80 nm at the IP when this data was taken.

It is important to note that the ~ 40 nm BPM resolution estimate follows from the single BPM studies discussed in Sec. 4.4, where the beam jitter was intentionally minimised at the BPM. It is necessary, therefore, to assess whether larger position jitters may degrade the BPM position resolution as a result of the larger signals processed by the BPM electronics. This is studied in Sec. 4.6.4.

4.6.4 Cuts on electronics saturation

As discussed in Sec. 2.8.3, the beam position at the waist does not correlate with the beam position off the waist. Therefore, any cuts placed on triggers according to their positions at the off-waist BPMs will not affect the position jitter at the waist. This allows triggers with larger beam offsets at the two BPMs to be removed from the data in Sec. 4.6.1 before repeating the interpolation analysis.

The hypothesis that the BPM resolution is degraded by the large jitter in IPB and IPC can be tested as follows. If the triggers further off-centre lead to a non-linear response in the electronics, their presence will degrade the BPM resolution and will increase the interpolated jitter that is deduced at the waist. In this case, removing these triggers from the analysis would result in a reduction in the interpolated jitter.

The results of the cuts on $\sqrt{I^2 + Q^2}$, representative of the signal level input into the BPM electronics, are presented in Table 4.8. The position jitter measured at the two BPMs decreases as the cut removes more triggers, as expected. On the contrary, the interpolated jitter at the waist remains constant indicating that the ~ 80 nm jitter interpolated at the waist is not resulting from a poorer BPM resolution when operating with ~ 3 µm jitters at the BPMs.

4.6.5 Scaling of interpolated position jitter measurement with attenuation

The variable attenuator at the dipole cavity output can be varied in order to change the BPM resolution relative to the beam jitter at the waist. Fig. 4.22 shows the interpolated

Table 4.8: IPB and IPC measured position jitter and interpolated jitter at the waist, σ_{i}, as a function of the number of triggers remaining after performing cuts on $\sqrt{I^2+Q^2}$. Standard errors on the jitter are given.

	Position jitter (μm)		
Triggers remaining	IPB	IPC	σ_{i} (nm)
994	3.14 ± 0.07	3.11 ± 0.07	82 ± 2
770	2.04 ± 0.05	2.02 ± 0.05	83 ± 2
540	1.35 ± 0.04	1.33 ± 0.04	84 ± 3
259	0.65 ± 0.03	0.64 ± 0.03	82 ± 4

position jitter at the waist as a function of the attenuation. The results at 0 dB have been discussed in detail in Sec. 4.6.1–4.6.4.

In the regime between 20 and 50 dB, the measured interpolated jitter σ_{i} is observed to scale linearly with attenuation. This follows from Eq. 4.20 which becomes

$$\sigma_{\mathrm{i}} = \frac{\sigma_{\mathrm{r}}}{\sqrt{2}} \tag{4.21}$$

when the true interpolated jitter σ_{t} is much smaller than the BPM resolution σ_{r} at the given attenuation. The measured interpolated jitter deviates from the linear scaling at the smaller attenuations as the true beam jitter at the waist is comparable to, or larger than, the BPM resolution. These results suggest that the true beam jitter was ~ 80 nm when the data was taken.

By linearly scaling the results at 50 dB, the regime in Eq. 4.21 can be extended to the case where the attenuation is 0 dB. As shown in Fig. 4.22, this produces a minimum jitter of 13 nm at 0 dB, which corresponds to a BPM resolution estimate of 18 nm. This resolution estimate assumes a linear system and therefore constitutes a lower limit to the resolution. The results are quoted for an operating charge of $\sim 0.48 \times 10^{10}$ electrons per bunch, and agree closely with the extrapolated resolution of 22 nm at 0 dB presented in Sec. 4.4.6.

4.7 3-BPM resolution

The fact that the IP BPM system is comprised of three BPMs allows a direct resolution estimate to be obtained. For a successful measurement, the BPM triplet needs to be well aligned such that the beam passes through the operating dynamic range of each BPM. In particular, the relative alignment of BPMs IPA and IPB is essential as the two BPMs are mounted on a common mover system, as presented in Sec. 3.2.

In order to achieve the required BPM alignment, a copy of the triplet of BPMs was manufactured during 2014 with the same design as the existing BPMs but with stricter machining tolerances; the BPM copies were delivered by the KNU group in October 2014 [111]. The internal alignment of the IPA-IPB block was adjusted to better than 5 μm [112]

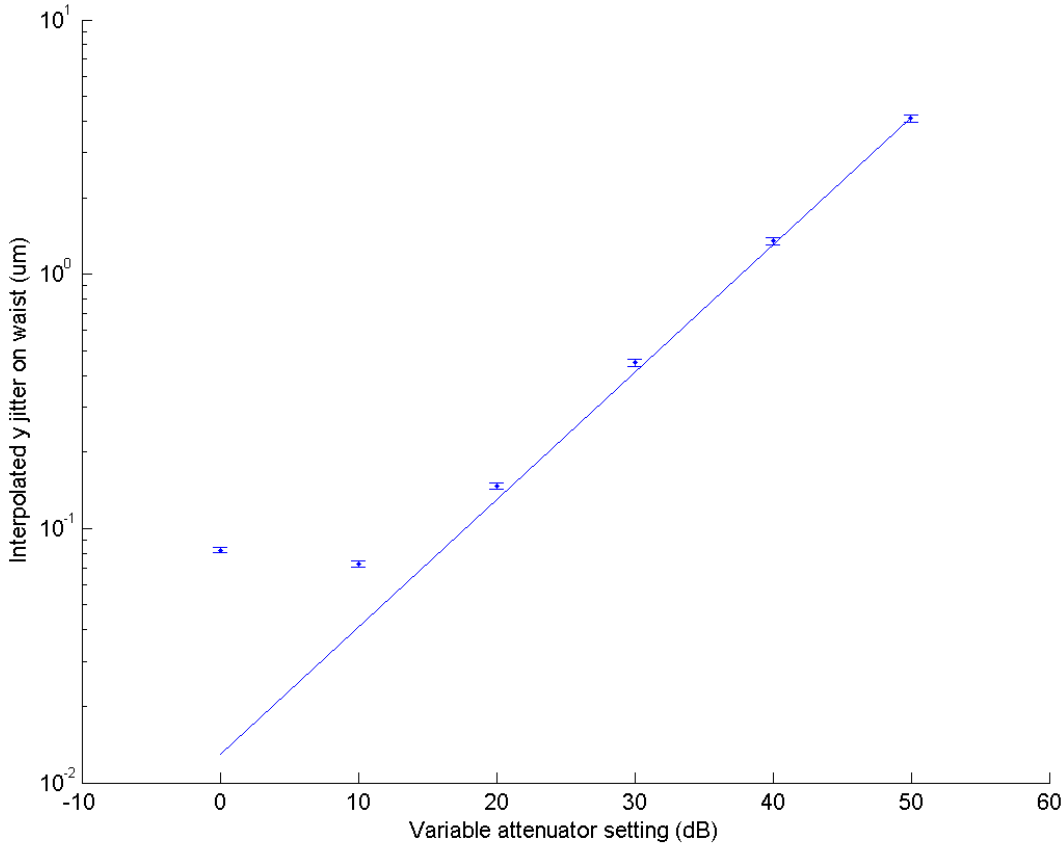

Figure 4.22: Interpolated vertical position jitter at the waist versus attenuation. Standard errors are shown. The line represents a linear scaling of the jitter at 50 dB to lower attenuation settings.

Table 4.9: Mean position and jitter measured at the three BPMs IPA, IPB and IPC for the resolution data set discussed in the text. Results using single-point sampling and multi-sample averaging are shown. Standard errors on the mean and jitter are given.

	Single sample		Averaging	
BPM	Mean position (μm)	Position jitter (μm)	Mean position (μm)	Position jitter (μm)
IPA	9.498 ± 0.010	0.444 ± 0.007	9.275 ± 0.010	0.437 ± 0.007
IPB	2.138 ± 0.005	0.239 ± 0.004	2.211 ± 0.005	0.237 ± 0.004
IPC	7.496 ± 0.011	0.483 ± 0.008	7.572 ± 0.011	0.484 ± 0.008

by the LAL group and the new IP BPM triplet was installed at ATF in November 2014. The 3-BPM resolution results presented here, and the IP feedback results discussed in Chapter 5, were taken in December 2014 with the aligned BPM set-up.

As discussed in Sec. 4.2.1, the high-frequency erratic component present in the I and Q waveforms is static and beam position-independent. In order to reduce the impact of the large static component on the second stage of the Honda electronics, a narrow-band BPF of ±10 MHz bandwidth was placed on the dipole cavity signals between the first and second stage downmixers. A BPF of similar bandwidth could be placed at the input of the first stage; such a custom-built C-band BPF may be introduced at a future date.

To ensure that all bunches pass through the narrow dynamic range of the BPMs, the beam position jitter was reduced at the IP BPMs. This was achieved by loading optics with a beta function at the IP, β_y^*, 1000 times larger than its nominal value [113]. This increase in β_y^* reduces the divergence of the beam in the IP area and, hence, lowers the beam jitter in the IP BPMs.

As discussed in Sec. 4.6, the path taken by the beam can be interpolated from the measurements performed at a pair of IP BPMs. The jitter calculated from these paths is shown, as a function of the longitudinal distance, in Fig. 4.23. Given that there are three BPMs, the interpolation can be performed between three pairs of BPMs; the results for each are shown. As discussed in Sec. 4.6 an interpolated position can have a greater precision than a single measurement; this is noticed in the fact that the interpolated jitter at IPB is 14 nm smaller than the measured jitter.

A comparison of Fig. 4.20, obtained with nominal optics, to Fig. 4.23, presented here, shows the effect of the change in optics. With the high-β_y^* optics, the jitter at the IP BPMs is reduced to a sub-micron level at the expense of increasing the jitter at the beam waist to over 100 nm. Table 4.9 shows the mean position and jitter measured at the three BPMs using the high-β_y^* optics. A close agreement is obtained using single-point sampling and multi-sample averaging; this observation results from the reduction in sample-to-sample variation with the introduction of the narrow-band BPF.

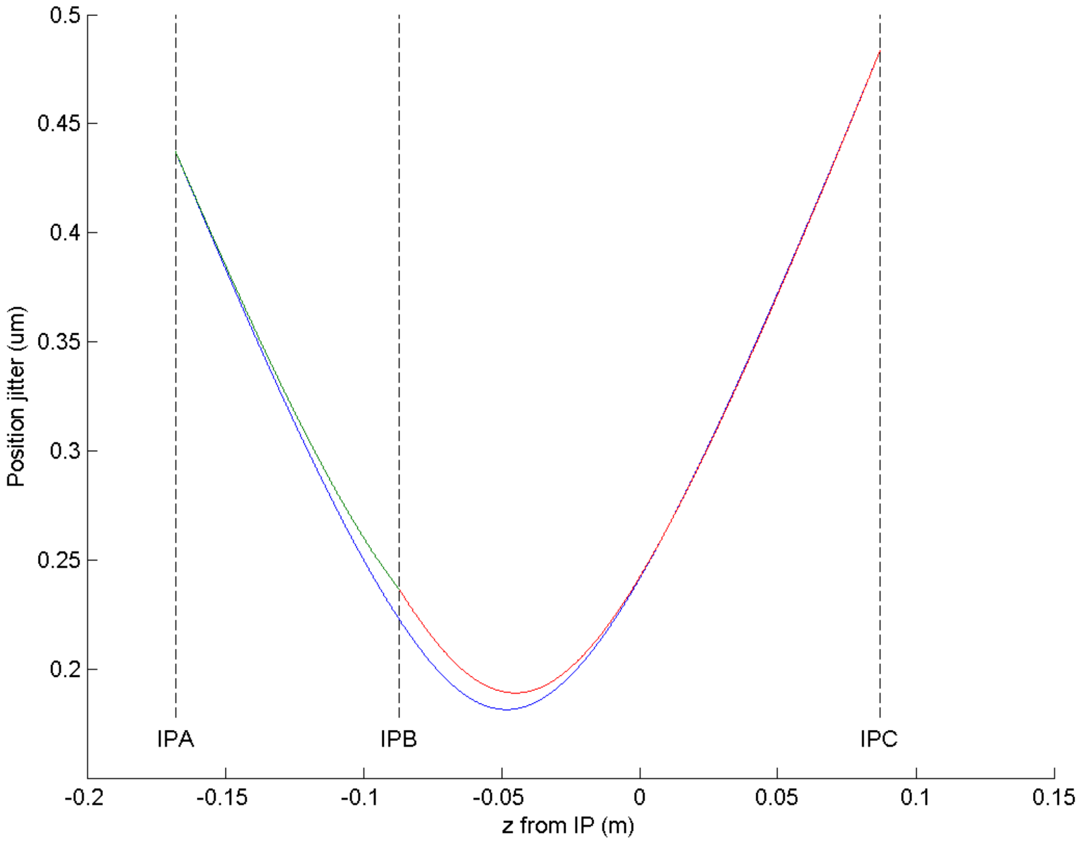

Figure 4.23: Position jitter versus longitudinal distance z from the IP for the resolution data set discussed in the text. The jitter is calculated across all triggers by interpolating the path taken by each trigger from IPA to IPB (green), from IPB to IPC (red) and from IPA to IPC (blue). Multi-sample averaging is used.

4.7.1 Resolution calculation

By making use of a linear beam transport model, the position at one BPM, y_i, can be expressed as a linear combination of the positions at the other two BPMs, y_j and y_k:

$$y_i = C_{ij}y_j + C_{ik}y_k, \tag{4.22}$$

where the coefficients C_{ij} and C_{ik} are constants. The ability to predict the position y_i using y_j and y_k is degraded by the BPM measurement error. The measured beam position y_i^{meas} can be expressed in terms of the true position y_i^{true} and an error ϵ_i:

$$y_i^{\text{meas}} = y_i^{\text{true}} + \epsilon_i, \tag{4.23}$$

where ϵ_i is a random variable taken from a normal distribution with standard deviation equal to the BPM resolution, σ_i.

Eq. 4.22 can be used to obtain a predicted position y_i^{pred} from the measured positions y_j^{meas} and y_k^{meas}. The residual δ_i is defined to be the difference between the measured y_i^{meas} and the predicted y_i^{pred}:

$$\begin{aligned}
\delta_i &= y_i^{\text{meas}} - y_i^{\text{pred}} && (4.24)\\
&= y_i^{\text{meas}} - C_{ij}y_j^{\text{meas}} - C_{ik}y_k^{\text{meas}} && (4.25)\\
&= (y_i^{\text{true}} - C_{ij}y_j^{\text{true}} - C_{ik}y_k^{\text{true}}) + (\epsilon_i - C_{ij}\epsilon_j - C_{ik}\epsilon_k), && (4.26)
\end{aligned}$$

where the last line follows from Eq. 4.23. The three terms in the first set of brackets of Eq. 4.26 cancel given Eq. 4.22. Taking the variance of Eq. 4.26 over many triggers produces:

$$(\text{std}(\delta_i))^2 = \sigma_i^2 + C_{ij}^2\sigma_j^2 + C_{ik}^2\sigma_k^2, \tag{4.27}$$

as the errors ϵ_i, ϵ_j and ϵ_k are uncorrelated [67] and have a standard deviation of σ_i, σ_j and σ_k, respectively.

In the absence of further information, one has to assume that all three BPMs have an equal resolution $\sigma_i = \sigma_j = \sigma_k = \sigma$. Hence, rearranging Eq. 4.27 gives an estimate for the BPM resolution in terms of the standard deviation of residuals:

$$\sigma = \frac{\text{std}(\delta_i)}{\sqrt{1 + C_{ij}^2 + C_{ik}^2}}, \tag{4.28}$$

where the term $\sqrt{1 + C_{ij}^2 + C_{ik}^2}$ is referred to as the geometric factor [78]. The resolution estimate σ is conditioned by the coefficients C_{ij} and C_{ik} defined in Eq. 4.22. Two methods to obtain these coefficients are outlined below: the geometric method, where the coefficients are deduced from the beam transport model, is given in Sec. 4.7.2 and the fitting method,

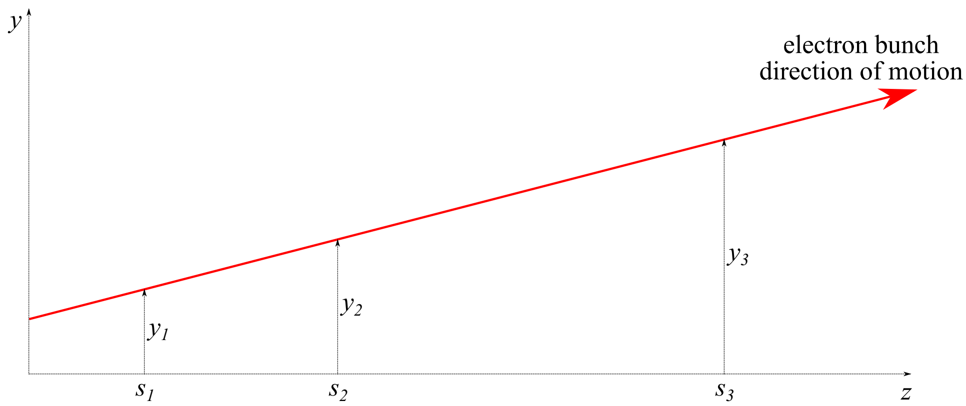

Figure 4.24: Definition of the vertical positions y_1, y_2, y_3 of the three BPMs at longitudinal locations s_1, s_2, s_3.

where the coefficients are obtained by fitting to the measured positions at the three BPMs, is presented in Sec. 4.7.3.

4.7.2 Geometric method

The geometric method consists in using the beam transport geometry between the IP BPMs to determine the prediction coefficients C_{ij} and C_{ik} in Eq. 4.22. As a result of the absence of magnetic elements in the beamline in the IP region, a ballistic beam trajectory can be assumed for each bunch. Taking the vertical beam position measurements y_1, y_2, y_3 at the three BPMs at the longitudinal locations s_1, s_2, s_3, as shown in Fig. 4.24, one can predict the position at each of the BPMs in terms of the other two BPMs as follows:

$$y_1^{\text{pred}} = y_2 - \frac{y_3 - y_2}{s_3 - s_2}(s_2 - s_1) = \big(1 + \frac{s_2 - s_1}{s_3 - s_2}\big)y_2 - \frac{s_2 - s_1}{s_3 - s_2}y_3; \tag{4.29}$$

$$y_2^{\text{pred}} = y_1 + \frac{y_3 - y_1}{s_3 - s_1}(s_2 - s_1) = \big(1 - \frac{s_2 - s_1}{s_3 - s_1}\big)y_1 + \frac{s_2 - s_1}{s_3 - s_1}y_3; \tag{4.30}$$

$$y_3^{\text{pred}} = y_1 + \frac{y_2 - y_1}{s_2 - s_1}(s_3 - s_1) = \big(1 - \frac{s_3 - s_1}{s_2 - s_1}\big)y_1 + \frac{s_3 - s_1}{s_2 - s_1}y_2. \tag{4.31}$$

Eqs. 4.29–4.31 can be used, together with the BPM separations quoted in Table 3.1, to obtain the position predictions at each BPM for the 2000 one-bunch trains in the resolution run of Fig. 4.23. The resulting distributions for the measured and predicted positions are presented in the top row of Fig. 4.25. As the mean beam position at each BPM is arbitrarily set by the BPM mover settings, the mean position of each distribution has been subtracted for this plot. The results show that the distributions of the predicted positions agree closely with the measured positions at each BPM demonstrating that the BPM calibrations and the beam transport model are consistent.

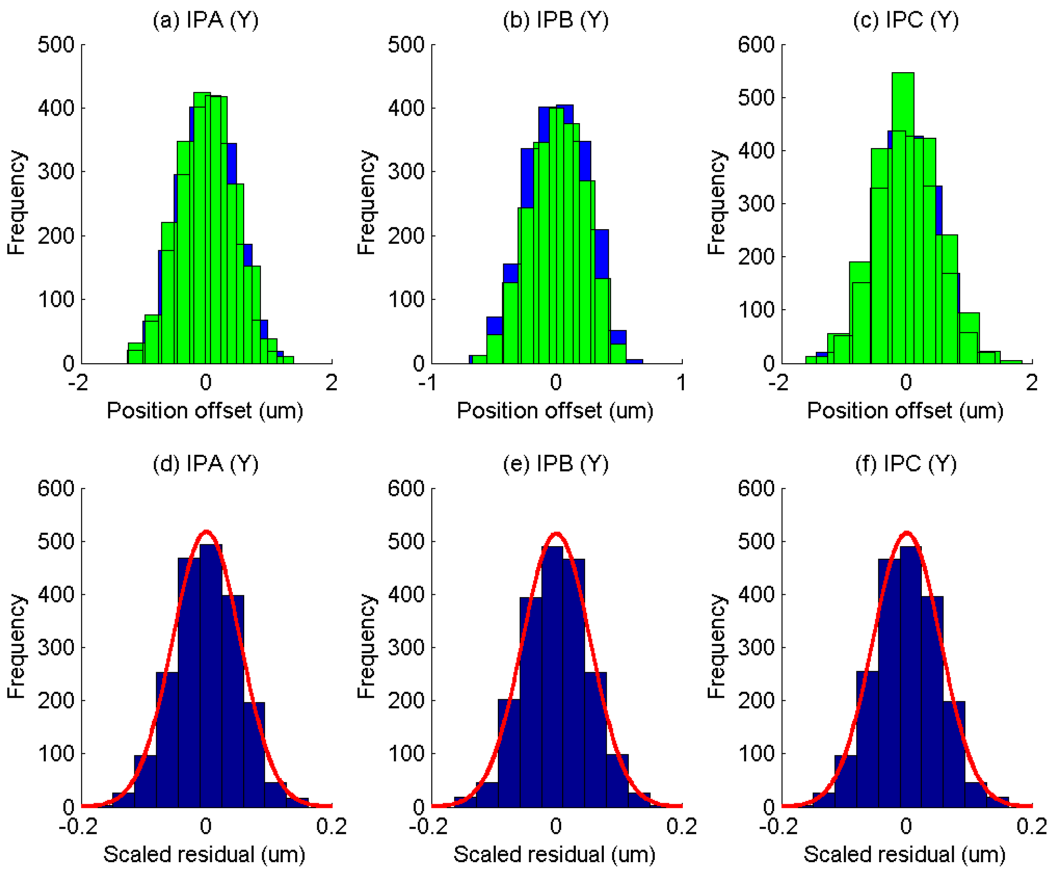

Figure 4.25: Distributions of the measured positions (blue) and the predicted positions obtained using the geometric method (green) at BPMs (a) IPA, (b) IPB and (c) IPC; and distributions of the corresponding scaled position residuals at BPMs (d) IPA, (e) IPB and (f) IPC. The red lines show Gaussian fits to the respective data.

The bottom row of Fig. 4.23 shows the distributions of scaled residuals $\widetilde{\delta_i}$ defined as:

$$\widetilde{\delta_i} = \frac{\delta_i}{\sqrt{1 + C_{ij}^2 + C_{ik}^2}}, \tag{4.32}$$

where δ_i are the residuals between the mean-subtracted measured positions and the mean-subtracted predicted positions. Each distribution of scaled residuals is fitted with a Gaussian curve obeying:

$$\frac{\mathrm{d}N}{\mathrm{d}\widetilde{\delta_i}} = A_i e^{-\frac{\widetilde{\delta_i}^2}{2\sigma^2}} \tag{4.33}$$

of width σ equal to the resolution estimate given in Eq. 4.28, where A_i is a normalisation factor.

The positions predicted by Eqs. 4.29–4.31 are fully constrained by the separation of the BPMs, so a common BPM resolution estimate is obtained regardless of the BPM at which the prediction is made. The Gaussian fits to the scaled residuals in Fig. 4.25 yield a resolution estimate of 54 ± 1 nm with multi-sample averaging. These results were obtained with a mean bunch charge of 0.46×10^{10} electrons and a bunch charge stability of better than 0.01×10^{10} electrons. A similar analysis, performed with single-point sampling, gives a resolution estimate of 57 ± 1 nm; the difference with the result obtained with averaging is small as a result of the narrow-band BPF reducing the sample-to-sample variation.

4.7.3 Fitting method

An alternative, model-independent method of determining the prediction coefficients C_{ij} and C_{ik} allows the results in Sec. 4.7.2 to be verified. The fitting method achieves this by performing a least-squares fit to

$$y_i = C_{ij} y_j + C_{ik} y_k + K_i \tag{4.34}$$

over the triggers in the resolution run [114], where C_{ij} and C_{ik} follow the definition in Eq. 4.22 and the constant K_i is included to account for the position offsets that can be set by the BPM movers.

The top row of Fig. 4.26 shows that the fitting method produces a distribution of predicted positions that agrees closely with the measured positions at each BPM. The scaled residuals calculated using Eq. 4.32 are plotted in the bottom row of Fig. 4.26, and the widths of the Gaussian fits are used to calculate the resolution estimates given in Table 4.10.

The geometric and fitting methods produce resolution estimates that agree strongly, confirming that the model-based calculation successfully describes the system. The fitting method allows multiple quantities to be fitted which are otherwise constrained in the geometric method. These quantities include the relative distances between the BPMs and the individual BPM calibrations. In addition, the fitting method removes any components

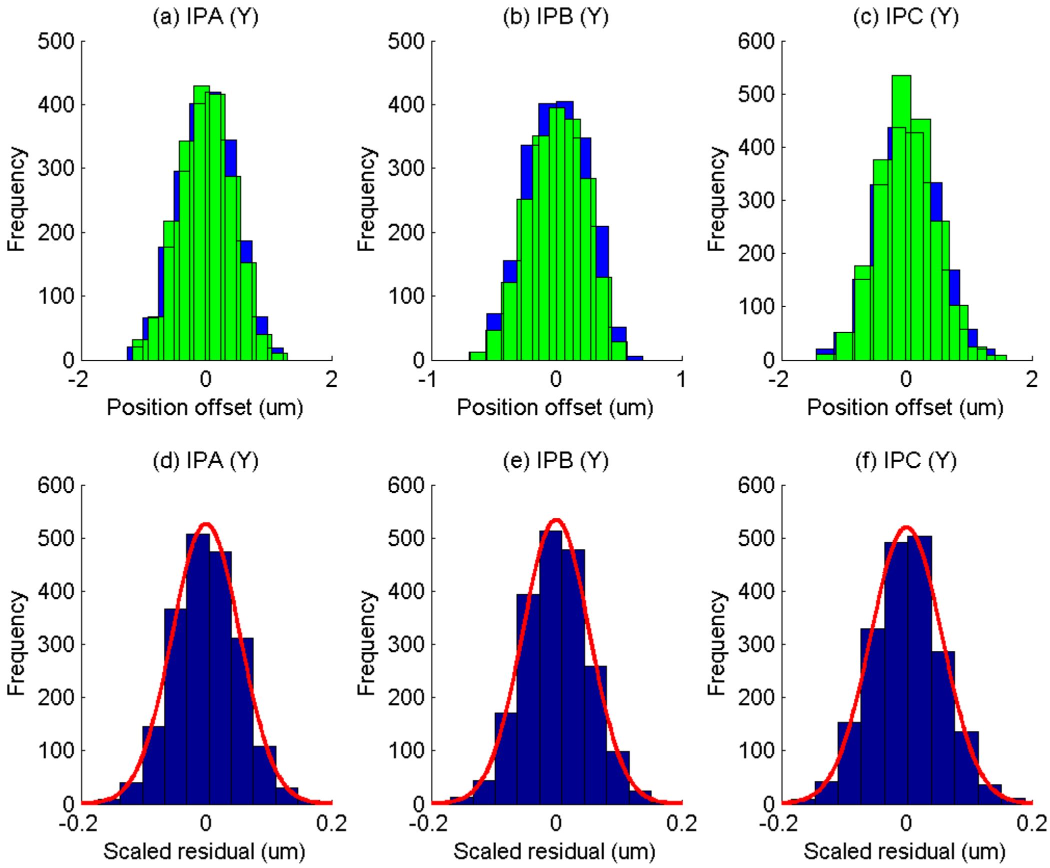

Figure 4.26: Distributions of the measured positions (blue) and the predicted positions obtained using the fitting method (green) at BPMs (a) IPA, (b) IPB and (c) IPC; and distributions of the corresponding scaled position residuals at BPMs (d) IPA, (e) IPB and (f) IPC. The red lines show Gaussian fits to the respective data.

Table 4.10: Estimated IP BPM resolution obtained with the geometric and fitting methods, using single-point sampling and multi-sample averaging. The data was taken on 20 December 2014. Standard errors on the resolution are given.

	Estimated resolution (nm)			
	Geometric method		Fitting method	
BPM of prediction	Single-point	Averaging	Single-point	Averaging
IPA	57 ± 1	54 ± 1	56 ± 1	54 ± 1
IPB	57 ± 1	54 ± 1	57 ± 1	53 ± 1
IPC	57 ± 1	54 ± 1	62 ± 1	57 ± 1

correlated in the position data across the three BPMs; these correlated components can be degrading the BPM resolution as discussed in Sec. 4.4.5. Nevertheless, the agreement of the two methods shows that the quantities constrained in the model are consistent and, hence, given that the model is sound, the quoted resolution estimates can be treated as actual resolution measurements.

The results presented here assume no coupling between the x and y planes. However, if the BPMs have different rolls (cf. Fig. 3.5), a fraction of the x beam position offset would be coupled into the y position read-out. In order to measure its effect, one would need to instrument the three BPMs in x and y. By including the three x position terms to the fit in Eq. 4.34 [76], a revised resolution estimate would be obtained. This new estimate would be independent of the relative BPM rolls and would indicate the mismatch in the rolls between the BPMs. The 3-BPM resolution measurement in x and y will be possible once the number of LO signals to the second-stage downmixers, described in Sec. 3.4.2, is increased from four to six.

4.8 Summary

This chapter has explored the performance of the IP BPMs operating in regimes involving the use of one, two and three IP BPMs. The beam set-up procedure was described. The features of the signal waveforms obtained from the Honda electronics were analysed, identifying a static position-independent component and a sinusoidal component resulting from the frequency mismatch between the reference and dipole cavity signals. The single-point sampling and multi-sample averaging techniques used to process the digitised signals were presented. The system linearity with attenuation and bunch charge were analysed.

The system has been analysed in detail, operating at a typical bunch charge of $\sim 0.5\times10^{10}$ electrons. A minimum beam position jitter of 40 ± 2 nm was measured at IPB using multi-sample averaging, after correcting for a drift in the longitudinal location of the beam waist. The noise floor limit to the resolution was estimated to be 23.0 ± 0.7 nm by splitting the signal from IPB into two sets of the Honda electronics and comparing their outputs. The successful operation of IPB and IPC with nominal ATF optics, and the ability to interpolate the position jitter to the beam waist, was demonstrated. The vertical position signals from the IP BPM triplet were used to obtain a BPM resolution estimate of 54 ± 1 nm using the model-based geometric method and of between 53 ± 1 and 57 ± 1 nm using the model-independent fitting method. These results demonstrate an IP BPM system resolution at or below the 50 nm level.

Chapter 5

IP feedback

5.1 Introduction

The goal of IP feedback is to stabilise the vertical beam position at the beam waist. The system presented here makes use of one of the IP BPMs to measure the vertical position of the first bunch in two-bunch trains. Provided that the bunch-to-bunch position correlation is high, the position of the first bunch can be used to predict, and hence correct, the position of the second bunch. The BPM whose measurement constitutes the input into the feedback loop is referred to as the feedback BPM.

The IP BPM signal from the first bunch is processed by the analogue cavity BPM electronics presented in Chapter 3 and the outputs are digitised by the FONT5 digital board. The FONT5 board performs a real-time calculation to produce an analogue signal that is then amplified and delivered to the IP kicker (IPK). As long as the timing is adequate, the kicker applies a kick to the orbit of the second bunch with the aim of zeroing its position at the feedback BPM. The performance of the feedback system is evaluated by measuring the level of correction at this BPM.

5.1.1 Experimental set-up

The IP feedback system consists of the cavity BPM IPB and the kicker IPK. The experimental set-up including the cavity BPM processing electronics, the FONT5 digital board and the kicker amplifier is given in Fig. 5.1. A more detailed schematic is given in Fig. 5.2.

The cavity BPM signal processing corresponds to the Honda electronics, described in Sec. 3.4.2. The output signals from the two ports of IPB are combined using the hybrid, before being passed through the BPF (Sec. 3.3) and variable attenuator. In parallel, the reference cavity output is passed through a BPF. The IPB and reference cavity signals are then processed by the two stages of the Honda electronics, which are given in Fig. 3.12 in Sec. 3.4.2. The IP feedback set-up makes use of a 714 ± 10 MHz BPF on the dipole cavity signal between the two stages of the Honda electronics. As discussed in Sec. 4.7, the filter is introduced to remove the unwanted static high-frequency components described in Sec. 4.2.1.

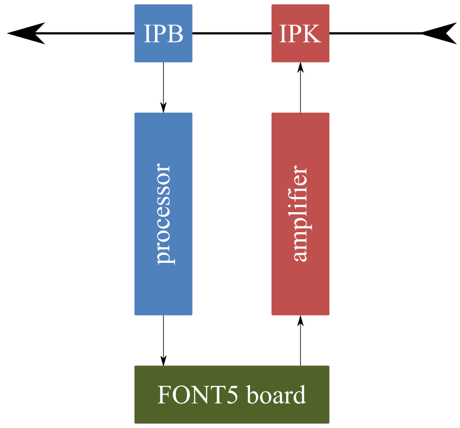

Figure 5.1: Simple block diagram of the IP feedback system.

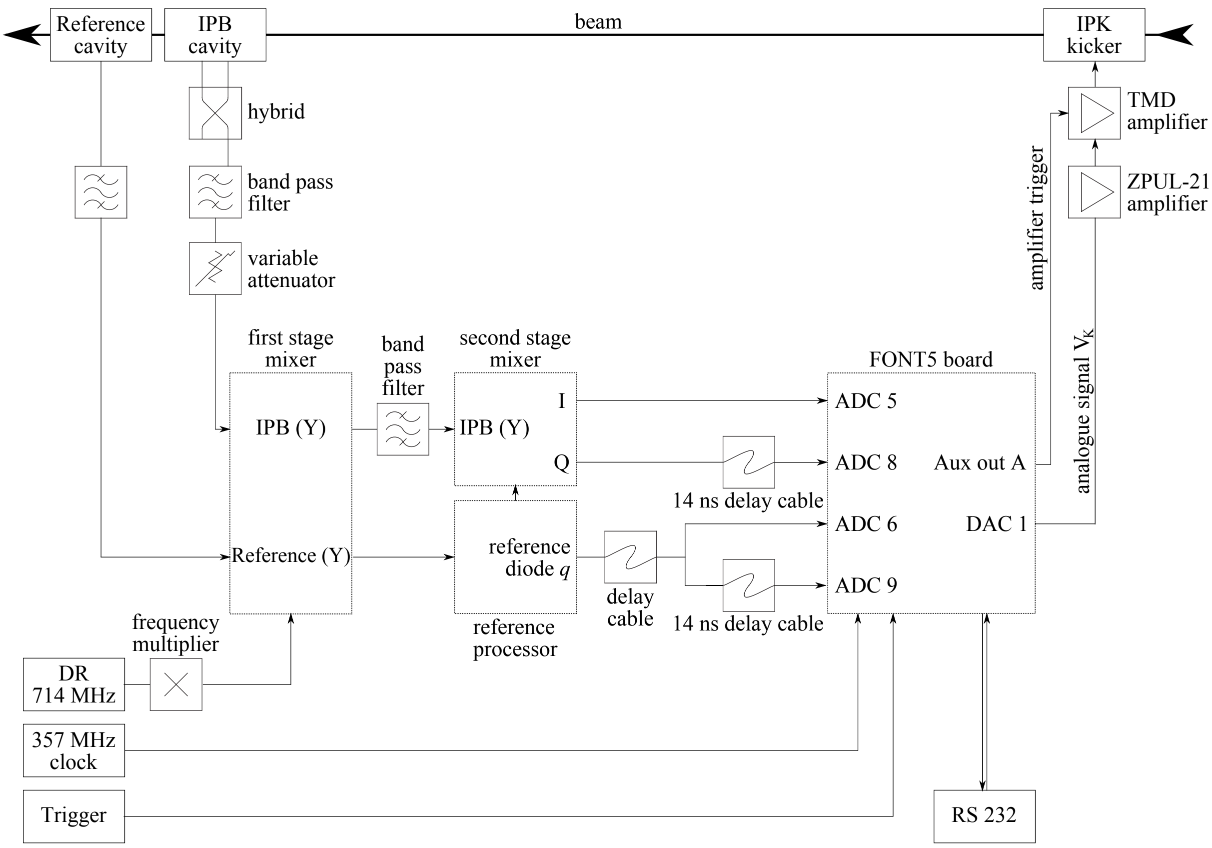

Figure 5.2: Detailed block diagram of the IP feedback system.

Table 5.1: Channel assignment for ADC channels involved in the feedback calculation on the FONT5 board for the upstream feedback and IP feedback set-ups.

ADC channel	Upstream feedback	IP feedback
5	P2 V_Δ	I
6	P2 V_Σ	q
8	P3 V_Δ	Q
9	P3 V_Σ	q

The outputs of the analogue signal processing are the baseband I and Q signals derived from the y ports of the IPB cavity, in addition to the reference diode signal used as a bunch charge q measurement. The I, Q and q signals are digitised by the FONT5 digital board; the particular ADC channels used and the requirement for delay cables are a consequence of the on-board FPGA firmware used and are discussed in Sec. 5.1.2. As presented in Sec. 2.5, the FONT5 board also requires a trigger (at the train repetition frequency), a fast clock at a frequency of 357 MHz (which establishes the sampling frequency) and a RS 232 serial interface for communication with the DAQ software.

As shown in Fig. 5.2, the FONT5 board generates an analogue output though the channel labelled DAC 1. This signal is ultimately applied to the IP kicker but is first amplified using the ZPUL-21 and TMD amplifiers described in Sec. 2.6. The trigger required for the TMD amplifier is generated by the FONT5 board through the 'Aux out A' digital output channel.

5.1.2 FONT5 board

As discussed in Sec. 5.1.1, the FONT5 digital board takes the analogue I, Q and q signals as inputs and generates an analogue output V_K to drive the IP kicker. The signal processing is done digitally on the FPGA using the firmware described in Sec. 2.5 but with the board's ADC channel assignment suitably selected.

Signals from four ADC channels constitute the input to the on-board feedback calculation. Table 5.1 shows the signals assigned to these channels when operating in the modes of upstream feedback and IP feedback. By substituting the signals used in the former case by those in the latter case, the on-board calculation in Eq. 2.33 becomes:

$$V_\mathrm{K} = G_1 \frac{I(t_1)}{q(t_1)} + G_2 \frac{Q(t_2)}{q(t_2)}, \tag{5.1}$$

where t_1, t_2 are the sampling times (or bunch strobes) for the corresponding signals and G_1, G_2 are pre-loaded gains. Due to the original firmware design, there is a requirement that $t_2 - t_1 \geq 14$ ns.

The linear combination of $\frac{I}{q}$ and $\frac{Q}{q}$ in Eq. 5.1 can be interpreted as the position of the first bunch (cf. Eq. 3.40); the voltage V_K of the kick applied to the second bunch is then set to remove the position offset measured in the first bunch. The method used to find the gain constants G_1, G_2 is explained in Sec. 5.1.4.

Table 5.2: Linear χ^2 fit gradients H for mean bunch 2 position at IPB versus constant DAC setting applied to IPK. The fits are applied to the data in the range between -400 and $+400$ DAC counts. The variable attenuator setting in the Honda electronics and the FONT5 board bunch 1 strobe setting are quoted. The first error represents the statistical uncertainty on the fit; the second error represents the systematic uncertainty due to the error on the BPM calibration (Sec. 3.6.3).

Attenuation (dB)	Bunch 1 strobe	H (μm/DAC)
10	8 samples early	$-0.01345 \pm 0.00005 \pm 0.00023$
10	On bunch 1	$-0.01422 \pm 0.00005 \pm 0.00024$
0	On bunch 1	$-0.01397 \pm 0.00003 \pm 0.00024$

Two features arise from the use of this particular firmware. Firstly, the charge q signal is used on both ADC channels 6 and 9 so the raw q signal is split to be used by both channels. Secondly, the required 14 ns interval between t_1 and t_2 is overcome by delaying the signals on ADC channels 8 and 9 using purpose-made 14 ns delay cables before the FONT5 board. This configuration is shown in the IP feedback block diagram in Fig. 5.2.

5.1.3 Kicker scan

As described in Sec. 2.7.2, the effect of the kick imparted by the kicker, as measured at the feedback BPM, can be determined by operating the kicker in constant DAC mode. Fig. 5.3 shows the effect of an IP kicker scan as measured at IPB, taken on 19 December 2014. The constant DAC setting is varied sequentially from -600 to $+600$ DAC counts in steps of 100 counts, and the mean measured position at IPB of the kicked second bunch is plotted for each setting. Apart from the use of the constant DAC mode, the set-up matches the one subsequently used for IP feedback: the variable attenuator (Fig. 5.2) is set to 0 dB and the bunch 1 strobe setting (that is, the time at which the ADC input signals are sampled) lies on the bunch 1 data.

The constant DAC scan shows a linear response for DAC settings between -400 and $+400$ counts with a corresponding kick dynamic range of ± 5 μm. The clear non-linearity at the edges of the scan is attributed to kicker amplifier saturation. A linear χ^2 fit is applied to the data in the linear range, giving a kicker calibration constant H of $-0.01397 \pm 0.00003 \pm 0.00024$ μm/DAC, where the first error is the statistical uncertainty on the fit and the second error is the systematic uncertainty due to the error on the BPM calibration (Sec. 3.6.3). A negligible beam drift, contributing -0.00006 μm/DAC, is deduced from the mean position drift of the first bunch, which is not being kicked.

Further kicker scans performed with the variable attenuator in the Honda electronics set to 10 dB are useful to test the consistency of the kicker calibrations. The results are presented in Table 5.2. In each case, the fit is only applied to the DAC settings in the range between -400 and $+400$ DAC counts.

Two entries are included with 10 dB data, obtained with different bunch 1 strobe settings.

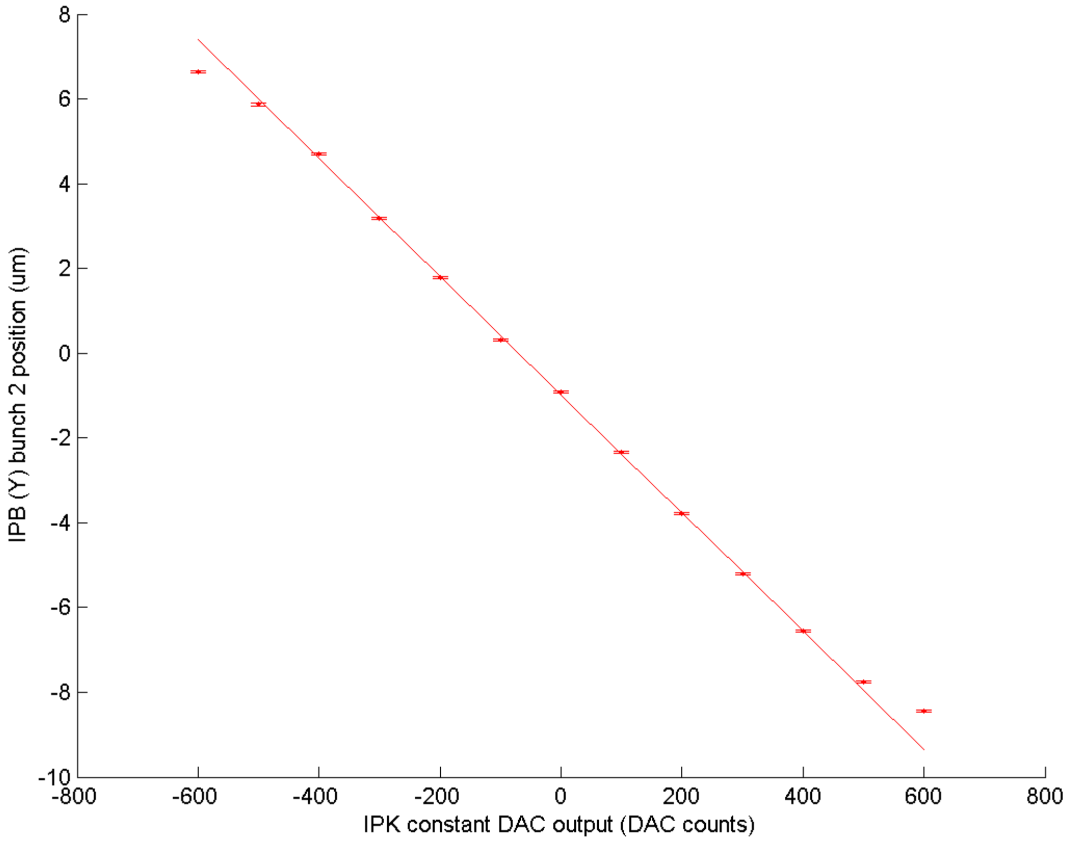

Figure 5.3: Mean bunch 2 position at IPB versus constant DAC setting applied to IPK. Standard errors are given. The line shows the result of a linear χ^2 fit to the data in the range between -400 and $+400$ DAC counts.

The top entry is obtained with the bunch 1 strobe set 8 samples (22.4 ns) before the strobe setting used for IP feedback. With a strobe setting 8 samples early, the DAC output too is generated 8 samples earlier. The second entry is obtained with the bunch 1 strobe setting as used for IP feedback. The χ^2 fit gradients for the two entries at 10 dB are similar indicating that the kicker signal rise is completed in time to kick the second bunch in both cases.

Table 5.2 also shows that comparable χ^2 fit gradients are obtained whilst operating the Honda electronics at 0 and 10 dB. The gradients agree to within the systematic errors.

5.1.4 Gain calculation

The measured bunch 1 position y_{m} (in µm) at the feedback BPM is given by Eq. 3.40:

$$y_{\mathrm{m}} = \frac{1}{k}\left(\frac{I}{q}\cos\theta_{IQ} + \frac{Q}{q}\sin\theta_{IQ}\right), \tag{5.2}$$

where k is the BPM calibration factor in units of (ADC/ADC)/µm. Operating on the assumption that the bunch positions within a train are fully correlated, the feedback acts by applying a kick y_{K} (in µm) correcting the beam position at the feedback BPM:

$$y_{\mathrm{K}} = -y_{\mathrm{m}} = -\frac{1}{k}\left(\frac{I}{q}\cos\theta_{IQ} + \frac{Q}{q}\sin\theta_{IQ}\right). \tag{5.3}$$

The required kick V_{K} in DAC counts can be evaluated by using the kicker calibration constant H in units of µm/DAC obtained as described in Sec. 5.1.3. Thus,

$$V_{\mathrm{K}} = \frac{y_{\mathrm{K}}}{H} = -\frac{1}{Hk}\left(\frac{I}{q}\cos\theta_{IQ} + \frac{Q}{q}\sin\theta_{IQ}\right). \tag{5.4}$$

Comparing Eqs. 5.1 and 5.4 gives the required feedback gains G_1 and G_2:

$$G_1 = -\frac{\cos\theta_{IQ}}{Hk}; \tag{5.5}$$

$$G_2 = -\frac{\sin\theta_{IQ}}{Hk}. \tag{5.6}$$

The product Hk has units of (ADC/ADC)/DAC and corresponds to the gradient of $\frac{I'}{q}$ versus DAC setting in a kicker scan; in practice this quantity is calculated directly from a bunch 2 kicker scan.

5.1.5 Resolution limit on feedback performance

The position jitter of the second bunch σ_{Y_2} that can be attained after an optimally-functioning feedback correction can be predicted using the mathematical treatment in Sec. 2.7.1.

Assuming that both incoming bunches have the same position jitter σ_y with a bunch-to-bunch position correlation ρ_{12}, Eq. 2.36 becomes:

$$\sigma_{Y_2}^2 = 2\sigma_y^2(1 - \rho_{12}). \tag{5.7}$$

The resolution of the feedback BPM, σ_r, will set a lower limit to the stabilised bunch jitter σ_{Y_2} that can be achieved. This limit corresponds to the case where the true beam jitter is much smaller than the BPM resolution, in which case, the measured incoming beam jitter $\sigma_y = \sigma_\mathrm{r}$ (Sec. 4.4) and $\rho_{12} = 0$, giving:

$$\sigma_{Y_2} = \sqrt{2}\sigma_\mathrm{r}. \tag{5.8}$$

5.1.6 Previous results

Previous beam tests of the IP feedback system employed one of the BPMs in the IP BPM doublet removed in July 2013. The system was used to stabilise the beam position jitter to 102 ± 5 nm [56]. The results presented in the following sections show how the commissioning and optimisation of the new IP BPMs, discussed in Chapters 3 and 4, have enabled the level of beam stabilisation to be improved.

5.2 IP feedback results

The IP feedback system has been operated on a number of dedicated ATF shifts. The results presented below were obtained on 19 December 2014, with the IP BPM system optimised as described in Chapters 3 and 4.

ATF was operated in two-bunch mode with a bunch spacing of 215.6 ns. The y beam waist was placed close to IPB in order to use it as the feedback BPM. Both bunches in IPB were calibrated following the procedure detailed in Sec. 3.6.3 and IP kicker scans were performed as presented in Sec. 5.1.3. The beam was centred relative to the BPM following the procedures described in Sec. 4.1.1. Included here are the results obtained with the variable attenuator in the Honda electronics set to 0 dB, corresponding to the best BPM resolution setting. The IP feedback analysis presented in this chapter is performed with single-point sampling by using the same sample numbers as used on shift by the feedback firmware, as the performance of the feedback is constrained by the position information available to the FONT5 feedback system.

In the discussion below, a feedback run consists of 200 triggers, each trigger containing a two-bunch train. As discussed in Sec. 2.7.1, the feedback is operated in interleaved mode: alternate trains are set to have feedback on or off. Thus, a run contains 100 triggers with feedback on and a similar number with feedback off.

Scans were performed to assess the performance of the feedback system as a function of two variables. The first variable relates to the longitudinal waist position and is adjusted

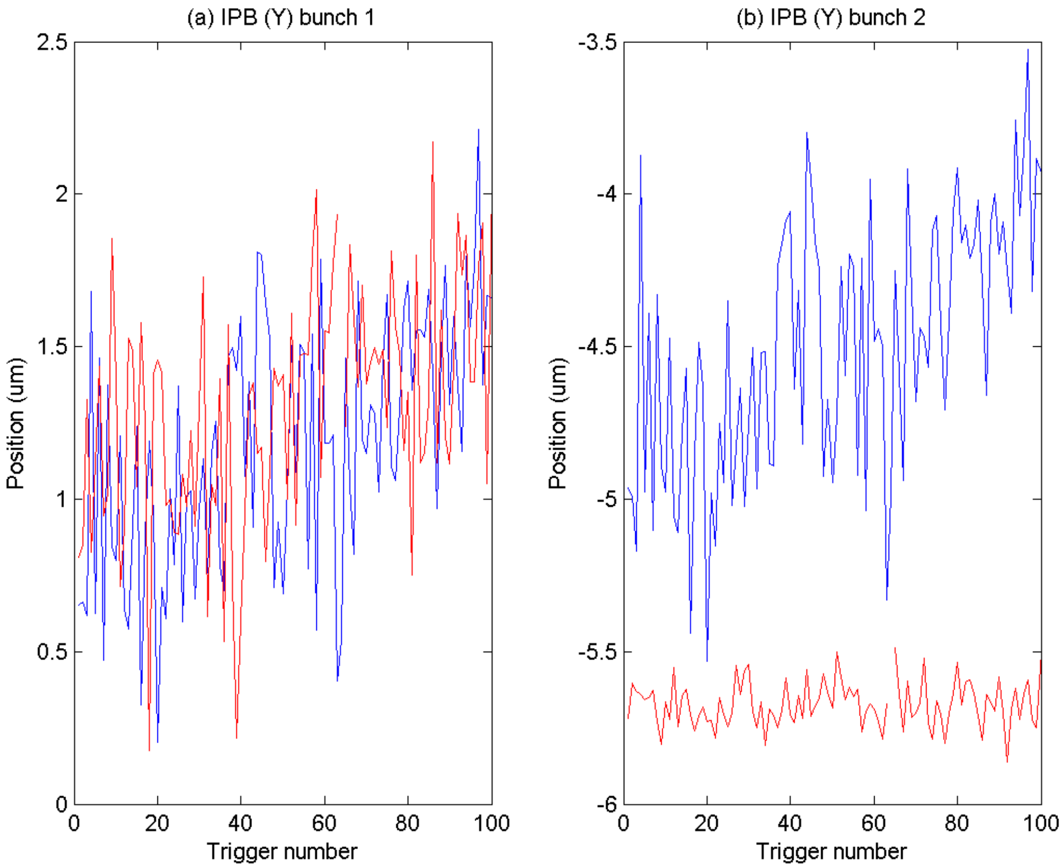

Figure 5.4: Measured vertical position at IPB versus trigger number for (a) the first bunch and (b) the second bunch, with feedback off (blue) and feedback on (red).

by applying changes to the QD0FF current; the results from this scan are presented in Sec. 5.3. The second involves correcting the mean vertical position of the second bunch at IPB, adjusted by applying a constant kick in addition to the feedback correction; the outcome is shown in Sec. 5.4.

For illustration, the results of a feedback run, taken with a QD0FF current of 137.4 A, are discussed in detail. The effect of the feedback is displayed in the plots of position versus trigger number in Fig. 5.4. The feedback off and on traces in Fig. 5.4(a) overlap as the first bunch is only measured but not corrected. Note that in addition to trigger-to-trigger jitter a slower position drift is also apparent over the scan.

The second bunch position with feedback off in Fig. 5.4(b) shows a similar dependence to that of the first bunch as a result of the high bunch-to-bunch position correlation. The position of the second bunch with feedback on displays how the feedback acts to stabilise the beam. As intended, the trigger-to-trigger jitter is reduced and the slow drift is removed.

The reduction in position jitter is apparent in the position distributions presented in Fig. 5.5, obtained for the same feedback run. The measured mean position and jitter are reported in Table 5.3. The feedback reduces the incoming beam jitter of ~ 400 nm down to 74 ± 5 nm, demonstrating sub-100 nm beam stabilisation.

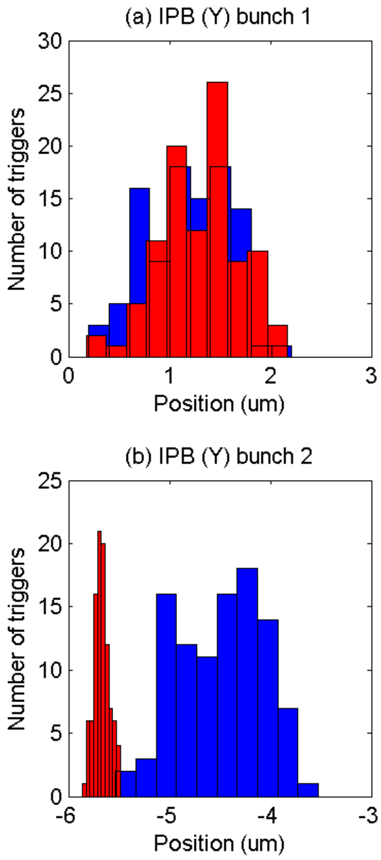

Figure 5.5: Distributions of positions measured at IPB for (a) the first bunch and (b) the second bunch, with feedback off (blue) and feedback on (red).

Table 5.3: Mean position and jitter with feedback off and on for bunches 1 and 2 at IPB. Standard errors on the mean and jitter are given.

	Mean position (µm)		Position jitter (nm)	
Bunch	Feedback off	Feedback on	Feedback off	Feedback on
1	$+1.18 \pm 0.04$	$+1.30 \pm 0.04$	412 ± 29	389 ± 28
2	-4.50 ± 0.04	-5.67 ± 0.01	420 ± 30	74 ± 5

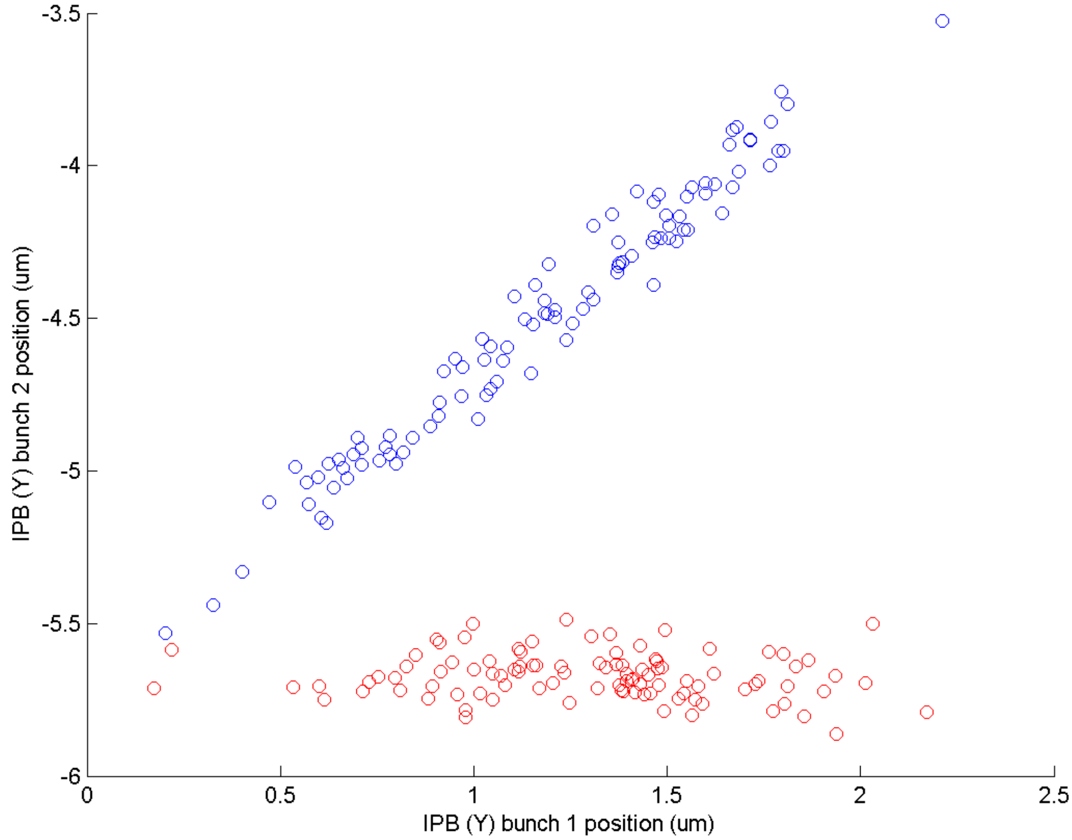

Figure 5.6: Bunch 2 position versus bunch 1 position measured at IPB with feedback off (blue) and feedback on (red).

Fig. 5.5 shows how the feedback kicks the second bunch away from zero. This is a consequence of the fixed bunch-to-bunch position offset: the first bunch has positive positions whilst the second one has negative positions. The feedback uses the first bunch position to determine the kick; in this case, the kick is towards negative positions at the feedback BPM, as observed. The bunch-to-bunch position offset is a consequence of the different trajectories of the two bunches along the accelerator. The different bunch orbits may be due to a difference in the kick imparted by the extraction kicker between the ATF DR and the extraction line. The constant bunch offset can be taken out by adding a constant kick to the second bunch in addition to the feedback correction; the application of this kick is addressed in Sec. 5.4.

A high bunch-to-bunch position correlation is required for a successful feedback operation. Fig. 5.6 shows the bunch 2 position versus bunch 1 position for this data set. The points with feedback off represent the bunch-to-bunch position correlation that can be corrected by the feedback. The feedback then acts to remove the correlated position component, removing the correlation and reducing the position jitter. The measured bunch-to-bunch position correlation, without and with feedback, is given in Table 5.4.

Following Sec. 2.7.1, the expected position jitter attainable by a perfect feedback system

Table 5.4: Position correlation ρ_{12} of bunch 1 to bunch 2 measured at IPB with feedback off and on. The errors on ρ_{12} correspond to 68.3 % confidence intervals.

Feedback	ρ_{12} (%)
Off	$+98.2^{+0.3}_{-0.4}$
On	-13 ± 10

can be calculated. Applying Eq. 2.36 to this data set gives an expected bunch jitter of $\sigma_{Y_2} = 79.6$ nm. This agrees with the measured jitter of 74 ± 5 nm indicating that the feedback and kicker system are working well.

5.3 Waist scan

As discussed in Sec. 4.1.2, the waist position can be shifted longitudinally by varying the QD0FF current. Scanning the QD0FF current sequentially from 136.2 A to 137.4 A in steps of 0.2 A allows the y waist to be moved longitudinally through IPB. An interleaved feedback run was taken at each QD0FF current setting.

Fig. 5.7 shows the mean position and jitter for the first bunch. The distributions with feedback off and on overlap as the first bunch is not corrected by the feedback. The vertical position of the first bunch was re-centred at each setting using the techniques described in Sec. 4.1.1. The minimum jitter is measured at a QD0FF current of 136.8 A, corresponding to the waist located at IPB.

The effect of the feedback on the second bunch is shown in Fig. 5.8. Fig. 5.8(a) shows the variation in the mean position of the second bunch as a function of the QD0FF setting. An offset between the position of bunch 1 and bunch 2 is observed; this offset depends on the QD0FF current setting. The origin of this dependence can be understood by propagating the bunch orbits from the upstream stripline BPMs P2 and P3 to the IP region using the MAD model (Sec. 2.8): the two bunches follow different orbits through QD0FF but are focused to approximately the same point at the waist. Thus, the bunch-to-bunch position offset is approximately zero at the waist but scales linearly with the longitudinal distance from the waist.

Fig. 5.8(a) also shows the mean position of the second bunch with feedback on across the scan. The feedback consistently kicks the second bunch towards negative positions. As noted in Sec. 5.2, this is due to the positive position of the first bunch which constitutes the basis for the correction of the second bunch.

Fig. 5.8(b) presents the second bunch jitter across the scan. As discussed in Sec. 5.2, the results with feedback off show a similar dependence as observed for the first bunch. The position jitter is then reduced when the feedback is operated. Table 5.5 gives the feedback off and on position jitters for both bunches across the scan. The expected jitter with the feedback on can be computed using the uncorrected beam jitter and bunch-to-bunch position correlation in Eq. 2.36. It is shown in Fig. 5.8(b) and, together with the feedback off bunch-

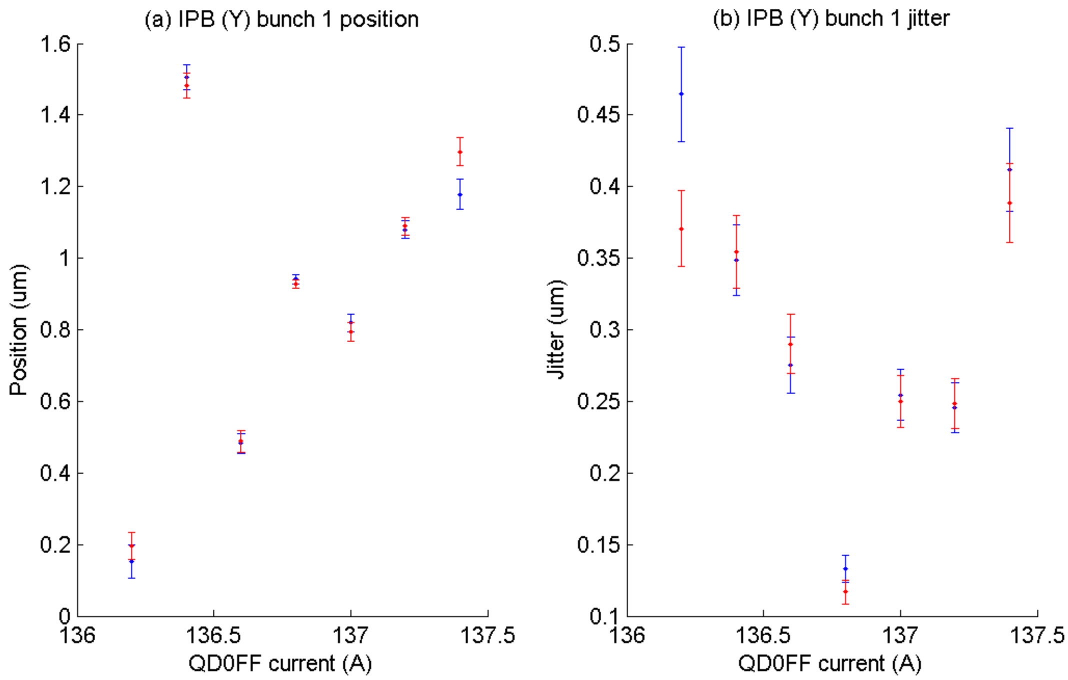

Figure 5.7: (a) Mean position and (b) position jitter for bunch 1 at IPB with feedback off (blue) and feedback on (red) versus QD0FF current setting. Standard errors on the mean and jitter are given.

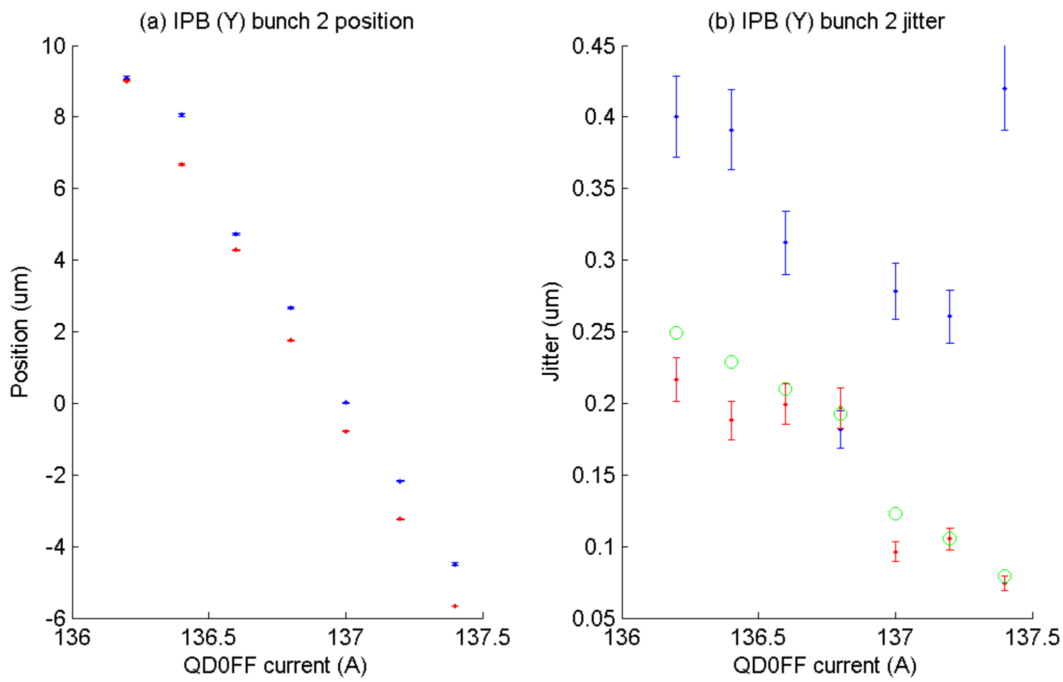

Figure 5.8: (a) Mean position and (b) position jitter for bunch 2 at IPB with feedback off (blue) and feedback on (red) versus QD0FF current setting. Standard errors on the mean and jitter are given. The green circles in (b) represent the predictions for the feedback-on position jitter based on the incoming jitter and bunch-to-bunch correlation using Eq. 2.36.

Table 5.5: Position jitter measured at IPB with feedback off and on for bunches 1 and 2 over the range of QD0FF current settings. Standard errors are given.

	Position jitter (nm)			
	Bunch 1		Bunch 2	
QD0FF current (A)	Feedback off	Feedback on	Feedback off	Feedback on
136.2	465 ± 33	371 ± 26	400 ± 28	217 ± 15
136.4	349 ± 25	354 ± 25	391 ± 28	188 ± 13
136.6	275 ± 20	290 ± 21	312 ± 22	200 ± 14
136.8	133 ± 9	117 ± 8	182 ± 13	197 ± 14
137.0	255 ± 18	250 ± 18	278 ± 20	96 ± 7
137.2	245 ± 17	248 ± 18	261 ± 18	105 ± 7
137.4	412 ± 29	389 ± 28	420 ± 30	74 ± 5

Table 5.6: Position correlation of bunch 1 to bunch 2 with feedback off, ρ_{12}, and predicted position jitter with feedback on, $\sigma(Y_2^{\text{pred}})$, at IPB over the range of QD0FF current settings. The prediction is based on the incoming jitter and bunch-to-bunch correlation using Eq. 2.36. The errors on ρ_{12} correspond to 68.3 % confidence intervals.

QD0FF current (A)	ρ_{12} (%)	$\sigma(Y_2^{\text{pred}})$ (nm)
136.2	$84.4^{+3.2}_{-2.7}$	249
136.4	$81.4^{+3.7}_{-3.1}$	229
136.6	$75.1^{+4.8}_{-4.1}$	210
136.8	$28.3^{+9.7}_{-9.1}$	192
137.0	$89.8^{+2.2}_{-1.8}$	123
137.2	$91.5^{+1.8}_{-1.5}$	105
137.4	$98.2^{+0.4}_{-0.3}$	80

to-bunch position correlation, in Table 5.6.

The results show that the feedback successfully reduces the position jitter to the expected level given the measured incoming beam conditions. This agreement demonstrates that the feedback system is functioning optimally. However, the corrected jitter experiences a marked improvement over the course of the scan, from over 200 nm at the start to under 100 nm at the end. The enhancement in the performance is a consequence of an improvement in the incoming beam conditions as measured at IPB.

The analysis of the beam conditions is complicated by the fact that the beam jitter at the BPM is intrinsically varied over a QD0FF current scan. As the beam jitter becomes smaller, the BPM resolution becomes more significant compared to the spread of positions being measured. Hence, the measured bunch-to-bunch position correlation appears to degrade when operating with smaller jitters even if the real beam bunch-to-bunch correlation is constant. The degradation in the measured bunch-to-bunch correlation ρ_{12} is observed in Table 5.6 at a QD0FF current setting of 136.8 A when the waist is at IPB.

By comparing two feedback runs with comparable uncorrected jitter, a meaningful result on the measured bunch-to-bunch position correlation can be extracted. Both QD0FF settings of 136.2 A and 137.4 A produce an uncorrected position jitter of $\sim$ 400 nm at IPB. Table 5.6 shows that the measured bunch-to-bunch position correlation increases significantly from $84.4^{+3.2}_{-2.7}$ % to $98.2^{+0.4}_{-0.3}$ % between the two runs.

It is necessary to establish whether the change in the measured bunch-to-bunch correlation may have been adversely affected by a change in BPM performance. As discussed in Sec. 4.4.5, the bunch charge and phase have been seen to affect the BPM position measurement. For this reason, the variation of these two bunch parameters over the course of the QD0FF current scan is studied in Sec. 5.3.1 and 5.3.2.

5.3.1 Dependence on bunch charge

As noted in Sec. 4.5.2, the BPM resolution scales inversely with the bunch charge so it is important to monitor the charge variation over the course of a scan. The mean bunch charge at each setting in the QD0FF current scan is shown in Fig. 5.9(a) and (b) measured using the reference diode signal and the upstream stripline BPM P2 V_Σ signal. The mean charge of the given setting is expressed as a fraction of the mean charge across the whole scan in order to allow the variation of the two sets of charge measurements to be compared. The results show that the mean bunch charge at the different settings varies by $\sim$ 1 % regardless of the charge measurement used, and the variation tracks between the two bunches. As the charge variation is small, the BPM resolution is expected to remain approximately constant over the scan.

Fig. 5.9(c) and (d) show the variation of the charge jitter across the scan. Once again, a consistent charge jitter of $\sim$ 1 % is observed across the scan for measurements by both the reference cavity and the stripline BPM. A higher charge jitter is observed for the QD0FF current setting of 136.2 A; its cause is associated with a $\sim$ 5 % step change in the charge measured by the reference cavity during the feedback run. Even if charge fluctuations were degrading the BPM resolution, the approximately constant charge jitter across the scan suggests that the BPM performance should be maintained for the duration of the scan.

The bunch-to-bunch charge correlation across the scan is shown in Fig. 5.10. In the absence of slow charge drifts, no bunch-to-bunch charge correlation is expected as bunches are generated independently by the electron source (Sec. 2.2). The QD0FF current settings reporting a larger bunch-to-bunch charge correlation are also those reporting a greater charge jitter; these observations are associated to a larger correlated charge drift common to both bunches. A higher charge correlation is measured using the reference diode that may result from a measurement error common to both bunches. Contamination of the second bunch signal by signal from the first bunch is expected to be small given the fast decay time of the cavities.

Therefore, the results in Figs. 5.9 and 5.10 indicate a high degree of charge stability over the duration of the QD0FF current scan. No trend is observed in the charge measurements that can be related to the steady improvement in the feedback performance across the

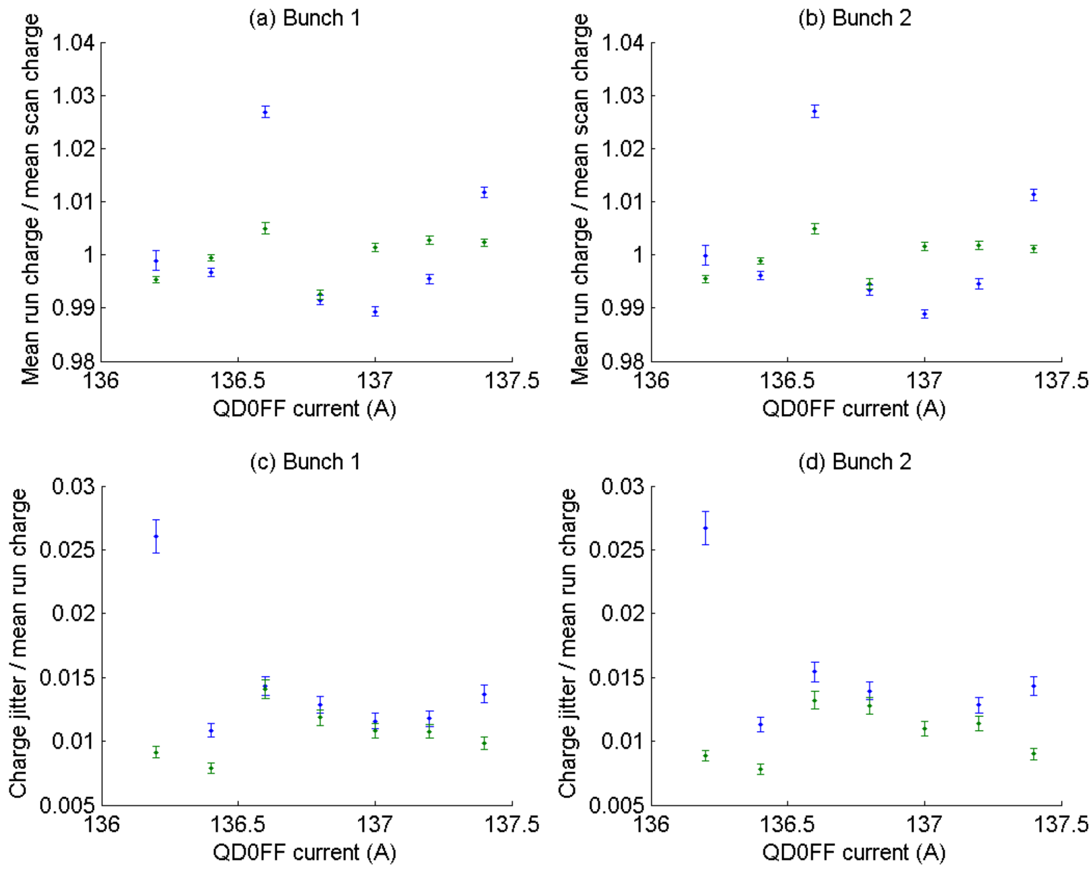

Figure 5.9: Mean charge at each setting (as a fraction of the mean charge across all settings) versus QD0FF current setting for (a) bunch 1 and (b) bunch 2; and charge jitter at each setting (as a fraction of the mean charge at the given setting) versus QD0FF current setting for (c) bunch 1 and (d) bunch 2. The bunch charge is measured using the reference diode (blue) and the stripline BPM P2 V_Σ (green). Standard errors are given.

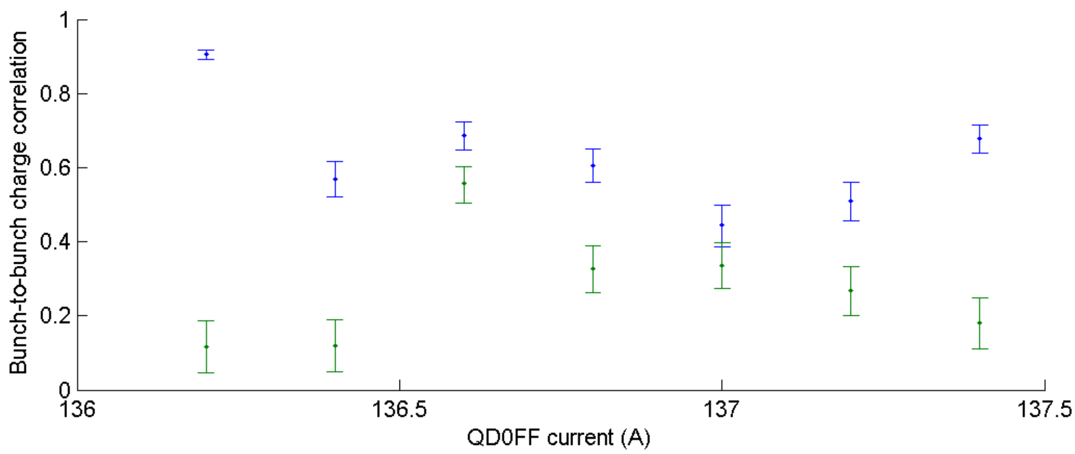

Figure 5.10: Bunch-to-bunch charge correlation versus QD0FF current. The bunch charge is measured using the reference diode (blue) and the stripline BPM P2 V_Σ (green). Standard errors are given.

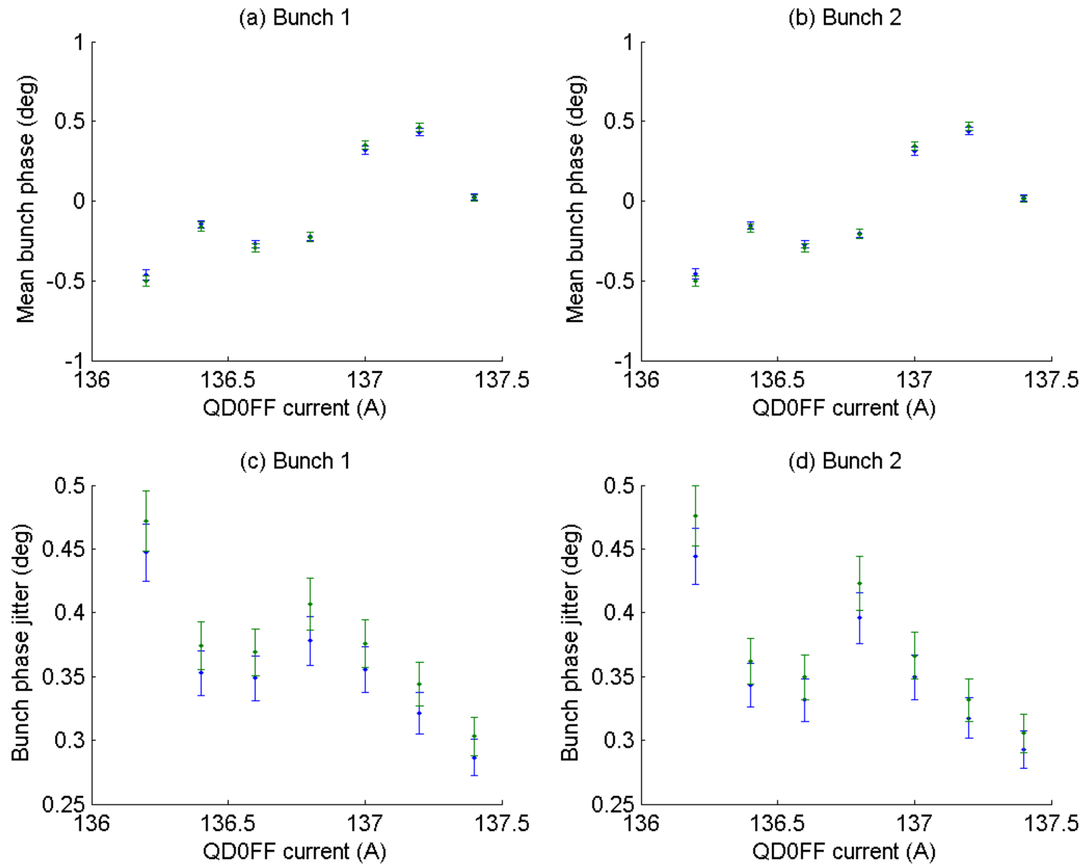

Figure 5.11: Mean bunch phase versus QD0FF current for (a) bunch 1 and (b) bunch 2; and bunch phase jitter versus QD0FF current for (c) bunch 1 and (d) bunch 2. The bunch phase is measured at the stripline BPMs P2 (blue) and P3 (green). Standard errors are given.

QD0FF current scan.

5.3.2 Dependence on bunch phase

As the beam position measurement has been found to be affected by the bunch phase (Sec. 4.4.5), the variation of the bunch phase over the course of the QD0FF current scan is studied to assess whether it is responsible for the change in the feedback performance across the scan. The bunch phase is measured at the upstream stripline BPMs P2 and P3, and the variation of the mean phase and phase jitter is shown in Fig. 5.11. A bunch phase jitter in the region of 0.3° to 0.4°, as well as a slow drift in the mean phase, are measured; both of these observations agree with measurements documented in the past [53].

A modest reduction in bunch phase jitter is observed over the course of the scan. This reduction does not appear sufficient to explain an improvement in the BPM performance. In particular, subsequent feedback runs discussed in Sec. 5.4 achieve successful beam stabilisation to under 100 nm whilst operating with bunch phase jitters of 0.4°. Therefore, the BPM resolution appears not to be affected by the small variation in bunch phase jitter observed over the scan.

5.4 Bunch 2 constant kick scan

The feedback firmware can be used to apply a constant kick to the second bunch which adds to the kick calculated by the feedback algorithm [51] and allows any static offset between the two bunches to be removed. The constant kick is represented by δ_2 in Eq. 2.35 and is set through the DAQ in units of DAC counts.

The δ_2 offset was varied from 0 to -700 DAC counts in order to find the setting required to centre the kicked second bunch in IPB, and to assess whether the feedback performance is maintained on applying the δ_2 offset. Fig. 5.12 shows the mean position and jitter of the first bunch for the range of δ_2 offset settings. All measurements are obtained with a QD0FF current of 137.4 A. The results at an offset setting of 0 correspond to data obtained as part of the QD0FF current scan discussed in Sec. 5.3 and is included here for comparison. No dependence is observed across Fig. 5.12 as neither the feedback correction nor the constant kick are applied to the first bunch.

The mean position and jitter for the second bunch is presented in Fig. 5.13. Feedback is operated in interleaved mode and the δ_2 offset setting is only applied when the feedback is on. As the first bunch is approximately centred the kick generated from the feedback calculation alone is in the region of 1 µm at IPB. The larger kick applied at non-zero δ_2 offset settings illustrates the effect of the constant kick. The second bunch is centred at a δ_2 offset setting of approximately -400 DAC counts.

The performance of the feedback across the scan can be studied from the jitter levels with feedback off and on shown in Fig. 5.13(b). The uncorrected beam jitter is $\sim$ 400 nm; the feedback acts to stabilise it to $\sim$ 80 nm. The jitter measured for each feedback run is shown in Table 5.7.

Table 5.8 shows the measured bunch-to-bunch position correlation with feedback off and, hence, the predicted position jitter with feedback on. The results show that a high bunch-to-bunch position correlation of over 97 % is sustained over the duration of the scan. The resulting expected corrected jitter is therefore also maintained at a constant level of between 71 and 84 nm.

The results in Fig. 5.13 show that the expected level of correction is attained for δ_2 offset settings between -500 and 0 DAC counts. The degraded performance at the δ_2 offset settings of -700 and -600 DAC counts can be explained in terms of the non-linear performance of the kicker system when the kicker amplifier is overdriven. As discussed in Sec. 5.1.3, the linear dynamic range of the kicker system corresponds to DAC output settings in the range of -400 to $+400$ DAC counts. Fig. 5.14 shows the DAC output issued for all 2-bunch trains as a function of offset setting. It can be seen that at δ_2 offset settings of -700 and -600 DAC counts, the DAC output lies outside the range of -400 to $+400$ DAC counts. Operating the kicker system outside its linear dynamic range gives rise to a suppressed output and an insufficient feedback correction.

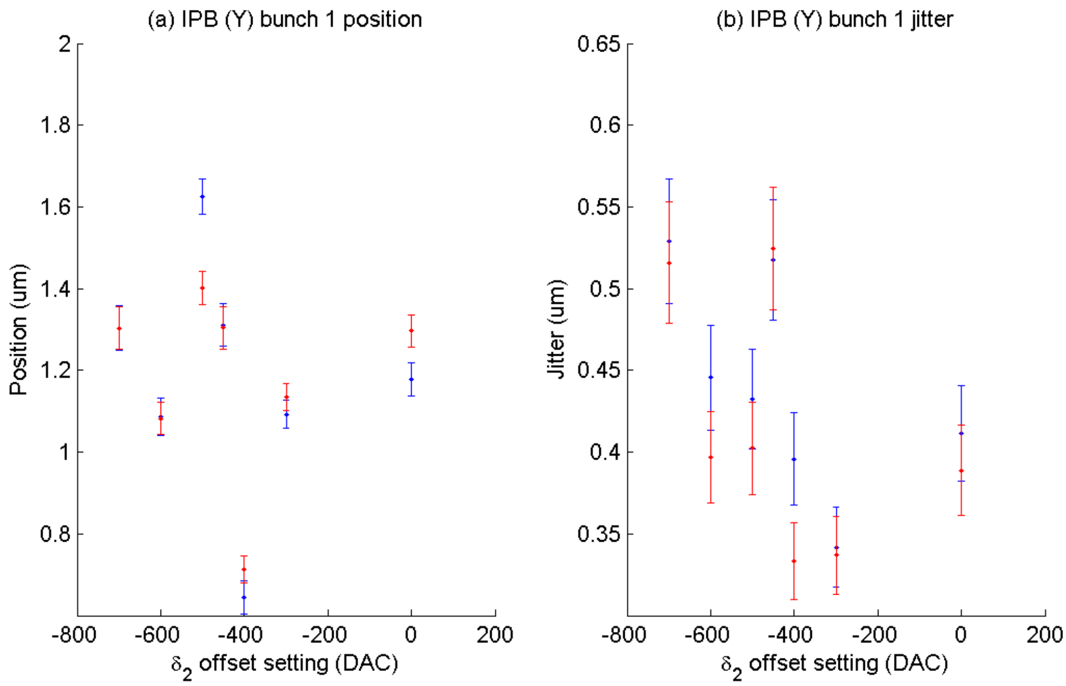

Figure 5.12: (a) Mean position and (b) position jitter for bunch 1 at IPB with feedback off (blue) and feedback on (red) versus δ_2 offset setting. Standard errors on the mean and jitter are given.

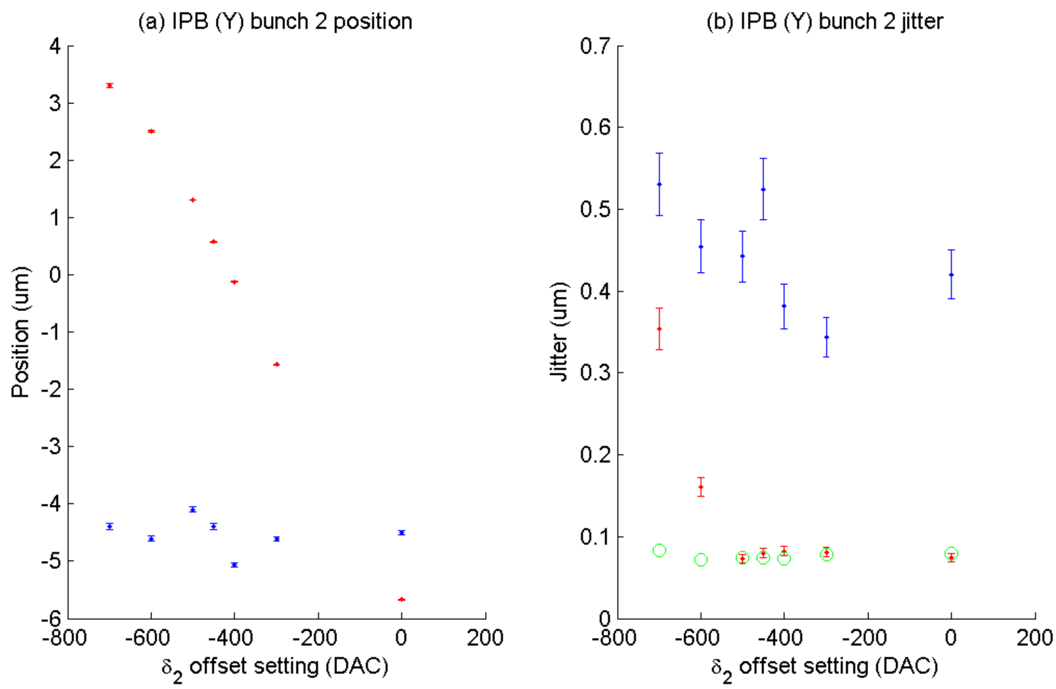

Figure 5.13: (a) Mean position and (b) position jitter for bunch 2 at IPB with feedback off (blue) and feedback on (red) versus δ_2 offset setting. Standard errors on the mean and jitter are given. The green circles in (b) represent the predictions for the feedback-on position jitter based on the incoming jitter and bunch-to-bunch correlation using Eq. 2.36.

Table 5.7: Position jitter measured at IPB with feedback off and on for both bunches over the range of δ_2 offset settings. Standard errors are given. The δ_2 offset setting is only applied when the feedback is on.

	Position jitter (nm)			
	Bunch 1		Bunch 2	
δ_2 (DAC)	Feedback off	Feedback on	Feedback off	Feedback on
-700	529 ± 38	516 ± 37	530 ± 38	354 ± 25
-600	446 ± 32	397 ± 28	454 ± 32	161 ± 11
-500	432 ± 31	402 ± 28	442 ± 31	73 ± 5
-450	518 ± 37	525 ± 37	525 ± 37	80 ± 6
-400	396 ± 28	333 ± 23	382 ± 27	83 ± 6
-300	342 ± 24	337 ± 24	344 ± 24	81 ± 6
0	412 ± 29	389 ± 28	420 ± 30	74 ± 5

Table 5.8: Position correlation of bunch 1 to bunch 2 with feedback off, ρ_{12}, and predicted position jitter with feedback on, $\sigma(Y_2^{\mathrm{pred}})$, at IPB over the range of δ_2 offset settings. The prediction is based on the incoming jitter and bunch-to-bunch correlation using Eq. 2.36. The errors on ρ_{12} correspond to 68.3 % confidence intervals.

δ_2 (DAC)	ρ_{12} (%)	$\sigma(Y_2^{\mathrm{pred}})$ (nm)
-700	$98.8^{+0.3}_{-0.2}$	84
-600	$98.8^{+0.3}_{-0.2}$	71
-500	$98.6^{+0.3}_{-0.3}$	74
-450	$99.0^{+0.2}_{-0.2}$	75
-400	$98.3^{+0.4}_{-0.3}$	73
-300	$97.4^{+0.6}_{-0.5}$	78
0	$98.2^{+0.4}_{-0.3}$	80

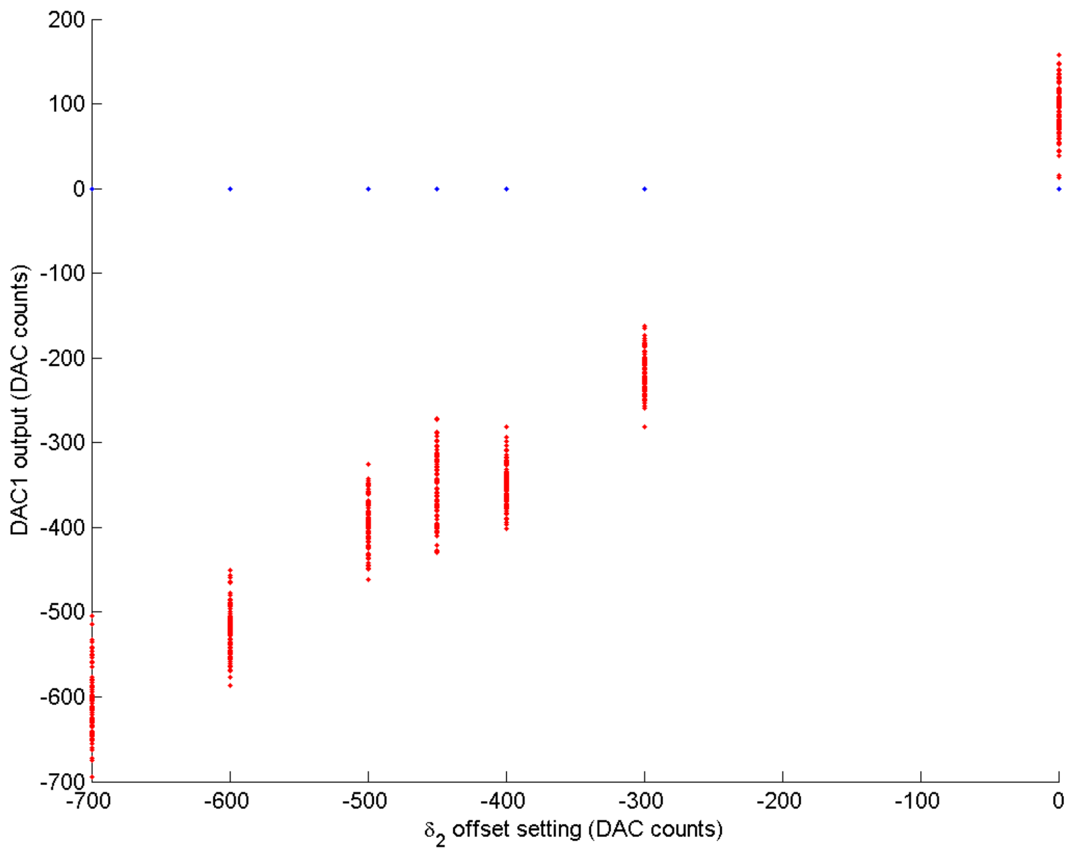

Figure 5.14: DAC1 output for all 2-bunch trains with feedback off (blue) and feedback on (red) versus δ_2 offset setting.

Table 5.9: Mean position and jitter measured at IPB with feedback off and δ_2 offset off and on for both bunches. The δ_2 offset applied is −450 DAC counts. Standard errors on the mean and jitter are given.

	Mean position (µm)		Position jitter (nm)	
Bunch	Kick off	Kick on	Kick off	Kick on
1	$+1.55 \pm 0.04$	$+1.45 \pm 0.04$	375 ± 27	392 ± 28
2	-4.22 ± 0.04	$+2.04 \pm 0.04$	373 ± 27	411 ± 29

It is important to ensure that the application of the δ_2 offset alone, in the absence of the feedback correction, only shifts the position of the second bunch but does not affect the position jitter. For this reason, a dedicated run was taken with a δ_2 offset setting of −450 DAC counts whilst setting the feedback gains G_1, G_2 to zero, effectively turning the feedback correction off. The results are shown in Table 5.9. The second bunch is kicked by ~ 6 µm but no reduction in jitter is observed.

Therefore, the feedback is seen to stabilise the beam over a range of δ_2 offset settings determined by the linear range of the kicker. The kicker dynamic range, deduced from the kicker scans in Sec. 5.1.3, has been measured to be ±5 µm; this dynamic range is over an order of magnitude larger than the uncorrected jitter expected at the beam waist. When the system is operated within its linear range, a sustained feedback stabilisation of between 73 ± 5 and 83 ± 6 nm is achieved.

5.5 Summary

This chapter has presented the operating principles and results of the IP feedback system. The IP kicker was exercised, demonstrating a linear response over a kick dynamic range of ±5 µm as measured at IPB. The feedback system has achieved beam stabilisation at the 75 nm level which constitutes a significant improvement on the 100 nm level achieved previously. This level of correction is consistent with a BPM resolution of ~ 50 nm (Eq. 5.8). The incoming beam position jitter was varied at IPB and the level of beam stabilisation matched the expectation given the measured incoming beam conditions. The static position offset between the first and second bunches in each train was successfully removed and a sustained feedback stabilisation of between 73 ± 5 and 83 ± 6 nm was achieved over the ±5 µm linear dynamic range.

Chapter 6

Conclusions

6.1 Summary

Following the discovery of a particle consistent with the Higgs boson at the LHC, the case for a linear lepton collider to study its properties has been demonstrated. In order to achieve a high luminosity, the design of the next generation linear electron-positron collider, such as the ILC, calls for a vertical beam size of only a few nanometres at the IP. As ground motion of up to the order of tens of nanometres is expected at the timescale of the train repetition frequency, the need for an intra-train feedback system is essential to achieve and maintain the required luminosity.

The FONT group has developed a prototype intra-train feedback system for use at such single-pass accelerators. Two FONT feedback systems have been commissioned at ATF and the operation, optimisation and performance of these systems is the subject of this thesis. The two systems have been operated in turn and the results from both are summarised below. In each case, the accelerator is operated with two-bunch trains with a bunch separation of around 200 ns, allowing the first bunch to be measured and the orbit of the second bunch to then be corrected. These systems would be suitable for the ILC whose design bunch spacing is 554 ns for a centre-of-mass collision energy of 500 GeV.

The first system, referred to as upstream feedback, consists of a coupled loop system where two stripline BPMs are used to characterise the incoming beam position and angle, and two kickers are used to stabilise the beam. The challenge in this system is the ability to provide a correction that then propagates downstream through the accelerator. The second system, described as IP feedback, consists of a beam position measurement at the IP that is used to drive a kicker to provide a local correction. Due to the sub-100 nm position jitter at the IP, the difficulty of this feedback system is to achieve the required BPM resolution to resolve and correct the beam jitter.

The performance of the upstream feedback system has been analysed both at the feedback BPMs and its propagation to the stripline BPM MFB1FF located 30 metres downstream. A factor ~ 3 reduction in position jitter has been demonstrated at the feedback BPMs, in line with the expectation given the measured incoming beam jitter and bunch-to-bunch position correlation. The successful propagation of this level of correction to MFB1FF has been confirmed.

The propagation of the beam has been studied using a MAD model of ATF. The model was used to predict the beam position at MFB1FF given the measured positions at the feedback BPMs. A comparison of the measured and predicted positions has given a BPM resolution estimate of 315 ± 5 nm. Further propagation of the beam to the IP region has produced a beam jitter prediction of 10 nm at the waist, that is reduced to 4 nm on operating the upstream feedback system. These predicted jitters are consistently smaller than those subsequently measured using the IP BPMs, which is explained in terms of the limitations of the model and the limited resolution of the IP BPMs. In order to stabilise the measured beam position jitter at the IP, the operation of a local IP feedback system has been adopted.

Three high-resolution cavity BPMs have been installed in the IP region at ATF for the purpose of beam monitoring and IP feedback operation. Each cavity has a fast decay time of around 20 ns designed to allow multiple bunches to be resolved. The analogue signal processing electronics has been described, and the steps taken to ensure the correct timing of the signals have been presented. The single-point sampling and multi-sample averaging techniques used to process the digitised signals were discussed. The performance of the IP BPM system has been studied in detail, demonstrating an IP BPM system resolution at or below the 50 nm level when operating at a typical bunch charge of $\sim 0.5 \times 10^{10}$ electrons, as summarised below:

Position jitter at a single BPM
Having reduced the measured beam jitter by placing the beam waist at the chosen BPM, the correlation of the measured beam position with other parameters was studied. An unexpected correlation with bunch phase and charge was observed, which was mitigated by using multi-sample averaging. A minimum beam position jitter of 40 ± 2 nm was measured after correcting for a drift in the longitudinal location of the beam waist.

Noise floor limit to the resolution
The noise floor limit to the resolution was estimated to be 23.0 ± 0.7 nm by splitting the signal from one BPM into two nominally identical sets of electronics and comparing their outputs.

Beam interpolation between two BPMs
The two BPMs on either side of the IP were successfully operated using nominal ATF optics. The ability to interpolate the position jitter to the beam waist was demonstrated.

3-BPM resolution
The vertical position signals from the IP BPM triplet were used to obtain a BPM resolution estimate of 54 ± 1 nm using the model-based geometric method and of between 53 ± 1 and 57 ± 1 nm using the model-independent fitting method. The agreement between the two methods confirms that the model-based calculation successfully describes the system.

The operating principles and results of the IP feedback system have been presented. The IP kicker was exercised, demonstrating a linear response over a kick dynamic range of ± 5 μm as measured at IPB. The feedback system has achieved beam stabilisation at the 75 nm level which constitutes a significant improvement on the 100 nm level achieved previously. This level of correction is consistent with a BPM resolution of ~ 50 nm. The incoming beam position jitter was varied at the feedback BPM and the level of beam stabilisation matched the expectation given the measured incoming beam conditions. The static position offset between the first and second bunches in each train was successfully removed and a sustained feedback stabilisation of between 73 ± 5 and 83 ± 6 nm was achieved over the ± 5 μm linear dynamic range.

6.2 Suggestions for further work

As described in Sec. 4.7, there are some additional studies that can be performed once the required hardware is available. The first consists in using narrow-band BPFs on the C-band cavity signal outputs in order to remove unwanted modes. The second deals with simultaneously instrumenting both x and y signals from the three IP BPMs once the required number of limiter output channels is available, allowing a 3-BPM resolution calculation to be performed using measurements from both planes.

Single-point sampling and multi-sample averaging techniques have been presented to analyse the digitised signals (Sec. 4.2). Further work could be undertaken to study other data processing techniques, such as first integrating the raw I and Q signals over a range of sample numbers and then calibrating the integrated data obtaining single k and θ_{IQ} constants (Sec. 3.6.3). This technique could resemble the one used by a firmware algorithm in the future [115].

The final suggestion would consist in using the signals from two IP BPMs as inputs to the IP feedback algorithm, thus stabilising the beam at an interpolated location. In addition to providing a correction at a location other than the BPM itself, the use of two BPMs could improve the position resolution at the interpolated waist location compared to only using a single BPM at the waist (Sec. 4.6).

Bibliography

[1] M. Herrero, The standard model, NATO Sci. Ser. C 534 (1999) 1–59.

[2] P. W. Higgs, Broken symmetries and the masses of gauge bosons, Phys. Rev. Lett. 13 (1964) 508–509.

[3] K. Kodama, et al., Observation of tau neutrino interactions, Phys. Lett. B 504 (2001) 218–224.

[4] G. Aad, et al., Observation of a new particle in the search for the Standard Model Higgs boson with the ATLAS detector at the LHC, Phys. Lett. B 716 (1) (2012) 1–29.

[5] S. Chatrchyan, et al., Observation of a new boson at a mass of 125 GeV with the CMS experiment at the LHC, Phys. Lett. B 716 (1) (2012) 30–61.

[6] K.A. Olive, et al. (Particle Data Group), Chinese Physics C38 (2014) 090001.

[7] A. Sessler, E. Wilson, Engines of discovery: A century of particle accelerators, World Scientific & Imperial College Press, Singapore, 2007.

[8] CERN press office, LHC experiments are back in business at a new record energy, press release (3 June 2015).
URL `http://press.web.cern.ch/press-releases/2015/06/lhc-experiments-are-back-business-new-record-energy`

[9] R. Hellborg, Industrial accelerators (2013) 27–31.

[10] K. Kim, Characteristics of synchrotron radiation, AIP Conference Proceedings 184 (1989) 565–632.

[11] E. Wilson, An Introduction to Particle Accelerators, Oxford University Press, 2001.

[12] K. Wille, The Physics of Particle Accelerators, Oxford University Press, 2000.

[13] M. Furman, M. Zisman, Luminosity, in: A. Chao (Ed.), Handbook of Accelerator Physics and Engineering, World Scientific, 1999, pp. 251–254.

[14] R. Heuer, Role of accelerators in 'dark world', in: ICFA seminar, Korea, 2005.
URL `http://chep.knu.ac.kr/ICFA-Seminar/program.php`

[15] K. Gan, Physics with low-energy e^+ e^- and e^- e^- collisions at tau charm factory, in: proceedings of the Tau-Charm Factory Workshop, 1989, pp. 576–588.

[16] R. Lipton, Muon collider: Plans, progress and challenges, in: proceedings of the DPF conference, 2012, pp. 1–6.

[17] G. Arduini, et al., Electron-positron collisions at 209 GeV in LEP, in: proceedings of the PAC conference, 2001, pp. 356–358.

[18] E. Wilson, A review of accelerators beyond 2000, Phys. Scripta T30 (1990) 69–76.

[19] T. Behnke, et al., The International Linear Collider Technical Design Report - volume 1: Executive summary, CERN-ATS-2013-037 (2013).

[20] M. Aicheler, et al., A multi-TeV linear collider based on CLIC technology: CLIC Conceptual Design Report, CERN-2012-007 (2012).

[21] F. Borzumati, E. Kato, The Higgs boson and the International Linear Collider, Frontiers in Physics 2 (2014) 32.

[22] H. Baer, et al., The International Linear Collider Technical Design Report - volume 2: Physics, CERN-ATS-2013-037 (2013).

[23] G. Geschonke, A. Ghigo, CTF3 design report, Tech. Rep. CERN/PS 2002-008, CERN (2002).

[24] W. Kilian, M. Kramer, P. Zerwas, Higgs-strahlung and WW fusion in e^+e^- collisions, Phys. Lett. B 373 (1996) 135–140.

[25] M. Pivi, Beam-beam effects in particle colliders, in: lectures from US Particle Accelerator School, January 2011.
URL `https://uspas.fnal.gov/materials/11ODU/Beam-Beam.pdf`

[26] R. Amirikas, A. Bertolini, W. Bialowons, H. Ehrlichmann, Ground motion & comparison of various sites, Tech. Rep. EUROTeV-Report-2005-023-1, EUROTeV (2005).

[27] P. Burrows, et al., The FONT4 ILC intra-train beam-based digital feedback system prototype, in: proceedings of the IPAC conference, 2007, pp. 416–418.

[28] K. Steffen, Basic course on accelerator optics, in: lectures of the CAS CERN accelerator school: General Accelerator Physics, CERN, 1985, pp. 25–63, CERN 85-19.

[29] E. Wilson, Transverse beam dynamics, in: lectures of the CAS CERN accelerator school: General Accelerator Physics, CERN, 1985, pp. 64–95, CERN 85-19.

[30] S. Lee, Accelerator Physics, World Scientific Publishing Co., 2004.

[31] KEK: High Energy Accelerator Research Organisation.
URL `http://www.kek.jp/en/`

[32] F. Hinode, et al., Accelerator Test Facility: Design and study report, Tech. Rep. 95-4, KEK Technical Report (1995).

[33] K. Kubo, et al., Extremely low vertical emittance beam in accelerator test facility at KEK, Phys. Rev. Lett. 88 (2002) 194801.

[34] B. Grishanov, et al., ATF2 proposal, Tech. Rep. 2005-2, KEK Report (2005).

[35] P. Raimondi, A. Seryi, Novel final focus design for future linear colliders, Phys. Rev. Lett. 86 (2001) 3779–3782.

[36] G. White, et al., Experimental validation of a novel compact focusing scheme for future energy-frontier linear lepton colliders, Phys. Rev. Lett. 112 (2014) 034802.

[37] C. Adolphsen, et al., The International Linear Collider Technical Design Report - volume 3.I: R&D in the technical design phase, CERN-ATS-2013-037 (2013).

[38] C. Swinson, Development of beam position monitors for final focus systems at the International Linear Collider, D.Phil. thesis, University of Oxford (2010).

[39] ATF collaboration, Aiming for nanobeams: Accelerator Test Facility.
URL http://www-atf.kek.jp/atf/files/ATF-E1227.pdf

[40] S. Sakanaka, et al., Design of an RF system for the ATF damping ring, Conf.Proc. C950501 (1995) 1791–1793.

[41] J. Urakawa, ATF Results and ATF II Plans, in: proceedings of the PAC conference, 2007, pp. 1950–1954.

[42] M. N. Nguyen, J. Krzaszczak, Trip report for the installation and commission of the double extraction-kicker system at KEK - ATF, Tech. Rep. 06-04, ATF internal report (2006).

[43] A. Faus-Golfe, et al., Upgrade and systematic measurement campaign of the ATF2 multi-OTR system, in: proceedings of the IPAC conference, 2013, pp. 933–935.

[44] K. Kubo, ATF2 progress report, in: CLIC Workshop, 28 January 2015.
URL https://indico.cern.ch/event/336335/session/0/contribution/100

[45] P. N. Burrows, Feedback on nanosecond timescales (FONT): Results from first beam tests at the NLCTA at SLAC, in: proceedings of the PAC conference, 2003, pp. 687–689.

[46] P. Burrows, et al., Nanosecond-timescale intra-bunch-train feedback for the linear collider: Results of the FONT2 run, in: proceedings of the EPAC conference, 2004, pp. 785–787.

[47] P. Burrows, et al., Tests of the FONT3 linear collider intra-train beam feedback system at the ATF, in: proceedings of the PAC conference, 2005, pp. 1359–1361.

[48] R. Apsimon, et al., The FONT5 bunch-by-bunch position and angle feedback system at ATF2, Physics Procedia 37 (0) (2012) 2063–2071, proceedings of the TIPP conference, 2011.

[49] D. Bett, The development of a fast intra-train beam-based feedback system capable of operating on the bunch trains of the international linear collider, D.Phil. thesis, University of Oxford (2013).

[50] P. Burrows, et al., Design of the ILC prototype FONT4 digital intra-train beam-based feedback system, in: proceedings of the EPAC conference, 2006, pp. 849–851.

[51] B. Constance, Design and beam testing of a fast, digital intra-train feedback system and its potential for application at the International Linear Collider, D.Phil. thesis, University of Oxford (2011).

[52] C. Adolphsen, et al., The International Linear Collider Technical Design Report - volume 3.II: Accelerator baseline design, CERN-ATS-2013-037 (2013).

[53] R. Apsimon, et al., Design and performance of a high resolution, low latency stripline beam position monitor system, Phys. Rev. ST Accel. Beams 18 (2015) 032803.

[54] Instituto de Física Corpuscular.
URL http://webific.ific.uv.es/web/en

[55] R. Avery, A. Faltens, E. Hartwig, Non-intercepting monitor of beam current and position, IEEE Trans. Nucl. Sci. 18 (1971) 920–922.

[56] M. Davis, The development of intra-train beam stabilisation system prototypes for a future linear collider, D.Phil. thesis, University of Oxford (2014).

[57] Y. Honda, et al., Achievement of ultralow emittance beam in the ATF damping ring, Phys. Rev. Lett. 92 (2004) 054802.

[58] V. Sargsyan, Comparison of stripline and cavity beam position monitors, Tech. Rep. DESY-TESLA-2004-03, DESY (2004).

[59] Xilinx, Virtex-5 FPGA User Guide, v5.4 Edition (16 March 2012).
URL http://www.xilinx.com/support/documentation/user_guides/ug190.pdf

[60] S. Brown, R. Francis, J. Rose, Z. Vranesic, Field-Programmable Gate Arrays, . VLSI, computer architecture and digital signal processing, Springer US, 1992.

[61] J. Rogers, Feedback systems for coupled bunch instabilities, in: A. Chao, M. Tigner (Eds.), Handbook of Accelerator Physics and Engineering, World Scientific, 1999, pp. 494–498.

[62] SLAC National Accelerator Laboratory.
URL http://www.slac.stanford.edu

[63] C. Perry, Proposed Conversion of Stripline BPM Design to an IP Kicker (9 January 2011).
URL http://atf.kek.jp/twiki/pub/ATF/IPBPM-old/ipkickerSpec

[64] Mini-Circuits, Datasheet for coaxial pulse amplifier ZPUL-21.
URL 194.75.38.69/pdfs/ZPUL-21.pdf

[65] TMD Technologies Limited.
URL http://www.tmd.co.uk/

[66] R. Apsimon, The development and implementation of a beam position monitoring system for use in the FONT feedback system at ATF2, D.Phil. thesis, University of Oxford (2011).

[67] L. Lyons, Statistics for nuclear and particle physicists, Cambridge University Press, 1986.

[68] K. Kubo, Towards an International Linear Collider: Experiments at ATF2, in: proceedings of the IPAC conference, 2014, pp. 1867–1871.

[69] CERN BE/ABP Accelerator Beam Physics Group, MAD - Methodical Accelerator Design.
URL http://mad.web.cern.ch/mad/

[70] N. Walker, An introduction to the physics and technology of e^+e^- linear colliders. lecture 9: a) beam based alignment, in: lectures from US Particle Accelerator School, June 2003.
URL http://www.desy.de/~njwalker/uspas/coursemat/handouts/unit_9_handout.pdf

[71] Y. I. Kim, Cavity beam position monitor system for the beam delivery and interaction point of the Accelerator Test Facility 2 and future linear collider, Ph.D. thesis, Kyungpook National University (2012).

[72] R. E. Collins, Field Theory of Guided Waves, IEEE Press, New York, 1991.

[73] R. Lorenz, Cavity beam position monitors, AIP Conference Proceedings 451 (1) (1998) 53–73.

[74] D. Pozar, Microwave Engineering, Wiley, 2011.

[75] Z. Li, R. Johnson, S. R. Smith, T. Naito, J. Rifkin, Cavity BPM with dipole-mode-selective coupler, in: proceedings of the PAC conference, 2003.

[76] Y. Inoue, et al., Development of a high-resolution cavity-beam position monitor, Phys. Rev. ST Accel. Beams 11 (2008) 062801.

[77] M. Ross, J. Frisch, D. McCormick, H. Hayano, RF cavity BPM's as beam angle and beam correlation monitors, in: proceedings of the PAC conference, 2003, pp. 2548–2550.

[78] S. Walston, et al., Performance of a high resolution cavity beam position monitor system, Nucl. Instrum. Meth. A 578 (2007) 1–22.

[79] Y. I. Kim, et al., Cavity beam position monitor system for the Accelerator Test Facility 2, Phys. Rev. ST Accel. Beams 15 (2012) 042801.

[80] ATF lattice v5.2 (2013).
URL http://atf2flightsim.googlecode.com/svn/trunk/ATF2/FlightSim/latticeFiles/src/v5.2/

[81] T. Shintake, Proposal of a nanometer beam size monitor for e+e linear colliders, Nucl. Instrum. Meth. A 311 (3) (1992) 453–464.

[82] J. Yan, et al., Measurement of nanometer electron beam sizes with laser interference using shintake monitor, Nucl. Instrum. Meth. A 740 (0) (2014) 131–137, proceedings of the first European Advanced Accelerator Concepts Workshop 2013.

[83] Kyungpook National University.
URL http://knu.ac.kr/

[84] Laboratoire de l'Accélérateur Linéaire.
URL http://www.lal.in2p3.fr/

[85] O. Blanco, BPMs Positioning System, revision 8 Edition (14 April 2014).
URL http://atf.kek.jp/twiki/pub/ATF/IP-IPBPM-Movers/user_manual.pdf

[86] O. Blanco, private communication.

[87] S. Jang, The KNU electronics repair schedule and new IPBPM fabrication schedule, in: ATF IP BPM meeting, 22 April 2014.
URL http://atf.kek.jp/twiki/bin/view/ATF/IPBPMmeetings2

[88] S.-W. Jang, E.-S. Kim, Y. Honda, T. Tauchi, N. Terunuma, Development of a cavity-type beam position monitors with high resolution for ATF2 (2013) 604–606.

[89] S. Jang, KNU IP-BPM and reference cavity, in: ATF IP BPM meeting, 7 October 2013.
URL http://atf.kek.jp/twiki/bin/view/ATFlogbook/IPBPMMeeting20131007

[90] S. Jang, IPBPM beam test results and electronics summary, in: ATF IP BPM meeting, 27 February 2014.
URL http://atf.kek.jp/twiki/bin/view/ATF/IPBPMmeetings2

[91] T. Tauchi, Data of dipole resonant frequencies of previous IPBPMs, in: ATF IP BPM meeting, 3 February 2015.
URL http://atf.kek.jp/twiki/bin/view/ATF/IPBPMmeetings2

[92] Vactron, Reference cavity BPM ass'y, drawing number: KNU-RCB-0000.
URL http://atf.kek.jp/twiki/pub/ATF/IPBPMbyKNU/Ref._BPM_layout.pdf

[93] O. Blanco, ATF2 - IP chamber.
URL http://atf.kek.jp/twiki/pub/ATF/IP-IPBPM-Movers/BPMs_displacement_system_with_BPMs_(spots_for_3D_machine_shown).pdf

[94] C. Perry, private communication.

[95] S. Jang, IP-BPM status, in: ATF IP BPM meeting, 11 November 2014.
URL http://atf.kek.jp/twiki/bin/view/ATF/IPBPMmeetings2

[96] D. Bett, private communication.

[97] Y. Honda, private communication.

[98] Tektronix, Datasheet for digital phosphor oscilloscopes, TDS7000B series. URL http://uk.tek.com/sites/tek.com/files/media/media/resources/55W_13766_11_1.pdf

[99] Y. Honda, Bench test of limiter/int detector module, note. Japanese (23 October 2006). URL http://atf.kek.jp/twiki/pub/ATF/IPBPMmeetings2/limiter_module_test_0.pdf

[100] P. Strehl, Beam Instrumentation and Diagnostics, Springer, 2006.

[101] J. Staples, Non-linear circuit elements: Square-law detector, mixer, in: lectures from US Particle Accelerator School, November 2007. URL http://uspas.fnal.gov/materials/08UCSC/mml17_nonlinear_circuit_elements.pdf

[102] M. Minty, F. Zimmermann, Measurement and Control of Charged Particle Beams, Particle Acceleration and Detection, Springer, 2003.

[103] O. Blanco, Effect of AQF7FF(Y) on IPB, in: ATF IP BPM meeting, 20 January 2015. URL http://atf.kek.jp/twiki/bin/view/ATF/IPBPMmeetings2

[104] The Lucretia project homepage. URL http://www.slac.stanford.edu/accel/ilc/codes/Lucretia/

[105] Operation Log on 2014/05/29 - Swing Shift. URL http://atf.kek.jp/twiki/bin/view/ATFlogbook/Log20140529s

[106] Y. Renier, Implementation and validation of the linear collider final focus prototype: ATF2 at KEK (Japan), High energy physics - experiment, Université Paris Sud - Paris XI (2010).

[107] Mini-Circuits, Datasheet for ZX10R-14-S+. URL 194.75.38.69/pdfs/ZX10R-14+.pdf

[108] G. White, private communication.

[109] K. Kubo, A. Lyapin, J. Snuverink, Wakefield issues for the linear colliders, in: W. Chou (Ed.), Beam Dynamics Newsletter, no. 61, International Committee for Future Accelerators, August 2013, pp. 69–84.

[110] T. Okugi, private communication.

[111] S. Jang, IPBPM status, in: ATF IP BPM meeting, 14 October 2014. URL http://atf.kek.jp/twiki/bin/view/ATF/IPBPMmeetings2

[112] S. Wallon, private communication.

[113] T. Okugi, Operation Log on 2014/12/10 - Owl Shift.
URL `http://atf.kek.jp/twiki/bin/view/ATFlogbook/Log20141210o`

[114] T. Suwada, N. Kamikubota, H. Fukuma, N. Akasaka, H. Kobayashi, Stripline-type beam-position-monitor system for single-bunch electron/positron beams, Nucl. Instrum. Meth. A 440 (2) (2000) 307–319.

[115] G. Christian, private communication.